On the Modelling of Granular Flows in Industrial Applications via the Particle Finite Element Method

C. E. Dávalos
J. C. Cante
J. A. Hernández
J. Oliver

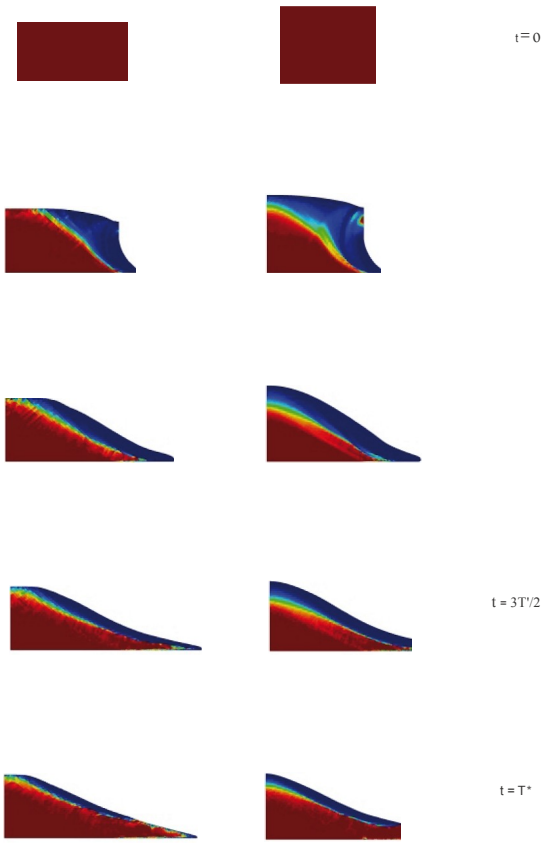

Monograph CIMNE Nº-151, November 2014

On the Modelling of Granular Flows in Industrial Applications via the Particle Finite Element Method

C. E. Dávalos
J. C. Cante
J.A. Hernández
J. Oliver

Monograph CIMNE Nº-151, November 2014

International Center for Numerical Methods in Engineering
Gran Capitán s/n, 08034 Barcelona, Spain

INTERNATIONAL CENTER FOR NUMERICAL METHODS IN ENGINEERING
Edificio C1, Campus Norte UPC
Gran Capitán s/n
08034 Barcelona, Spain
www.cimne.com

First edition: November 2014

ON THE MODELLING OF GRANULAR FLOWS IN INDUSTRIAL APPLICATIONS VIA THE PARTICLE FINITE ELEMENT METHOD
Monograph CIMNE M151

ISBN: 978-84-943307-3-5
Depósito legal: B-23560-2014

Abstract

The aim of this work is to present a new procedure for modelling industrial processes that involve granular material flows, using a numerical model based on the Particle Finite Element Method (*PFEM*). The numerical results herein presented show the potential of this methodology when applied to different branches of industry. Due to the phenomenological richness exhibited by granular materials, the present work will exclusively focus on the modelling of *cohesionless dense granular flows*.

The numerical model is based on a continuum approach in the framework of large-deformation plasticity theory. For the constitutive model, the yield function is defined in the stress space by a Drucker-Prager yield surface characterized by two constitutive parameters, the cohesion and the internal friction coefficient, and equipped with a non-associative deviatoric flow rule. This plastic flow condition is considered nearly incompressible, so the proposal is integrated in a $u-p$ mixed formulation with a stabilization of the pressure term via the Polynomial Pressure Projection (*PPP*). In order to characterize the non-linear dependency on the shear rate when flowing a visco-plastic regularization is proposed.

The numerical integration is developed within the *Impl-Ex* technique, which increases the robustness and reduces the iteration number, compared with a typical implicit integration scheme. The spatial discretization is addressed within the framework of the *PFEM* which allows treating the large deformations and motions associated to granular flows with minimal distortion of the involved finite element meshes. Since the Delaunay triangulation and the reconnection process minimize such distortion but do not ensure its elimination, a dynamic particle discretization of the domain is proposed, regularizing, in this manner, the smoothness and particle density of the mesh. Likewise, it is proposed a method that ensures conservation of material or Lagrangian surfaces by means of a boundary constraint, avoiding in this way, the geometric definition of the boundary through the classic α-shape method.

For modelling the interaction between the confinement boundaries and granular material, it is advocated for a method, based on the Contact Domain Method (*CDM*) that allows coupling of both domains in terms of an intermediate region connecting the potential contact surfaces by a domain of the same dimension than the contacting bodies. The constitutive model for the contact domain is posed similarly to that for the granular material, defining a correct representation of the wall friction angle.

In order to validate the numerical model, a comparison between experimental results of the spreading of a granular mass on a horizontal plane tests, and finite element predictions, is carried out. These sets of examples allow us validating the model according to the prediction of the different kinematics conditions of granular materials while spreading – from a stagnant condition, while the material is at rest, to a transition to a granular flow, and back to a deposit profile.

The potential of the numerical method for the solution and optimization of industrial granular flows problems is achieved by focusing on two specific industrial applications in mining industry and pellet manufacturing: the silo discharge and the calculation of the power draw in tumbling mills. Both examples are representative when dealing with granular flows due to the presence of variations on the granular material mechanical response.

Contents

List of symbols

$\mathbf{1}$	Second order symmetric unit tensor
Γ	Boundary domain
κ	Bulk modulus
κ_e	Kinetic energy
μ	Lamé's second parameter or shear modulus
π	Pressure term for mixed formulation (Cauchy stress tensor)
ρ	Density
$\boldsymbol{\sigma}$	Cauchy stress tensor
τ_R	Relaxation time
$\boldsymbol{\tau}$	Kirchhoff stress tensor
ϕ	Mohr-Coulomb internal friction angle
Ω	Geometrical region or continuum domain
$\mathbf{A}$, $\mathbf{a}$	Material and spatial description for the acceleration field
b_1	Internal friction parameter of Drucker-Prager type model
b_2	Cohesion parameter of Drucker-Prager type model
$\mathbf{b}$	Spatial description for body force vector
c	Mohr-Coulomb cohesion parameter
$\boldsymbol{c}$	Fourth order spatial elasticity tensor
$\mathbf{d}$	Rate of deformation tensor
$\boldsymbol{\mathcal{i}}$	Fourth order symmetric unit tensor
J	Jacobian determinant
$\mathbf{e}$	Euler-Almansi strain tensor
$\mathbf{F}$, $\mathbf{f}$	Total and incremental deformation gradient tensor
$\boldsymbol{l}$	Spatial velocity gradient
$\mathcal{P}_{\text{int}}$	Rate of the internal mechanical work
$\mathcal{P}_{\text{ext}}$	Rate of external mechanical work
p	Mean stress (Kirchhoff stress tensor)

$\tilde{p}$	Pressure term for mixed formulation (Kirchhoff stress tensor)
q	Norm of deviatoric stress (Kirchhoff stress tensor)
$\mathbf{U}$, $\mathbf{u}$	Material and spatial description for the displacement field
$\mathbf{V}$, $\mathbf{v}$	Material and spatial description for the velocity field
$(\bullet)^e$	Elastic part of a tensor
$(\bullet)^p$	Plastic part of a tensor
$(\bullet)_n$	Intermediate configuration
$(\bullet)_{n+1}$	Current configuration

Chapter 1
Modelling of granular materials

1.1. Introduction

Granular materials can be broadly defined as large conglomerations of discrete particles. They are ubiquitous in nature and handled in a large number of industrial processes. However, in spite of the wide use of these materials and the apparent simplicity of their definition, a complete understanding of their mechanical properties and their behaviour is far from being achieved.

Some of these difficulties arise from the many materials that encompass this definition as well as the peculiar response of the material itself under external mechanical excitations. The physics of granular materials embrace different phenomena, varying from large rock debris flows to the consolidation of the material under sustained pressures; all of them presenting different responses and difficulties in their comprehension.

Due to the intrinsic interaction of the particles that comprise granular materials, these materials present complex behaviours that could be related to different states of matter. Their mechanical response differs from other standard materials: in static conditions they could be considered and modelled as solid bulks; under dynamic conditions the kinematics could be described by the physics of fluids; and subject to an interstitial fluid, their response could be represented as a gas. These particularities make granular materials an interesting topic where many proposals have been developed in order to clarify and understand their behaviour and influence in industrial processes and nature.

It is pretentious the attempt to develop a numerical model able to capture –in a unified manner– the phenomenological richness exhibited by granular materials. Rather, the present work will exclusively focus on the modelling of *cohesionless*

dense granular flows. In specific, this work concerns with the development of a numerical model suitable for the simulation of granular flows in order to predict diverse configurations in static and dynamic conditions as well as their non-equilibrium dynamic transition. The model is based on a rate-dependent constitutive model in the framework of the Particle Finite Element Method (*PFEM*). The fundamental goal of this work is to contribute to a better understanding of cohesionless dense granular flows occurring in processes that have important repercussions in industry and society.

1.2. Understanding granular materials

When talking about a mathematical model of a certain physical system, it is taking for granted that the model contains several simplifying assumptions. Granular material models are not exception to this fact. Therefore, it is important to have a deep understanding of the implication derived from these assumptions, as well as the effect in modifying the main parameters that characterize the behaviour of the material.

Since the response of granular materials to external loads –such as shearing or vibration– is strongly influenced by the particles that conform the material as well as the bulk itself, it is important to clarify some concepts such as: which materials fall within the category of granular media, how to characterize and model them, and which mechanical properties are relevant and which are unessential.

As mentioned above, the scope of this section is not to explore the whole universe of granular materials but to define and narrow the main mechanical and material properties as well as the kinematic conditions that are going to be modelled. Lastly, some numerical models and formulations that have been developed along time by different authors are presented.

1.2.1. Granular material definition

Granular materials comprise any conglomeration of a large number of discrete macroscopic particles [48]. As the term macroscopic deals with objects that are at least visible to the naked eye, many materials are included in this definition. From this point of view, granular material definition embraces objects of several orders of magnitude. Some authors, like [29], state that the physical laws that govern the granular material behaviour cover at least twelve decades of sizes.

The mechanical properties of a granular domain depend on the interaction of the particles in their surrounding neighbourhood. This interaction is defined through the contact forces –friction or/and collisions– between the particles as well for the surrounding environment where the particles are located. Since granular media represents discrete solids that are in contact most of the time, the interstitial fluid or sur-

rounding media has to allow the particle interaction. This consideration excludes other materials as suspensions or fluidized beds.

The interaction between particles could be catalogued by two main characteristics: discrete elements dispersed in a continuous phase, referred as the interstitial fluid; and particles in direct contact where the continuous phase is neglected [18]. The first regime is defined by hydrodynamic interactions and the interaction of the particles within the liquid molecules defines the material cohesion. The force required to place into a relative motion two particles is higher as the distance h is reduced; see Figure 1-1(a).

If the influence of the environment is neglected, the granular material is defined as *dry* or *cohesionless*. This assumption is given when the distance between particles h is smaller than the roughness of the particle ε which defines as negligible the existence of an interstitial fluid, see Figure 1-1(b). In a cohesionless material, friction and gravity forces of the particles dominate the physics of its behaviour and the shape of the domain is defined by its confining boundary [48]. Even though the dry granular assumption is considered as a laboratory condition, it is widely used since it simplifies the resulting system in order to its study. Otherwise, depending on the surrounding media involved, other assumptions have to be in mind to model the cohesion between particles [71].

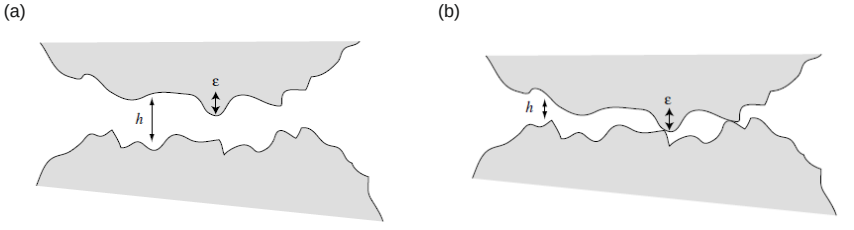

Figure 1-1. Schematic representation of two different types of direct interaction between solid particles: (a) lubricated contact; (b) direct contact [18].

In a meso and macro-scale, granular materials are considered athermal. This condition is due to the order of magnitude between the discrete particles and the bulk domain [96]. As the internal processes do not involve either heat or a change in temperature, the kinetic and potential energies play a fundamental role. Every friction and collision between particles lead to a dissipation of the kinetic energy causing that the granular material represent a non-ergodic material.

1.2.2. Problems in nature and industry involving granular material flows

Granular materials have a direct impact in our daily lives, since in nature they are one of the most abundant materials and in the industry the second most manipulated

material, just behind water [84]. Below are described some of the most relevant problems generated by granular flows in nature and industry.

1.2.2.1. Granular materials in nature

The relevance of granular materials in nature is not because the obviousness of their presence, but rather by the large and diverse phenomena where they are involved. Among these are found stratification of rocks and sands in rivers due to segregation [29]; cliff collapse and landslides [68]; and mechanisms of mass spreading like avalanches and debris-flows [44]. These actions represent natural hazards that nowadays constitute a threat to population and infrastructure.

Figure 1-2. Landslide in the population Las Teclas, El Salvador in 2001 [100].

The definition of landslides, debris flows, and avalanches are quite similar since they are large volumes of granular material with particles of considerable size flowing. Attempts to classify these phenomena vary depending on the author or engineering area where the classification is made. A classification according to the material components (granular or cohesive) is given by [19] as seen in Figure 1-3. The flow is defined depending on the amount of volume fraction and the particles size that comprises.

From this classification, *muddy debris* flows are characterized by containing a large fraction of fine particles, as well as a large volume of cohesive material like particle-water mixture. On the other hand, *granular debris* flows feature particles with larger size, and small or none cohesive interactions.

According to Coussot [19], due to the proper characteristics of granular debris flows –dilatancy, segregation, bistability, thixotropy, jamming, among others effects, the confined rheometrical tests are not suitable to cast realistic data to comprehend these phenomena.

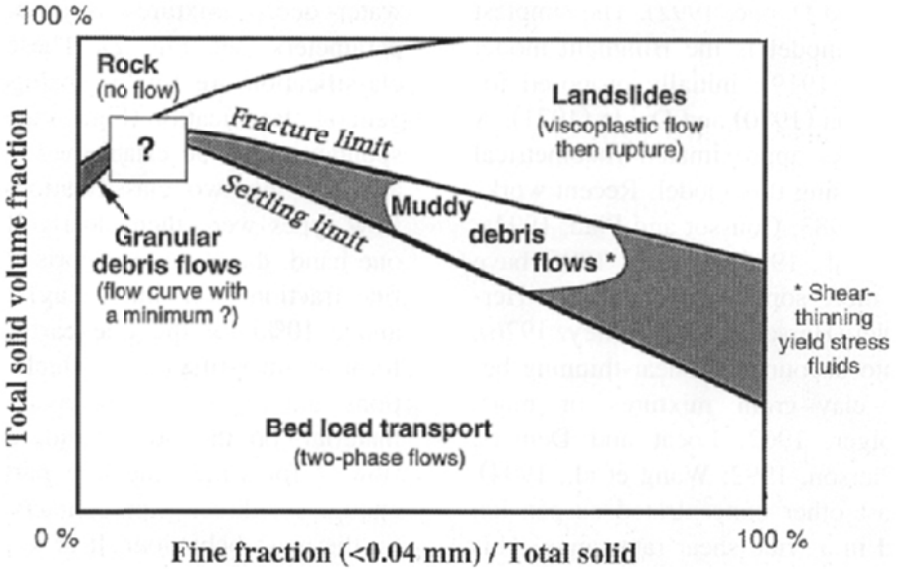

Figure 1-3. Conceptual rheological classification of mass movements as a function of fine content and solid fraction [19].

1.2.2.2. Granular material in industry

Industry consumes about 10% of all the energy produced on the planet for the handling and processing of these materials [29]. Their presence includes construction, pharmaceutical, mining, agricultural, among other industries. The processes vary depending on the sector, all of them carrying different problems intrinsic to the behaviour of the material: blockage, segregation, arching, jamming, dilatancy, etc. Despite the significance of the impact of granular materials in economy, many of these problems are treated with inchoate solutions.

The problems associated to granular flows vary depending on the industrial processes and the material. Granular materials that involve particles of different sizes or composition are conditioned to the presence of segregation. In processes where the mixture of these types of particles has to be homogeneous, segregation is a perennial problem.

Many industries which involve the use of granular materials have the requirement of the confinement of the material –for storage purposes or industrial processes. Processes that implicate silos storage and discharge of granular materials are of special interest. The pressure patterns could vary abruptly from the storage condition to the discharge process. Depending on geometrical properties of the silo, including the outlet placement, the maximum wall pressures would vary largely from the storage condition to its discharge. Other problems as blockage during discharge are strongly influenced by the grain size as well as the outlet diameter. Chapter 5 is precisely devoted to numerically assess the influence of flow patterns in silos as well

as the mechanisms of stress propagation found during the discharge. Figure 1-4 shows an experimental silo built in order to develop tests for the understanding of silos discharge patterns [89].

Figure 1-4. Facilities built for the experimental discharge of a full scale silo [89].

Another industrial branch of special interest when speaking of granular materials is the mining industry. Several processes involve the handling and manipulation of granular materials since their extraction to their final placement. One of them is the comminution of the material, more specifically through a tumbling milling process, see Figure 1-5.

(a) (b)

Figure 1-5. Milling facilities: (a) autogenous mill in Garpenberg, Sweden [97]; (b) an inside view of mill drum at Gays River, Canada [32].

Comminution of the material consumes 50% of the total mineral processing cost [17]. The study of the kinematics of the charge during the tumbling process allows us to understand how energy is consumed and what efforts could be done in order to improve it. Similarly, Chapter 5 presents a numerical study of a simplified milling process.

1.2.3. Characterization of granular materials

The mechanical response of granular materials depends on numerous material parameters of the bulk[1], as well as the mechanical properties of the particles themselves. Any variation of these properties will produce a significant change in the response of the material whereby it is essential to characterize the material one wishes to simulate –for this work, the model is narrowed to *cohesionless dense granular materials* defining the main material parameter as the internal friction.

Two geometrical parameters that play a fundamental role in their response are the size and shape of the particles. Regarding the particle size, their dimensional range varies from micro particles to large rocks. Depending on the concerned industry, we could find different classifications. A coarse classification is given by [29] where the departing size is for a powder where the granular medium is formed by particles smaller than 100 μm in diameter, broken solids constituted by particles larger than 3 mm, and rocks that could reach their upper limit by a few meters.

Other classifications are found for geotechnical purpose since soils are bodies composed by granular material. Traditionally, the soil relationships and classification is based in a grain-size criterion. Generally, soils are non-homogeneous materials with different sizes and grain shapes but their classification is based on a percentage of the material that sieves through certain size. There are different classification systems, among them one of the most used is the presented by the Unified Soil Classification System. A simple classification is given, determining as coarse grained soils those where 50% of the material is retained in a No. 200 sieve (0.075 mm), and fine grained soils those that pass [104]. Other system classifications, such as the one given by the American Association of State Highway and Transportation Officials (AASHTO), have similar considerations.

For the purpose of this work, it is followed the classification given by [75] in Table 1-1. Even though the material considered for this model follows the classification as granular solid or broken solid, bigger size particles could be modelled with this classification, as long as the bulk they conform is considerably larger compared with the particle size.

The shape of the grains, characterized by the aspect ratio, angularity, and convexity, has large influence in the mechanical properties of the bulk. It is reported that this shape effect is reflected mainly in the porosity of the material, but also some blockage could be present in the flow with particles of large aspect ratio [7]. Similarly to the size of the particles, the shape influence is reduced as the volume of the granular domain is larger compared to the grain.

[1] The mechanical properties of granular materials to consider depend directly on the enginery branch of study. Among them are found the internal friction angle, cohesion, specific weight or weight density, degree of saturation, the void ratio, the plastic limit, etc.

Particle size range	Name of material	Name of individual component
0.1 μm – 1.0 μm	Ultra-fine powder	Ultra-fine particle
1.0 μm – 10 μm	Superfine powder	Superfine particle
10 μm – 100 μm	Granular powder	Granular particle
100 μm – 3.0 mm	Granular solid	Granule
3.0 mm – 10 mm	Broken solid	Grain

Table 1-1. Granular material size classification [75].

1.2.4. Granular material behaviour

The understanding and modelling of granular materials are difficult tasks since they do not behave as other familiar states of matter. In static conditions, when the contacts between particles are well established, the material could be considered as a solid with high strength to compression. In other configurations, where the external excitation snaps off these contacts, the material behaves as a fluid.

The mechanical response of the granular material is mainly influenced by the interactions between particles –dissipative, inelastic collisions and frictional properties [48]. Temperature changes do not play a significant role or could be neglected, at least at a macroscale level. For this reason granular materials are considered athermal.

Regarding the dissipation of kinetic energy due to friction, it can be studied in terms of the set of laws for frictional bodies, generally attributed to Coulomb. Those laws state that the force of traction required to set a system in motion is proportional to the normal force acting between the bodies, and the force of traction is independent of the surface area of the bodies. Both concepts as well as the distinction between the static and dynamic friction between particles are completely applicable to granular materials.

In order to define a correct model, it is necessary to delve into the static and dynamic conditions in granular materials. Even though their behaviour is characterized in some moments as solid or fluid, they could not be either studied or represented with similar formulations. The following sections will focus on the static and dynamic conditions of granular materials.

1.2.4.1. Static properties of a granular medium

Granular material equilibrium is reached when the system of inter-particle forces is in equilibrium. Due to the forces acting on them (body forces, excitation), the transmission of the loads are carried via these inter-particle contacts or force chains [95]. The behaviour of the material is considered elastic as long as the displacement between particles is slight. These displacements could rearrange the contacts but the bulk deformation is considered recoverable.

An example of this equilibrium is found in a pile of dry sand. It is impossible to build a pile with nearly vertical sides. The material tends to equilibrate collapsing

the pile of material until it is generated a slope with an equilibrium angle, which is called *angle of repose*. The equilibrium is attained when frictional forces avoid rolling and gliding of the particles. In an ideal configuration of homogeneous particles in size and shape, as a stack of cannon balls, the pattern of the contacts between them could be considered highly ordered but in reality there exists a large number of solutions where the contacts are produced with an indeterminate solution [29]. The sheer number of possible solutions in the contact configuration between particles complicates the task of setting or defining a unique angle of repose.

The transmission of loads in a confined domain follows the same principle. As the external load is increased, new clusters of force chains are defined, producing additional stress paths. Figure 1-6 shows a two dimensional representation of stress paths presented while a granular material is subject to compressive loads.

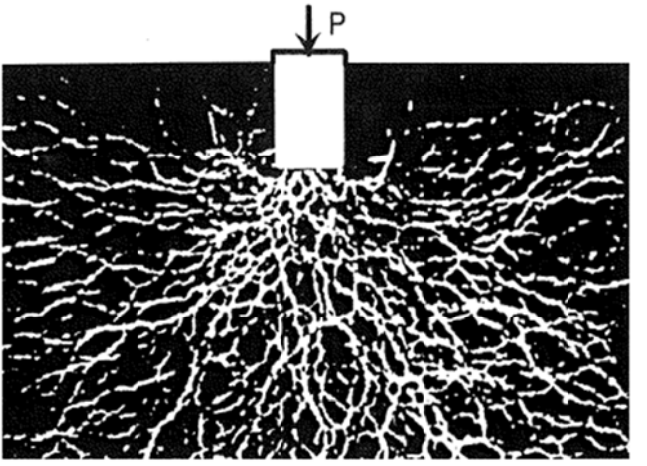

Figure 1-6. Stress pattern observed in a two-dimensional granular material under compressive external loads [29].

By increasing the contact zones, the void ratio is reduced which leads to an increment of the structure stiffness, leading to significant deviations from the linear response of an elastic regime [29].

The many indeterminacies and hysteresis phenomena affect the packing of granular materials. Depending on the filling process for any container, the volume fraction of packed material will vary between 0.55 and 0.64 [48]. The density of the bulk only is affected by the disturbances in the container induced by an external source. Studies report that the relaxation of granular media under vibrations is logarithmically slow [58]. An example is a tube filled with granular material that could present significant compaction before reaching a steady state after 100,000 vibration cycles.

Materials confined in tall recipient, such as in silos, present peculiar characteristics. As opposed to fluids, pressure does not increase proportionally with height. Due to the internal friction angle and the static friction with the container, the pres-

sure distribution reallocates, being able to exert compression forces on the walls of the order of 80% of the weight [83].

1.2.4.2. Dynamic properties of a granular medium

The flow in granular materials occurs when the displacement between the particles is large enough that the contact between those is lost, causing the particles to roll and glide between them. The transition from the static or stagnant condition to flow is known as a non-equilibrium *dynamic transition* or *jamming transition* [96]. An example is given with any pile of granular material which is at repose, Figure 1-7 (a). It will tend to flow as long as the base is raised to a certain angle that breaks its internal friction angle, see Figure 1-7 (b).

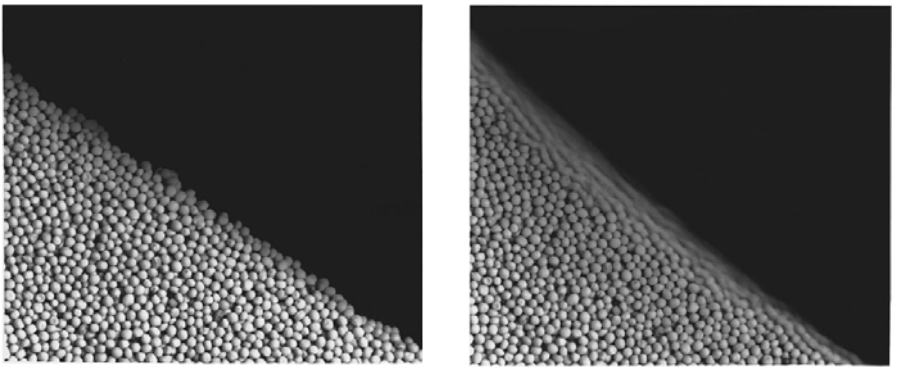

Figure 1-7. (a) A pile of mustard seeds at repose. (b) The same pile after the base is raised causing sliding of the seeds [48].

The jamming transition is a topic that deserves special attention. It relates the transition from a stagnant condition to a fluidization of the material. A simplified model is presented by [15]. The model assumptions neglect the frictional forces between particles in order to focus on the interaction of the chain forces clusters. The system will remain in equilibrium as long as the supported loads are compatible with the chain forces, in this case the longitudinal compressive forces, see Figure 1-8 (a). The particles in an elastic regime may present finite deformability, carrying transverse loads Figure 1-8 (b). A disturbance in the granular structure will occur when the loads are not compatible with the cluster. For real domains of granular material, it means it is present when the transversal load exceeds the frictional forces in the chain.

(a) (b)

Figure 1-8. (a) Compatible loads for a force chain without friction resistance. (b) Finite deformation in particles carrying small transverse loads [15].

The transition from static to a dynamic condition for granular materials is ruled not only by the friction between particles, but also by the collisions among them. The predominance of friction or collision between particles is directly defined by the coefficient of elastic restitution of the material, prevailing collision in the material for larger values of this coefficient. Due to these conditions, it has been stated by different authors that the representation of a flow in a granular medium could not be described by the Brownian motion ([48], [29]). An example to discard this representation is the segregation presented in the medium when it is applied shaking cycles to the domain.

The classification of granular flows is in terms of the predominant regime of interaction between the particles. *Rapid* granular flows are characterized by large velocity gradients, presenting high collisions between particles; in contrast, *slow* flows present particles in contact most of the time [9].

1.2.5. Granular material numerical simulations

Numerical simulations offer the possibility to explore the effect of diverse parameters which are not accessible to experimentation. Simulation of granular flows is not the exception. There is not a full comprehensive theory to predict their behaviour in the industrial processes neither in nature phenomena; therefore, the use of numerical models allows us to compare with experimental as well to explore diverse parameters that are not possible through experimentation.

Due to the inherent behaviour of granular flows, many proposals for their modelling have been defined. Generally, they could be classified in two main groups: *discrete methods* and *continuum methods*, both of them presenting their own advantages and drawbacks [29].

Discrete methods born from the natural idealization of the particles interaction controlled by their contact and defining their motion explicitly [21]. These methods

are generally considered as the more suitable way to describe granular materials since they are a conglomeration of discrete particles. The application of these methods in slow and rapid flows arise from the similitude with the material applying kinetic theory to obtain constitutive relations that govern the interaction between the particles [85].

In classic discrete methods, the particles are characterized as hard and soft spheres. In the first case are the so-called event-driven models (*ED*), which the collisions between grains are nearly energy conserving; the second are defined for the molecular dynamics models (*MD*), taking into account the elastic restitution of the spheres, allowing to penetrate into each other.

The velocity profiles play a fundamental role for comprehending granular flows. On discrete methods, the formulation for the velocity prediction is established in terms of kinematic models. Generally this assumption is considered as a drawback of these models since the velocity profiles are defined as a function of geometric parameters instead of a stress-strain relation.

The use of discrete methods for modelling granular flows in industrial processes has been widely investigated over the last three decades. They have been used widely for silos discharge simulations ([41],[35],[60]); milling processes in mining industry ([70],[53]); among other processes. Numerical results have been useful to understand the kinematics of granular flows in those industrial processes. However, they present important drawbacks, such as the large number of particles needed to represent real processes; the large computational cost to define the contacts between particles; and the difficult to represent stresses and pressures in the material.

The use of the continuum approach to formulate a model for granular materials is not recent. This assumption has been traditionally used for soils mechanics, generally under static and compression conditions, and in recent decades it has been extended for granular flow problems. In order to relate a discrete system as a granular domain into a continua, studies such as the one given by Duran [29], demonstrate that describing the kinematics of the media by differential equations is correct as long as the number of particles involved is large enough. The concept is merely intuitive and consists in relate the discrete description into a continuum by defining a surrounding space over each particle, large enough to overlap neighbouring particles. Defining a proper function for the surrounding *cloud* of each particle, the assumption enables to define variables, as density ρ and macroscopic velocity $\mathbf{v}$, through a set of macroscopic quantities continuous in space and time.

The Smoothed-Particle Hydrodynamic method (*SPH*) is a *meshfree* method that consists in the representation of a domain by a set of arbitrary distributed particles with specific mass, momentum and energy where no connectivity is needed. The internal density and internal forces are given by the conservation equations of continuum mechanics. The computation of the solution is given through the function value at each node as a result of a summation of the neighbouring nodes where their influence are varying with the distance between the nodes and the value of the kernel function [37]. It was originally conceived for astrophysical problems in three-dimensional space, but its application was extended for dynamic fluid flows [66]. In

recent years, the capability of this method to model granular material has been also explored [11].

The finite element method is based on the discretization of the variational principles defined for the continuum theory. Extensive studies on variational principles for granular materials can be found in ([20],[22],[61]). As any other continuum-based model, the balance equations for mass and momentum are to be complemented by an appropriate constitutive model that represents both the failure and the flow mechanisms in the material. One of the drawbacks of the continuum approach is connected with the description of velocity fields equations, since there is no agreement as how to express these equations. One of the solutions to overcome this difficulty arrives from plasticity theory, assuming that stresses and velocity profiles are correlated by the proper definition of a flow rule ([75],[90]).

Due to the large deformations exhibited by granular flows, the Eulerian description is in principle more suited for models in stationary regime. For industrial processes, like silos discharge, we could find diverse works that employ Eulerian mesh descriptions ([81],[56],[31],[106]); similarly, simulations of debris flows following this approach can be encountered in [72]. The advantage of the Eulerian approach is that the description of the granular flow can be carried out with a fixed mesh; likewise, the prediction of internal stresses and pressures in the material as well as in the containers are relatively straightforward to obtain. On the other hand, among the main disadvantages, it may be mentioned the difficult to determine the free surface, and the study of transient phenomena.

By contrast, Lagrangian descriptions do allow us to model free surfaces conditions. The first attempts to leverage this were made through the Arbitrary Lagrangian-Eulerian (*ALE*) method, a hybrid technique that captures the advantages of both descriptions and minimizes their disadvantages [3]. Even though we could find work exploring *ALE* in granular flows [103], it has not been so extensive its inclusion. One of the main drawbacks of the technique is the arbitrary definition of the Eulerian and Lagrangian meshes by the user, being susceptible to present abrupt deformations and numerical singularities. This condition constraints the methodology to model large deformation problems (e.g. milling processes and impact of granular flows as in debris-flows).

The Particle Finite Element Method (*PFEM*) arises as an evolution of meshless methods applied to fluid flows. It is defined in a Lagrangian description, but the drawbacks inherent due to the large deformation of the mesh are avoided with robust techniques of discretization and remeshing [46]. In the field of granular materials, recent works have explored the possibilities of such a technique in the simulation of bed erosion due to fluid-structure interaction [80]; ground excavations [14]; and dam structures [64].

The *PFEM* technique enables us to study large deformation problems such as granular flows. This advantage, together those inherit to the standard finite element method –proper description of internal stresses and pressure– allow us to define an appropriate and robust numerical tool to perform models of granular flows in industrial processes as the milling of granular and the discharge of silos.

1.2.6. Constitutive models for granular flows

The basis of a continuum description is the relationship between deformation and stresses given by the constitutive model. Nowadays, there is no a constitutive model capable to reproduce every singular condition of granular flows, let alone for granular materials in general. It is of fundamental importance, therefore, to develop theories able to characterize and predict the complex behaviour of granular materials.

The description of constitutive models for granular materials generally is defined in terms of the *Saint-Venant's* hypothesis (also known as the coaxiality condition [40]). This hypothesis states that the principal axes of the stress and strain-rate tensor should coincide. This assumption leads to material isotropy as well as to the definition of the rate of strain tensor as a function of the Cauchy stress tensor.

Granular materials present a pressure sensitive behaviour, which means, the flow properties of the material depend on the first invariant of the stress. Although this dependence is usually assumed linear, experimental studies [105] reveal that for large compaction levels the deviation from the linear dependence may become significant. Therefore, the adoption of such assumption excludes the possibility of modelling processes where compaction due to external loads is significant [43].

Mohr-Coulomb and Drucker-Prager models define their failure criterion in this pressure linear dependency. Both models are defined essentially in terms of two material parameters, namely, the internal frictional angle θ and the material cohesion c.

The Mohr-Coulomb yield surface defines, in terms of principal stresses, the failure of the material through a critical combination of the shear stress and its volumetric pressure for any plane [3]. This relationship is linear and the failure is reached when some point is located on the limit of the elastic domain defined by its yield surface. This linear relation is stated through the following equation:

$$q_{MC} = c - \sigma \tan\theta \tag{1.1}$$

where q_{MC} is the magnitude of the shear stress and σ the normal stress on the plane. This criterion could be seen as a generalization of Tresca's criterion[2] since its maximum tangential stress strength depends of its stress state [107].

In terms of the principal stresses, the Mohr-Coulomb yield surface can be rephrased as

$$F(\boldsymbol{\sigma}) \equiv \frac{1}{2}(\sigma_1 - \sigma_3) + \frac{1}{2}(\sigma_1 + \sigma_3)\sin\theta - c\cos\theta = 0 \tag{1.2}$$

Observe that the failure criterion depends on the maximum and minimum principal stresses.

The other well-known alternative is the Drucker-Prager yield surface. Similarly to the previously described criterion, this model establishes a linear dependence between the material strength and the pressure exerted on the material. The expres-

[2] Tresca's and Mohr-Coulomb yield surfaces will coincide setting the internal friction angle to a null value for the frictional material and defining its cohesion as the maximum shear stress possible.

sion for the failure criterion, expressed in tensor invariants, is given by the following expression:

$$F(\boldsymbol{\sigma}) \equiv \alpha I_1 + \left(J_2^{'}\right)^{1/2} - \beta = 0 \tag{1.3}$$

where I_1 and J_2 are the first and second invariants (the apostrophe stands for the invariant of the deviatoric tensor), and α and β the Drucker-Prager internal friction angle and cohesion respectively. The invariants for the stress tensor are defined as follows:

$$\begin{aligned} I_1 &= J_1 = \sigma_{ii} = \mathrm{Tr}(\sigma) \\ J_2 &= \frac{1}{2}\sigma_{ij}\sigma_{ji} = \frac{1}{2}(\boldsymbol{\sigma} : \boldsymbol{\sigma}) = \frac{1}{2}\mathrm{Tr}(\boldsymbol{\sigma}\cdot\boldsymbol{\sigma}) \\ J_3 &= \frac{1}{2}\sigma_{ij}\sigma_{jk}\sigma_{ki} = \frac{1}{2}\mathrm{Tr}(\boldsymbol{\sigma}\cdot\boldsymbol{\sigma}\cdot\boldsymbol{\sigma}) \end{aligned} \tag{1.4}$$

As may be inferred from the preceding equations, the model is independent of the third stress invariant, which means that for a certain point that reaches the yield surface, all the rest of points with the same magnitude of the other two invariants will yield.

The material parameters, internal friction angle and cohesion, of the Drucker-Prager and Mohr-Coulomb models are related using the proposal of [51]

$$\alpha = \frac{2\sin\theta}{\sqrt{3}(3-\sin\theta)} \tag{1.5a}$$

$$\beta = \frac{6c\cos\theta}{\sqrt{3}(3-\sin\theta)} \tag{1.5b}$$

In contrast with the Mohr-Coulomb failure criterion, it represents a cone along the hydrostatic axe, being the Mohr-Coulomb surface embedded inside the Drucker-Prager surface, as shown on Figure 1-9.

As opposed to the Mohr-Coulomb criterion, the Drucker-Prager model establishes the failure condition for all points with the same value of the invariants I_1 and $J_2^{'}$, since it is independent of the third invariant.

In order to improve the capability of the models, many enhancements have been developed. Among them it is found the use of multiple surfaces, as in the *Cam Clay* model proposed by [88] and its subsequent modifications; multiple parameters cap models like the one proposed by [91]; formulations based on the bounding surface, developed by [27], and extended in ([65],[8]); isotropic and anisotropic kinematic hardening ([74],[5],[82]); and endochronic plasticity theory for cycling loads ([1],[101]). All these enhancements in the models provide more accurate descriptions of granular media, but at the expense of simplicity, forcing to characterize the material in terms of several parameters [105].

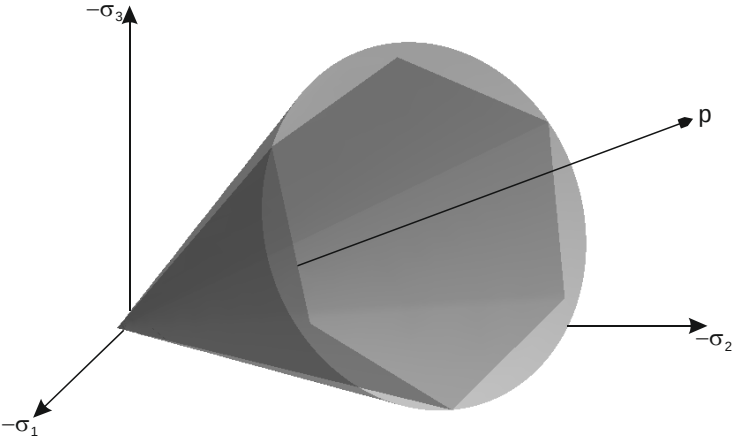

Figure 1-9. Drucker-Prager / Mohr-Coulomb yield surfaces.

Broadly speaking, the modelling of granular flows has two relevant aspects to be considered. First, the volume variations present on granular material during deformations. Granular flows present dilatation or volume expansion, while in other cases due to shearing or large compaction forces there is presence of contraction [40]. In consolidated materials or dense flows, the dilation effect occurs at the initial stages, decreasing until the effect dissipates [75]. It is important, in plasticity theory, to ensure a correct flow rule that predicts with sufficient accuracy the deformation path.

The second consideration in the modelling process is the energy dissipation for cohesionless materials [40]. The model has to represent the dissipative mechanisms due to the friction and collisions between particles. Some approaches to overcome this difficulty is through hardening and softening rules or by the formulation of plasticity failure using a non-associative flow rule [107].

1.3. Objective and scope

The overall goal of this work is to develop a numerical tool for the simulation of *cohesionless dense granular flows*, with emphasis on applications for *industrial processes*. Two main objectives are defined in order to achieve this goal:

- To establish a constitutive model capable to reproduce the stress-strain relations for cohesionless granular slow flows.
- To develop a numerical algorithm capable to perform large deformation transient problems based on the *PFEM*.

The scope for each main objective is summarized as follows. First, the constitutive model is developed in the framework of large deformation visco-elasto-plasticity. The model has to be able to reproduce the kinematics of cohesionless granular flows, as well as the jamming transition from the stagnant condition. As mentioned earlier, the variations in volume are not relevant; for this reason, the material is treated as nearly incompressible.

In order to circumvent locking problems, it is proposed the decoupling of the constitutive model via a mixed formulation in terms of displacements and pressures. The stabilization method for the pressures is defined via the polynomial pressure projection proposed by [28].

The proposed numerical algorithm is based on the Particle Finite Element Method (*PFEM*), a method specially conceived for large deformation problems. The spatial discretization and remeshing process is enhanced by a robust reconnection algorithm capable to correct and optimize the mesh as the deformation proceeds. The granular material-structure interaction is treated using a contact method derived from the Contact Domain Method proposed by [77]. The assembly of these algorithms will allow handling large deformation problems with relative coarse meshes in a robust and efficient manner.

It has been stated before that no model for granular materials is capable to reproduce all kinematic and static conditions –for any material and geometric parameters. Needless to say, the proposed model is no exception; the following assumptions have been taken into account in developing it:

- The domain under study has to be considerable larger than the size of particles in order to use a continua formulation.
- The material model is suitable for dense granular materials. This means that during the flow condition, particles tend to remain in contact. Intrinsically, this assumption leads to slow granular flows, since for rapid flows the kinematic condition that prevails is the collapsing of particles instead of the frictional.
- The constitutive model is defined through a Drucker-Prager yield function, which is based on the coaxiality condition. This assumption is correct for materials with isotropic behaviour. In order to satisfy this condition, the granular particles have to be homogeneous in size and shape.

The scope of this work is to fulfil the objectives by modelling dense granular flows in diverse kinematic conditions. The set of experimental examples conducted by [62] has been chosen to validate the constitutive model. The robustness and efficiency of the numerical simulation is studied by comparing the model results with the experimental study of a silo discharge performed by [89]. A second industrial application is explored; it consists in the study of the motion of a charge in a tumbling mill; we compare the numerical simulation of our method with experimental results of a rotational cylinder as a scale model of a milling drum conducted by [94].

1.4. Document outline

The document layout is as follows: Chapter 2 presents the employed continuum constitutive model. The model is based on a Drucker-Prager yield function in the framework of plasticity theory for large deformation problems. The incompressibility condition is solved by expressing the formulation in a mixed scheme with a proper stabilization method for pressures.

The numerical formulation is developed in Chapter 3. A brief summary of the *PFEM* is described as well as the implemented remeshing criteria. Thereafter, it is presented the numerical integration for the constitutive model. The chapter ends with the description of the contact method proposed to model the solid-granular material interaction.

A validation example is presented in Chapter 4. It is based on the experimental model of a granular material spreading over a plane surface proposed by [62]. The numerical results are compared with those obtained by the experiment.

In order to assess the capabilities of the proposed model to replicate granular flows in practical situations, Chapter 5 presents numerical simulations of two industrial applications. The first simulation is based on the experiment conducted by [89], where a full scale silo discharge was studied in order to determine characteristic flow patterns. A comparison between experimental results of the silo discharge, and finite element prediction, is carried out. The second and last example is a simplified milling process proposed by [94]. Granular material is placed in a cylindrical drum in order to study the energy system required to keep it in motion.

Chapter 6 presents a summary of the achievements reached as some concluding remarks.

Chapter 2
Continuum description of dense granular flows

Granular materials are defined as large conglomerations of discrete particles connected each other by the contact between them. The assumption of modelling a discrete media as a continuum has been subject of extensive study. It has been demonstrated that the differential equations used to define the kinematics of their deformation become correct as the number of particles increases ([29], [38]). The continuum approach allows us to interpret the particle interaction as a transmission of energy through the domain by a mathematical formulation. Under some considerations, the microscopic relations of the particles are properly transformed into macroscopic equivalents in terms of the material properties.

The definition of a unique model capable of representing any physical condition for any material is difficult to establish, if not impossible. Granular materials models are not an exception, even more when it has been stated in the previous chapter the diverse behaviours that these materials present under different kinematic conditions. This chapter presents a constitutive model in a continuum formulation proposed to simulate dry dense granular slow flows, able to differentiate stagnant and flow zones as well as the jamming transition between these conditions.

The constitutive model is based on the concepts of plasticity at large strains. The yield surface is defined in terms of a Drucker-Prager yield function characterized by two constitutive parameters, the cohesion and the internal friction coefficient, and provided with a solely deviatoric plastic flow. The material flow condition is considered nearly incompressible so the proposal is integrated in a $u - p$ mixed formulation with a pressure stabilization proposed by [28]; and the elastic part is defined by a hypoelastic model.

The present chapter comprises the development of the model from the kinematic equations necessary to state the constitutive model, through its formulation via a visco-elasto-plastic formulation and the statement of the weak form of the balance equations.

2.1. Phenomenological description of dense granular flows

The model is derived within the framework of continuum, large deformations; as mentioned in the previous chapter, the domain under study has to be large enough to be described properly by this approach. Figure 2-1 shows the continuum idealization of a control volume in a granular domain.

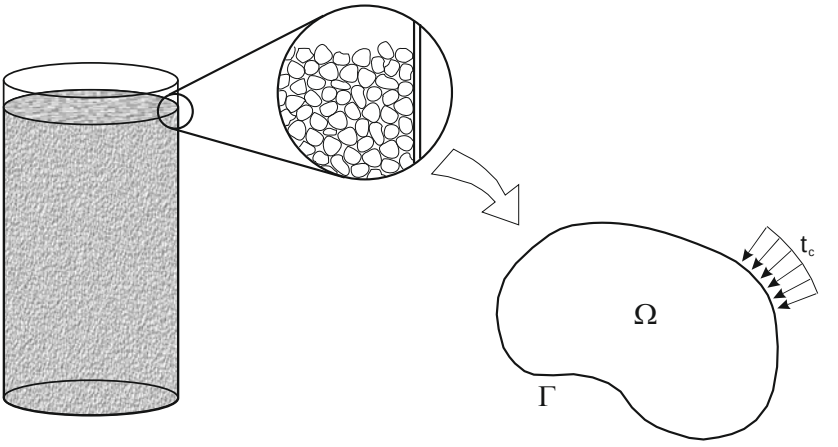

Figure 2-1. Continuum representation of a granular media in a container.

The representation defines an open and bounded domain Ω, delimited by its boundary Γ, and subject to external stresses $\mathbf{t}_c$, generally due to the interaction with a container. The flow problems to be presented here are strongly influenced by the container where the phenomena take place. The kinematic response of the material is affected by the interaction between the granular material and its confinement. The numerical model has to be suitable to represent two limit cases, as shown in Figure 2-2: one in which the material interacts with a frictionless surface, and another in which the surface exhibits a high degree of roughness. Likewise, the contact methodology has to be robust enough to support the presence of large deformations and to be capable of interacting with non-regular geometries.

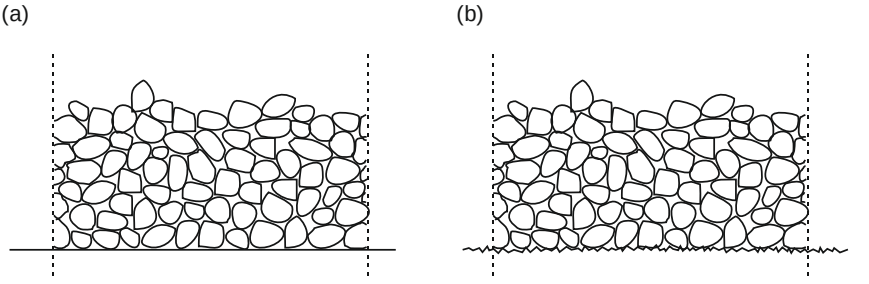

Figure 2-2. Limit cases for a solid-granular material interaction: (a) frictionless surface, (b) high roughness on the surface.

It is important to define the flow conditions and granular materials that the model intents to represent. The model is proposed for dry dense granular materials, with the aim to characterize the static condition of the materials at rest as well as for slow granular flows, including its jamming transition. The statement of dense granular flows implies small velocities in the material as well as the assumption for the granular particles to remain in contact while the material spreads or flows. The term dry refers for granular materials with a negligible interstitial fluid between the particles, defining a non-cohesive or nearly cohesionless state for the particles interaction.

The mechanical properties of dense granular materials are governed by the frictional interaction between the particles, which means that the deformations that the material experiences while flowing do not present significant volumetric variations; this fact allows us to assume that the material is nearly *incompressible*. In this sense, the model is not suitable for industrial processes where granular materials are subject to compaction or to dispersion.

The material properties are considered for non-cohesive granular media. In order to represent a frictional response between the particles, the presence of any other material between the grains is ignored. The isotropy assumption of the model is conserved maintaining a high homogeneity in size and shape of the granular particles. Even so, this assumption is achieved when the particle size is considerable small compared to the size of the domain under consideration.

The model herein described is defined in a two dimensional space for numerical aspects that will be described in the following chapters; nevertheless, the model is suitable to handle a full three dimensional description. The numerical simplification has impact in the examples to be chosen. These examples are industrial processes that could be described in an axisymmetric and plain strain description as shown in Figure 2-3.

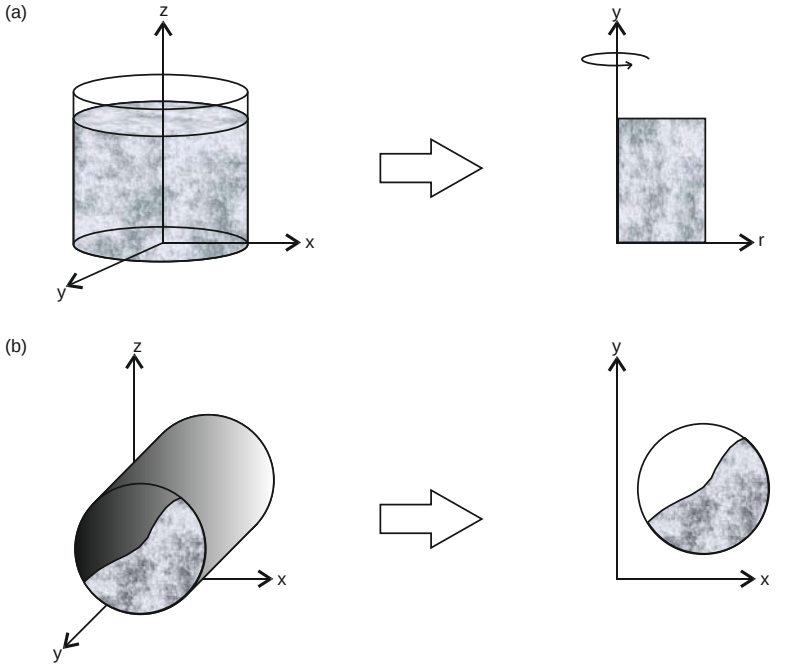

Figure 2-3. Two-dimensional modelling of volumetric examples. (a) Axisymmetric representation of a cylindrical container. (b) Plain strain model of a rotational drum.

2.2. Kinematic of plastic large deformations

The mathematical description of continuum mechanics is defined through the motion of continuous finite particles in a body. The flow of granular media naturally entails large variations in their geometry; therefore, the kinematic description of the body is to be established within the frame of a large deformation formulation.

The domain to represent is denoted by $\Omega \in \mathbb{R}^2$, and it is assumed to be formed by a continuous set of particles enclosed by a boundary Γ. The notion of particles here corresponds to infinitesimal material points of the domain and not to the granular particles of the medium. The mechanical response of the body is given by the deformation of the body under its loading condition in a certain time interval $t = [0, T]$.

The analysis is defined through a reference configuration, generally stated at $t = 0$; the subindex $(\bullet)_o$ stands for all variables established in the reference configuration. The body motion is expressed as the mapping of a material point between a

reference configuration and the current one, defined by the subindex $(\bullet)_t$. The mapping states a unique correspondence between configurations, expressed by

$$\mathbf{x} = \varphi(\mathbf{X}, t) = \varphi_t(\mathbf{X}) \tag{2.1}$$

for all $\mathbf{X} \in \Omega_0$ and $t > 0$; and φ is a smooth mapping function defined by $\varphi : \Omega_0 \to \Omega_t \subset \mathbb{R}^2$. A two-dimensional representation for the motion of a continuum body is expressed in Figure 2-4.

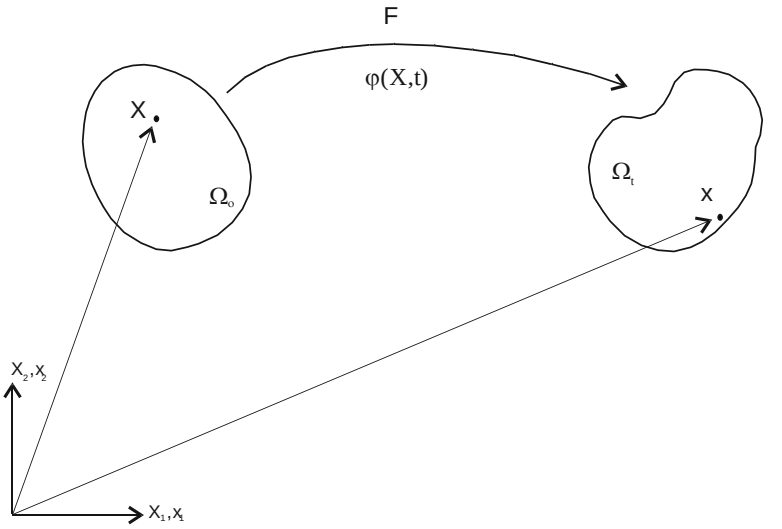

Figure 2-4. Configuration and motion of a continuum body – two-dimensional representation.

The displacement is a vector field relating the position of a particle between the current and the reference configuration. Its expression in a Lagrangian or material description is given by

$$\mathbf{U}(\mathbf{X}, t) = \varphi(\mathbf{X}, t) - \mathbf{X} \tag{2.2}$$

and let denote by $\mathbf{u}(\mathbf{x}, t)$ the spatial counterpart of $\mathbf{U}$. The velocity and acceleration fields are defined by the first and second time derivatives of the motion φ, respectively; the material description of the velocity field and the acceleration field reads,

$$\mathbf{V}(\mathbf{X}, t) = \frac{\partial \varphi(\mathbf{X}, t)}{\partial t} \tag{2.3a}$$

$$\mathbf{A}(\mathbf{X}, t) = \frac{\partial \mathbf{V}(\mathbf{X}, t)}{\partial t} = \frac{\partial^2 \varphi(\mathbf{X}, t)}{\partial t^2} \tag{2.3b}$$

denoting $\mathbf{v}(\mathbf{x}, t)$ and $\mathbf{a}(\mathbf{x}, t)$ the spatial counterparts of $\mathbf{V}$ and $\mathbf{A}$, respectively.

An important tensor in the description of the deformation in nonlinear continuum mechanics is the *deformation gradient* $\mathbf{F}$. It represents the Jacobian matrix of the motion of the body; its expression in Cartesian coordinates reads:

$$\mathbf{F} = \frac{\partial \varphi(\mathbf{X},t)}{\partial \mathbf{X}} = \frac{\partial \mathbf{U}(\mathbf{X},t)}{\partial \mathbf{X}} + \mathbf{1} \tag{2.4}$$

where $\mathbf{1}$ is the second order symmetric unit tensor with components $1_{ab} = \delta_{ab}$. The determinant of the deformation gradient is known as the Jacobian determinant, and it is a scalar variable useful to relate the integrals in the current and reference configurations.

$$J = \det \mathbf{F} \tag{2.5}$$

As it is customary in the literature of large plasticity theory, it is adopted the assumption of the local multiplicative decomposition of the deformation gradient into a plastic and an elastic part:

$$\mathbf{F} = \mathbf{F}^e \cdot \mathbf{F}^p \tag{2.6}$$

where $\mathbf{F}^p$ represents a pure plastic deformation from Ω_0 to a certain stress-free intermediate configuration [93], and $\mathbf{F}^e$ a pure elastic loading from such an intermediate configuration to the current configuration Ω_t.

On the other hand, the rate of deformation tensor $\mathbf{d}$ is defined by the symmetric part of the spatial velocity gradient $\boldsymbol{l} = \nabla \mathbf{v}$.

$$\mathbf{d} = \frac{1}{2}\left(\boldsymbol{l} + \boldsymbol{l}^T \right) \tag{2.7}$$

For the particular case of granular material flows, it is also assumed that the elastic deformations of the body are small compared with the total ones. In this sense, it is assumed a kinematic description that considers arbitrarily large plastic deformations and small elastic strains. A valuable implication of this assumption is that the Euler-Almansi strain tensor, defined as

$$\mathbf{e} = \frac{1}{2}\left(\mathbf{1} - \mathbf{F}^{-T}\mathbf{F}^{-1} \right) \tag{2.8}$$

inherits the additive structure of classical small strain formulations [57]

$$\mathbf{e} = \mathbf{e}^e + \mathbf{e}^p \tag{2.9}$$

where $\mathbf{e}^e$ and $\mathbf{e}^p = \frac{1}{2}\left(\boldsymbol{1} - \mathbf{F}^{p^{-T}}\mathbf{F}^{p^{-1}} \right)$ are the elastic and plastic parts of the rate of deformation tensor, respectively. This property holds also for the rate of deformation tensor:

$$\mathbf{d} = \mathbf{d}^e + \mathbf{d}^p \tag{2.10}$$

where $\mathbf{d}^e$ and $\mathbf{d}^p$ are the elastic and plastic parts of the rate of deformation tensor, respectively. This decomposition allows us to afford a remarkable aspect of simplicity in deriving the ensuing constitutive equations.

2.3. Constitutive model for dense granular flows

The proper definition of a model entails a balance between its capacity to represent a phenomena and the simplicity of the model. Granular materials exhibit mechanical properties corresponding to solids and fluids depending on its kinematic condition; in order to represent this phenomenon, the model proposed has to be enriched enough to differentiate both behaviours as well to remain as simple as it gets to be efficient in the numerical analysis.

The constitutive model is developed within the framework of large plastic-small elastic deformations through a *hypoelastic* model. The condition of plastic yielding is based on a Drucker-Prager yield function that relates linearly the norm of the deviatoric stresses with the hydrostatic pressure exerted on the material. The mechanical condition to define a stagnant and fluid zone in the material is given by the elasto-plastic formulation. The plastic condition allows the material to yield when the stress state reaches the strength capacity of the material, while the elastic condition permits the material to reach a stagnant configuration. The flow regime requires the inclusion of viscous behaviour; here it is proposed a visco-plastic regularization via a Duvaut-Lions type model.

2.3.1. Elastic response

For the elastic response, it is proposed a class of model of phenomenological, rate independent, plasticity obtained by an ad-hoc extension of the infinitesimal theory, which relies on a hypoelastic characterization of the elastic behaviour. In this sense, the relation strain-stress is defined in terms of the rate of deformation tensor, given by:

$$\overset{\circ}{\boldsymbol{\tau}} = \boldsymbol{c} : \left[\mathbf{d} - \mathbf{d}^{p} \right] \tag{2.11}$$

where $\boldsymbol{\tau}$ is the Kirchhoff stress tensor, $\boldsymbol{c}$ is an isotropic elastic module, constant in the spatial reference configuration, and $\overset{\circ}{(\bullet)}$ denotes any objective stress rate. The model is posed for large plastic – small elastic deformations.

The objective derivative for equation (2.11) is defined by the Lie derivative of the Kirchhoff stress tensor. Therefore

$$L_{v}\boldsymbol{\tau} = \boldsymbol{c} : \left[\mathbf{d} - \mathbf{d}^{p} \right] \tag{2.12}$$

and the spatial elasticity tensor $\boldsymbol{c}$ is defined as:

$$\boldsymbol{c} = 2\mu \left(\boldsymbol{\iota} - \frac{1}{3}\mathbf{1} \otimes \mathbf{1} \right) + \kappa \mathbf{1} \otimes \mathbf{1} \tag{2.13}$$

Where μ is the Lamé's second parameter or shear modulus, κ the bulk modulus, and $\boldsymbol{\iota}$ the fourth symmetric unit tensor, with components $\iota_{abcd} = \frac{1}{2}[\delta_{ac}\delta_{bd} + \delta_{ad}\delta_{bc}]$.

This fourth order tensor is characterized by possessing both major and minor symmetries.

$$C_{abcd} = C_{cdab} = C_{bacd} = C_{abdc}$$

2.3.2. Yield condition

As previously mentioned, the yield condition used in this work is derived, essentially, from the Drucker-Prager type criterion. It defines a linear relation between the hydrostatic pressure and the deviatoric part of the stress tensor; this idealization have been studied and applied for different granular models. The Drucker-Prager yield surface is widely used instead of the Mohr-Coulomb model, since the first is independent of the third invariant – embedding the Mohr-Coulomb model by a conical surface.

The equation for the yield surface, described previously in equation (1.3), can be rephrased, after some manipulation, as

$$\phi(\boldsymbol{\tau}) = \|\operatorname{dev}\boldsymbol{\tau}\| + \frac{1}{3} b_1 \operatorname{tr}\boldsymbol{\tau} - b_2 \tag{2.14}$$

where $\boldsymbol{\tau}$ is the Kirchhoff stress tensor; parameter b_1 represents the slope of the Drucker-Prager line, being referred as the parameter of the internal friction; and b_2 is customarily referred to as the material cohesion, and it can be interpreted as the shear strength under zero hydrostatic stress – defined by the intersection of the Drucker-Prager yield surface with the q-axis[3]. Equation (2.14) is rewritten, in terms of the Kirchhoff stress invariants, by the following equation:

$$\phi(\boldsymbol{\tau}) = q + \frac{1}{3} b_1 p - b_2 \tag{2.15}$$

The relation of b_1 and b_2 with the Mohr-Coulomb's material internal friction angle and cohesion is deduced comparing equation (2.14) with (1.3) and using the correlation of those parameters given in equations (1.5a) and (1.5b):

$$b_1 = \frac{6}{\sqrt{2}}\alpha = 2\sqrt{6}\frac{\sin\theta}{(3-\sin\theta)} \tag{2.16a}$$

$$b_2 = \frac{2}{\sqrt{2}}\beta = 2\sqrt{6}\frac{c\cos\theta}{(3-\sin\theta)} \tag{2.16b}$$

Thereby, b_1 could be seen as an equivalent internal friction angle, while b_2 as an equivalent material cohesion in the Drucker-Prager model. A two-dimensional

[3] From now on, the yield condition is formulated in terms of the Kirchhoff stress invariants $p = 1/3\, I_1 = 1/3 \operatorname{tr}\boldsymbol{\tau}$ and $q = \sqrt{2J_2} = \sqrt{\operatorname{dev}\boldsymbol{\tau} : \operatorname{dev}\boldsymbol{\tau}}$ as the mean stress and the norm of the deviatoric stress, respectively

representation of the Drucker-Prager yield surface is given in Figure 2-5; it is observed the full dependency on these two parameters to describe the model.

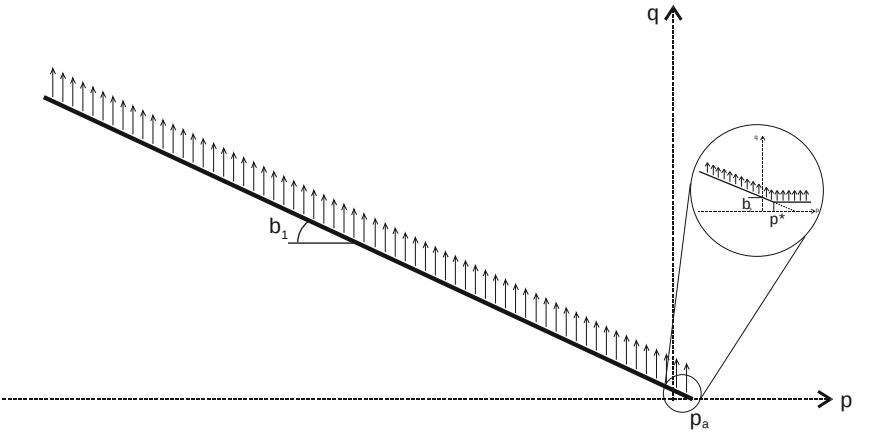

Figure 2-5. Two-dimensional Drucker-Prager model.

The relation between Drucker-Prager material parameter b_1 and the internal friction angle of the Mohr-Coulomb's model θ is plotted in Figure 2-6. It is observed that the maximum value is reached when the Mohr-Coulomb internal friction angle is equal to $\pi/2$.

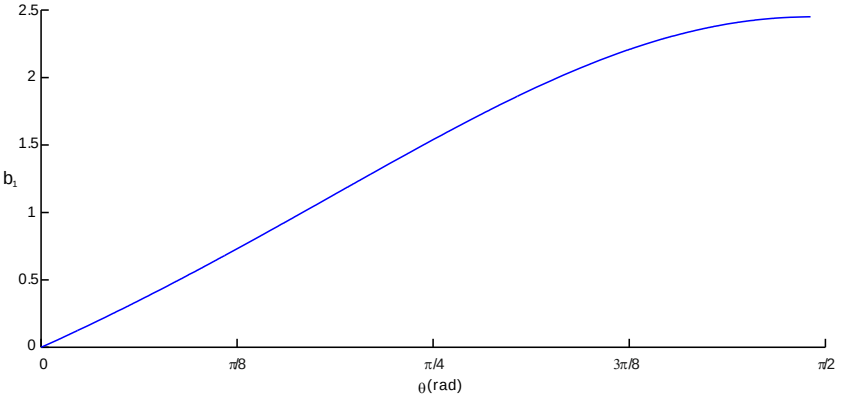

Figure 2-6. Drucker-Prager and Mohr-Coulomb internal friction angle relationship.

Constitutive models for granular materials with a linear dependency between the hydrostatic pressures and their resistance to shear – as the Mohr-Coulomb or Drucker-Prager – are defined until certain value corresponding to the vertex of the surface, in this case p_a, see Figure 2-5. In order to define a valid stress state for loading

conditions with pressures greater than the vertex, it is necessary to introduce a proper regularization.

In this work we propose to regularize the function at the vertex by a von Mises yield criterion, as displayed in the circled area in Figure 2-5. As it is observed, the regularization takes place after a certain pressure level $p^* < p_a$ and defines a well-posed load state for pressures greater than this pressure reference. The yield surface for the von Mises regularization is defined similarly than equation (2.14)

$$\phi^*(\boldsymbol{\tau}) = \|\mathrm{dev}\,\boldsymbol{\tau}\| - q^* \tag{2.17}$$

where $q^* = b_2 - b_1 p^*$ is the norm of the deviatoric stress tensor corresponding to p^*. This implementation is considered as a regularization for the Drucker-Prager yield surface and not a two-surface model since the examples here treated represent dense granular domains mainly on compressive regimes, and as it will show in Chapter 4 and Chapter 5, it is few the amount of material with pressures above the vertex (tensile regime).

2.3.3. Flow rule and plastic potential

For large deformation problems, the rate of deformation tensor is decoupled as shown in equation (2.10). The plastic rate of deformation tensor $\mathbf{d}^p$ is computed using the concept of flow rule:

$$\mathbf{d}^p = \dot{\lambda}\mathbf{m} \tag{2.18}$$

where $\dot{\lambda}$ is a positive definite scalar factor referred to as consistency parameter or plastic multiplier, and $\mathbf{m}$ a plastic flow vector associated to the yield surface. The plastic multiplier must obey the standard Karush-Kuhn-Tucker loading/unloading conditions plus the consistency condition [93]. In the context of rate-independent plasticity the former conditions read as:

$$\begin{aligned} \dot{\lambda} &\geq 0 \\ \phi(\boldsymbol{\tau}) &\leq 0 \\ \dot{\lambda}\phi(\boldsymbol{\tau}) &= 0 \end{aligned} \tag{2.19}$$

and the consistency condition is given by

$$\dot{\lambda}\dot{\phi}(\boldsymbol{\tau}) = 0 \tag{2.20}$$

Furthermore, each plastic flow vector $\mathbf{m}$ is presumed to be aligned with the gradient of a certain plastic potential function φ, i.e. $\mathbf{m} = \partial\varphi/\partial\boldsymbol{\tau}$.

The plastic potential states the mechanical behaviour of the deformation once the loading state reaches the yield condition. For *slow* and *dense* granular flows the mechanical behaviour of the material is governed by frictional forces rather than collision of the particles. In this case the material is considered nearly incompressible [9]; for this reason, it is proposed a non-associative plastic potential with a solely deviatoric component for the model.

$$\varphi(\boldsymbol{\tau}) = \frac{1}{2}\|\operatorname{dev}\boldsymbol{\tau}\|^2 \tag{2.21}$$

Therefore, the plastic rate of deformation tensor can be written as

$$\mathbf{d}^p = \dot{\lambda}\frac{\partial\varphi(\boldsymbol{\tau})}{\partial\boldsymbol{\tau}} = \dot{\lambda}\operatorname{dev}\boldsymbol{\tau} \tag{2.22}$$

Since $\mathbf{d}^p$ is proportional to the deviatoric tensor, the flow rule asserts plastic incompressibility. While dilation in dense flows do occur, it is typically on the order of only a few percent and quickly reaches a steady value over large deformations [90]; hence, the plastic incompressibility approximation should have negligible effect on the velocity field of a dense granular flow.

The solution of the elasto-plastic part of the proposed model for dense granular flows are defined by equations (2.12), (2.15), and (2.22), plus the loading/unloading and consistency conditions given by equations (2.19) and (2.20).

Even though the concavity of the overlapped yield surface, due to the deviatoric non-associative plastic potential, all the returning maps are well posed in a single value. The admissibility of the proposal is reviewed by the energy dissipation of the system or thermodynamic consistency that should satisfy the following inequality

$$\mathcal{D} = \boldsymbol{\tau} : \mathbf{d}^p \geq 0 \tag{2.23}$$

which could be seen as the Drucker's inequality for large deformation problems. Substituting equation (2.22) into equation (2.23)

$$\mathcal{D} = \dot{\lambda}(\operatorname{dev}\boldsymbol{\tau} : \operatorname{dev}\boldsymbol{\tau}) \geq 0 \tag{2.24}$$

and considering the definition of the slip rate, it is ensured that the plastic dissipation as the double contraction product of the deviatoric stress tensor is a non negative scalar value.

2.3.4. Visco-plastic regularization

As pointed out in the previous chapter, constitutive equations for granular material flows are still a matter of debate. One difficulty is that granular material can behave like a solid (e.g. in a powder heap), a liquid (granular flows), or a gas (existence of interstitial fluid). For the solid-like state, the elasto-plastic constitutive model described in Section 2.3.3 characterizes this condition; however, the jamming transition and the flow regime require the inclusion of a viscous behaviour.

The fundamental features of granular flows in this regime are: a yield condition that defines a shear stress limit below which the grain does not move; and a general non-linear dependence on shear rate when flowing. In this sense, granular behaviour shares similarities with classical visco-plastic models that were developed to ensure that dynamic problems remain hyperbolic since the existence of well-defined yield stresses are difficult to achieve [67].

The regularization is defined via a Duvaut-Lions type model. The new flow rule reduces to

$$\mathbf{d}^{\mathrm{vp}} = \frac{1}{\tau_R}\boldsymbol{c}^{-1} : \left[\boldsymbol{\tau} - \boldsymbol{\tau}^{\mathrm{ep}} \right] \tag{2.25}$$

where τ_R refers to the relaxation time, and $\boldsymbol{\tau}^{\mathrm{ep}}$ corresponds to the solution of the elasto-plastic part of the model described in previous section.

Now, the strain-stress relationship defined by the hypoelastic model given in equation (2.12) is modified by decoupling the rate of deformation tensor in an elastic and a visco-plastic part.

$$L_v\boldsymbol{\tau} = \boldsymbol{c} : \left[\mathbf{d} - \mathbf{d}^{\mathrm{vp}} \right] \tag{2.26}$$

which is rewritten replacing the visco-plastic definition of the rate of deformation tensor given in equation (2.25).

$$L_v\boldsymbol{\tau} = \boldsymbol{c} : \mathbf{d} + \frac{1}{\tau_R}\left(\boldsymbol{\tau} - \boldsymbol{\tau}^{\mathrm{ep}} \right) \tag{2.27}$$

Box 2.1 summarizes the constitutive model proposed in this work to describe the behaviour of a dense granular flow.

Elastic response

$$L_v\boldsymbol{\tau} = \boldsymbol{c} : \left[\mathbf{d} - \mathbf{d}^{vp} \right]$$

Yield function and elastic domain in stress space

$$\phi(\boldsymbol{\tau}) = \|\mathrm{dev}\,\boldsymbol{\tau}\| + \frac{1}{3} b_1 \,\mathrm{tr}\,\boldsymbol{\tau} - b_2$$

$$E_{\hat{\tau}} \coloneqq \{ \hat{\boldsymbol{\tau}} \mid \varphi(\boldsymbol{\tau}) \leq 0 \}$$

Flow rule

$$\mathbf{d}^{\mathrm{vp}} = \frac{1}{\tau_R}\boldsymbol{c}^{-1} : \left[\boldsymbol{\tau} - \boldsymbol{\tau}^{\mathrm{ep}} \right]$$

where $\boldsymbol{\tau}^{\mathrm{ep}}$ is solution of the following sub-problem

$$L_v\boldsymbol{\tau} = \boldsymbol{c} : \left[\mathbf{d} - \mathbf{d}^{p} \right]$$

$$\mathbf{d}^{p} = \dot{\lambda}\,\mathrm{dev}\,\boldsymbol{\tau}$$

$$\dot{\lambda} > 0 \qquad \phi(\boldsymbol{\tau}) \leq 0 \qquad \dot{\lambda}\phi(\boldsymbol{\tau}) = 0$$

Box 2.1. Visco-elasto-plastic model for dense granular flows.

2.4. Initial boundary value problem

The local equations of motion, in the Eulerian description, take the form:

$$\nabla \cdot \boldsymbol{\sigma} + \rho \mathbf{b} - \rho \frac{D\mathbf{v}}{Dt} = 0 \tag{2.28}$$

where $\boldsymbol{\sigma}$ is the Cauchy stress tensor, ρ the density, $\mathbf{b}$ the body force, and $\mathbf{v}$ the spatial velocity field. The term $D(\bullet)/Dt$ denotes the material time derivative of the spatial velocity field.

In order to state the problem properly it has to be completed with appropriate boundary conditions; towards this end, the boundary of the domain is assumed to be split as

$$\Gamma = \Gamma_t \cup \Gamma_u \tag{2.29}$$

and

$$\Gamma_t \cap \Gamma_u = 0 \tag{2.30}$$

where Γ_u stands for the portion of Γ in which Dirichlet boundary conditions are imposed – displacement fields; whereas Γ_t corresponds to the portion into the Neumann conditions are prescribed, tractions [42]. These boundary conditions are given by the following relations (the overline $(\bar{\bullet})$ stand for prescribed boundary functions)

$$\mathbf{u} = \bar{\mathbf{u}} \quad \text{on} \quad \Gamma_u \tag{2.31}$$

and

$$\boldsymbol{\sigma} \cdot \mathbf{n} = \bar{\mathbf{t}} \quad \text{on} \quad \Gamma_t \tag{2.32}$$

where $\mathbf{u}$ is the displacement field in its spatial description, and $\mathbf{n}$ a unit vector normal to an infinitesimal surface section.

The loading conditions in the system for granular flows are strongly related to the body forces (gravity forces) and for industrial processes by the interaction with their confinement. In the case of the interaction of the material with its confinement, the contact forces have to be well posed by a contact methodology.

The dynamic analysis for the model requires initial conditions for the displacement and velocity fields which in turn have to achieve compatibility with the boundary conditions. The formulation, in the strong form, of the initial boundary value problem is given in Box 2.2.

Balance equation

$$\nabla \cdot \boldsymbol{\sigma} + \rho \mathbf{b} - \rho \frac{D\mathbf{v}}{Dt} = 0$$

Boundary conditions

$$\mathbf{u} = \bar{\mathbf{u}} \quad \text{on} \quad \Gamma_{\mathrm{u}} = \varphi_t(\partial\Omega_o)$$

$$\boldsymbol{\sigma} \cdot \mathbf{n} = \bar{\mathbf{t}} \quad \text{on} \quad \Gamma_{\mathrm{t}} = \varphi_t(\partial\Omega_o)$$

Initial conditions

$$\mathbf{u}(\mathbf{x}, t_o) = \mathbf{u}_o(\mathbf{x})$$

$$\dot{\mathbf{u}}(\mathbf{x}, t_o) = \mathbf{v}_o(\mathbf{x})$$

Compatibility restriction

$$\bar{\mathbf{u}}(\mathbf{x}, t_o) = \mathbf{u}_o(\mathbf{x})$$

$$\dot{\bar{\mathbf{u}}}(\mathbf{x}, t_o) = \mathbf{v}_o(\mathbf{x})$$

Box 2.2. Strong form of the initial boundary value problem for a given time t

2.5. Incompressibility problem

In section 2.3.2 the plastic flow rule proposed for the model was described. This plastic flow rule is a (non-associative) deviatoric flow rule, which aims at describing the incompressible behaviour of the material while flowing. Indeed, the material is allowed to deform only by shear stresses, without volumetric changes in the plastic regime; in its elastic range the volumetric variations are considered small. Due to these characteristics, the so-called locking phenomena may emerge when solving the weak form of the momentum equation using standard, irreducible formulations. In order to circumscribe this problem, a mixed formulation is proposed.

The mixed form is expressed in terms of the displacement field $\mathbf{u}$ and the pressure π (in terms of a Cauchy stress tensor, being defined below) as variables to solve. The construction of the mixed formulation is defined by the decoupling of the Cauchy stress tensor into its deviatoric $\mathrm{dev}\,\boldsymbol{\sigma}$ and volumetric $\pi\mathbf{1}$ parts. The balance of momentum, equation (2.28), can be expressed as:

$$\nabla \cdot \mathrm{dev}\,\boldsymbol{\sigma} + \nabla \cdot \pi\mathbf{1} + \rho \mathbf{b} - \rho \frac{D\mathbf{v}}{Dt} = 0 \tag{2.33}$$

The pressure π is provided from a hyperelastic deduction of the pressure for a nearly incompressible material, given in Ref. [6], by the following expression:

$$\pi = \kappa \frac{\ln J}{J} \tag{2.34}$$

Equation (2.34) could be expressed as a dimensionless equality as follows

$$\frac{\ln J}{J} - \frac{1}{\kappa}\pi = 0 \tag{2.35}$$

Equations (2.33) and (2.35) are the basis to formulate the finite element method equations to solve our problem.

2.6. Weak forms

As usual, the weak form of the momentum equation is obtained by taking the dot product of equation (2.33) by a test function $\delta \boldsymbol{w}$ and then, integrating over the current configuration:

$$\int_{\Omega_t} \delta \boldsymbol{w} \cdot (\nabla \cdot \operatorname{dev} \boldsymbol{\sigma} + \nabla \cdot \pi \mathbf{1} + \rho \mathbf{b} - \rho \dot{\mathbf{v}}) d\Omega_t = 0 \tag{2.36}$$

where the displacement field $\mathbf{u}(\mathbf{x},t)$ and test functions should satisfy respectively the following conditions.

$$\mathbf{u}(\mathbf{x},t) \in \vee_{\varphi} = \left\{ \mathbf{u}(\mathbf{x},t) : \varphi_t(\Omega_0) \to \mathbb{R}^2, \quad \mathbf{u} = \bar{\mathbf{u}} \text{ for } \mathbf{x} \in \Gamma_{\mathbf{u}} \right\} \tag{2.37}$$

$$\delta \boldsymbol{w}(\mathbf{x}) \in \bar{\vee}_{\varphi} = \left\{ \delta \boldsymbol{w}(\mathbf{x}) : \varphi_t(\Omega_0) \to \mathbb{R}^2, \quad \delta \boldsymbol{w} = \mathbf{0} \text{ for } \mathbf{x} \in \Gamma_{\mathbf{u}} \right\} \tag{2.38}$$

Using the divergence theorem, equation (2.36) we get

$$\begin{aligned} \int_{\Omega_t} \nabla(\delta \boldsymbol{w}) : [\operatorname{dev} \boldsymbol{\sigma} + \pi \mathbf{1}] d\Omega_t - \int_{\Omega_t} \delta \boldsymbol{w} \cdot (\rho \mathbf{b}) d\Omega_t \\ - \int_{\Gamma_t} \delta \boldsymbol{w} \cdot \bar{\mathbf{t}} \, d\Gamma + \int_{\Omega_t} \delta \boldsymbol{w} \cdot (\rho \dot{\mathbf{v}}) d\Omega_t = 0 \end{aligned} \tag{2.39}$$

The weak form of equation (2.35) reads

$$\int_{\Omega_t} \delta q \left(\frac{\ln J}{J} - \frac{1}{\kappa}\pi \right) \frac{1}{J} d\Omega_t = 0 \tag{2.40}$$

where δq is a square-integrable function over $\varphi_t(\Omega)$.

Both equation (2.39) and (2.40) are the variational form of the balance equations for a mixed formulation, expressed in a given time t, in terms of the Cauchy stress tensor. Box 2.3 summarizes the weak form of the problem.

Find $(\mathbf{u}, \pi)$ such that

$$\int_{\Omega_t} \nabla(\delta \boldsymbol{w}) : \boldsymbol{\sigma}\, d\Omega_t - \int_{\Omega_t} \delta \boldsymbol{w} \cdot (\rho \mathbf{b}) d\Omega_t - \int_{\Gamma_t} \delta \boldsymbol{w} \cdot \bar{\mathbf{t}}\, d\Gamma + \int_{\Omega_t} \delta \boldsymbol{w} \cdot (\rho \dot{\mathbf{v}}) d\Omega_t = 0$$

$$\int_{\Omega_t} \delta q \left(\frac{\ln J}{J} - \frac{1}{\kappa} \pi \right) \frac{1}{J} d\Omega_t = 0$$

and the corresponding initial and boundary conditions

Box 2.3. Weak form of balance equations

Chapter 3
Numerical formulation

Due to the large displacements and deformations during granular flows, the modelling of these phenomena must be suitable to represent these characteristics in an efficient and robust manner. In this chapter, the numerical formulation of the constitutive model given in the previous chapter is presented. It is developed in the framework of the Particle Finite Element Method (*PFEM*) and the numerical integration is developed within the *Impl-Ex* technique. Finally, the modelling of the solid/granular material interaction is addressed with the proposal of a new method based on the Contact Domain Method (*CDM*) proposed in Ref. [77].

3.1. The Particle Finite Element Method (*PFEM*)

Over recent years, the *PFEM* has demonstrated to be a powerful numerical algorithm for the solution of large deformation problems. It is a numerical method formulated in an updated Lagrangian description capable to capture the transient and stationary motion of a deformable body. This work is based on the *PFEM*; in this section the basic concepts of the method are described, as well as the numerical enhancement, introduced in this work, in order to improve the numerical response of the method.

3.1.1. *PFEM* background

The *PFEM* arose as a proper evolution of the particle methods used to simulate incompressible fluid flows, on a Lagrangian formulation. This methodology was

first proposed by [46] in the context of a meshless finite element method with the aim to solve large deformation problems in the field of incompressible fluid flows. One of the advantages that the authors present, among others, is the capability to easily define the fluid-solid interaction.

Even though the method was first proposed for incompressible fluid flows, as in ([47],[98],[69]), its extension to other mechanic fields have been also adressed. Among them are found the exploration in the field of a multibody interaction, as bed erosion in free surface flows [80], or the fluid-structure response ([45],[79]). In the field of solid mechanics different applications have been studied as plasticity problems [76] or soils excavations [14].

Nowadays, some studies are found for granular materials as the response of rockfill dams on overtopping conditions [64]; or industrial explorations for powder materials ([12],[36]), where it is demonstrated the capability of the method.

The methodology is based on the macroscopic representation of a continuum domain through a finite number of particles of infinitesimal dimension. These particles are view as material points that describe the kinematic and mechanical behaviour of a given domain. The system of equations describing the kinematics of these particles is proposed to be solved in terms of an updated Lagrangian formulation – explained in more detail in following section.

The *PFEM* could be described as a set of numerical strategies combined for the solution of large deformation problems. The standard algorithm of the *PFEM* for the solution of solid mechanics problems, in a given incremental step, is schematically represented in Figure 3-1, and summarized as follows[4]:

- Definition of the domain(s) Ω_n in the last converged configuration, $t = t_n$, keeping existing spatial discretization $\overline{\Omega}_n$.
- Transference of variables by a Smoothing process – from Gauss points to nodes.
- Discretization of the given domain(s) in a set of particles of infinitesimal size – elimination of existing connectivities $\overline{\Omega}_n$.
- Reconstruction of the mesh through a triangulation of the domain's convex-hull and the definition of the boundary applying the α-shape method [30], defining a new spatial discretization $\widetilde{\Omega}_n$
- A contact method to recognize the multibody interaction.
- Transference of information, interpolating nodal variables into the Gauss points.
- Solution of the system of equations for $t_{n+1} = t_n + \Delta t$.

[4] In Section 3.2 and Section 3.3 are described the temporal and spatial discretization of the variational problem presented in previous chapter. The description of the *PFEM* algorithm is given using the discretization notation.

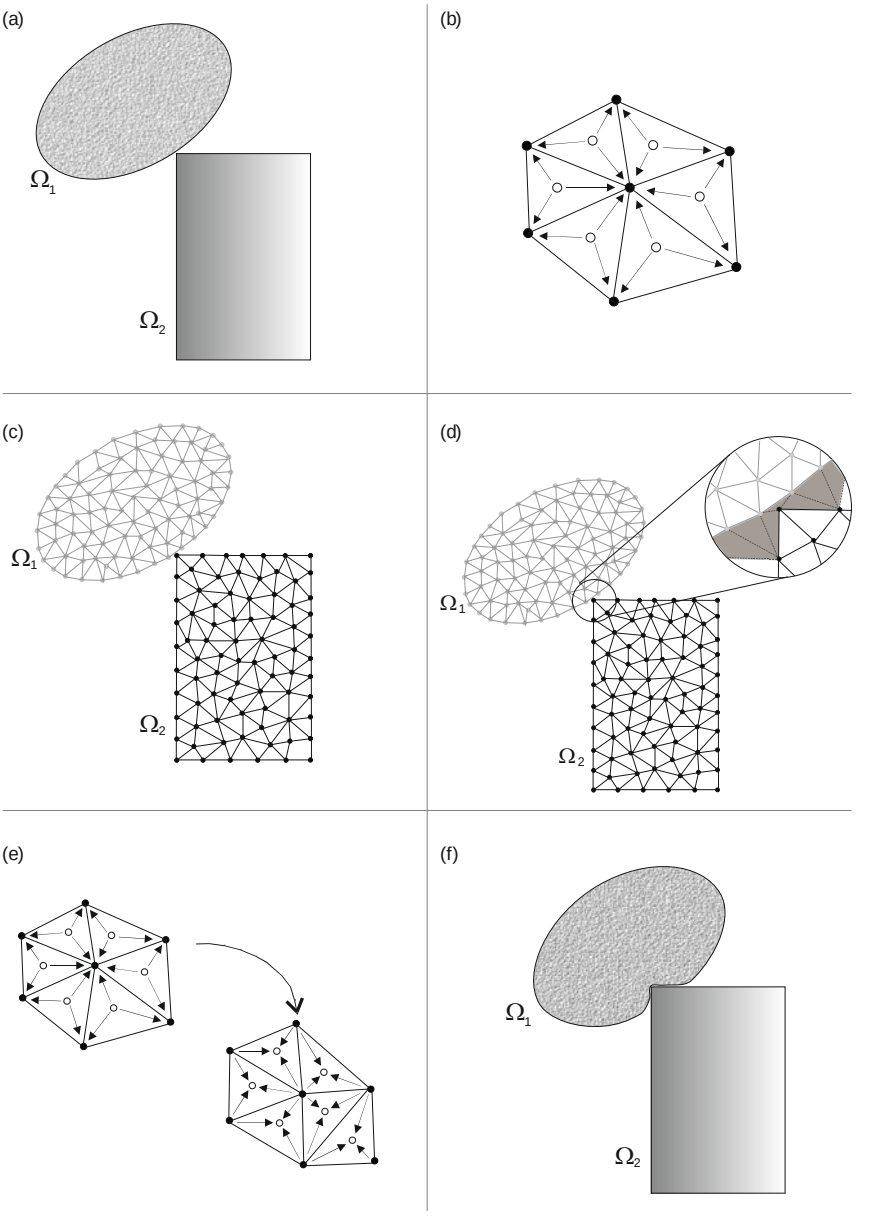

Figure 3-1. Schematic representation of *PFEM* algorithm for an incremental step: (a) Converged time step at t_n ; (b) Transference of internal variables information from Gauss points to nodes (smoothing process) (c) Mesh algorithm (reconnecting procedure and boundary definition); (d) Definition of a contact interface to define a multi-body interaction; (e) Nodal interpolation of internal variables to Gauss points; and (f) Solution of the system for t_{n+1}

The inherent reconnection procedure of the method reduces significantly the mesh distortion presented on large deformation problems. Even so, the implementation of the classic algorithm for solving granular flow problems presented some limitations to be solved in order to perform a more robust analysis and to define a smoother response of the solution. Among the problems found using the above mentioned algorithm is the loss of a well-defined mesh, presenting zones with a large conglomeration of particles, while other regions with a dispersion of them; and numerical instabilities due to the α-shape algorithm used for the boundary definition. Next are discussed some improvements on the algorithm that are required to solve these conditions.

3.1.2. *PFEM* enhancement

The numerical algorithm of the classic *PFEM* is enhanced in order to improve its response in three main areas: the dynamic process for the discretization of the domain into particles, varying the number of them depending on the deformation of the body; the boundary recognition, eliminating the geometric criterion of the α-shape method; and the transference of the internal variables, from a nodal smoothing through a variable projection.

3.1.2.1. Mesh quality – Dynamic process for particle discretization

The quality of the numerical solution depends directly of the correct discretization of the domain in study, including the quality of the elements of the mesh [34]. In large deformation problems the original mesh is strongly deformed presenting large distortions. The *PFEM* reduces significantly this problem by reconnecting the existing particles on each time step, even though the problem is not fully resolved. In order to circumvent this condition, the discretization of the domain into particles is proposed to be modified varying the number and position of the particles along time.

The remeshing process in this work is enhanced by the definition of geometrical metrics to identify potential regions of the mesh, where these problems could be found, in order to modify them (see Appendix A). This process is given in three main areas: the insertion, the removal or collapsing, and the repositioning of particles.

The *insertion* of particles is given on those elements presenting a greater dimension than a reference tolerance. Generally, the insertion of the new particles is given at the barycentre of the elements. An essential condition, for triangular elements, is that no angle has to be close to 180º [2]. If the vertex angle of the internal node in a boundary element is wider than a tolerance angle, it is inserted the new particle in the boundary length of the element.

The *removal* or *collapsing* procedure is defined to control the particle density of the mesh and possible singularities during the solving process. In contrast with the insertion process, which is controlled at an element level, the removal of particles depends on a nodal metric. The element sizes of the connecting elements in a node

are averaged, and the particle is removed if the averaged value is smaller than a defined tolerance value.

Once the domain is redefined in a new set of particles, the quality of the mesh is inspected in order to avoid remaining distortion of the new elements. This control is given by the algebraic quality metric given by [59]. The metric is defined in an elemental level and by the connectivities for each node will be identified those particles to *reposition*. The new coordinates for those particles are defined by a local Laplacian smoothing.

In Appendix A, the dynamic discretization process is explained in more detail. The whole remeshing algorithm has been shown sufficient in order to define a proper spatial discretization, robust enough, to solve granular flow problems as it will be shown in the following chapters. The remeshing process is summarized in Box 3-1.

Given a converged mesh $\overline{\Omega}_n$ in t_{n+1}

1. Insertion of particles if needed
2. Removal of particles if needed
3. Delaunay triangulation
4. Local smoothing to relocate particles if needed

Box 3-1. Remeshing process for a dynamic particle discretization.

3.1.2.2. Boundary treatment

In the classical version of the *PFEM*, the boundary treatment is given in terms of the α-shape method proposed in [30]. The advantages of the α-shape method for defining a mesh boundary are summarized as: an efficient time in the boundary construction, by applying an $O(n\log n)$ algorithm in time (Delaunay triangulation) and $O(n)$ in space, where n is the number of particles. In terms of robustness, the method reduces the overlapping of boundaries while presence of large deformations (*wave* effect). The main drawbacks of the method are the inconsistency of the mass conservation, while some elements are eliminated or augmented, and numerical instabilities produced on the residual due to the sudden remotion of the elements at the boundary. The latter presenting a major repercussion in a mixed $u-p$ formulation. These instabilities are present both the momentum and incompressibility equations, shown schematically in Figure 3-2.

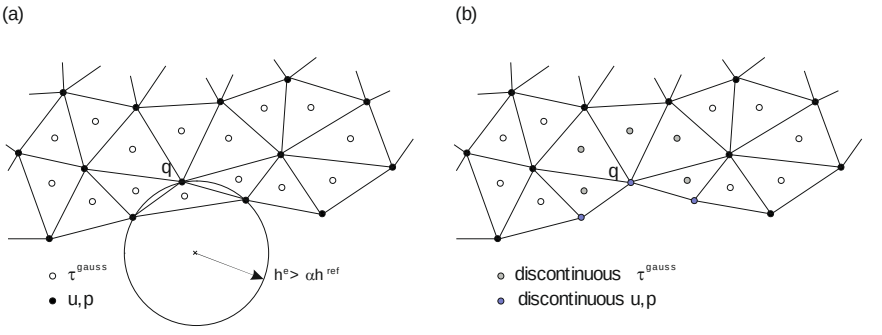

Figure 3-2. Pressure discontinuity caused by α-method boundary recognition: (a) Boundary element recognized exceeding reference size, (b) Elimination of boundary element.

It is observed, that for a given point q, the nodal internal forces should satisfy the equilibrium condition

$$\left\| \mathbf{F}_q^{res} \right\| = 0, \qquad \mathbf{F}_q^{res} = \sum_e \mathbf{F}_q^{res,e} \tag{3.1}$$

where the sudden removal of an element will generate the instability. It has to be recalled that the α-shape criterion is given in the whole boundary, which in case for a large variation on the definition of the previous and new boundary will generate a lack of convergence.

Due to the computational capacity nowadays, we consider the advantage of time efficiency has a minor repercussion against the drawbacks mentioned above. It is proposed a constraint boundary in order to circumvent these problems.

The constraint of the boundary, in large deformation problems, is susceptible to present material overlapping. The problem that arises from this overlapping lies on the reconnecting process and the transference of information between meshes. In this sense, the construction of a convex-hull of the domain by the Delaunay triangulation and the definition of the boundary through the α-shape method overcomes this problem; for a constraint boundary algorithm, they are sorted using two treatments.

The first case is given when regions apart of the same domain tend to overlap, see Figure 3-3(a); in this case, the problem is circumventing with a proper auto contact algorithm. At the end of this chapter, in section 3.4, it is discussed our proposal for a contact methodology that allows the auto contact condition.

The second case is presented when two adjacent boundary lengths tend to collapse, see Figure 3-3(b). The collapsing of two adjacent boundary sections is a geometrical aspect present when the concave angle of both sections tends to diminish. The treatment is similar as the one discussed in last section; its geometrical treatment is presented in the Appendix A.

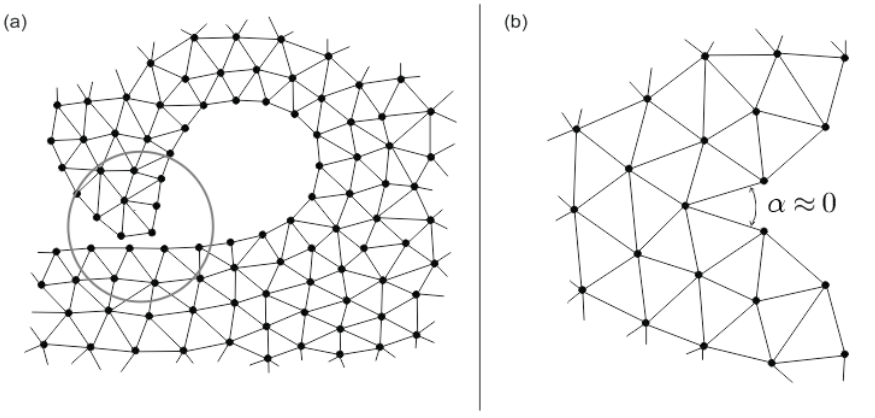

Figure 3-3. Singularities in a constraint boundary in large deformation problems: (a) Material overlapping, and (b) Collapsing of adjacent lengths.

3.1.2.3. Gauss points variables transference

In solid mechanics the computation of the stress state in a body, at a given time, requires the history of its deformation. For this reason, it is necessary to save this information. Since the *PFEM* remeshing process modifies the nodal connectivities, in the implementation of the *PFEM* for solid mechanics, the transference of internal variables was established through a nodal scheme ([76],[36]). It is performed by a smoothing process of all internal variables, of a patch, in its corresponding nodal connectivity; some techniques are reported by ([109],[23],[54]), among others. These algorithms have been proved correct for a variable transference, even though for the purpose of this work it is proposed a variable transference among a projection operator from one mesh to another using former and new integration points.

The modification of the transference of information criterion arrives due to the large variation of number and position of particles during the discretization of the domain. In the processes of insertion and removal of particles, the standard smoothing process could be executed, see Figure 3-4.

The problem arises after the repositioning of particles; once the particle is located at a new position, a local search has to be done in order to interpolate the nodal information. Since this process has to be accomplished, besides the smoothing process, the transference of Gauss point variables between meshes is set directly through a mesh projection. The variables projection is done after the remeshing processes, as shown in Figure 3-5 for a patch test.

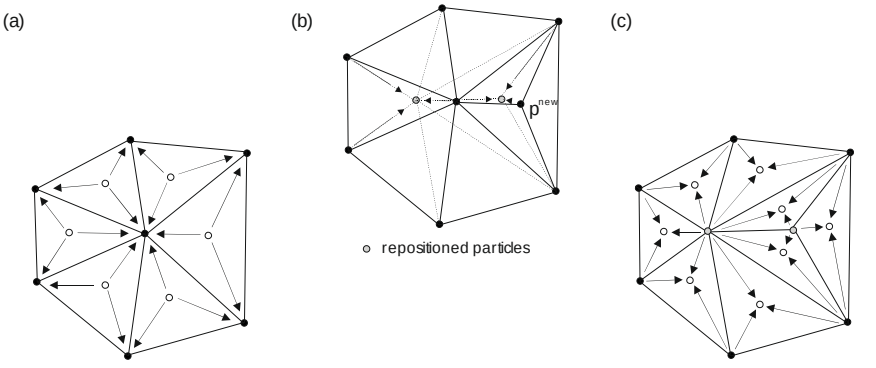

Figure 3-4. Internal variable transference via nodal smoothing. (a) Nodal smoothing process; (b) remeshing process, a new particle is inserted and thereafter both internal particles are repositioned (the nodal information of the repositioned particles has to be updated by an interpolation); and (c) Transference to Gauss points from nodal interpolation.

In this work the projection is carried out by a direct search of the position of the new integration points on the former mesh. More sophisticated algorithms could be implemented as the projection of internal variables by applying Lie groups [73].

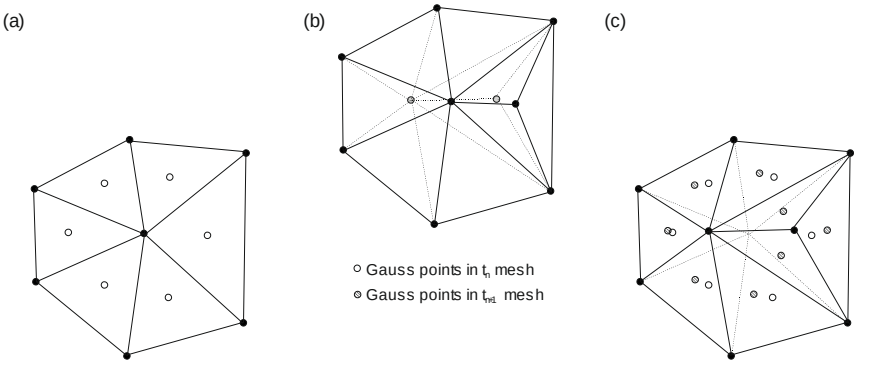

Figure 3-5. Internal variable transference via a mesh projection. (a) Converged mesh; (b) remeshing process, a new particle is inserted and thereafter both internal particles are repositioned; (c) Variable projection.

3.2. Integration of the constitutive model

In this section, the integration of the numerical model is described. The numerical solution is computed, following the basis of the *PFEM*, via an incremental algorithm within the framework of an updated Lagrangian formulation. The temporal and spatial discretizations of the weak form of the balance equations, mentioned in previous chapter, are presented, as well as the corresponding numerical formulation. For the constitutive model, the implicit/explicit (*Impl-Ex*) integration scheme proposed in [78] is used.

3.2.1. Implicit integration of the constitutive model

Given a time interval $[0,T] \subset \mathbb{R}$ that describes the motion of the body, the numerical solution is obtained through a temporal discretization of the time interval in terms of a given time step $\Delta t_{n+1} = t_{n+1} - t_n$. In an updated Lagrangian formulation, the motion is described in terms of the last converged configuration, see Figure 3-6, and the incremental solution is described assuming the knowledge of the converged stress tensor $\boldsymbol{\tau}_n$ at the time step t_n – the subindex $(\bullet)_n$ stands for all variables established in the intermediate reference configuration, and $(\bullet)_{n+1}$ for those variables in the current configuration.

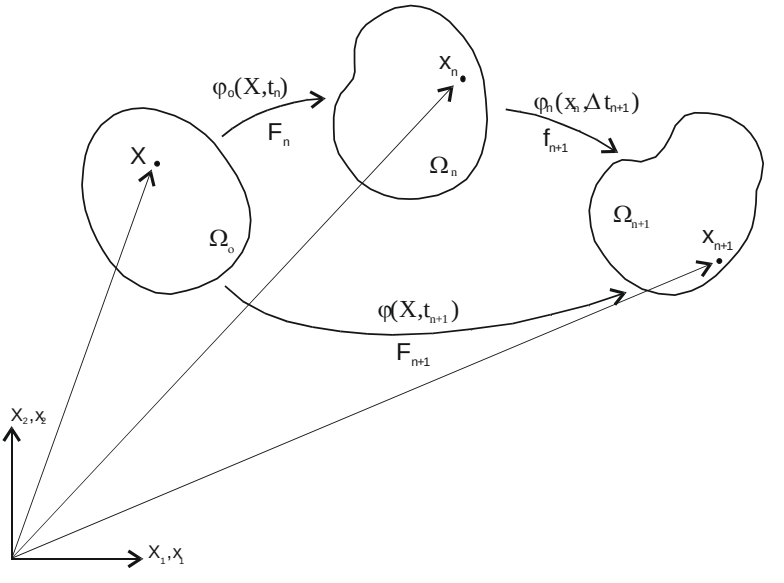

Figure 3-6. Mapping of a given body Ω under different configurations.

For the temporal discretization, the multiplicative decomposition of the deformation gradient, given by equation (2.4), is used

$$\mathbf{F} = \mathbf{F}_{n+1} \cdot \mathbf{f}_n \tag{3.2}$$

As mentioned in section 2.3.1, the strain-stress relationship is defined in terms of a hypoelastic type model given by equation (2.12). It is essential to calculate the objective derivative of the constitutive model in order to ensure the definition of the Kirchhoff stress tensor frame-invariant. The objective derivative of the Kirchhoff stress tensor is calculated by the algorithmic approximation given by [93]

$$L_v \boldsymbol{\tau}_{n+\alpha} = \frac{1}{\Delta t_{n+1}} \boldsymbol{f}_{n+\alpha} \cdot \left[\boldsymbol{f}_{n+1}^{-1} \cdot \boldsymbol{\tau}_{n+1} \cdot \boldsymbol{f}_{n+1}^{-T} - \boldsymbol{\tau}_n \right] \cdot \boldsymbol{f}_{n+\alpha}^{T} \tag{3.3}$$

being objective for all $\alpha = [0,1]$.

In this work, the integration is defined in the current configuration t_{n+1}, with $\alpha = 1$. The Lie derivative is expressed as the time variation of the increment of the Kirchhoff stress tensor.

$$L_v \boldsymbol{\tau}_{n+1} = \frac{1}{\Delta t_{n+1}} \left[\boldsymbol{\tau}_{n+1} - \boldsymbol{f}_{n+1} \cdot \boldsymbol{\tau}_n \cdot \boldsymbol{f}_{n+1}^{T} \right] \tag{3.4}$$

It is observed, in the second term of the RHS of equation (3.4), the description in the current configuration of the Kirchhoff stress tensor of the converged configuration t_n carried out by the push-forward operator.

With the aim of obtaining a description of the stress tensor, the flow rule given in equation (2.22) is approximated as:

$$\mathbf{d}_{n+1}^{p} = \frac{\Delta \lambda_{n+1}}{\Delta t_{n+1}} \operatorname{dev} \boldsymbol{\tau}_{n+1} \tag{3.5}$$

where $\Delta \lambda_{n+1} = \lambda_{n+1} - \lambda_n$.

The expression for the Kirchhoff stress tensor in the current configuration is obtained setting equal the discretized equation (2.12) and equation (3.4) and by substituting the expression of the plastic part of the rate of deformation tensor by the discretized form of the flow rule given in equation (3.5). Rearranging terms and multiplying the expression by Δt_{n+1}, the following equality is obtained:

$$\boldsymbol{\tau}_{n+1} - \boldsymbol{f}_{n+1} \cdot \boldsymbol{\tau}_n \cdot \boldsymbol{f}_{n+1}^{T} = \boldsymbol{c} : [\Delta t_{n+1} \mathbf{d}_{n+1} - \Delta \lambda_{n+1} \operatorname{dev} \boldsymbol{\tau}_{n+1}] \tag{3.6}$$

The rate of deformation tensor is described as the push-forward of the covariant time derivative of the Green-Lagrange strain tensor $\mathbf{E}$ [42].

$$\mathbf{d} = \mathbf{F}^{-T} \cdot \dot{\mathbf{E}} \cdot \mathbf{F}^{-1} \tag{3.7}$$

Equation (3.7) is described, after some manipulations, in the current configuration by the Almansi strain tensor. Its numerical approximation is given by:

$$\mathbf{d}_{n+1} = \frac{1}{\Delta t_{n+1}} \mathbf{e}_{n+1} \tag{3.8}$$

The expression for the Kirchhoff stress tensor in the current configuration is completed substituting equation (3.8) into equation (3.6).

$$\boldsymbol{\tau}_{n+1} = \boldsymbol{f}_{n+1} \cdot \boldsymbol{\tau}_n \cdot \boldsymbol{f}_{n+1}^T + \boldsymbol{c} : [\mathbf{e}_{n+1} - \Delta\lambda_{n+1} \mathrm{dev}\, \boldsymbol{\tau}_{n+1}] \tag{3.9}$$

Equation (3.9) is simplified using the definition of the trial elastic state given by the freezing of the plastic flow.

$$\boldsymbol{\tau}_{n+1}^{\text{trial}} = \boldsymbol{f}_{n+1} \cdot \boldsymbol{\tau}_n \cdot \boldsymbol{f}_{n+1}^T + \boldsymbol{c} : \mathbf{e}_{n+1} \tag{3.10}$$

or

$$\boldsymbol{\tau}_{n+1}^{\text{trial}} = \hat{\boldsymbol{\tau}}_{n+1} + \boldsymbol{c} : \mathbf{e}_{n+1} \tag{3.11}$$

where $\hat{\boldsymbol{\tau}}_{n+1} = \boldsymbol{f}_{n+1} \cdot \boldsymbol{\tau}_n \cdot \boldsymbol{f}_{n+1}^T$.

The simplified description of the Kirchhoff stress tensor is obtained substituting equation (3.10) into (3.9).

$$\boldsymbol{\tau}_{n+1} = \boldsymbol{\tau}_{n+1}^{\text{trial}} - \Delta\lambda_{n+1} \boldsymbol{c} : \mathrm{dev}\, \boldsymbol{\tau}_{n+1} \tag{3.12}$$

The plastic regime is defined for a loading state where the evaluation of the yield conditions for the auxiliary state, $\boldsymbol{\tau}_{n+1}^{\text{trial}}$, exceeds the yield surface expressed by equation (2.14):

$$\phi\left(\boldsymbol{\tau}_{n+1}^{\text{trial}}\right) > 0 \tag{3.13}$$

where

$$\phi(\boldsymbol{\tau})^{\text{trial}} = \left\| \mathrm{dev}\, \boldsymbol{\tau}_{n+1}^{\text{trial}} \right\| + \frac{1}{3} b_1 p_{n+1} - b_2 \tag{3.14}$$

and

$$p_{n+1} = \mathrm{tr}\, \boldsymbol{\tau}_{n+1} = \mathrm{tr}\, \boldsymbol{\tau}_{n+1}^{\text{trial}} \tag{3.15}$$

The deviatoric part of the Kirchhoff stress tensor, defined by equation (3.12), is rewritten in terms of the elastic fourth order tensor $\boldsymbol{c}$.

$$\mathrm{dev}\, \boldsymbol{\tau}_{n+1} = \mathrm{dev}\, \boldsymbol{\tau}_{n+1}^{\text{trial}} - \Delta\lambda_{n+1} [2\mu + \lambda \mathbf{1} \otimes \mathbf{1}] : \mathrm{dev}\, \boldsymbol{\tau}_{n+1} \tag{3.16}$$

The double contraction of the volumetric part of this tensor with the deviatoric stress is null, reducing the above expression into

$$\mathrm{dev}\, \boldsymbol{\tau}_{n+1} = \mathrm{dev}\, \boldsymbol{\tau}_{n+1}^{\text{trial}} - 2\mu\Delta\lambda_{n+1} \mathrm{dev}\, \boldsymbol{\tau}_{n+1} \tag{3.17}$$

The expression of the deviatoric stress tensor is given in terms of the trial stress by solving $\mathrm{dev}\, \boldsymbol{\tau}_{n+1}$ from equation (3.17)

$$\mathrm{dev}\, \boldsymbol{\tau}_{n+1} = \frac{1}{1 + 2\mu\Delta\lambda_{n+1}} \mathrm{dev}\, \boldsymbol{\tau}_{n+1}^{\text{trial}} \tag{3.18}$$

The expression for the slip rate $\Delta\lambda_{n+1}$, of the flow rule, is given for that stress state such that $\phi(\boldsymbol{\tau}_{n+1}) = 0$

$$\left\| \mathrm{dev}\, \boldsymbol{\tau}_{n+1} \right\| + b_1 p_{n+1} - b_2 = 0 \tag{3.19}$$

Substituting eq. (3.18) into (3.19)

$$\frac{1}{1+2\mu\Delta\lambda_{n+1}}\left\|\operatorname{dev}\boldsymbol{\tau}_{n+1}^{\text{trial}}\right\|+b_1 p_{n+1}-b_2=0 \tag{3.20}$$

and manipulating equation (3.20), the expression for $\Delta\lambda_{n+1}$ is obtained

$$\Delta\lambda_{n+1}=\frac{\left\|\operatorname{dev}\boldsymbol{\tau}_{n+1}^{\text{trial}}\right\|+b_1 p_{n+1}-b_2}{2\mu(b_2-b_1 p_{n+1})} \tag{3.21}$$

The slip rate $\Delta\lambda_{n+1}$ is simplified by substituting equation (3.14) into (3.21), reading as:

$$\Delta\lambda_{n+1}=\frac{\phi(\boldsymbol{\tau})^{\text{trial}}}{2\mu(b_2-b_1 p_{n+1})} \tag{3.22}$$

Finally, the Kirchhoff stress tensor reads as:

$$\boldsymbol{\tau}_{n+1}=\alpha_{n+1}\operatorname{dev}\boldsymbol{\tau}_{n+1}^{\text{trial}}+p_{n+1}\mathbf{1} \tag{3.23}$$

where:

$$\alpha_{n+1}=\alpha_{n+1}(\Delta\lambda_{n+1})=\left(\frac{1}{1+2\mu\Delta\lambda_{n+1}}\right) \tag{3.24}$$

Model integration of the Von-Mises regularization

The Drucker-Prager yield surface is well-defined for all those stress states with a hydrostatic pressure smaller or equal than p_a – defined by the vertex of the surface, as shown in Figure 2-5. As mentioned in section 2.3.2, a von Mises regularization is proposed for those loading states whose hydrostatic pressure is beyond the apex. A pressure reference p^* is defined, which is the pressure value where the regularization starts.

The elasto-plastic condition, for those pressures on the compression regime

$$p_{n+1}\leq p^* \tag{3.25}$$

where $p_{n+1}=\operatorname{tr}\boldsymbol{\tau}_{n+1}$, could present two loading states

$\phi(\boldsymbol{\tau})<0$ Elastic regime

$\phi(\boldsymbol{\tau})=0$ Plastic regime

The numerical integration for the regularization, proposed in section 2.3.2 for those stress states with pressures greater than p^*, is developed similarly as for the Drucker-Prager model.

The expression for the slip rate $\Delta\lambda$ is obtained similarly by defining a stress state on the yield surface of the von Mises regularization, given by equation (2.17), such that $\phi^*(\boldsymbol{\tau}_{n+1})=0$. Substituting equation (3.18) into equation (2.17)

$$\frac{1}{1+2\mu\Delta\lambda}\left\|\operatorname{dev}\boldsymbol{\tau}_{n+1}^{\text{trial}}\right\|-q^*=0 \tag{3.26}$$

and solving for the plastic multiplier, the expression reads:

$$\Delta\lambda = \frac{\left\| \operatorname{dev} \boldsymbol{\tau}_{n+1}^{\text{trial}} \right\| - q^*}{2\mu q^*} \tag{3.27}$$

Equation (3.27) is rewritten substituting the numerator with the definition of the yield surface in terms of the trial stress tensor.

$$\Delta\lambda = \frac{\phi^*(\boldsymbol{\tau})^{\text{trial}}}{2\mu q^*} \tag{3.28}$$

Integration of the visco-plastic regularization

The integration described in previous section is completed incorporating the visco-plastic regularization given in section 2.3.4. The integration of the visco-plastic regularization is obtained, similarly as in previous section, comparing the Lie derivatives defined for the visco-plastic model, expressed by equation (2.27), and the algorithmic approximation given in equation (3.4). Rearranging common terms, the expression reads:

$$\left(1 - \frac{\Delta t}{\tau_R}\right)\boldsymbol{\tau}_{n+1} = \boldsymbol{f}_{n+1} \cdot \boldsymbol{\tau}_n \cdot \boldsymbol{f}_{n+1}^T + \boldsymbol{c} : \mathbf{e}_{n+1} + \frac{\Delta t}{\tau_R}\boldsymbol{\tau}_{n+1}^{\text{ep}} \tag{3.29}$$

where $\boldsymbol{\tau}_{n+1}^{\text{ep}}$ corresponds to the solution of the elasto-plastic part of the model given by equation (3.23) and τ_R refers to the relaxation time.

Equation (3.29) is rewritten regrouping terms and substituting the definition of the trial stress tensor $\boldsymbol{\tau}_{n+1}^{\text{trial}}$ in order to obtain an expression for $\boldsymbol{\tau}_{n+1}$ in terms of the visco-plastic regularization

$$\boldsymbol{\tau}_{n+1} = \frac{1}{1 + \Delta t/\tau_R}\boldsymbol{\tau}_{n+1}^{\text{trial}} + \frac{\Delta t/\tau_R}{1 + \Delta t/\tau_R}\boldsymbol{\tau}_{n+1}^{\text{ep}} \tag{3.30}$$

The following term is defined in order to simplify the expression

$$\eta = \frac{1}{1 + \Delta t/\tau_R} \tag{3.31}$$

The Kirchhoff stress tensor in the visco-plastic formulation is expressed substituting the above expression into equation (3.30)

$$\boldsymbol{\tau}_{n+1}^{\text{vp}} = \eta\boldsymbol{\tau}_{n+1}^{\text{trial}} + (1-\eta)\boldsymbol{\tau}_{n+1}^{\text{ep}} \tag{3.32}$$

where hereinafter it is taken indistinctly $\boldsymbol{\tau}_{n+1}^{\text{vp}}$ and $\boldsymbol{\tau}_{n+1}$.

The algorithm for the implicit integration of the Kirchhoff stress tensor is summarized in Box 3-2.

Given: $\{\varphi_n(\Omega), \boldsymbol{\tau}_n, \Delta t_{n+1}, \mathbf{u}_{n+1} : \varphi_n(\Omega) \to \mathbb{R}^2, \kappa, \mu, b_1, b_2, p_a = b_2/b_1, p_a^*\}$,

compute trial stresses

$$\boldsymbol{f}_{n+1} = \mathbf{1} + \nabla \mathbf{u}_{n+1}$$

$$\mathbf{e}_{n+1} = \frac{1}{2}\left(\mathbf{1} + \boldsymbol{f}_{n+1}^{-T} \cdot \boldsymbol{f}_{n+1}^{-1}\right)$$

$$\boldsymbol{\tau}_{n+1}^{\text{trial}} = \boldsymbol{f}_{n+1} \cdot \boldsymbol{\tau}_n \cdot \boldsymbol{f}_{n+1}^{T} + \boldsymbol{c} : \mathbf{e}_{n+1}$$

$$p_{n+1} = p_{n+1}^{\text{trial}} = \frac{1}{3}\text{tr}\,\boldsymbol{\tau}_{n+1}^{\text{trial}}$$

Define pressure condition, p_{n+1}

IF $p_{n+1} \le p_a$ THEN – Drucker-Prager yield surface

$$\phi(\boldsymbol{\tau})^{\text{trial}} = \left\|\text{dev}\,\boldsymbol{\tau}_{n+1}^{\text{trial}}\right\| + \frac{1}{3} b_1 p_{n+1} - b_2$$

IF $\phi(\boldsymbol{\tau})_{n+1}^{\text{trial}} \le 0$ THEN (Elastic regime)

$$\boldsymbol{\tau}_{n+1} = \boldsymbol{\tau}_{n+1}^{\text{trial}}$$

ELSE (Plastic regime)

$$\Delta\lambda = \frac{\phi(\boldsymbol{\tau})^{\text{trial}}}{2\mu(b_2 - b_1 p_{n+1})}$$

END

ELSE (von-Mises regularization)

$$\Delta\lambda = \frac{\phi^*(\boldsymbol{\tau})^{\text{trial}}}{2\mu q^*} = \frac{\|\text{dev}\,\boldsymbol{\tau}\| - q^*}{2\mu q^*}$$

END

Kirchhoff stress tensor calculation

$$\text{dev}\,\boldsymbol{\tau}_{n+1} = \frac{1}{1 + 2\mu\Delta\lambda}\text{dev}\,\boldsymbol{\tau}_{n+1}^{\text{trial}}$$

$$\boldsymbol{\tau}_{n+1} = \text{dev}\,\boldsymbol{\tau}_{n+1} + p_{n+1}\mathbf{1}$$

Visco-plastic regularization

$$\eta = \frac{1}{1 + \Delta t_{n+1}/\tau_R}$$

$$\boldsymbol{\tau}_{n+1} = \eta\boldsymbol{\tau}_{n+1}^{\text{trial}} + (1-\eta)\boldsymbol{\tau}_{n+1}^{\text{ep}}$$

Box 3-2. Integration algorithm for the visco-plastic formulation of the granular material flow model.

3.2.2. Integration of the constitutive equation – *Impl-Ex* scheme

For non-linear problems, the implicit integration schemes are widely used since they present a higher stability compared to explicit schemes. Their advantage, compared

to explicit ones, is the definition of larger time steps on the solving process with a high degree of accuracy. In our case, near the apex of the Drucker-Prager surface, the matrix of the system to solve may be ill-conditioned. In order to increase the robustness of the model, the model is integrated based in an implicit/explicit integration scheme (*Impl-Ex*) proposed in Ref. [78]. This strategy combines the implicit and explicit integration schemes aiming to exploit the benefits and minimize the drawbacks of both.

The method follows the standard implicit integration scheme of the stresses $\boldsymbol{\tau}_{n+1}$ in the constitutive model discussed in previous section, with an explicit extrapolation of the slip rate $\Delta\lambda$.

From the temporal discretization of the flow rule, given in equation (3.5), the discretization of the consistency parameter or plastic multiplier $\dot{\lambda}$ is observed.

$$\dot{\lambda}_{n+1} = \frac{\Delta\lambda_{n+1}}{\Delta t_{n+1}} \tag{3.33}$$

The *Impl-Ex* scheme requires the explicit interpolation of the plastic multiplier, as the internal variable of the constitutive model, expressed as

$$\frac{\Delta\lambda_{n+1}}{\Delta t_{n+1}} \approx \frac{\Delta\lambda_n}{\Delta t_n} \rightarrow \Delta\tilde{\lambda}_{n+1} = \frac{\Delta t_{n+1}}{\Delta t_n}\Delta\lambda_n \tag{3.34}$$

where $\Delta t_{n+1} = t_{n+1} - t_n$, $\Delta t_n = t_n - t_{n-1}$. Substituting in equation (3.18) the discretized plastic multiplier by equation (3.34), the deviatoric part of the Kirchhoff stress tensor given in equation (3.23) reads

$$\operatorname{dev}\tilde{\boldsymbol{\tau}}_{n+1} = \frac{1}{1+2\mu\Delta\tilde{\lambda}_{n+1}}\operatorname{dev}\boldsymbol{\tau}^{\text{trial}}_{n+1} \tag{3.35}$$

and similarly, the expression of the elastic factor α_{n+1} given in equation (3.24) is expressed in the *Impl-Ex* scheme as

$$\tilde{\alpha}_{n+1} = \frac{1}{1+2\mu\Delta\tilde{\lambda}_{n+1}} \tag{3.36}$$

The *Impl-Ex* scheme is summarized in Box 3-3. As it is observed, it is necessary to take into account the computation of the slip rate $\Delta\lambda$, given in equation (3.22), to fulfil the algorithm given in Box 3-3 for the following time step.

Likewise, the calculation of the tensor $\boldsymbol{\tau}_{n+1}$ given in Box 3-2 allows us to estimate the error that implies the integration of the model via the *Impl-Ex* scheme so that if:

$$\left\|\boldsymbol{\tau}_{n+1} - \tilde{\boldsymbol{\tau}}_{n+1}\right\| > tol \tag{3.37}$$

the new time step is modified according to $\Delta t^{new}_{n+1} = \beta\Delta t_{n+1}$, where $\beta < 1$.

Given: $\{\varphi_n(\Omega), \boldsymbol{\tau}_n, \Delta t_n, \Delta t_{n+1}, \mathbf{u}_{n+1} : \varphi_n(\Omega) \to \mathbb{R}^2, \kappa, \mu, \Delta\lambda_n\}$,
compute trial elastic stresses

$$\boldsymbol{f}_{n+1} = \mathbf{1} + \nabla \mathbf{u}_{n+1}$$

$$\mathbf{e}_{n+1} = \frac{1}{2}\left(\boldsymbol{1} + \boldsymbol{f}_{n+1}^{-T} \cdot \boldsymbol{f}_{n+1}^{-1}\right)$$

$$\boldsymbol{\tau}_{n+1}^{\text{trial}} = \boldsymbol{f}_{n+1} \cdot \boldsymbol{\tau}_{n+1} \cdot \boldsymbol{f}_{n+1}^{T} + \boldsymbol{c} : \mathbf{e}_{n+1}$$

$$p_{n+1} = p_{n+1}^{\text{trial}} = \frac{1}{3}\operatorname{tr}\boldsymbol{\tau}_{n+1}^{\text{trial}}$$

Extrapolate plastic multiplier, $\Delta\tilde{\lambda}_{n+1}$

$$\Delta\tilde{\lambda}_{n+1} = \frac{\Delta t_{n+1}}{\Delta t_n}\Delta\lambda_n$$

Extrapolate plastic multiplier, $\Delta\tilde{\lambda}_{n+1}$

$$\tilde{\boldsymbol{\tau}}_{n+1} = \frac{1}{1 + 2\mu\Delta\tilde{\lambda}_{n+1}}\operatorname{dev}\boldsymbol{\tau}_{n+1}^{\text{trial}} + p_{n+1}\mathbf{1}$$

Box 3-3. Explicit algorithm for the *Impl-Ex* integration scheme.

3.2.3. Algorithmic tangent constitutive tensor

The non-linear problem is solved using a traditional iterative Newton-Raphson procedure of the linearized system of equations – as it will be described in next section. Then, the linearization of the constitutive equation requires the algorithmic tangent constitutive tensor. This tensor is defined following the standard procedure of computing all derivatives on the material (intermediate reference) configuration followed by its expression in the spatial or current configuration by the *push-forward* operator.

The elasto-plastic tangent tensor $\boldsymbol{c}^{\text{ep}}$ relates the objective derivative of the stress tensor $\boldsymbol{\tau}_{n+1}$, with the objective derivative of the strain tensor $\mathbf{e}_{n+1}$, reading as [13]:

$$L_v(\boldsymbol{\tau}_{n+1}) = \boldsymbol{c}^{\text{ep}} : L_v(\mathbf{e}_{n+1}) \tag{3.38}$$

The elasto-plastic constitutive tensor for equation (3.38), deduced by an implicit/explicit (*Impl-Ex*) integration scheme, is expressed as

$$\begin{aligned}\boldsymbol{c}^{\text{ep}} = \frac{2}{3}\alpha_{n+1}\left[\operatorname{tr}\hat{\boldsymbol{\tau}}_{n+1}\boldsymbol{\iota} - \mathbf{1}\otimes\hat{\boldsymbol{\tau}}_{n+1}\right] + \alpha_{n+1}\left(\boldsymbol{a}^{\text{dev}}(\mathbf{e}_{n+1}) + \boldsymbol{c}^{\text{dev}}\right) + \\ \kappa(\mathbf{1}\otimes\mathbf{1}) + -2p_{n+1}\boldsymbol{\iota}\end{aligned} \tag{3.39}$$

where α_{n+1} is given by expression (3.36).

Finally, for the numerical formulation with a visco-plastic regularization, the algorithmic tangent tensor is expressed as

$$\boldsymbol{c}^{\text{vp}} = \eta \boldsymbol{c}^{\text{trial}} + (1-\eta)\boldsymbol{c}^{\text{ep}} \tag{3.40}$$

where:

$$\boldsymbol{c}^{\text{trial}} = \boldsymbol{c} + \boldsymbol{a}(\mathbf{e}_{n+1}) \tag{3.41}$$

Full development of the algorithmic tangent tensor is given in Appendix B.

3.3. Linearization of the variational problem

Recalling the weak form of the balance equations given in Box 2.3, both equations are expressed as

$$\begin{aligned}\int_{\Omega_{n+1}} \nabla_{n+1}(\delta \boldsymbol{w}) : \boldsymbol{\sigma}_{n+1}\, d\Omega_{n+1} - \int_{\Omega_{n+1}} \delta \boldsymbol{w} \cdot (\rho \mathbf{b}) d\Omega_t - \\ \int_{\Gamma_{n+1}} \delta \boldsymbol{w} \cdot \bar{\mathbf{t}}\, d\Gamma_{n+1} + \int_{\Omega_{n+1}} \delta \boldsymbol{w} \cdot (\rho \dot{\mathbf{v}}) d\Omega_{n+1} = 0\end{aligned} \tag{3.42}$$

$$\int_{\Omega_o} \delta q \left(\frac{\ln J_{n+1}}{J_{n+1}} - \frac{1}{\kappa} \pi \right) d\Omega_o = 0 \tag{3.43}$$

The expressions for the generalized forces are obtained from equations (3.42) and (3.43), and taking into account the nodal interpolation of the variables[5]. The displacement field is approximated by the standard linear shape functions

$$\mathbf{u}^e(\mathbf{x}) \approx \sum_{i=1}^{n_p} N_i(\mathbf{x}) \mathbf{u}_i \tag{3.44}$$

and the pressures by

$$p^e(\mathbf{x}) \approx \sum_{i=1}^{n_p} N_i(\mathbf{x})\, p_i \tag{3.45}$$

where the subscript $(\bullet)^e$ stands for the each subdomain or element with characteristic size h, n_p is the number of nodes defining the element – in this case three for the linear triangle used, and N_i the standard shape function, such that its value is 1 at the associated node i and zero for the rest of the element nodes. Similarly, the test functions δw and δq are interpolated by the following expressions

$$\delta w^e(\mathbf{x}) \approx \sum_{i=1}^{n_p} N_i(\mathbf{x}) \delta w_i \tag{3.46}$$

[5] The subscript $(\bullet)_{n+1}$ is omitted in this section, unless expressly stated otherwise, in order to simplify the notation of the spatial discretization.

$$\delta q^e(\mathbf{x}) \approx \sum_{i=1}^{n_p} N_i(\mathbf{x})\delta q_i \tag{3.47}$$

The residual of internal forces $\mathbf{R}^u$, obtained from equation (3.42), is expressed as

$$\left[\mathbf{R}^u\right] = \left[\mathbf{F}^{\text{int,mix}}\right] - \left[\mathbf{F}^{\text{ext}}\right] + \left[\mathbf{F}^{\text{ine}}\right] = 0 \tag{3.48}$$

where:

$$\left[\mathbf{F}^{\text{int,mix}}\right]_I^e = \int_{\Omega^e} \boldsymbol{\sigma}^e \cdot \nabla(N_I)\, d\Omega^e \tag{3.49}$$

$$\left[\mathbf{F}^{\text{ext}}\right]_I^e = \int_{\Omega^e} N_I \rho^e \mathbf{b}^e d\Omega^e + \int_{\Gamma^e} N_I \bar{\mathbf{t}}^e\, d\Gamma^e \tag{3.50}$$

$$\left[\mathbf{F}^{\text{ine}}\right]_I^e = \int_{\Omega^e} N_I \rho^e \dot{\mathbf{v}}^e d\Omega^e \tag{3.51}$$

The discrete form of the generalized forces $\mathbf{R}^q$ from the incompressibility equation, given by equation (3.43), reads as:

$$\left[\mathbf{R}^q\right]_I^e = \int_{\Omega_0^e} N_I \left(\frac{\ln J^e}{J^e} - \frac{1}{\kappa} N_A \pi^e \right) d\Omega_0^e \tag{3.52}$$

Finally, the vector of residual forces $\mathbf{F}^{\text{res}}$ is obtained using equation (3.48) and the global assemble of equation (3.52)

$$\mathbf{F}^{\text{res}} = \begin{bmatrix} \mathbf{R}^{u,\text{res}} \\ \mathbf{R}^{q,\text{res}} \end{bmatrix} = \begin{bmatrix} \mathbf{F}^{\text{int,mix}} - \mathbf{F}^{\text{ext}} + \mathbf{F}^{\text{ine}} \\ \mathbf{R}^q \end{bmatrix} \tag{3.53}$$

Now, the stiffness matrix is obtained from the linearization of the vector of residual forces, which in a mixed formulation reads:

$$\delta\mathbf{F}^{\text{res}} = \begin{bmatrix} \delta\mathbf{R}^{u,\text{res}} \\ \delta\mathbf{R}^{q,\text{res}} \end{bmatrix} \tag{3.54}$$

where $\delta(\bullet)$ stands for the directional derivative of the corresponding tensor.

The Gâteaux derivative is defined as the product of the gradient of a scalar field in the direction of a specific vector. The equivalent representation for the directional derivative of the scalar field in a certain point, $\mathbf{x}$, is given by

$$D_\varphi \Phi(\mathbf{x}) = \frac{\mathrm{d}}{\mathrm{d}\varepsilon} \Phi(\mathbf{x} + \varepsilon\varphi)\Big|_{\varepsilon=0} \tag{3.55}$$

Equation (3.55) characterizes the rate of change of the field Φ along the normal vector φ through the point $\mathbf{x}$. The full development of the linearization of the vector of residual forces, expressed in equation (3.54), is given in Appendix C. Finally, the elemental Jacobian or stiffness matrix reads:

$$\mathbf{K}_{IA}^{h} = \begin{bmatrix} \mathbf{K}^{uu} & \mathbf{K}^{u\pi} \\ \mathbf{K}^{\pi u} & \mathbf{K}^{\pi\pi} \end{bmatrix}_{IA}^{h} \tag{3.56}$$

A summary of the definition and implementation of the discretized stiffness matrix is given in Box 3-4.

Element stiffness matrix $\mathbf{K}^e$

$$\mathbf{K}^e = \begin{bmatrix} \mathbf{K}^{uu} & \mathbf{K}^{u\pi} \\ \mathbf{K}^{\pi u} & \mathbf{K}^{\pi\pi} \end{bmatrix} = \begin{bmatrix} \left(K^{uu}\right)_{Ii,Jj} & \left(K^{u\pi}\right)_{Ii,A} \\ \left(K^{\pi u}\right)_{I,Ak} & \left(K^{\pi\pi}\right)_{I,A} \end{bmatrix} \qquad \begin{matrix} (I,J,A=1:3) \\ (i,j,k=1:2) \end{matrix}$$

where:

$$\left[K^{uu}\right]_{Ii,Jj} = \left[K^{\text{geo}}\right]_{Ii,Jj} + \left[K^{\text{mat}}\right]_{Ii,Jj}$$

$$\left[K^{\text{geo}}\right]_{Ii,Jj} = \delta_{ij} \frac{\partial N_I}{\partial x_k} \frac{\partial N_J}{\partial x_l} \sigma_{lk} \left|\Omega^e\right|$$

$$\left[K^{\text{mat}}\right]_{Ii,Jj} = \frac{\partial N_I}{\partial x_k} \mathsf{c}^{\text{ep}}_{iklj} \frac{\partial N_J}{\partial x_l} \left|\Omega^e\right|$$

$$\left[K^{u\pi}\right]_{Ii,A} = \frac{\partial N_I}{\partial x_i} N_A \left|\Omega^e\right|$$

$$\left[K^{\pi u}\right]_{I,Ak} = \left(\frac{1-J}{J^2}\right) N_I \frac{\partial N_A}{\partial x_k} \left|\Omega^e\right|$$

$$\left[K^{\pi\pi}\right]_{I,A} = \frac{1}{\kappa} N_I N_A \left|\Omega^e\right|$$

Vector of residual forces $\left[\mathbf{R}^u\right]$

$$\left[\mathbf{R}^u\right] = \left[\mathbf{F}^{\text{int,mix}}\right] - \left[\mathbf{F}^{\text{ext}}\right] + \left[\mathbf{F}^{\text{ine}}\right] = 0$$

where:

$$\left[\mathbf{F}^{\text{int,mix}}\right]_I^e = \int_{\Omega^e} \boldsymbol{\sigma}^e \cdot \nabla(N_I)\, d\Omega^e$$

$$\left[\mathbf{F}^{\text{ext}}\right]_I^e = \int_{\Omega^e} N_I \rho^e \mathbf{b}^e d\Omega^e + \int_{\Gamma^e} N_I \bar{\mathbf{t}}^e d\Gamma^e$$

$$\left[\mathbf{F}^{\text{ine}}\right]_I^e = \int_{\Omega^e} N_I \rho^e \dot{\mathbf{v}}^e d\Omega^e$$

Vector of residual forces $\left[\mathbf{R}^q\right]$

$$\left[\mathbf{R}^q\right]_I^e = \int_{\Omega^e} N_I \left(\frac{\ln J^e}{J^e} - \frac{1}{\kappa} N_A \pi^e\right) d\Omega^e$$

And

$$\left|\Omega^e\right| = \int_{\Omega^e} d\Omega^e$$

Box 3-4. Element stiffness matrix $\mathbf{K}^e$ and vector of residual forces $\mathbf{R}$ (integration for a three nodes linear triangle in the current configuration t_{n+1}).

3.3.1. Stabilization method for mixed element – Polynomial Pressure Projection (*PPP*)

The introduction of a $u-p$ mixed formulation overcomes the incompressibility problem but for linear triangles $P1/P1$ the Babuška-Brezzi stability conditions are not assured [10]. For this reason, a stabilization of the pressure field is required. Several methods have been proposed in this field, and it is not our aim perform a comparative analysis of the advantages and drawbacks of them. In this work, a direct pressure stabilization, proposed in Ref. [28], is implemented.

This Polynomial Pressure Projection is proposed as a stabilized finite element method for the Stoke problem [28] and extended to solid mechanics problems [87]. The stabilization is defined by modifying the mixed variational equation in terms of a local L^2 polynomial pressure projection and does not require the use of the momentum equation residual [28]. This condition poses two advantages in its implementation: it is not necessary to calculate higher-order derivatives, and its implementation is given at an element level.

The projection operator $\breve{\pi}$ of the pressure $\pi \in L^2(\Omega)$ is given by

$$\breve{\pi} = \pi^h \in \mathrm{P}^0 \tag{3.57}$$

if and only if

$$\int_{\Omega^e_{n+1}} \delta\breve{q}\,(\pi - \breve{\pi})\, d\Omega^e_{n+1} = 0 \qquad \forall \delta\breve{q} \in \mathrm{P}^0 \tag{3.58}$$

where P^0 is the space of polynomials of order zero; from equation (3.58), it is observed that the method looks at the difference between the interpolated pressure (same order as the displacement) and its projection, a one order lower expansion consistent with that of the stresses [108].

The stabilization term is augmented (subtracted) of the incompressibility equation given by equation (3.43)

$$\begin{aligned}\int_{\Omega^e_o} \delta q \left(\frac{\ln J_{n+1}}{J_{n+1}} - \frac{1}{\kappa}\pi \right) d\Omega^e_o - \\ \frac{\alpha}{\mu}\int_{\Omega^e_o} (\delta q - \delta\breve{q})(\pi - \breve{\pi})\, d\Omega^e_o = 0\end{aligned} \tag{3.59}$$

where α is a dimensionless stabilization parameter, and μ the Lamé's second parameter.

The second term of the LFH of equation (3.59), defined from now on as ψ_{sp}, is extended

$$\psi_{sp} = \frac{\alpha}{\mu}\int_{\Omega^e_o} \left(\pi^e \delta q^e - \pi^e \delta\breve{q}^e - \breve{\pi}^e \delta q^e + \breve{\pi}^e \delta\breve{q}^e \right) d\Omega^e_o \tag{3.60}$$

The discretization of equation (3.60) is obtained by the standard approximation of the variables. The nodal approximations of π and δq have been given by equa-

tions (3.45) and (3.47), respectively. The discretization of the projection operator $\breve{\pi}$ and test function $\delta\breve{q}$ in a three-node linear triangle are given by:

$$\breve{\pi} = \frac{1}{3}(\pi_1 + \pi_2 + \pi_3) \tag{3.61}$$

and

$$\delta\breve{q} = \frac{1}{3}(\delta q_1 + \delta q_2 + \delta q_3) \tag{3.62}$$

The discretization of equation (3.60) leads to an equation formed by four mass matrices that read as

$$\psi_{sp} = \frac{\alpha}{\mu}\left(\delta\mathbf{q}^e\right)^T \left[\mathbf{M}^e - \tilde{\mathbf{M}}^e - \tilde{\tilde{\mathbf{M}}}^e + \tilde{\tilde{\tilde{\mathbf{M}}}}^e\right]\boldsymbol{\pi}^e \tag{3.63}$$

where:

$$\mathbf{M}^e = \int_{\Omega_0^e} N_I N_J d\Omega_0^e \tag{3.64}$$

$$\tilde{\mathbf{M}}^e = \begin{bmatrix} 1/3 \\ 1/3 \\ 1/3 \end{bmatrix}\left[\int_{\Omega_0^e} N_1 d\Omega_0^e,\ \int_{\Omega_0^e} N_2 d\Omega_0^e,\ \int_{\Omega_0^e} N_3 d\Omega_0^e\right] \tag{3.65}$$

$$\tilde{\tilde{\mathbf{M}}}^e = \begin{bmatrix} \int_{\Omega_0^e} N_1 d\Omega_0^e \\ \int_{\Omega_0^e} N_2 d\Omega_0^e \\ \int_{\Omega_0^e} N_3 d\Omega_0^e \end{bmatrix}\left[1/3,\ 1/3,\ 1/3\right] \tag{3.66}$$

$$\tilde{\tilde{\tilde{\mathbf{M}}}}^e = \begin{bmatrix} 1/3 \\ 1/3 \\ 1/3 \end{bmatrix}\left[1/3,\ 1/3,\ 1/3\right]\left\|\Omega_0^e\right\| \tag{3.67}$$

In a plane strain problem, equations (3.65)-(3.67) are reduced to

$$\tilde{\mathbf{M}}^e = \frac{1}{9}A^e\begin{bmatrix} 1 & 1 & 1 \\ 1 & 1 & 1 \\ 1 & 1 & 1 \end{bmatrix} = \tilde{\tilde{\mathbf{M}}}^e = \tilde{\tilde{\tilde{\mathbf{M}}}}^e \tag{3.68}$$

where $A^e = \left\|\Omega_0^e\right\|$. Finally, the implementation of the stabilization term given in equation (3.60) is given, using equations (3.64) and (3.68), as

$$\psi_{sp} = -\frac{\alpha A^e}{36\mu}\begin{bmatrix} 2 & -1 & -1 \\ -1 & 2 & -1 \\ -1 & -1 & 2 \end{bmatrix} \tag{3.69}$$

3.3.2. Time integration algorithm

The time integration algorithm implemented for this work is the generalized-α method, given in Ref. [26]. The method seeks the step-by-step time integration assuring the conservation of linear momentum, and similar to those of the Newmark family, it has a one step, three stages structure.

Equation (3.48) is rewritten as

$$\left[\mathbf{R}^{u}_{n+1}\right] = \left[\mathbf{F}^{\text{int}}_{n+1}\right] - \left[\mathbf{F}^{\text{ext}}_{n+1}\right] + \left[\mathbf{M}\ddot{\mathbf{u}}_{n+1}\right] \tag{3.70}$$

where $\mathbf{M}$ is the mass matrix from the discretization of the vector of inertial forces.

The problem consists of finding a displacement function that satisfies equation (3.70) and the corresponding initial conditions; the set of equations for the generalized-α method defines the displacement and velocity fields as a weighing of the acceleration field in t_n and t_{n+1}, which for the displacement fields reads:

$$\mathbf{u}_{n+1} = \mathbf{u}_n + \Delta t\dot{\mathbf{u}}_n + \Delta t^2\left[\left(\frac{1}{2} - \beta\right)\ddot{\mathbf{u}}_n + \beta\ddot{\mathbf{u}}_{n+1}\right] \tag{3.71}$$

and velocity

$$\dot{\mathbf{u}}_{n+1} = \dot{\mathbf{u}}_n + \Delta t\left[(1-\gamma)\ddot{\mathbf{u}}_n + \gamma\ddot{\mathbf{u}}_{n+1}\right] \tag{3.72}$$

where β and γ are purely algorithmic parameters which control the numerical dissipation and numerical dispersion of the method [26]. The description of both parameters could be described, among other forms, in terms of the so-called spectral radius ρ_∞:

$$\beta = \frac{1}{(\rho_\infty + 1)^2} \tag{3.73a}$$

$$\gamma = \frac{3 - \rho_\infty}{2(\rho_\infty + 1)} \tag{3.73b}$$

The spectral radius allows relating these parameters with the dissipation needed for high-frequency modes. The spectral radius is defined as $\rho_\infty = [0,1]$ where 0 states a total dissipation and 1 for no dissipation.

As it could be observed from equations (3.71) and (3.72), the algorithm is one step depending solely of the solution history at time $t = t_n$ and three stages since the solution is a function of $\mathbf{u}_n$, $\dot{\mathbf{u}}_n$, and $\ddot{\mathbf{u}}_n$.

Since the variable to solve is the displacement field, an expression for the velocity and acceleration fields are easily deduced. After manipulating equation (3.71) , the expression for the accelerations reads:

$$\ddot{\mathbf{u}}_{n+1} = \frac{1}{\beta \Delta t^2}(\mathbf{u}_{n+1} - \mathbf{u}_n) - \frac{1}{\beta \Delta t}\dot{\mathbf{u}}_n + \left(1 - \frac{1}{2\beta}\right)\ddot{\mathbf{u}}_n \tag{3.74}$$

and the expression for the velocity is defined by substituting equation (3.74) into (3.72).

$$\dot{\mathbf{u}}_{n+1} = \frac{\gamma}{\beta \Delta t}(\mathbf{u}_{n+1} - \mathbf{u}_n) + \left(1 - \frac{\gamma}{\beta}\right)\dot{\mathbf{u}}_n + \Delta t\left(1 - \frac{\gamma}{2\beta}\right)\ddot{\mathbf{u}}_n \tag{3.75}$$

The vector of residual forces, expressed in equation (3.70), for the generalized-α method reads:

$$\left[\mathbf{R}^u_{n+1}\right] = \left[\mathbf{F}^{\text{int}}_{n+1-\alpha_f}\right] - \left[\mathbf{F}^{\text{ext}}_{n+1-\alpha_f}\right] + \left[\mathbf{M}\ddot{\mathbf{u}}_{n+1-\alpha_m}\right] \tag{3.76}$$

where α_f and α_m are parametric values also defined in terms of the spectral radius ρ_∞:

$$\alpha_f = \frac{2\rho_\infty - 1}{\rho_\infty + 1} \tag{3.77a}$$

$$\alpha_m = \frac{\rho_\infty}{\rho_\infty + 1} \tag{3.77b}$$

The computation for the displacement and velocity fields, as well as for the internal and external forces is given in terms of the weighing of their description in the current and reference configuration; for all these expressions with the subindex $(\bullet)_{n+1-\alpha_f}$, is given by

$$(\bullet)_{n+1-\alpha_f} = (1 - \alpha_f)(\bullet)_{n+1} + \alpha_f (\bullet)_n \tag{3.78}$$

Similarly, acceleration vector is described in term of the α_m parameter. Same for those with the subindex $(\bullet)_{n+1-\alpha_m}$ its definition is given by

$$(\bullet)_{n+1-\alpha_m} = (1 - \alpha_m)(\bullet)_{n+1} + \alpha_m (\bullet)_n \tag{3.79}$$

The third term of the RHS of equation (3.76), by substituting the description of $\ddot{\mathbf{u}}_{n+1-\alpha_m}$ given by equation (3.79) and after some manipulation, is rewritten as

$$\mathbf{M}\ddot{\mathbf{u}}_{n+1-\alpha_m} = \frac{1 - \alpha_m}{\beta \Delta t^2}\mathbf{M}\mathbf{u}_{n+1} - \mathbf{M}\mathbf{u}^*(\mathbf{u}_n, \dot{\mathbf{u}}_n, \ddot{\mathbf{u}}_n) \tag{3.80}$$

where:

$$\mathbf{u}^* = \left[\frac{1 - \alpha_m}{\beta \Delta t^2}\mathbf{u}_n + \frac{1 - \alpha_m}{\beta \Delta t}\dot{\mathbf{u}}_n + \frac{1 - 2\beta - \alpha_m}{\beta}\ddot{\mathbf{u}}_n\right] \tag{3.81}$$

Substituting equation (3.80) into (3.76), the vector of residual of forces is given by:

$$\left[\mathbf{R}^{u}_{n+1}\right] = \left[\mathbf{F}^{\text{int}}_{n+1-\alpha_f}\right] - \left[\mathbf{F}^{\text{ext}}_{n+1-\alpha_f}\right] + \\ - \frac{1-\alpha_m}{\beta\Delta t^2}\left[\mathbf{M}\mathbf{u}_{n+1}\right] + \left[\mathbf{M}\mathbf{u}^{*}(\mathbf{u}_n, \dot{\mathbf{u}}_n, \ddot{\mathbf{u}}_n)\right] \tag{3.82}$$

The implementation of the time integration is summarized in Box 3-5

Given: $\{\mathbf{u}_n, \dot{\mathbf{u}}_n, \ddot{\mathbf{u}}_n, \Delta t_{n+1}, \mathbf{u}_{n+1} : \varphi_n(\Omega) \to \mathbb{R}^2, \rho_\infty, \gamma, \beta, \alpha_f, \alpha_m,$
compute $\ddot{\mathbf{u}}_{n+1}$ and $\dot{\mathbf{u}}_{n+1}$

$$\ddot{\mathbf{u}}_{n+1} = \frac{1}{\beta\Delta t^2}(\mathbf{u}_{n+1} - \mathbf{u}_n) - \frac{1}{\beta\Delta t}\dot{\mathbf{u}}_n + \left(1 - \frac{1}{2\beta}\right)\ddot{\mathbf{u}}_n$$

$$\dot{\mathbf{u}}_{n+1} = \frac{\gamma}{\beta\Delta t}(\mathbf{u}_{n+1} - \mathbf{u}_n) + \left(1 - \frac{\gamma}{\beta}\right)\dot{\mathbf{u}}_n + \Delta t\left(1 - \frac{\gamma}{2\beta}\right)\ddot{\mathbf{u}}_n$$

Calculate vector of residual forces

$$\left[\mathbf{R}^{u}_{n+1}\right]^{h}_{I} = \left[\mathbf{F}^{\text{int}}_{n+1-\alpha_f}\right]^{h}_{I} - \left[\mathbf{F}^{\text{ext}}_{n+1-\alpha_f}\right]^{h}_{I} + \\ - \frac{1-\alpha_m}{\beta\Delta t^2}\left[\mathbf{M}\mathbf{u}_{n+1}\right]^{h}_{I} + \left[\mathbf{M}\mathbf{u}^{*}(\mathbf{u}_n, \dot{\mathbf{u}}_n, \ddot{\mathbf{u}}_n)\right]^{h}_{I}$$

where:

$$(\bullet)_{n+1-\alpha_f} = (1-\alpha_f)(\bullet)_{n+1} + \alpha_f(\bullet)_n$$

$$(\bullet)_{n+1-\alpha_m} = (1-\alpha_m)(\bullet)_{n+1} + \alpha_m(\bullet)_n$$

$$\mathbf{u}^{*} = \left[\frac{1-\alpha_m}{\beta\Delta t^2}\mathbf{u}_n + \frac{1-\alpha_m}{\beta\Delta t}\dot{\mathbf{u}}_n + \frac{1-2\beta-\alpha_m}{\beta}\ddot{\mathbf{u}}_n\right]$$

Box 3-5. Dynamic integration scheme – generalized-α method

3.4. Contact method proposal

The rheological behaviour of granular flows is a function not only of the direct interaction of the granular particles themselves but also has complete dependency on the boundary conditions. In order to fulfil this requirement, it is necessary to define a proper solid-granular material interaction.

The contact method proposed in this work emerges in a natural manner from the *PFEM*. The contact method has been proved robust for performing large deformation problems.

3.4.1. Background of the contact method

Several techniques have been proposed to solve coupled problems representing accurately the interaction of the multi-body system; among them, there is found the *penalty method*, the *Lagrange multiplier method*, and the *augmented Lagrange method*. Despite their precise response to determine the resulting contact forces, the implementation of these methods for large deformation problems is limited since they are not robust enough – an example of complex geometries and geometric non-linearities are given in the tumbling mill problem, where the interaction with the lifters and the large deformation of the granular domain require a more robust treatment.

Due to the reconnecting algorithm of the *PFEM*, the method has shown suitable to simulate the multi-body interaction. This interaction is defined through a geometrical discretization via the α-shape method between the contact bodies. This technique shows robustness for large deformation problems as shown in ([46],[80]) but in some cases due the boundary definition given by the α-shape method it presents lack of accuracy as well as some instabilities in the pressure field.

A contact method with high performance in large deformation problems is given by the *contact domain method* reported by [77]. It is based in the definition of an interface domain between the potential contact bodies and it have been used in a variety of large deformation problems ([39],[102],[55]). The method present advantages due the generation of the contact interface, of the same dimension as the contact bodies, that allows the formulation in dimensionless, strain-like measures, both for normal and tangential gaps. Despite the robustness in many non-linear problems, in the modelling of granular-solid interaction shows a reduced convergence when the strength of the materials differs some order of magnitudes as well as the discretization that defines the contact bodies present a small number of elements.

The contact herein proposed is based in the *contact domain method* in terms of the definition of the interface domain. In general, contact methods define the contact constraints in terms of a subdomain one dimension lower than the contact bodies, see Figure 3-7(a). In contrast, contact domain methods construct an interface domain of the same dimension as the potential contact bodies, Figure 3-7(b).

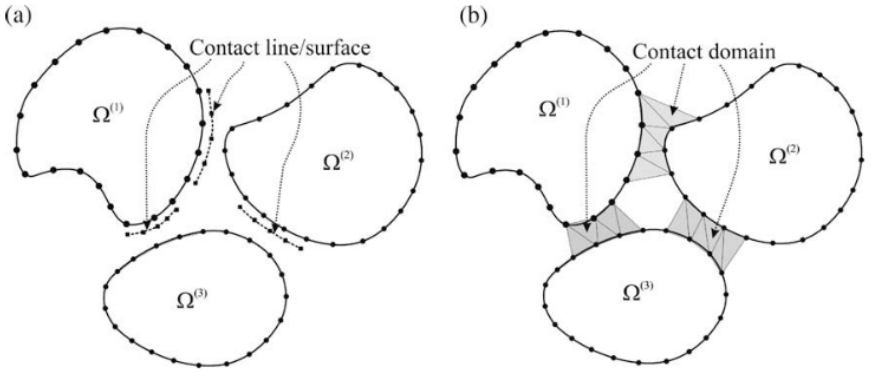

Figure 3-7. Imposition of contact constraints: (a) Classical methods, and (b) Contact domain methods [77].

The difference of our proposal with the so-called *CDM* lies on the definition of the interface. Regarding the latter, the interface is considered as fictitious and it is solved in terms of *Lagrange multiplier*; in our proposal, the interface has size h and the contact conditions, normal and friction forces, are supplied via a constitutive model similar than the given for the granular material.

3.4.2. *Algorithm description*

The construction of the contact interface Ω_{cd} is given in terms of a constrained Delaunay triangulation between the potential contact boundaries of the bodies. In order to avoid the definition of the *active elements* in terms of the α-shape method, as in the classic *PFEM* algorithm, it is determined if an element is active if it fulfils the geometrical impenetrability and normal contact traction conditions. In Figure 3-8(a), a sketch of the active elements of the contact domain is given.

As mentioned in previous section, the definition of this interface domain differs from the *CDM* to ours. For the first case, it is defined as a fictitious interface of gap $g_N = 0$ while in the present method it is given a tolerance, reading as $g_N = h^{(p)}$, where $h^{(p)}$ is the height of the element from the base to point p, see Figure 3-8(b).

The modelling of the contact forces, contact and friction, is established via the constitutive model for the interface domain. Taking into account the frictional and incompressible response of the constitutive model for the granular material given in equation (3.23), for our method it is proposed providing the same constitutive model for the whole contact interface.

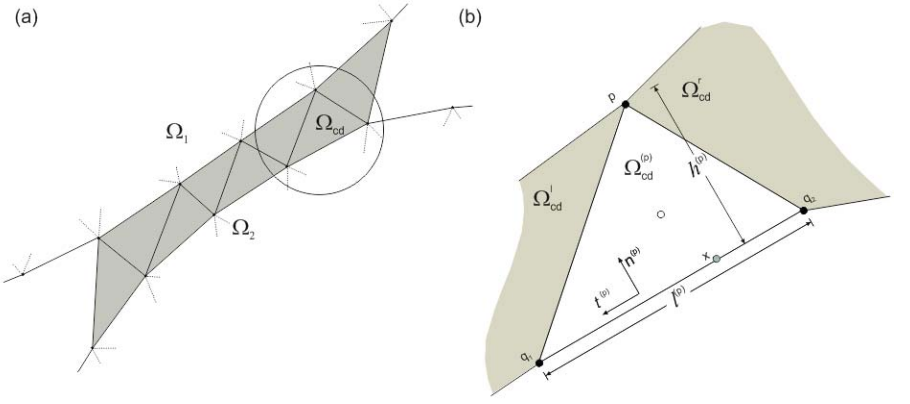

Figure 3-8. Contact interface domain: (a) Active elements between contact bodies; (b) Linear triangle contact patch.

With the gap definition for the interface and the constitutive model to satisfy the contact forces, the stick-slip conditions are established in the form of the classical Karush-Kuhn-Tucker conditions. First, the geometrical impenetrability condition is stated using the gap definition, reading as:

$$\mathrm{g}_N(\mathbf{x}) = h^{(p)} \geq 0 \qquad \forall \mathbf{x} \in \Omega_{cd}^{(p)} \tag{3.83}$$

The second condition refers to the normal contact traction $\mathbf{t}_N$, where the only admissible state is for compression:

$$\mathbf{t}_N(\mathbf{x}) = \boldsymbol{\tau}_n \cdot \mathbf{n}(\mathbf{x}) \leq 0 \qquad \forall \mathbf{x} \in \Omega_{cd}^{(p)} \tag{3.84}$$

Finally, the definition for an active element is summarized using the classical form of the Karush-Kuhn-Tucker conditions, using equations (3.83) and (3.84).

$$\lambda_N \leq 0, \qquad \mathrm{g}_N \geq 0, \qquad \lambda_N \mathrm{g}_N = 0 \quad \text{in } D_n^l \tag{3.85}$$

3.4.3. Calibration of the Drucker-Prager internal friction angle and Coulomb friction parameter

The following example is proposed as a simple path to characterize the Coulomb friction parameter of a system in terms of the internal friction angle b_1 of the yield surface defined in equation (2.14). The example consists in the slide of a rigid body of mass m through an inclined plane of angle θ as shown in Figure 3-9.

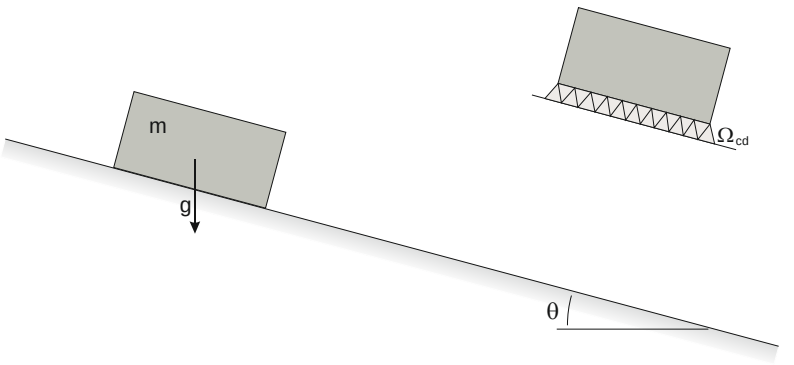

Figure 3-9. Slide of a rigid body in an inclined plane. Validation example for characterization of the wall friction angle in terms of the Coulomb friction parameter.

The slide of the rigid body could be described by an analytical equation which deduction is obtained by defining the free body equations

$$mg\sin(\theta) - f = ma \tag{3.86}$$

and

$$mg\cos(\theta) = N \tag{3.87}$$

where f is the friction force, g the gravity, a the system acceleration, and N the normal force. The static condition of the system is given whenever

$$f \leq \mu N = \mu mg\cos(\theta) \qquad \text{or} \qquad \mu \geq \tan(\theta) \tag{3.88}$$

For the sliding condition, $\mu < \tan(\theta)$, it could be deduced, by manipulating equation (3.86), the definition of the acceleration of the system in terms of the Coulomb friction parameter and the slope of the plane.

$$a = g\cos[\tan(\theta) - \mu] \tag{3.89}$$

The integration along time of equation (3.89) allows to define the position of the body in certain period of time in terms of the Coulomb friction parameter and the inclination angle, given by

$$x(t) = x_o + v_o t + g\cos\theta(\tan\theta - \mu)\frac{t^2}{2} \tag{3.90}$$

where x_o the original position, and v_o the original velocity. In order to characterize the value of the wall friction in terms of the internal friction angle, a set of different internal angles for the material were conducted. The comparison of the response of the displacement of the model and the one deduced analytically by equation (3.90), permits to calibrate both frictional parameters.

The validation of equation (3.90) as a calibration method of the wall friction angle is given comparing the analytical solution using a frictionless plane, $\mu = 0$, with

The validation of equation (3.90) as a calibration method of the wall friction angle is given comparing the analytical solution using a frictionless plane, $\mu = 0$, with the numerical results using the corresponding internal friction angle $b_1 = 0$. The comparison is also extended to a numerical model of the slide of the rigid body without a contact definition, only restraining the displacements of the body in the direction normal to the plane. Figure 3-10 shows the comparison of the analytical solution with respect both numerical responses.

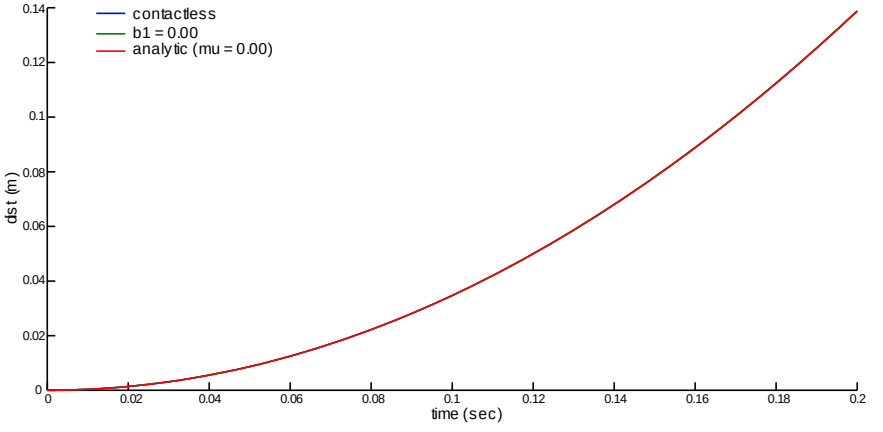

Figure 3-10. Validation of analytic solution for a frictionless surface.

The displacement response given by the three curves is identical for each of them, which validates the usage of the analytic equation for the calibration. The internal friction angle of the material was varied in a range $b_1 = [0,1.00]$ in order to observe the behaviour of the sliding of the rigid body and thereafter compared to the analytic response. Figure 3-11 shows the variation in the displacement reached depending of the internal friction angle used in the contact domain.

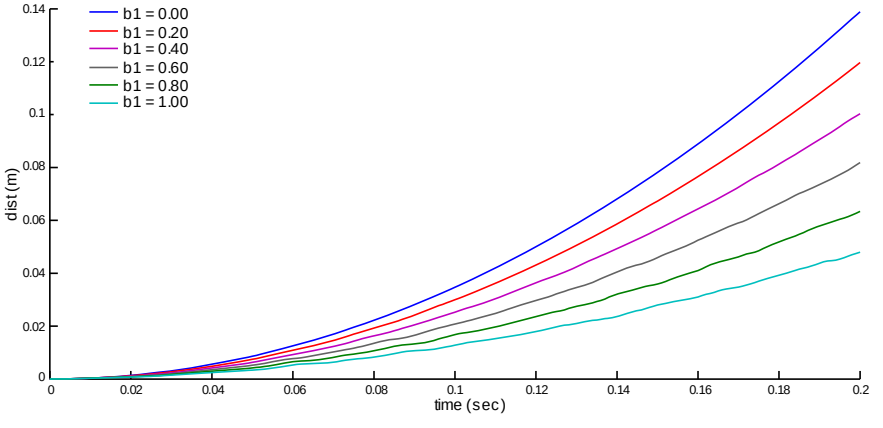

Figure 3-11. Displacement varying wall friction angle.

Varying the Coulomb friction parameter, the analytic displacement is compared, defining a corresponding value of the parameter for each internal friction angle in the numerical model. Figure 3-12 displays the comparison between the numerical response of the internal friction angle and its corresponding analytical description varying this coefficient.

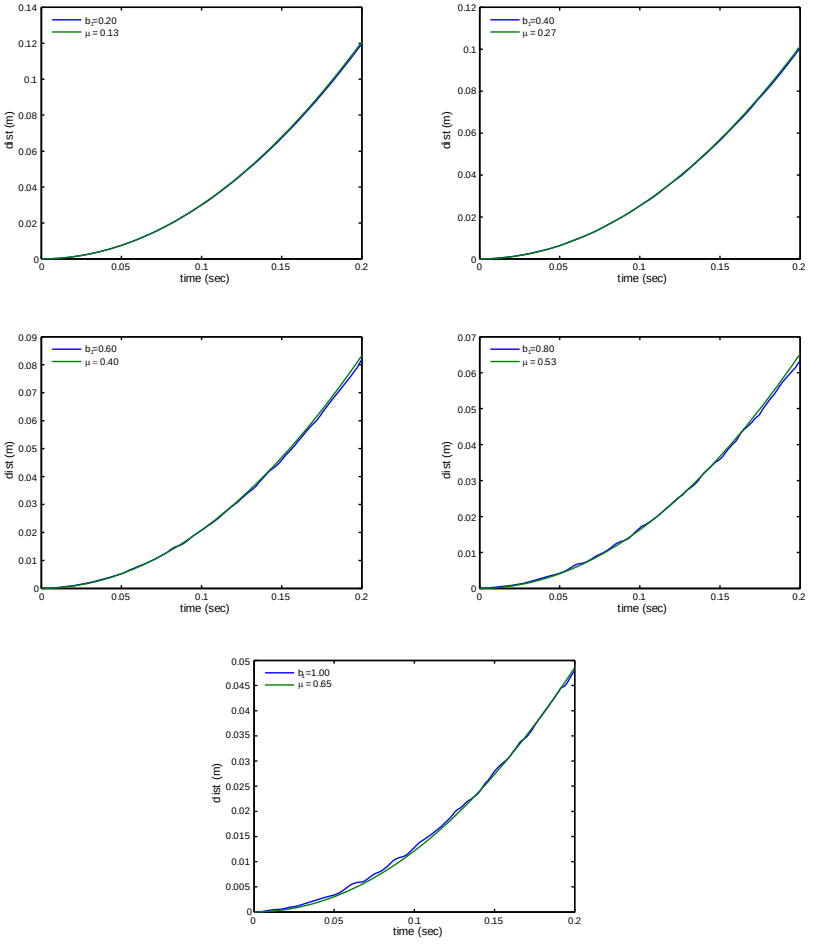

Figure 3-12. Analytical comparison of displacement

Relating the internal friction angle of the Drucker-Prager yield model of the contact elements and its corresponding value of the Coulomb friction coefficient obtained analytically it could be observed a linear response between them as observed in Figure 3-13.

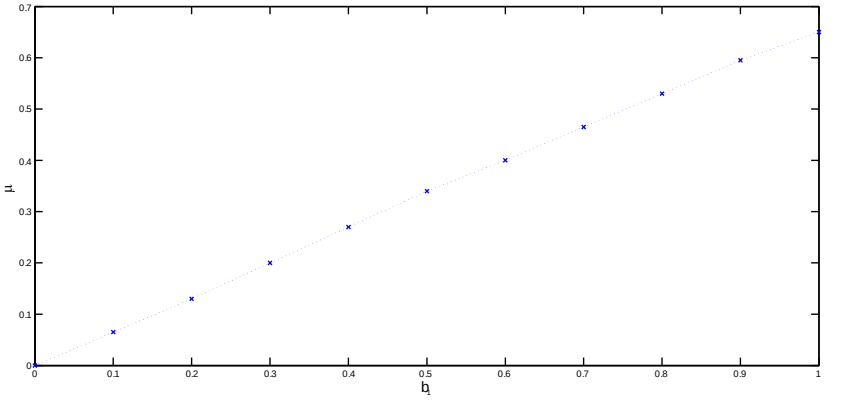

Figure 3-13. Coulomb friction coefficient and internal friction angle comparison

The example allows defining, in a proper manner, the wall friction angle between the material and its container.

Chapter 4
Numerical simulation of the spreading of a granular media on a horizontal plane

This chapter addresses the validation of the constitutive model proposed for the simulation of dense granular flows. Any numerical simulation has to be validated through a proper comparison with analytical or experimental models. Dense granular flows, as explained in previous chapters, present a complex behaviour that an analytical description is not suitable to capture – effects of bistability, thixotropy, jamming, among others; for this reason the natural manner of the validation is via experimental modelling. The complexity of choosing reliable experimental models for granular materials is given by two main features: the reproducibility of the experiment and the kinematic phenomenon to represent – in this case dense granular flows.

The first concept, reproducibility, is an inherent limitation of granular materials; their mechanical response is constrained by the material properties such as the degree of voids, the particle shape and size, and homogeneity of the material that could vary for a same granular media. This feature forces us to use experimental tests conducted for a large number of samples, where the reported average data defines properly the material response. The second condition refers to the kinematic response that is modelled on the experimental tests; it is essential to identify those experimental models suitable to represent granular flows where there are recognizable stagnant and flow regions as well as their jamming transition.

The model is validated through a comparison with the experimental results of the spreading of a granular mass on a horizontal plane reported in Ref. [62]; the experimental tests capture the kinematics of the media on different stages: the mate-

rial at repose on its container, the spreading of it when it is released, and its deceleration until its stagnation.

In the next sections, a brief description of the experimental tests used for the validation is presented, followed by the corresponding numerical simulations. First, a test for calibrating material and numerical properties is selected; then the predictive ability of the model is validated in both stationary and transient scenarios. The numerical simulations herein presented follow the next assumption:

- The numerical simulations are simplified in a two-dimensional axisymmetric model. This assumption is given straightforward from the experimental tests since the authors described a full axisymmetric response on the material spreading [62]. The axisymmetric description for a mixed formulation is given in Appendix D.

4.1. Scope and setup of the experimental tests

The experiments carried out by Lajeunesse, *et al*. [62] – which are the ones employed in the present work for validation purposes – have the aim of characterizing the slumping and spreading of the granular material from an initial configuration of confinement, being the gravitational forces the only perturbation exerted on the material. One of their objectives was to determine the influence of the material and several parameters like the mass M, the initial aspect ratio a of the granular volume, the substrate roughness, and the bead size on the spreading of a granular mass as well as in its final disposition.

The experimental setup consists of a cylinder of inner radius R_i resting on a horizontal plane wide enough to contain the spread of the granular material. The tube was filled with a mass M of glass beads of uniform size and shape ($d = 350 \pm 50 \mu m$) and an averaged density $\rho = 2500\, kg/m^3$. The filling procedure was standardized in order to ensure reproducible initial conditions; they poured the glass beads onto a sieve defining a homogeneous downfall of the material. The height of the column h_i is defined according to the amount of material, which in turn, defines its initial aspect ratio $a = H_i / R_i$. The scheme of the experimental setup is shown in Figure 4-1.

The experimental procedure consists in releasing the cylinder pile by the quick removal of the container via a pulley system[6]. Once the material is released, it spreads on the horizontal surface due to gravitational forces until it comes to rest forming a final deposit. Lajeunesse, *et al*. [62] define the time necessary to set the

[6] In a following paper, Lajeunesse, *et al*. [63] E. Lajeunesse, J. B. Monnier, and G. M. Homsy, "Granular slumping on a horizontal surface," *Physics of Fluids*, vol. 17, pp. -, 2005. detail the used methodology of the cylinder removal. They placed constant weights on the lifting system in order to maintain reproducibility on the experimental tests.

granular mass in motion as $T_m = \sqrt{2H_i/g}$. The time of removal for the cylinder T_r has to be fast enough in order to reduce its influence on the flow pattern of the material; in order to achieve a proper procedure where the removal of the cylinder does not influence on the spreading T_r has to be small compared to T_m.

The slumping and spreading of the granular pile was captured using a digital camera acquiring 500 images per second. The camera was connected to a computer to capture and digitalize images at short intervals of time being capable to define the shapes of the bulk as it spreads. Lajeunesse, *et al*. [62] reported that, as the granular mass spreads axisymmetric, the profiles reached by the material provide enough information to fully characterize its three-dimensional shape.

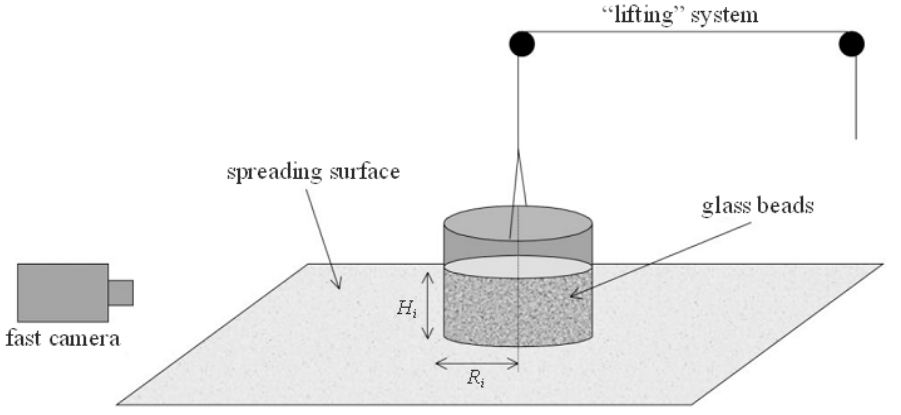

Figure 4-1. Scheme of the experimental setup [62].

The experimental tests comprised several geometries and initial aspect ratios to characterize the mechanisms of spreading for the granular material. A first set of examples were conducted to verify the axisymmetric spreading of the material; it was confirmed by placing the camera vertically above the cylinder and the measuring of the radial spreading.

Lajeunesse, *et al*. [62] concluded that the most relevant parameter that characterizes the spreading and final deposit of the material is the initial aspect ratio a. They identified that, depending on the initial aspect ratio, the spreading of the granular material has two distinct dynamical regimes leading to three different deposit morphologies. The first regime is observed for smaller initial aspect ratios, with a limit $a \leq 3$; the spreading is characterized by a flow front that develops at the foot of the pile, and that propagates radially outward, see Figure 4-2(a) and Figure 4-2(b). The image sequences show how the sides of the initial column of granular material crumble through an avalanche.

The final configuration varies depending on the initial aspect ratio; for small values, the material does not spread completely, leaving a central undisturbed region and creating a *truncated cone* deposit, Figure 4-2(a). For values close to $a = 0.74$

the spreading of the material reaches the centre of the bulk, defining a *cone* shape of the deposit, Figure 4-2(b).

The second dynamical regime is shown in Figure 4-2(c). It can be appreciated that the spreading of the material develops a flow front at the bottom of the cylinder pile in a small region, shown in the first three snapshots; by contrast, the upper part of the column keeps its shape while descending – considered as a free falling rigid body. At the end of the process, the shape of the deposit resembles, in words of Lajeunesse, *et al*. [62], a Mexican hat.

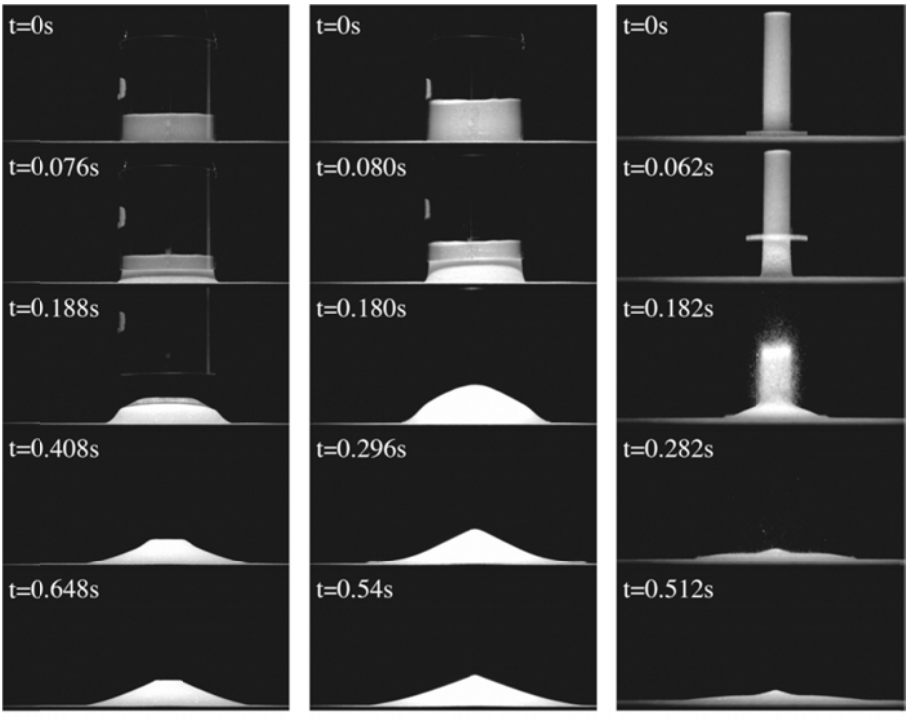

Figure 4-2. Three sequences of images corresponding to different initial aspect ratios: (a) regime 1, $a = 0.56$; (b) regime 1, $a = 0.8$; and (c) regime 2, $a = 5.4$ [7] [62].

Lajeunesse, *et al*. [62] contrasted different geometries while keeping the same initial aspect ratio and concluded that the kinematic behaviour and final profile are independent of the mass of the material, being only a function of the initial aspect

[7] The initial aspect ratio given by the authors for Figure 4-2(c), $a = 5.4$, does not correspond to the initial aspect ratio of the sequences shown in the figure, $a = 8.94$. The reported series of successive profiles correspond to the lower value ($a = 5.4$), which are used for the model validation given in section 4.4. The sequence of images of Figure 4-2(c) is used to validate the transient response of the model, using the higher value of the initial aspect ratio ($a = 8.94$).

ratio. Figure 4-3 shows the comparison of different geometries for three different initial aspect ratios – one for each of the deposit morphologies.

The normalized deposit profiles, shown in Figure 4-3, are used for the validation of the numerical model in the following sections. These results clearly corroborate the influence of the initial aspect ratio in the final profile, being independent of the mass. Figure 4-3(a) stands for the normalized comparison of the final profiles for cylinder piles with the smallest initial aspect ratio $a = 0.41$. It shows the truncated cone for the deposit profile, defining a flow front by the lateral sides.

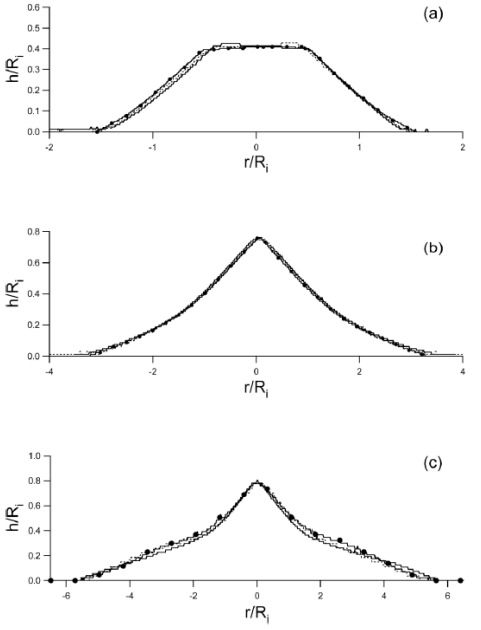

Figure 4-3. Deposit profiles normalized to the tube radius for three different initial aspect ratios, varying geometries: (a) $a = 0.41$. Plain line: $M = 135$ g, $R_i = 40$ mm. Dotted line: $M = 50$ g, $R_i = 28$ mm. Plain line with circles: $M = 50$ g, $R_i = 28$ mm. (b) $a = 1.95$. Plain line: $M = 600$ g, $R_i = 40$ mm. Dotted line: $M = 200$ g, $R_i = 28$ mm. Plain line with circles: $M = 50$ g, $R_i = 40$ mm. (c) $a = 6.20$. Plain line: $M = 675$ g, $R_i = 28$ mm. Dotted line: $M = 75$ g, $R_i = 13$ mm. Plain line with circles: $M = 80$ g, $R_i = 13$ mm [62].

The second set of geometries, corresponding to an initial aspect ratio $a = 1.95$, shows the same normalized deposit profiles for different amounts of mass, see Figure 4-3(b). It is observed the correspondence with the second profile morphology, which describes a cone. The last pattern is shown in Figure 4-3(c), and corresponds to the second dynamical regime of spreading. The difference of both dynamical regimes, shown in first two figures and the third one respectively, is observed by contrasting their deposit profiles: for the first case, the deposits show smooth slopes while for the last regime, the centre of the bulk shows a cone, identified to be from

the upper region of the cylinder, while the material at the bottom shows a different slope on its profile.

4.2. Modelling of material settlement

In order to dissipate initial oscillations due to the gravitational loads, all the simulations shown follow the assumption of allowing the material, within the container, to settle down. Once the material reaches a state of negligible kinetic energy, the corresponding kinematic conditions are applied (in this case, the removal of the container).

The geometry given in Figure 4-2(a) is taken as reference example for the calibration of material and numerical parameters. It consists of the axisymmetric modelling of a cylinder pile of radius $R_i = 70.5$ mm and a height $H_i = 39.48$ mm with a corresponding initial aspect ratio of $a = 0.56$. This particular choice of the initial aspect ratio aims at reducing the effects of abrupt changes in potential energy on the numerical response. This numerical response is expected to follow the first dynamical regime for the material spreading and to define the observed profile morphology of a truncated cone.

Figure 4-4(a) shows the evolution, during material settlement, of the computed volumetric pressures measured at the bottom centre of the material – in the axisymmetric model at the bottom of this axis. The graph displays a barely perceptible dissipation on the oscillations along time, a fact that is contrary to expectations, since the coefficient of elastic restitution in granular materials is practically null [48]. As may be inferred, these physically unrealistic pressure oscillations are due to oscillations in the normal stress in the vertical direction, see Figure 4-4(b).

The above observations clearly indicate that the model proposed in previous chapter has to be equipped with some additional means to dissipate the spurious oscillations. To this end, a visco-elastic regularization based on a Kelvin-Voigt model is proposed.

This type of visco-elastic models is based on a rheological representation of a purely viscous damper and an elastic spring. In this case the additional term will be described as a function of the rate of deformation tensor. Since the numerical model is based on a mixed formulation, the pressure variable defined by equation (2.34) is rewritten using the new term corresponding to the viscoelastic regularization – expressed in the current configuration.

$$\pi_{n+1} = \kappa \frac{\ln J_{n+1}}{J_{n+1}} + \eta \operatorname{tr} \mathbf{d}_{n+1} \tag{4.1}$$

where η is a coefficient that defines the degree of dissipation required to characterize the coefficient of elastic restitution of the material.

Details on the deduction and numerical implementation of this visco-elastic regularization are given in Appendix E.

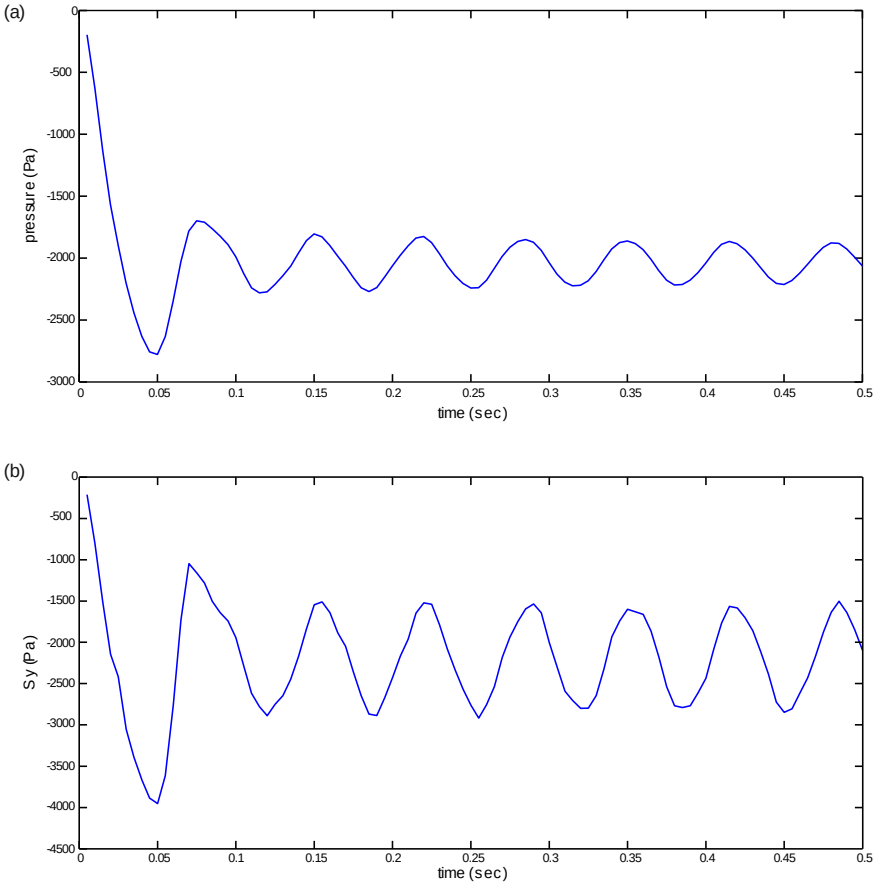

Figure 4-4. Dynamic oscillations presented in (a) pressure, and (b) vertical stresses after settlement of the material at the bottom centre of the cylinder pile.

Figure 4-5(a) shows the comparison of the volumetric pressures at the bottom centre of the material for different values of the dissipation coefficient η (expressed as the product of a dimensionless constant and the bulk modulus). Comparing the corresponding values of a null value of the coefficient (green line) and $\eta = 10^{-4}\kappa$ (blue line), it could be defined the last as a numerical zero, nullifying any dissipation. It can be readily appreciated how the amplitude of the oscillations diminishes when increasing values of the dissipative coefficient. For $\eta = 10^{-2}\kappa$ (black line), the oscillations are completely eliminated.

In Figure 4-5(b), the influence of the dissipative coefficient on the evolution of the vertical stress component (σ_y) is examined. As expected, the introduced regularization proves effective in mitigating also oscillations in this variable. It is worth noting that, in contrast to the situation observed in the pressure variable, the magnitude of the mean value of σ_y remains approximately constant for all values of η.

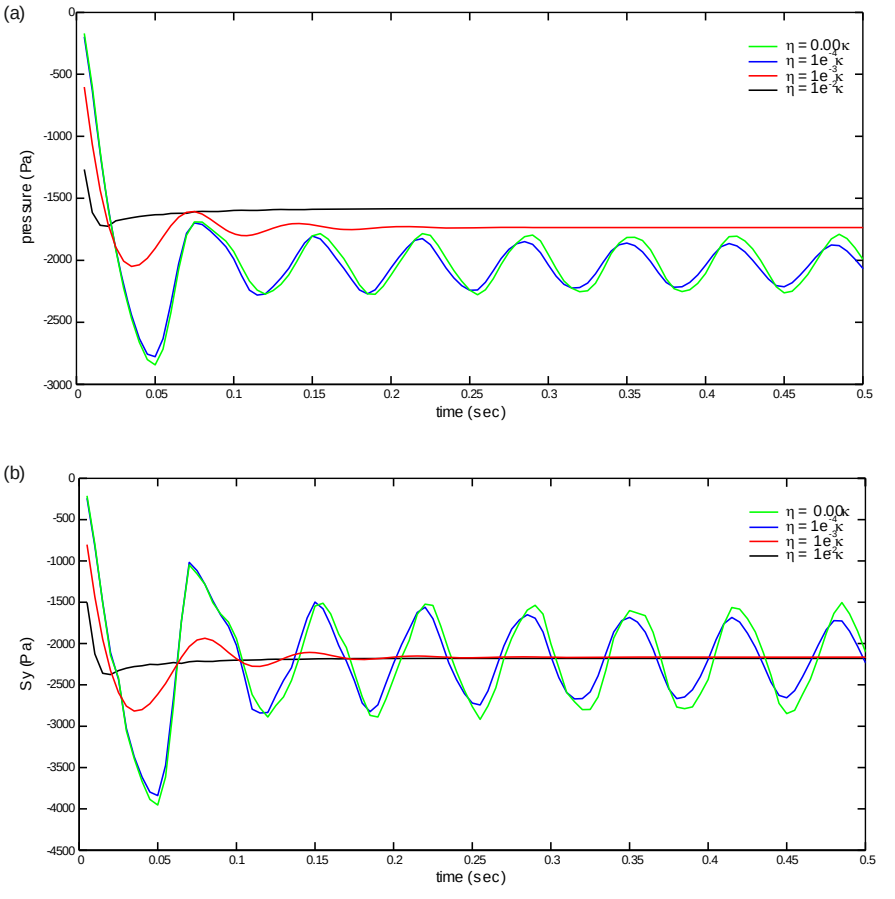

Figure 4-5. Variation on the dynamic oscillations presented in (a) pressure and (b) vertical stresses, after settlement of the material at the bottom centre of the cylinder pile using the viscoelastic regularization.

4.3. Model calibration – deposit profile

As mentioned in the previous section, the calibration of the parameters of the model is carried out using the experimental test corresponding to the configuration shown in Figure 4-2(a). This test corresponds to an axisymmetric model of a cylinder with initial aspect ratio of $a = 0.56$; a sketch of the initial geometry is displayed in Figure 4-6.

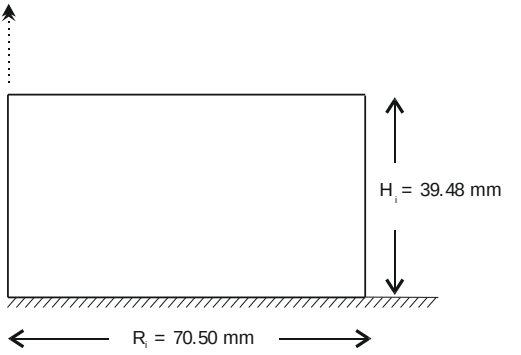

Figure 4-6. Axisymmetric model for reference example with initial aspect ratio $a = 0.56$.

The constitutive model herein proposed for dense granular flows is characterized by four parameters, namely: the internal friction angle, the cohesion, and the visco-plastic and visco-elastic parameters. The cohesion coefficient is set to a very small positive constant, $b_2 = 10^{-2}$ Pa , to reflect the fact that the grains employed in the experiments are assumed cohesionless. Regarding to the visco-plastic coefficient τ_R , preliminary numerical tests show that transient behaviour is accurately replicated with a vanishing negligible coefficient (that is, the visco-plastic regularization in this test does not play a significant role). As for the visco-elastic part, the dissipation constant is set to $\eta = 10^{-2}\kappa$ (the value obtained in the previous section to eliminate oscillations in the volumetric pressures).

In all the examples, calibration and validation models, calculations have been run with a time-step length $\Delta t = 1 \times 10^{-4}$ sec ; the number of elements for each model are a function of the geometry of the model, remaining constant the element size $h^e = 1.5mm$. The modelling of the granular material / surface interaction was in terms of defining the same value for the internal friction angle and the wall friction angle; for the interaction with the cylinder's wall it was defined frictionless in Ref. [62].

The calibration of the remaining parameter, the internal friction parameter b_1 , is carried out by comparing the final deposit profile, obtained for varying values of this parameter, with the corresponding experimental result. Figure 4-7 shows this comparison in terms of the normalized deposit profile for values of b_1 ranging from 0.4 to 1.20.

Observe that the material tends to fluidize for lower values of b_1. For $b_1 = 0.40$, the "truncated cone" shape observed experimentally is not present; one has to increase the internal friction parameter over 0.65 to reproduce this typical shape. For the maximum value used, $b_1 = 1.20$, the deposit profile shows, as expected, the wider region of material undisturbed; presenting material crumbling approximately at half the radius of the cylinder.

Maximum resemblance between numerical and experimental profiles is achieved at $b_1 = 0.75$ (the equivalent internal friction angle in a Mohr-Coulomb model is $\phi = 23.474^o$, a value that lies between the values reported by Lajeunesse, *et al.* [62] for the repose angle and the avalanche angle, $\theta_r \approx 21^o$ and $\theta_a \approx 29^o$ respectively).

It should be remarked that the match is almost perfect except at the outer portion of the deposit. This deviation may be explained by the fact that, at this region, the grains are too loose to be collectively represented as a continuum medium.

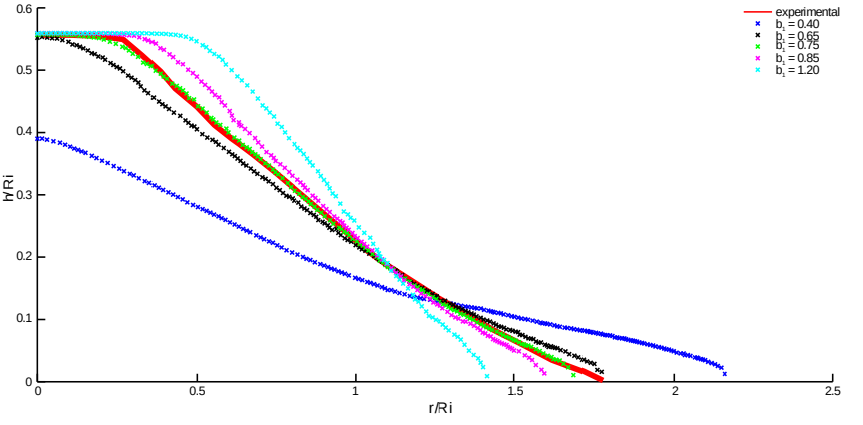

Figure 4-7. Final (normalized) deposit profile for varying values of the internal friction parameter. Comparison with the experimental result reported by Lajeunesse, *et al.* [62].

A striking conclusion of the experimental study conducted by Lajeunesse, *et al.* [62] is that the shape of the final deposit is practically independent of the rigid/erodible nature of the rough ground; according to Lajeunesse, *et al*, the final shape should only depend on the initial aspect ratio (at least for the range of values studied in their work).

To check whether the numerical model is consistent with this observation, in Figure 4-8, the final profiles predicted by the model for varying values of the wall friction parameter at the interface domain are compared.

It is readily seen that, indeed, the model does capture the experimental behaviour in this respect, since variations of the wall friction parameter does not induce significant changes of the final shape of the deposit – only a slight deviation is detected at $b_1^{wall} = 0.2$.

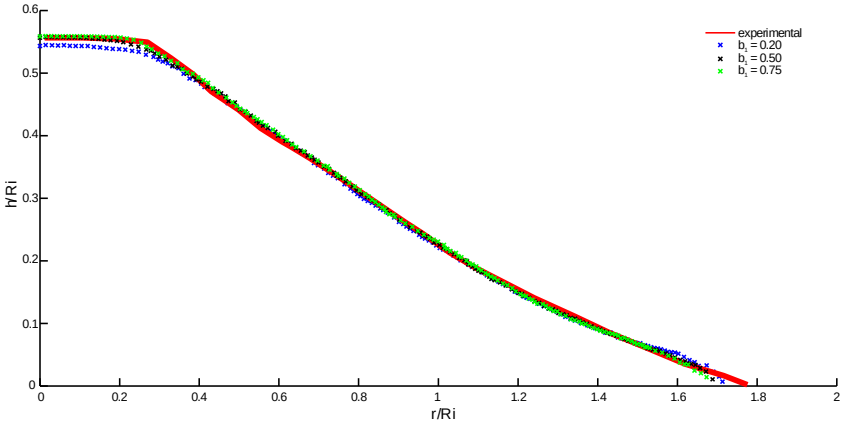

Figure 4-8. Deposit profiles obtained varying the wall friction angle of the contact interface.

4.4. Model validation – deposit profiles

The validation of the numerical model is carried out using two sets of examples. The first set corresponds to the remaining two geometries, shown in Figure 4-2(b) and Figure 4-2(c). The second set has the aim of further corroborating the conclusion made in Ref. [62] regarding their statement, that indicates that the deposit profile is only a function of the initial aspect ratio of the granular pile, being negligible the influence of the mass pile on the morphology – it will compared with the normalized deposit profiles shown in Figure 4-3.

The geometries of the axisymmetric models of the remaining examples are shown in Figure 4-9. The first initial aspect ratio $a = 0.80$ corresponds to the first dynamic regime – a flow front that develops at the bottom of the pile and crumbles through an avalanche, presenting a *cone shape* type final deposit morphology. The second initial aspect ratio $a = 5.40$ belongs to the second dynamical regime; its final deposit profile corresponds to the *Mexican hat* shape type.

The validation process consists in comparing the remaining configurations using the same internal friction material obtained earlier by the calibration example $b_1 = 0.75$ – it is emphasized that all material and numerical parameters are kept the same as well as the model conditions.

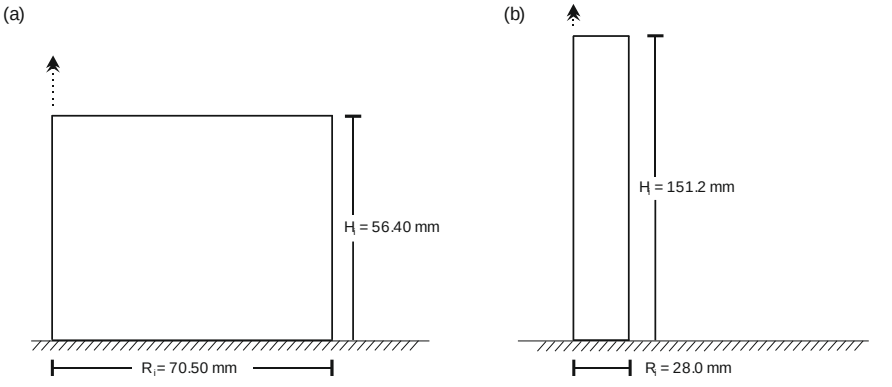

Figure 4-9. Axisymmetric models used for model validation: (a) Regime 1, $a = 0.80$; (b) Regime 2, $a = 5.40$.

In Figure 4-10, the experimental and numerical final profiles corresponding to the first initial aspect ratio $a = 0.80$ are depicted. To better appreciate the evolution of the pile, the initial configuration is also displayed. Observe that, except at the outer part – in which as previously pointed out, the grains becomes too loose as to be modelled as a continuum medium – the deposit profile predicted by the numerical model runs above, and approximately parallel, to the one observed experimentally. On average, discrepancies in height are less than 10%.

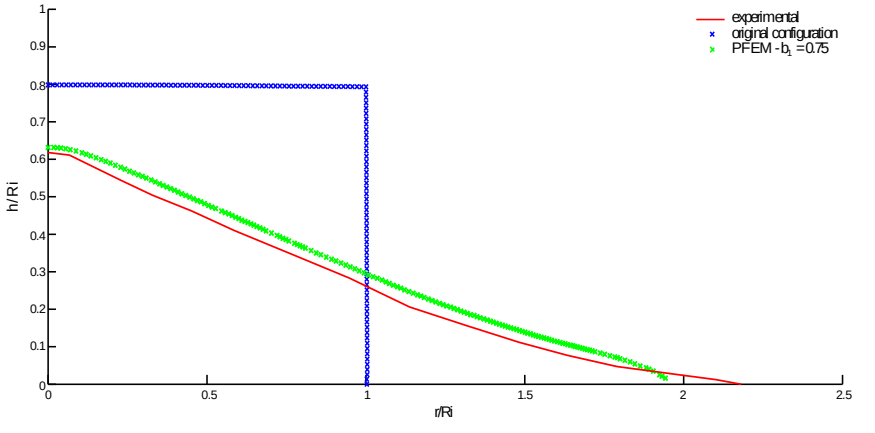

Figure 4-10. Validation of the numerical model for a cylinder pile with an initial aspect ratio $a = 0.80$.

Figure 4-11 contains the profiles corresponding to the initial aspect ratio $a = 5.40$. Remarkably, in this case, the deposit profiles of the experimental and numerical models exhibit an excellent agreement, even at the concave slopes of the free surfaces that defines the *Mexican hat* shape; the only deviations are observed, as in the previous cases, at the outer region.

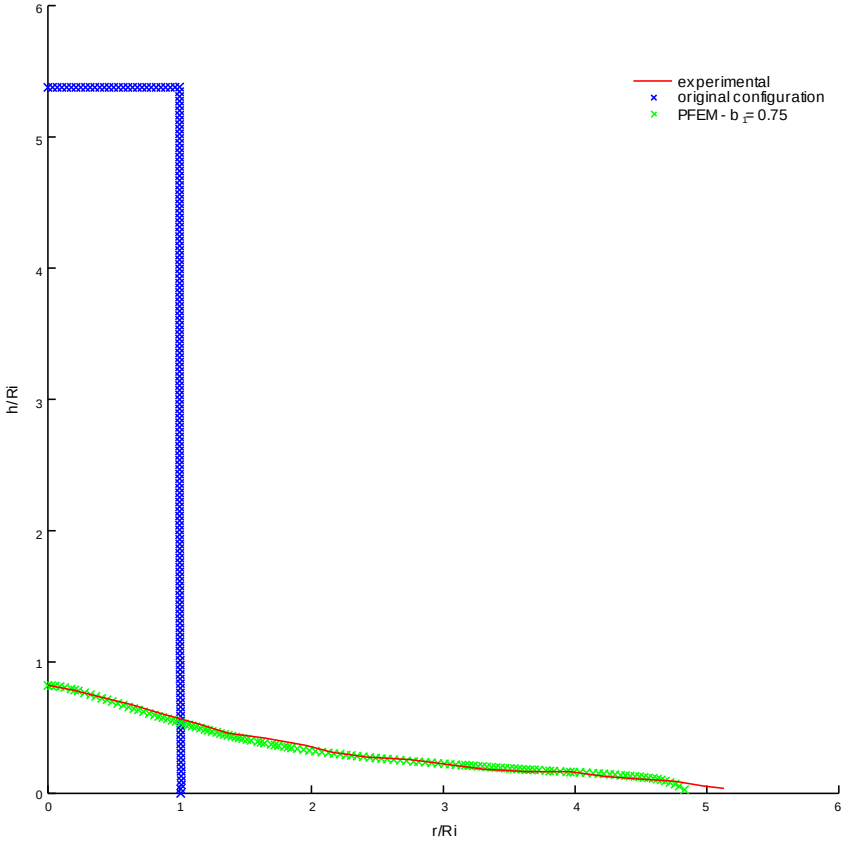

Figure 4-11. Validation of the numerical model for a cylinder pile with an initial aspect ratio $a = 5.40$.

Even though the scope in this section is not the study of the transient response of the granular spreading, for completeness, in Figure 4-12, the evolution during the spreading process, of the experimentally recorded profiles (left column) along with the predictions furnished by the numerical model (right column) is compared.

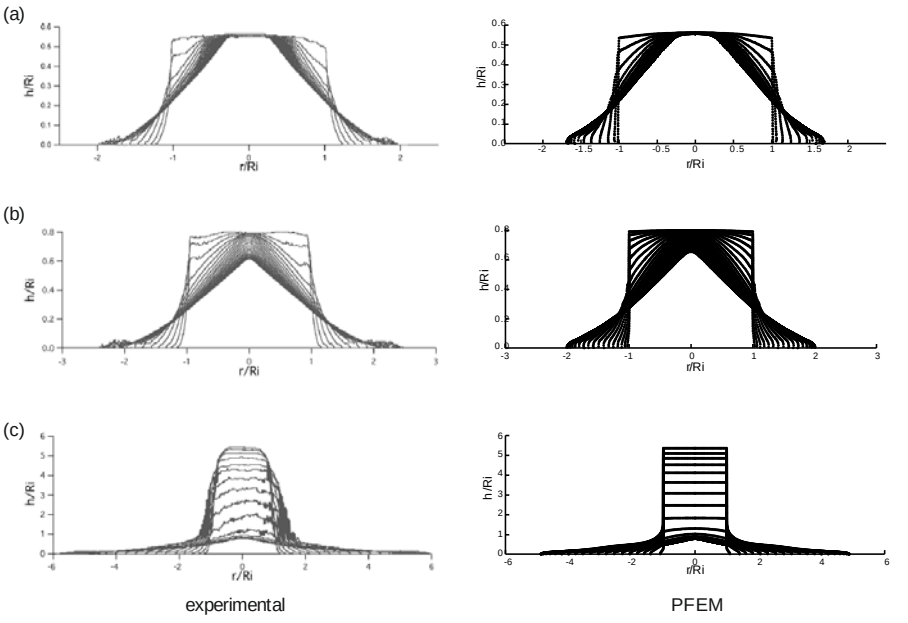

Figure 4-12. Comparison of the evolution of experimental [62] and numerical profiles corresponding to (a) initial aspect ratio $a = 0.56$; (b) initial aspect ratio $a = 0.8$; and (c) initial aspect ratio $a = 5.4$.

Figure 4-12(a) and (b) correspond to initial aspect ratios of $a = 0.56$ and $a = 0.8$, respectively (first dynamical regime of spreading). Computed profiles in these two cases bear close similarity to those monitored experimentally. In the third case (the one corresponding to the slender column, see Figure 4-12(c)), the similarity is not so marked: in the computed results, the upper portion of the column maintains its initial shape during most of the process, while in the profiles reported in Ref. [62], the column seems to widen as its top surface descends. A glance at the sequence of images shown previously in Figure 4-2(c) may aid in disclosing the actual origin of these discrepancies. Indeed, observe that, upon removal of the container ($t = 0.182$ sec), the outer layer of particles *detach* from the bulk mass due to some friction presented during the removal of the cylinder. Such detachment is an inherently discontinuous phenomenon, and therefore, not amenable to continuum modelling; hence the discrepancies between observed and computed results. Nevertheless, it should be noted that the influence of these discrepancies on the predictions of the final profile is practically negligible (since it is considered the discrepancy on the outer layer of particles), for both computed and experimental graphs are practically coincident, as previously seen in Figure 4-11.

In Ref. [62], Lajeunesse, *et al*. report that, independently of the mass, a set of cylinders with the same initial aspect ratios but different dimensions will exhibit similar normalized deposit profiles. To check whether this behaviour is also cap-

tured by the numerical model, we launch several analyses with varying initial dimensions. Table 4-1 shows the employed initial aspect ratios described in Ref. [62], one corresponding for each of the deposit morphologies, and the dimension of its radius.

Tag	a	$R_i\,(mm)$
A1	0.41	40
A2	0.41	28
B1	1.95	40
B2	1.95	28
C1	6.2	28
C2	6.2	13

Table 4-1. Set of geometries for diverse initial aspect ratios for analysis of the deposit profiles.

In Figure 4-13, numerical results obtained for each pair of initial aspect ratios (blue and black cross marks for the first and second geometry respectively) are compared with the corresponding experimental normalized deposit profiles (continuous red line).

In the first two cases, Figures 4-13(a) and (b), the computed profiles are practically indistinguishable. For both cases, the crumbling of the material spreads from the outher regin through the centre of the pile; a difference for the second initial aspect ratio, is that for both the experimental and numerical profiles, a curvature on the profile is given, instead of a straight slope present for the smaller value. This morphology, that is more characteristic of the second dynamical regime, is given since the initial aspect ratio $a = 1.95$ is closer to the limit between the first and second dinamical regime ($a \leq 3$) than the limit between the first and second deposit morphology ($a > 0.74$).

In the third case, Figure 4-13(c), differences are observed at the peak of the *Mexican hat* profile, and at the outer regions[8]. However, these deviations are not very pronounced (less than 7% at the peak). It may be concluded, thus, that numerical predictions are in accordance with the experimentally observed [62] about the independence of the scaled profiles to the volume of released material.

[8] As pointed out earlier, discrepancies at the outer regions are due the model's inability to represent the detachment of grains at the flow front.

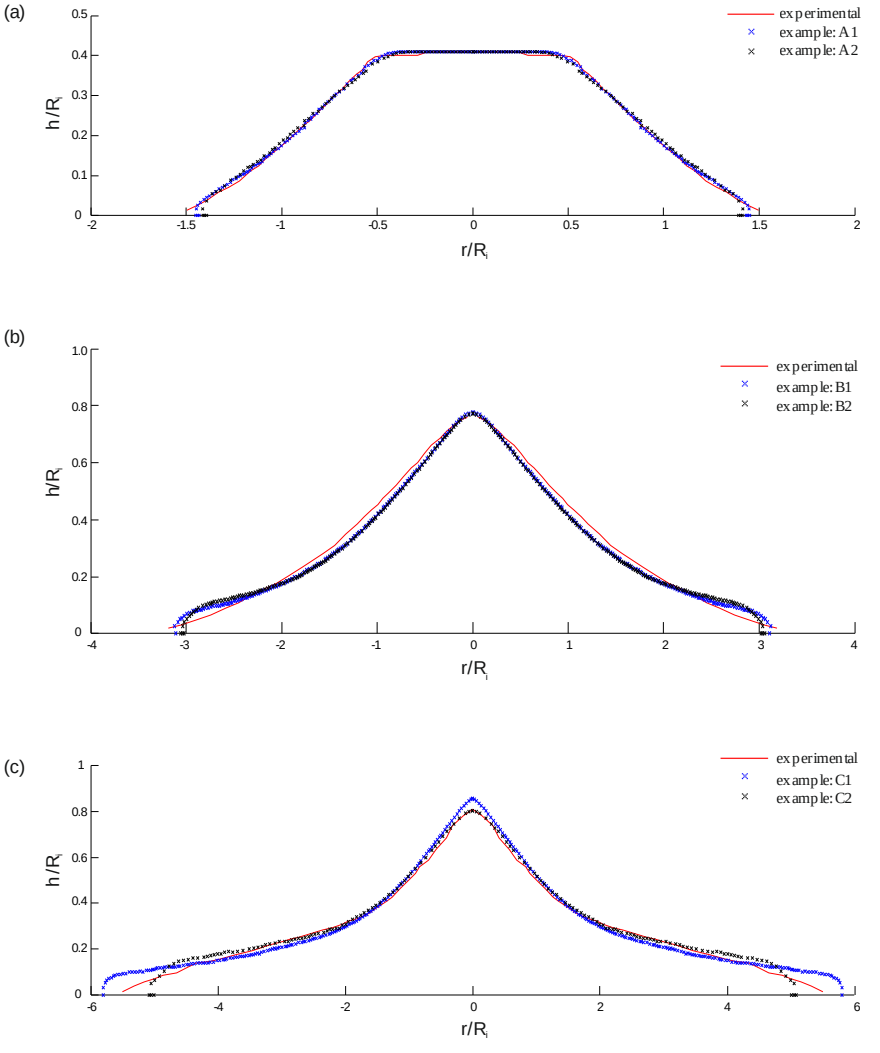

Figure 4-13. Comparison of the deposit profiles for pairs of initial aspect ratios with different dimensions: (a) initial aspect ratio $a = 0.41$, (b) initial aspect ratio $a = 1.95$, and (c) initial aspect ratio $a = 6.2$.

Lajeunesse, *et al*. [62] devised an experimental procedure that permits the visualization of the internal structure of the granular material in its final state. In this experiment, a cylinder is filled with the same glass beads, painted accordingly to differentiate seven alternating layers of red and white particles, see Figure 4-14 (a).

The cylinder pile has an initial aspect ratio $a = 1.00$ with a radius and height $R = H = 70.5\ mm$. After spreading, the granular deposit is symmetrically split into two parts by means of a thin glass, Figure 4-14(b); then, one of the halves is removed so as to observe the final distribution of layers, Figure 4-15(a). The dotted line indicates the boundary of the *stagnant zone* (*i.e.* the region inside which flow has not taken place). Lajeunesse, *et al*. [62] determined that, for this particular initial aspect ratio ($a = 1.00$), the stagnant zone is approximately a circular cone with radius equal to the base radius of the initial cylinder pile.

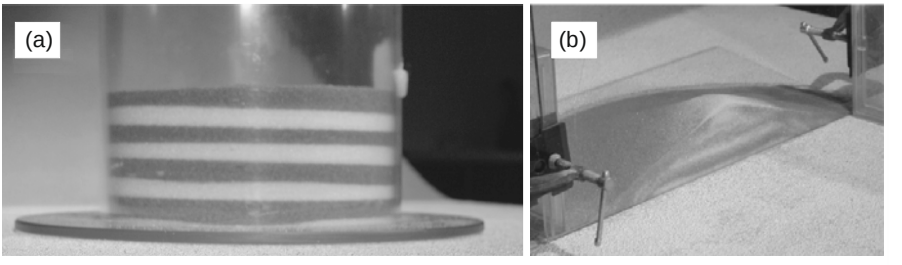

Figure 4-14. Experimental procedure to explore the internal structure of the deposit. (a) Initial state: tube filled alternatively with layers of two colour glass beads. (b) Deposit split in two parts by mean of a thin glass plate [62].

In order to assess the ability of the proposed numerical model to replicate internal flow patterns, a simulation of the spreading of the cylinder pile described above is carried out. The final configuraiton of the pile is shown in Figure 4-15(b); to facilitate the comparison with the experiment, the lines defining the experimentally measured stagnant zone (circular cone of radius $R = 70.5\ mm$) are also plotted in Figure 4-15(b).

Inspection of Figure 4-15(b) clearly indicates that the spreading of material was localized at the outer zones, close to the free surface, where particles can move easily compared to those within the core of the deposit. The region enclosed by the plotted lines remains practically undisturbed; this fact is in qualitative agreement with experimental observations, see Figure 4-15(a). Another interesting feature that can be gleaned from Figure 4-15(b) (and that it is also consistent with experimental observations given in [62]) is that granular motion occurs in such a way that top layers slide over layers beneath with no apparent intermix between them.

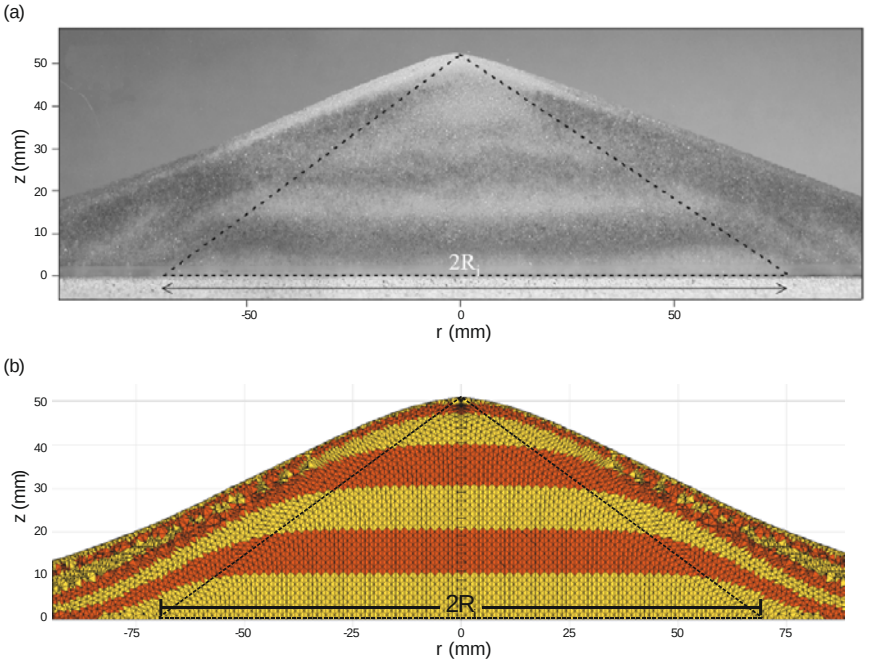

Figure 4-15. Comparison of internal structure of the deposit: (a) Experimental response [62], (b) Numerical solution.

4.5. Transient flow

We focus now on the validation of the model's performance in the transient regime. The validation is carried out by comparing the evolution, upon removal of the confining tube, of experimentally recorded and computed pile profiles. Experimental data has been obtained from the sequence of images displayed previously in Figure 4-2, from Ref. [62].

Intuitively, it is reasonable to expect that the speed at which the tube is lifted affects, to a greater or lesser extent, the velocity at which the granular pile spreads afterward. Thus, a proper assessment of the model's ability to describe the transient response requires accurate data of the tube lifting speed. Unfortunately, information in Ref. [62] concerning this aspect of the experiment is quite vague and somehow inconsistent. Indeed, Lajeunesse et al. [62] limit themselves to point out that the lifting speed is "of the order" of $v_r \approx 1.6\, m/s$; however, this speed is not consistent with the time labels accompanying the sequence of snapshots in Figure 4-2.

For instance, in the case of the cylinder with initial aspect ratio $a = 0.56$ (and initial radius $R_i = 70.5$ mm), the release time corresponding to $v_r = 1.6\, m/s$ is,

assuming constant speed, $T_r = aR_i / v_r = 0.024\,\text{sec}$, while in the sequence of images displayed in Figure 4-2(a), this time can be estimated, by interpolation between the time labels of the second and third snapshots, at $T_r \approx 0.179\,\text{sec}$.

To shed light on this apparent inconsistency, we have carried out numerical simulations of the spreading process for lifting speeds v_r ranging from 0.1 to 1 m/s. In Figure 4-16, we show (for the case of initial aspect ratio $a = 0.56$) the plot of the computed position $r_f(t)$ of the foot of the spreading pile versus time, together with the pertinent experimental data (obtained, in turn, from Figure 4-2(a)). The speed $v_r = 0.220\,\text{m/s}$ (green line) corresponds to the speed calculated from the aforementioned "guessed" release time $T_r = 0.179\,\text{sec}$.

Results displayed in Figure 4-16 conforms to intuitive expectations: the faster the tube is removed, the greater the rate of spread of the collapsing column front (and therefore, the sooner the stationary state is achieved). These results also provide a definite clue to resolve the controversy concerning the actual lifting speed employed in the experiments by Lajeunesse *et al.* [62]: the curve corresponding to the "guessed" lifting speed $v_r = 0.220\,\text{m/s}$ is the one that bests fits experimental values. By contrast, the graph with $v_r = 1.0\,\text{m/s}$ (the one closer to the estimation suggested by Lajeunesse [62], $v_r = 1.6\,\text{m/s}$) overpredicts the average spread rate in almost 100%.

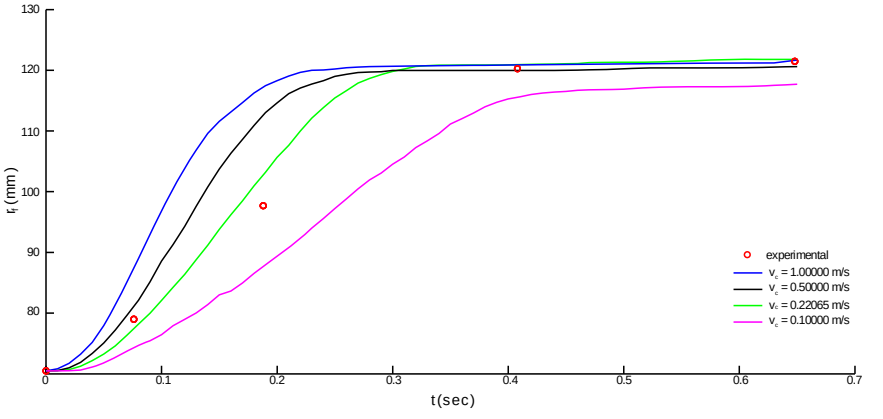

Figure 4-16. Position $r_f(t)$ .of the foot of the spreading granular pile for different v_r. Initial aspect ratio $a = 0.56$.

Pile profiles computed, using the seemingly correct lifting speed $v_r = 0.220\,\text{m/s}$, are compared with their corresponding experimental images in Figure 4-17.

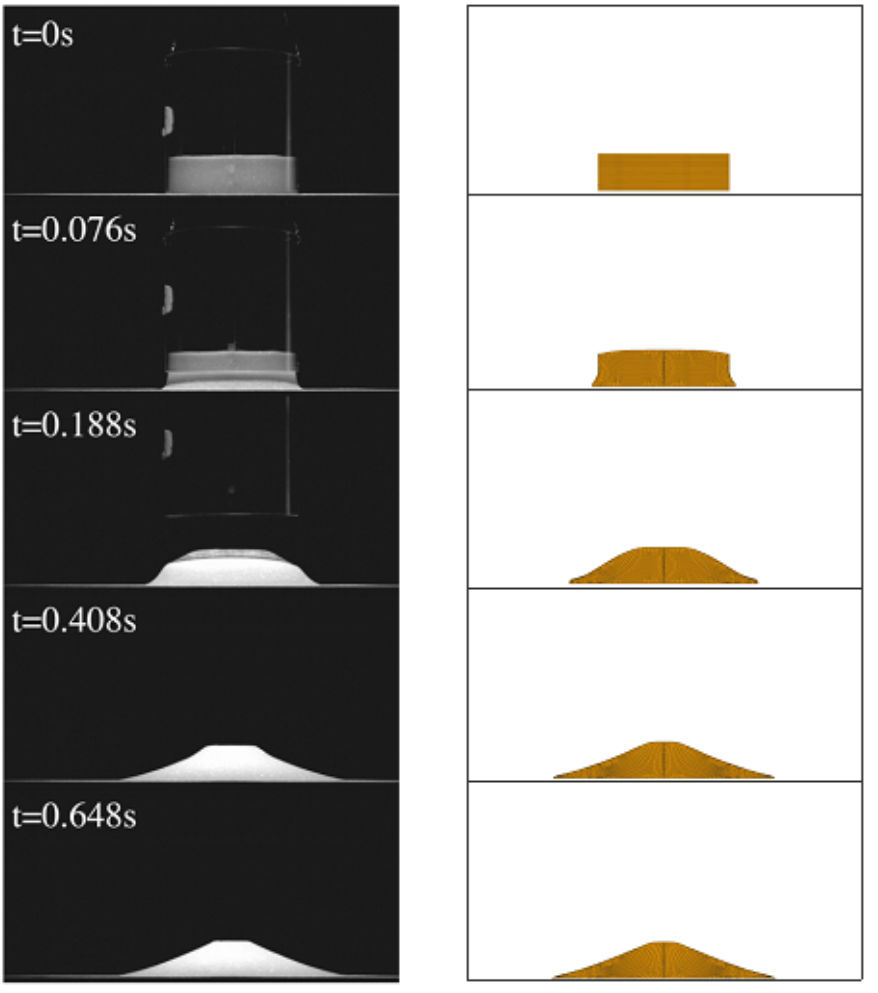

Figure 4-17. Comparison of sequences of profiles for an initial aspect ratio $a = 0.56$: (a) experimental [62], (b) PFEM.

The analysis under varying lifting speed, described above, is repeated for the column of initial aspect ratio $a = 0.8$. In Figure 4-18, the position of the foot of the pile versus time for the case $a = 0.8$ is plotted. The release speed, $v_r = 0.258\ m/s$, is the speed estimated from the relative location of the tube in the first and second snapshots in Figure 4-2(b).

Similarly to the situation encountered in the previous case, the curve corresponding to this "guessed" speed (green line) is the one that best fits experimental values (notably, the curve passes through four of the five experimentally measured points). The time to let the mass in motion corresponding to this initial aspect ratio is $T_m = 0.107\,\text{sec}$, which presents a higher value than the time for the cylinder removal $T_r > T_m$ l, doubling the value similar than for the previous example.

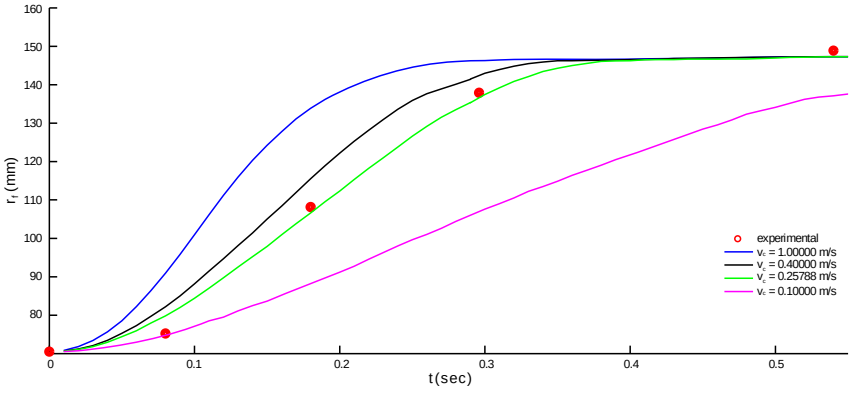

Figure 4-18. Position $r_f(t)$ of the foot of the spreading granular pile for different v_r. Initial aspect ratio $a = 0.80$.

On the other hand, Figure 4-19 provides the comparison of the evolution of computed and experimentally recorded pile profiles for this tube lifting speed. The agreement (both quantitative and qualitatively) is also remarkable even with the assumption of a constant velocity.

Lastly, we show in Figure 4-20 the evolution of the foot of the pile of initial aspect ratio $a = 8.94$ versus time for different tube lifting speeds. Using the same procedure as before, we get a lifting speed[9] of $v_r \approx 1.29\,m/s$. As in the previous cases, the curve corresponding to this speed (black line) matches closely the experimental points. It is interesting to note that the influence of the release velocity on the spreading velocity in this case is comparatively less pronounced than in the previously shown graphs for the thicker columns (Figure 4-16 and Figure 4-18).

[9] Indeed, it can be appreciated in Figure 4-2(c) that in the second snapshot, time 0.062 s, the tube has travelled approximately 32% of the initial height. Therefore, we have $v_r = 0.32 \cdot a \cdot R_i / t = 0.32(8.94)(0.028)/0.062 \approx 1.29\,m/s$.

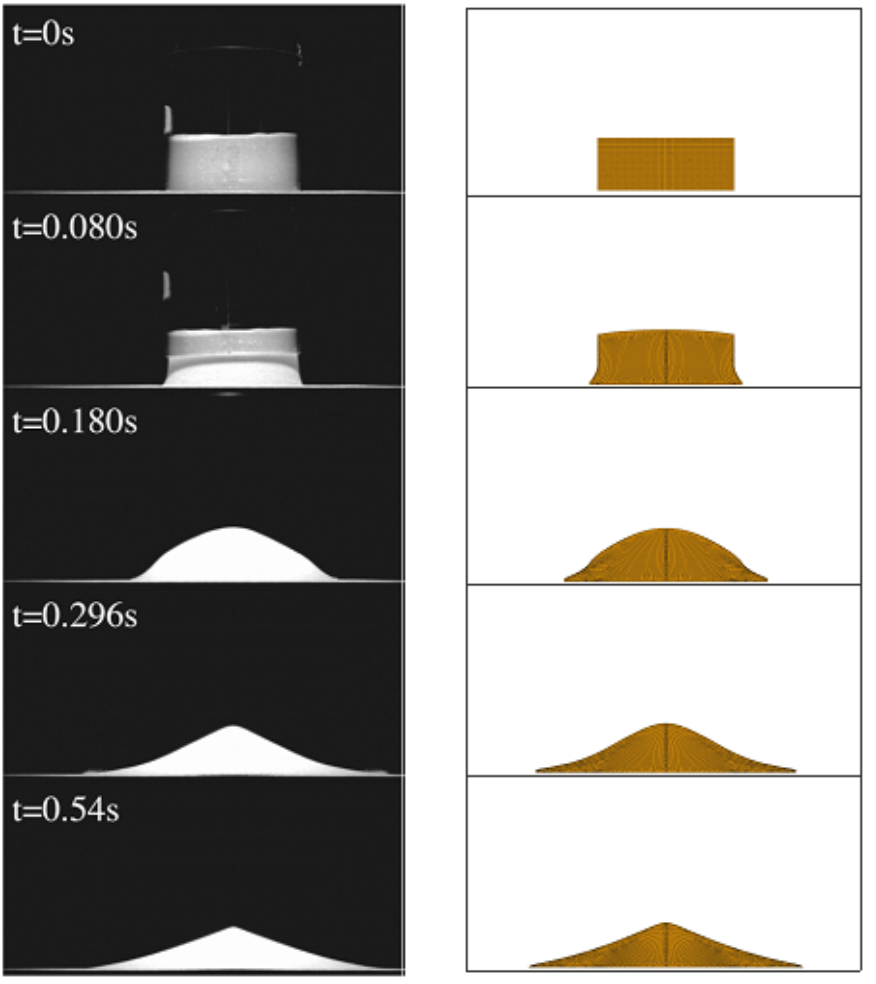

Figure 4-19. Comparison of sequences of profiles for an initial aspect ratio $a = 0.80$: (a) experimental [62], (b) PFEM.

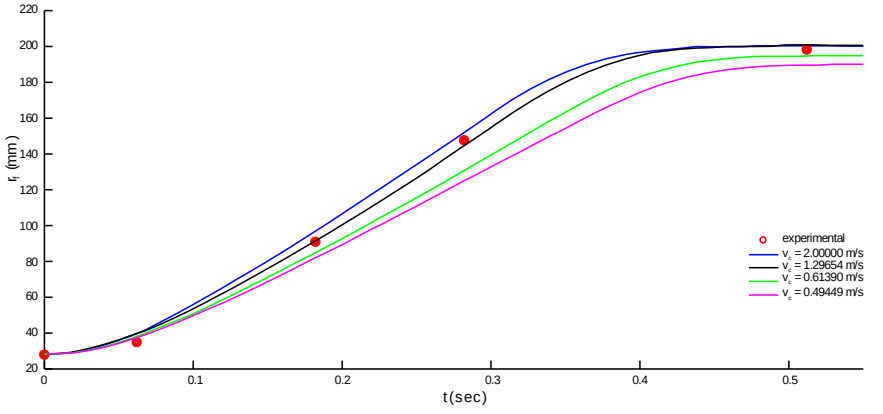

Figure 4-20. Position $r_f\,(t)$ of the foot of the spreading granular pile for different v_r. Initial aspect ratio. $a = 8.94$.

Figure 4-21 compares the experimental and numerical snapshots for this initial aspect ratio while spreading. The second dynamic regime is readily perceptible: the whole upper region of the granular column starts to move instantaneously; falling as a *rigid body*, so to speak.

The kinematics that represents this dynamic regime explains why, for this geometry or initial aspect ratio, the curves given in Figure 4-20 show a narrow distribution of the position of the foot of the spreading during the process. Since the material crumble takes place at the bottom of the pile, the material on the upper levels tend to fall as a rigid body and the confinement that are subject to does not play a significant role.

The spreading of the material takes place at the foot of the pile developing a flow front and the transition from this *rigid body* to a flow regime remains at the same level. Another worthy that deserves notice from these snapshots is the cloud of diffuse granular points. As earlier explained, this cloud appear because of the abrupt release that takes contact with the container; in the third frame it is clearly identified loosen particles due to the wall friction. As mentioned earlier, the impact of such cloud of points is negligible in the final configuration of the deposit.

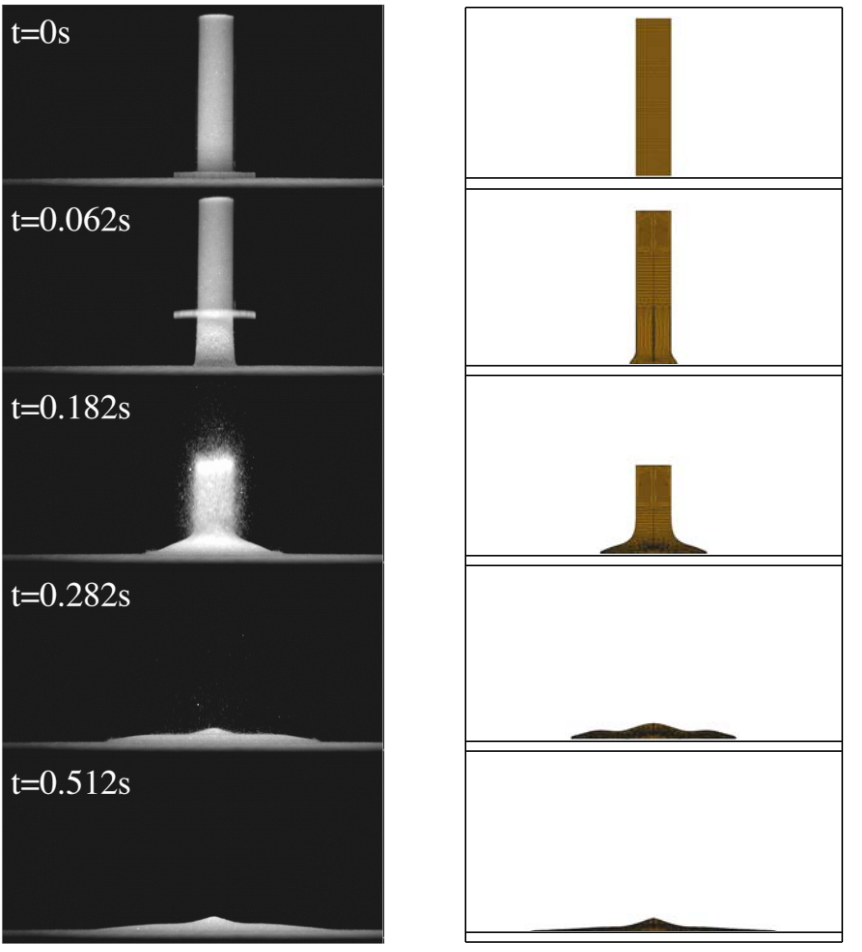

Figure 4-21. Comparison of sequences of profiles for an initial aspect ratio $a = 8.94$: (a) experimental [62], (b) PFEM.

4.6. Mechanical behaviour while spreading

In order to gain further insight into the different flow regimes occurring depending on the initial aspect ratio of the collapsing column, we examine next the evolution of contour plots of the plastic multiplier α defined in equatio (3.36) of Chapter 3.

The usefulness of these plots lies in that they convey at a glance – without the need to scrutinize velocity fields or other kinematic variables – qualitative information regarding the state of motion of the granular material at each time step. Indeed, recall that this variable indicates the phenomenological events that occur at each point of the material. Regions undergoing purely elastic deformations (stagnant zones) are characterized by $\alpha = 1.0$, whereas zones at which fully plastic flow is present are associated to values close to $\alpha = 0.0$. Finally, regions at which the transition from fully developed flow to static condition takes place (jamming zones) are identified by values between these two extremes.

Figure 4-22 depicts the evolution of the plastic multiplier for the three initial aspect ratios used to validate the transient regime. Time is normalized with respect the full time needed to reach their respective final deposit profile T^*. Figure 4-22(a) and Figure 4-22(b) corresponds to piles with initial aspect ratios $a = 0.56$ and $a = 0.8$, respectively. The key qualitative features reported in the experimental work by Lajeunesse et al. [62] can be readily observed in these sequences of plots – the margins of the pile crumble through an avalanche, and the flow front propagates then outward. In the first case ($a = 0.56$), Figure 4-22(a), it can be easily discern how the free upper surface divides into an inner, static region ($\alpha = 1$) and an outer flowing region ($\alpha = 0.0$). On the other hand, in the second case, Figure 4-22(b), the distribution of this variable reveals that the entire outer surface starts to flow immediately (no static, outer regions are observed in the second contour plot). Once the material stops flowing, all zones tend to the static condition ($\alpha = 1.0$), as can be seen in the last row of plots.

Lastly, in Figure 4-22(c), the contour plots corresponding to the third aspect ratio are displayed. The portrayal of undeformed and flowing regions provided by these plots is reasonably in accord with the previously outlined experimental observations by Lajeunesse et al. [62] (second dynamical regime). Indeed, the distribution of variable alpha in the second snapshot clearly indicates that the upper part of the column remains practically unaltered ($\alpha = 1.0$ in the, approximately, upper half region) during the initial stages of the collapse, while, simultaneously, a flow front develops at the base of the column.

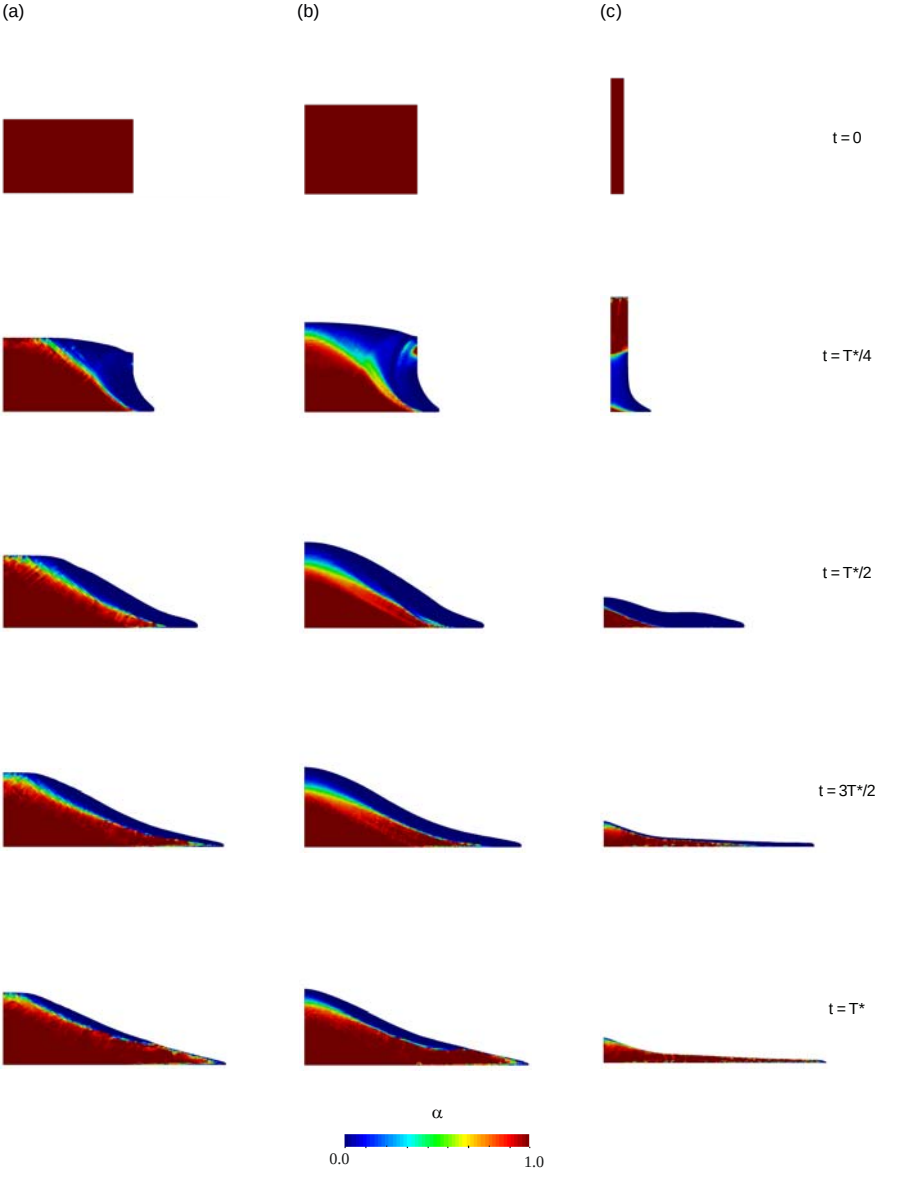

Figure 4-22. Evolution of the elastic factor $\alpha(\Delta\lambda)$ while spreading a granular pile for three different initial aspect ratios (where T^* stands for the normalized time): (a) $a = 0.56$, (b) $a = 0.80$, and (c) $a = 8.94$.

Chapter 5
Industrial applications

Many industrial processes involve the manipulation and transformation of granular materials. The presence of granular flows during these processes is a strong source of problems that they are partially understood and sometimes neglected. For this reason, it is important to explore and analyse via experimental and numerical models the mechanisms that are developed when granular flows are present. The scope of this chapter is to validate the capability of our numerical model to reproduce real industrial processes where dense granular flows are involved.

The examples focus on two industrial problems related to pellet manufacturing in mining industry: the silo discharge and the tumbling mills. Both examples are representative when dealing with granular flows due to the presence of variations on the granular material mechanical response –varying from a stagnant configuration to a flow condition. A general setback related to granular materials flows is that there is no a large number of reliable and accurate experimental examples, being more difficult to find for industrial processes. In order to validate our numerical model, it was necessary to identify experimental models conducted and reported rigorously.

The silo discharge is validated using the experimental data collected by Rotter et al [89] on a full scale flat bottomed cylindrical silo. The simulation was conducted with the aim to characterize and understand the correlation between flow patterns and pressures for concentric and eccentric discharges. Numerical and experimental flow patterns are compared for different levels of discharge. The effect on the flow patterns due to the variation of the mechanical properties and the outlet diameter is also analysed.

In the second example, the potential of *PFEM* as a numerical tool to track the positions of the particles in the interior of a rotational drum is analysed. The tumbling process is compared with the experimental model of a rotational drum con-

ducted by [94]; the power draw is computed and validated against the experimental results in which the power is plotted in terms of the rotational speed of the drum.

5.1. Silo discharge modelling

This section is devoted to the numerical simulation of a silo discharge. First, a brief description of the main aspects that characterize the mechanisms presented in the granular material during its confinement and its discharge is given. Thereafter, it is described the experimental setup and main results reported by [89] that are expected to be compared with the numerical simulation. Finally, it is shown the numerical comparison of the simulations as well as some studies and conclusions that the model allows us to identify.

5.1.1. Silos behaviour during discharge

The granular material behaviour in silos has been a topic of interest since late nineteenth century ([86],[49]); this is due to the wide number of problems that are present during its storage and discharge. The problems found are not only on the structure itself, but also on the material. The first type of problems involves instabilities on the foundations, buckling of silo walls, blockage of the material at the outlet, and discharge overpressures [83]. The second set of problems refers to the material and embraces material ageing, crushing of the material due to large compression pressures, segregation, among others [29]. Despite the significance of the impact of granular materials in economy, many of these problems are treated with inchoate solutions.

Internal pressures and the pressures exerted on the silo walls are strongly influenced by the flow patterns of the granular material during its discharge [75]. Generally, the flow mechanisms for a silo discharge can be broadly classified as either *mass* flow or *funnel* flow [50]. Mass flow patterns are smooth and relatively uniform; the velocity profiles for a mass flow exhibit the highest values at the centreline of the outlet, and decreasing progressively toward the silo walls. This type of flows presents a depression on the bulk of the material since the discharge is faster at the centre than at the outer portions. On the other hand, Brown and Hawksley characterized in 1947 the funnel flows by a stagnant zone toward the silo walls, a region of vertical motion at the centre of the outlet, and a transition or *jamming* zone [75], see Figure 5-1.

The definition of mass flow or funnel flow is a function of the material properties, the geometry of the silo, and the interaction between the silo's wall and the granular material. It is observed that whenever the mass flow is not achieved, the patterns given by a funnel flow have significant implications both on the functional and structural design of the silo [24].

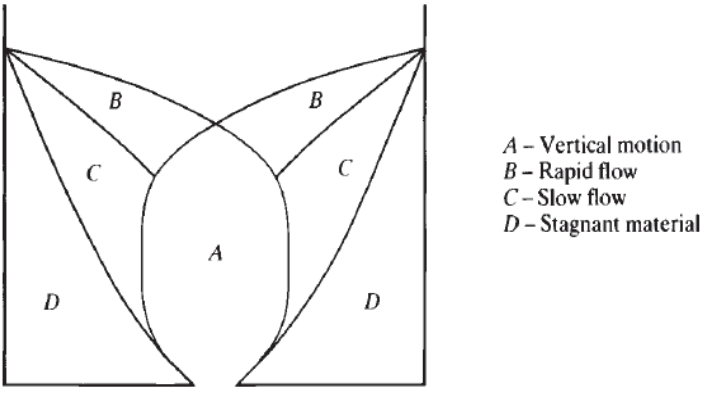

Figure 5-1. Flow zones proposed by Brown and Hawksley [75]

The distribution, size, and shape of the particles have a wide influence on the material discharge. Blockage of the material at the outlet is related to the size and shape of the particles as well as the dimension of the opening; with this condition, the flow may present sporadic or complete obstruction of the material by remarkably stable arches [29]. About the shape of particles, bulks formed by rounded well shaped particles are prone to define regular and smooth flows comparing with those formed by particles of higher degree of angularity and granulometry –which present periodic formation of rupture zones [75]. The material in the silo is also affected by the filling process and hence the flow patterns during its discharge [24]. This affectation is given due to the particle packing of the bulk solid, getting to present density unevenness, irregular stagnant zones, and wall overpressures.

Other factor that affects the discharge patterns is the geometry of the silos. Experimental tests show that for large height to breadth ratios the mass flow is more predominant, while for lower ratios the funnel flow is more frequent [83]. The influence of the relationship between the wall friction angle and the hopper angle has been reported for several authors as ([50],[4]). It is also observed that funnel flows tend to form for large hopper angles and large wall friction angles; in the other hand, for smaller values the predominant flow is a mass type, see Figure 5-2. Despite the strong influence of this relationship, the transition between a mass flow and a funnel flow depends on the internal friction angle of the material [56].

The pressures during discharge are strongly influenced by the flow regime. It is important to understand and define the pressures distribution since they have repercussions on the structure of the silo and its functionality. Problems due to the pressures are found when there is a large gradient of the pressures exerted on the walls, causing serious implications on the integrity of the structure [25].

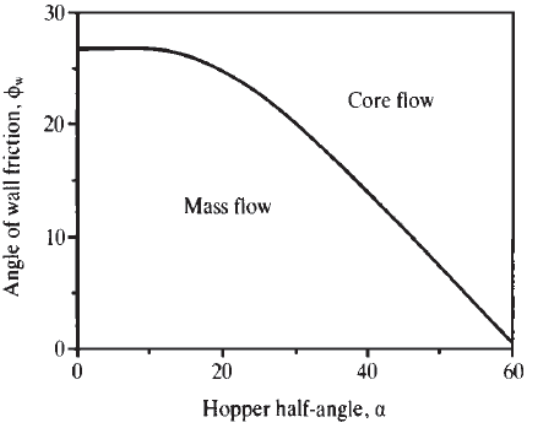

Figure 5-2. Criterion for the transition between core and mass flow [75]

As a result of the requirement of a well understanding of the pressure distribution and the functioning of the system, it is essential to establish models to predict these conditions. Unfortunately, modelling of the response of granular materials on silos is not a trivial task – neither on experimental nor numerical models. Experimental models have the setback of the affectation on the response due to the scale factor; for this reason it is important to determine full scale models which make expensive to run tests for every condition. Likewise, another difficulty is the instrumentation required for data recollection. The flow patterns are difficult to determine since walls are opaque and there is no a direct disposal to measure and observe those patterns.

Analytical models have been proposed in order to predict the load distribution. One of the most used is the proposed by Janssen in 1895 [49], based on a heuristic model on the framework of continuum mechanics [29]. The model resides on the observation that the granular media tends to redirect the vertically applied loads toward the walls.

Computational techniques allow us to define numerical models to simulate silos discharge. Traditionally these models are based on discrete methods. The drawbacks with these methods are the limitation in the number of particles to simulate real applications, the lack of an accurate definition of the particles interaction, as well as the difficult to have a direct coupling of the forces and stresses on the structure. An alternative is found in the use of a continuum approach. The Particle Finite Element Method (*PFEM*) is a numerical method suitable to solve the governing equations for large deformation problems, allowing us to determine the transitory and stationary regime of a problem.

5.1.2. Experimental setup

The experimental model used to validate the numerical model is reported by Rotter, et al [89]. The importance of this experiment lies on the use of a full-scaled silo; since it is identified the influence on the experimental response given by the scale of the model ([83],[25]). The model is a full-scaled flat bottomed cylindrical silo, instrumented to study the flow patterns and their correlation with the wall pressures. Several conditions of discharge and materials were tested.

The silo is flat bottomed, which does not include a hopper. The silo is 4200 mm in diameter with a 9500 mm high barrel section, see Figure 5-3(a). The walls of the silo were instrumented with strain gauges to measure the deformation, located one inside the wall and a pair outside the wall. The material discharge was tested with three different outlets, one concentric and the other two eccentrics – one fully eccentric and one half way between. The outlets have circular dimensions with a full opening diameter of 480 mm. Each outlet has a hydraulically controlled slide gate, which operates from one side. This slide gate is opened partially, which makes the outlet in a shape of a circular segment.

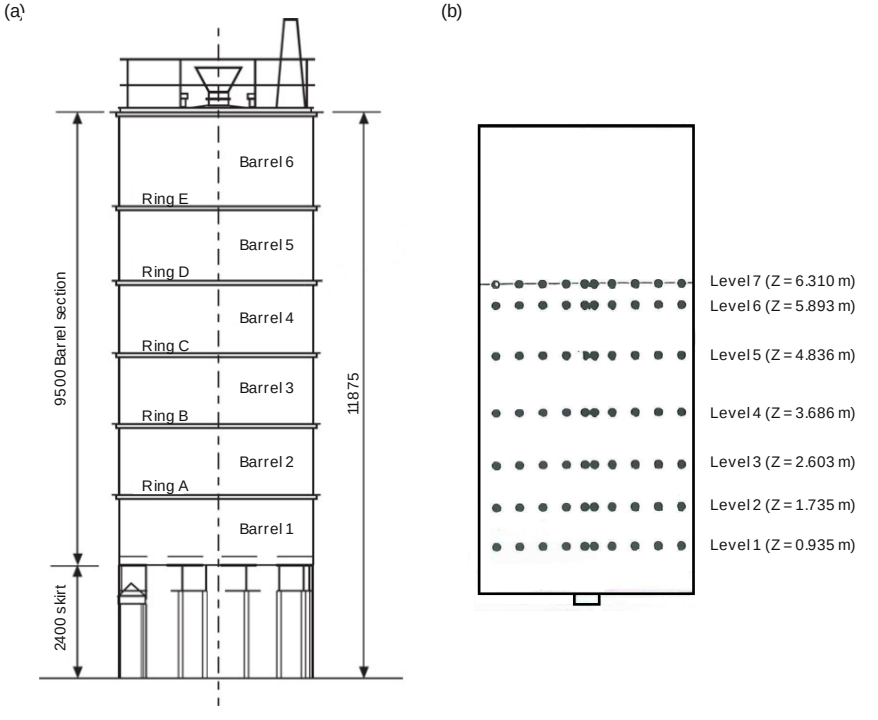

Figure 5-3. Full-scaled experimental silo: (a) Elevation view (all dimensions in mm) [25]; (b) Seeding of radio tags per levels [89].

The measurement of the flow patterns is not obtained directly. Several proposals have been used but only applicable to laboratory conditions – direct visual observation, photographic and radiographic techniques, residence time measurement, indicator bars in silo walls penetrations [89]. In the experiment, radio tags were placed in the silo with the aim of predicting flow patterns during the discharge.

The radio tags were carefully located along and across the material. A total of 280 radio tags were placed uniformly at seven different levels and eight spokes for each level separated at five different radiuses, see Figure 5-3(b). The silo was filled concentrically to avoid localization of pressures due to the particle packing. The filling of the material was stopped at each level and the bulk was raked in order to dispense a flat surface; afterward, the template with the seeding position was located to define the exact position of the tags. In order to avoid damage of the radio tags, they were placed inside tennis balls. The logging system for the tags consisted on an aerial wired straight into an amplification box. The signal was processed in order to identify the radio tag at the moment it was expelled through the outlet.

The flow patterns were calculated via an extrapolation of the position of the tags and their residence time. For the position of the tags along the discharge, the authors of the experiment define the assumption of a trajectory defined by the shortest path, which for many markers and mass flow it is correct; and for the velocity, it was determined an exponential changing velocity supported by the time residence of the markers. It was observed that even for concentric discharge, a full symmetric pattern was not obtained; however, the difference is too slight to be considered significant.

The experiment results are taken from the case corresponding to a concentric discharge of the iron ore pellets – several technical aspects of the experiment, described as PCB test, are reported in Ref. [89]. The silo was filled concentrically until a mean height of 6400 mm with iron ore pellets with particle size with a range between 12-15 mm, and a bulk density of 2.3 tonne/mm^3.

Due to the large number of industrial processes that involve the handling and storing of iron ore pellets, the mechanical characterization of this material was carefully analysed by Gustaffson, in Ref. [37]. The reported internal friction coefficient is $\mu = 0.67$, the bulk modulus is $\kappa = 32$ MPa, and the wall friction angle between iron ore pellets and steel plate is $\theta = 23.7^o$.

5.1.3. Silos discharge, numerical simulation

The numerical simulations described in this section show the model capability for industrial applications. The validation of the model is given comparing the numerical and experimental flow patterns. Thereafter, it is shown some numerical variations that allow us to comprehend in a deeper way the influence of the material properties and the opening of the outlet.

The computational model is a flat-bottomed cylindrical silo with a concentric outlet. The dimensions and filling height are based upon the full-scale PCB experimental test reported by Rotter [89]. The diameter of the silo is 4200 mm and the

filling height 6400 *mm*; and a full opening outlet of 480 mm diameter is used as a reference example.

The simulation is performed via *PFEM*, using an axisymmetric formulation. The edge of the outlet is rounded using a radius of 40 mm in order to reduce geometrical singularities, see circled region in Figure 5-4. A non-uniform unstructured discretization of 6250 nodes is used to describe the initial configuration of the pellets domain; each node represents 3 degrees of freedom – 2 for displacements and 1 for the nodal pressure – as a consequence of the mixed formulation.

The non-uniform discretization is fundamental for the simulation, since the opening of the outlet is considerable small compared to the size of the silo. The average element size is $h_1^e = 100\ mm$ except near the outlet, where the element size is $h_2^e = 25\ mm$ approximately, see Figure 5-4.

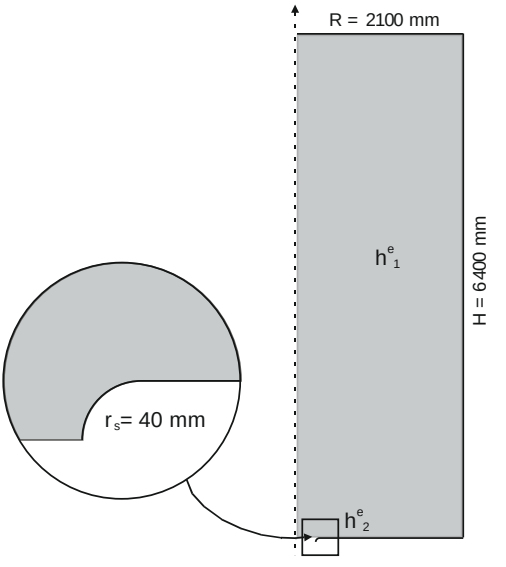

Figure 5-4. Computational model for a full-scale silo. Spatial discretization in terms of a mesh with two mean element sizes of: $h_1^e = 100mm$ for the whole domain, except near the outlet, and $h_2^e = 25mm$ for the region surrounding the outlet. A rounded edge for the outlet is defined in order to reduce geometrical singularities, $r_s = 40mm$.

In all the examples, calculations have been made with the following material data: bulk density $\rho = 2300\ \text{kg/m}^3$, bulk modulus $\kappa = 60\ \text{MPa}$, shear modulus $G = 7\ \text{MPa}$, internal friction coefficient $b_1 = 1.00$ (where the internal friction coefficient is 30.57^o), cohesion $b_2 = 1\times10^{-8}\ \text{MPa}$ (a close to zero value to define a cohesionless material, but defined for the von Mises regularization proposed in Chapter 2), relaxation time $\tau_R = 2\times10^{-7}\ \text{sec}$, and Coulomb's dry friction $\mu = 0.60$. The simulations has been run with a time-step length $\Delta t = 2\times10^{-4}\ \text{sec}$. The total time analysed is 95 sec, corresponding to a volume silo discharge of 20m^3. To obtain a steady start after the gravity is applied the outlet is closed the first 0.5s of the simula-

tion time. Figure 5-5 shows the particle discretization of the initial, an intermediate and the final configuration of the numerical silo.

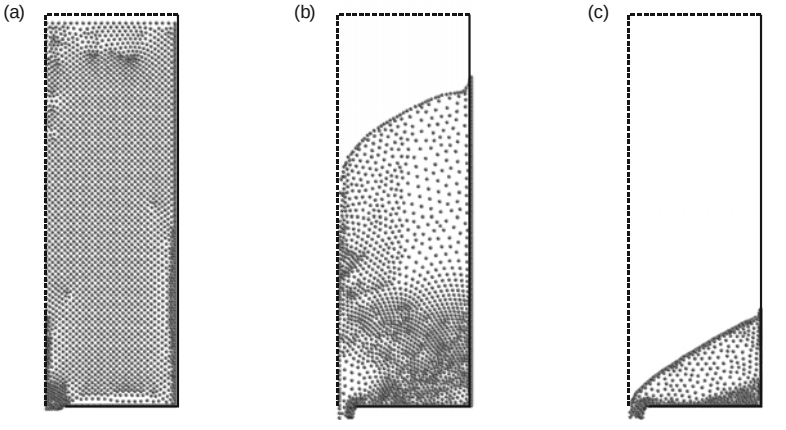

Figure 5-5. Particle discretization of the domain at different stages of the silo discharge: (a) Initial outlet opening, (b) 20m^3 of material discharged, (c) last stage of discharge defining the remaining material on silo.

5.1.3.1. Flow pattern comparison

To compare the flow patterns achieved by the numerical simulation with those from the experiment, there are defined seven horizontal lines in the numerical silo are marked and traced through the solution – the position of those lines is at the same height than from the experiment described in Figure 5-3(b). The positions at three different volumes of discharge are compared with the computer visualization of the experiment in Figure 5-6. The blue lines stand for the numerical results and the red cross marks for the computer visualization of the tags position. The comparison is extended to 17m^3 of discharged material.

In general, the trends between numerical results and the computer visualization of the tags are similar in most of the stages. For 1m^3 of the discharged volume, particles adjacent to the outlet are in motion, followed by particles further afield. A velocity wave propagates upward and the funnel flow behaviour is clearly initiated. Ore pellets located toward the wall remain stagnant – the continuous lines, at least for the five lower levels, remain horizontal at a significant distance from the wall – indicating that the material does not crumbles toward the outlet; the material that is discharged is the one located at the centre of the silo.

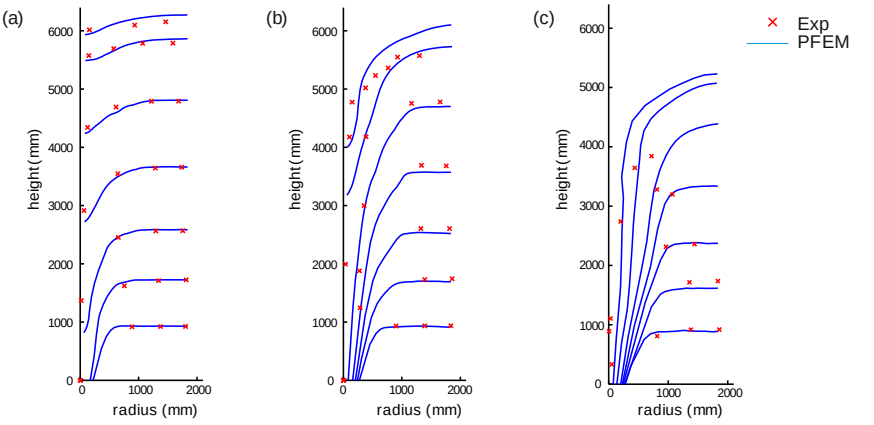

Figure 5-6. Flow patterns comparison between experiment and *PFEM* for different volumes of discharge: (a) 1m3, (b) 5m3, (c) 17m3.

The definition of the funnel flow is more pronounced as the material is discharged; for $5m^3$ only the material located at the centre of the silo of the last two levels remains in the silo, and for $17m^3$ the funnel is developed completely. This can be seen by the clearly definition of two principal zones: a stagnant region located toward the silo walls and the flow region defined by a loose material above the outlet of the silo.

Nonetheless, significant differences with computer visualization data are observed, as it is detailed in what follows. For $5m^3$ of discharge, the last two blue lines (corresponding to the upper levels) exhibit a separation between them and a small horizontal platform toward the wall is still apparent; by contrast, the plot of the corresponding experimental tags defines a unique overlapped contour level.

The material volume defined by the skyline of the tags seems less than the one defined by the numerical result, however the experimental volume discharged is $5m^3$. The progressive decrease of volume observed experimentally at $17m^3$ of discharge is more pronounced that the decrease in volume predicted by the model, which even retain horizontal platforms of stagnant material. This markedly distinct response highlights concern with the characterization of the material response, which should clearly receive careful consideration in future improvements of the model.

The differences between the experimentally *observed* and the computational calculated flow pattern responses may be attributed to three main reasons. The first one is the numerous simplifying assumptions made in Section 2 in deriving the constitutive model, the second reason due to assumptions introduced to be able to do the simulation, and the third reason concerns the computer visualization code required to visualize the position of the tags. Among the simplifying assumptions made in the model, we suppose that the internal friction coefficient is independent of the pres-

sure or of the material density being not sensitive to the particle packing of the bulk. A similar comment can be done on other parameters like the viscosity (defined in terms of a relaxation time).

Another contributor to these discrepancies may be found in the elementary character of the outlet's size and shape. As commented in Section 5.1.2, the outlet has a hydraulically controlled slide gate, which is opened partially, making the outlet in a shape of a circular segment; by contrast, in order to minimize the computational cost, we assume an axisymmetric geometry, removing in this way the intrinsic 3D character of the outlet.

The third reason is the computer visualization code itself. As pointed out by the authors of the experiment in [25], the interpretations of the residence time measurements were made following previous studies by portraying residence times in horizontal and vertical cross-sections through the silo. These contours are more as a qualitative indicator of the flow pattern than a quantitative description.

An alternative numerical representation of the flow patterns is discussed in what follows. The idea is to plot in the same domain the evolution of a fixed material line. In order to get a clear visualization only a few time steps are included in the analysis. The different positions for each level (counting from the bottom) have been drawn in Figure 5-7. There are plotted several particles at each level identified by black dots and joined by a continuous blue line; the material position of the particles at different time steps defines the flow mechanisms present during its discharge.

It is identified a similar pattern of discharge on all the levels which define the evolution of a funnel flow with a small contribution of a mass pattern –defined as a *mixed flow* with funnel flow predominance. The particles located close to the wall do not present a noticeable separation in their relative position, but, close to the outlet, they change abruptly as they converge on the flow. In other words, it is observed that the material on the walls is displaced toward the centre of the silo at small velocities; once the material reaches the region of vertical displacement its velocities is increased. The material presents the larger velocities on the centre of the structure and closer to the outlet – it is represented by a larger distance between the black points plotted in Figure 5-7.

The discharge mechanism is not considered fully of the funnel type, since it is identified that the material located toward the wall is not completely stagnant, i.e. it is observed that the particles diminish their level, indicating a discharge of some material below them.

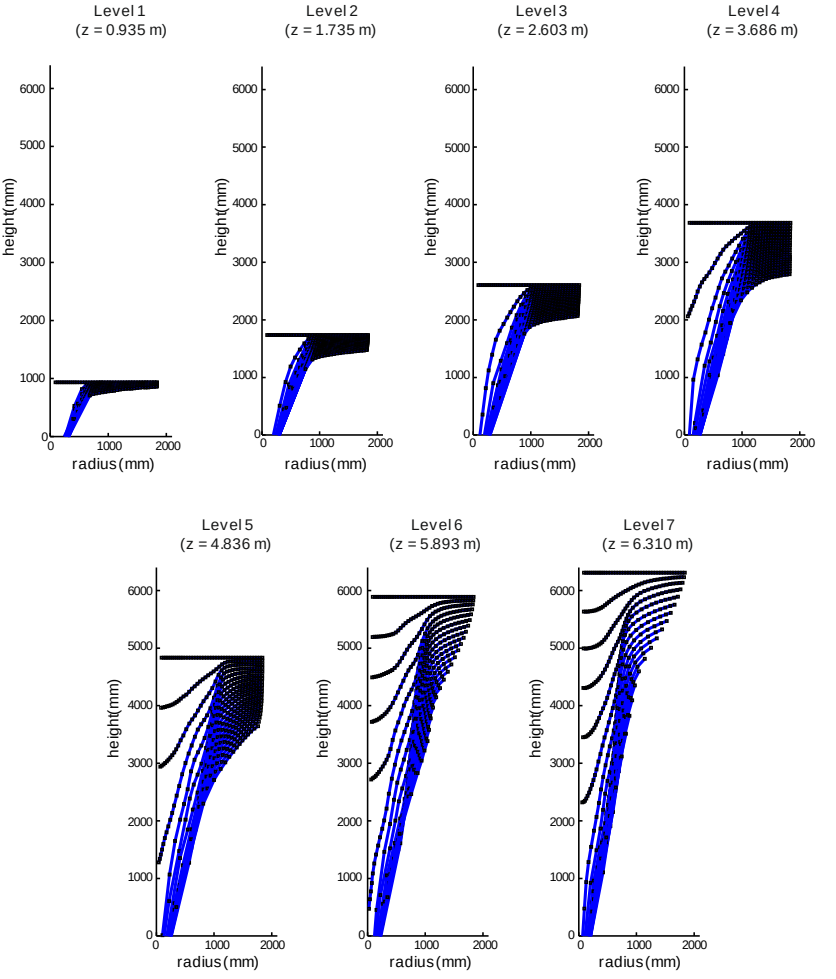

Figure 5-7. Evolution of the position for different levels during the material discharge.

A second alternative to understand the discharge mechanism of the silo is through the mean residence time of the material. Following the philosophy of the experimental test, the time residence calculated for the material particles located at the position of the radio tags is shown in Figure 5-8.

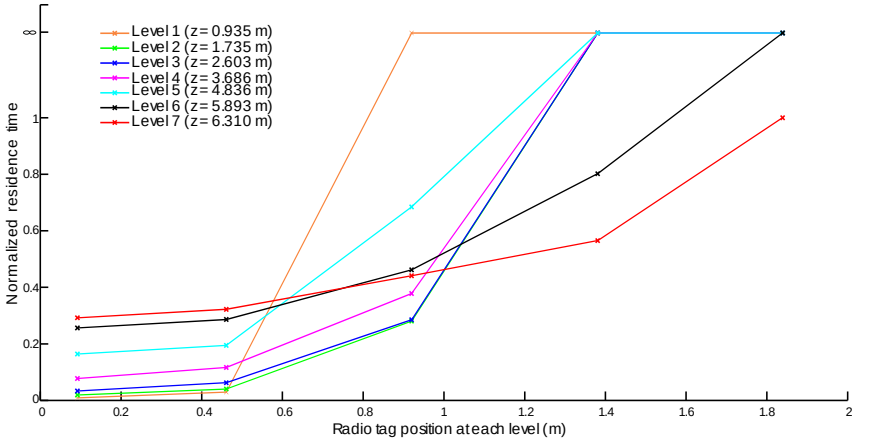

Figure 5-8. Mean residence time calculation for material particles located at the positions of the radio tags used on PCB experiment.

The mean residence time allows us to identify the flow behaviour of the material during its discharge. As it is expected, the material particles located closer to the outlet and above it are the first to be released; for the tags located just at the centre of the silo or its axisymmetric axis, the particles are released in order, being the last to be released the corresponding to level 7. This tendency is inverted as more material is discharged and the funnel flow is fully developed; it is observe this transition is presented for those material particles located at a distance close to 1m from the outlet. Once that the funnel flow is developed, all the tags corresponding to the upper region, level 7, are released in a narrow band of time.

The curves shown in Figure 5-8 also define the presence of stagnant material during and after the granular flow; this is defined observing that those particles closer to the wall on the bottom of the silo were never released – only the two first material particles of level 1 were released while for the whole level 7 all material was discharged.

5.1.3.2. Influence of material and geometric parameters on the flow patterns

The advantage of numerical simulations is the capability of easily varying parameters in order to have a wider understanding of the phenomenon; in this section it is studied the influence of the material and geometric parameters on the discharge mechanisms of a silo.

The first set of examples corresponds to the study of the flow patterns varying the internal friction coefficient b_1. In order to identify a proper variation of the discharge mechanism due to this coefficient, it was defined a set of values above and under the reference one; this material coefficient was varied using the following set $b_1 = [0.7, 0.85, 1.15]$ – the calibrated coefficient with respect the experimental essay is $b_1 = 1.00$.

The results of this study are summarized in Figure 5-9, where the flow patterns for the set of internal friction coefficients are compared.

In the figure are plotted, in a front view with a continuous blue line, the position of the markers at each level for different volumes of material discharged – $1m^3$, $5m^3$, $10m^3$, $15m^3$, and $20m^3$; with a dotted red line, it is marked the original height for the second and fourth levels, to observe its variation during the discharge. The front views show for the four cases, from left to right, how the flow evolves since the material is released.

For the whole set of internal friction angles, the flow is identified as being of the funnel type; it is observed on the first column, $1m^3$, that the flow is formed at the centre or axisymmetric axis of the silo. As the material continue to be discharged, the stagnant zones are more clearly identified – shown at the fourth and fifth columns of each internal friction coefficient, corresponding to $15m^3$ and $20m^3$ of material discharged.

As it is expected, the internal friction coefficient of the model plays a fundamental role in the behaviour of the material. Lower values of internal friction coefficient allow the material to develop larger deformations for the same external excitation – in this case gravitational forces. Figure 5-9(a) shows a funnel flow with a high contribution of mass flow during the discharge, which is described by a flow nourished by material located of the bottom region of the silo. The lower levels of markers show a narrow region of stagnant material toward the wall, which describes a funnel flow. The mass flow contribution is identified by the large amount of material discharged from the bottom of the silo since the upper tags markers remain on the silo – level 6 and 7 for $15m^3$ and level 7 for $20m^3$ of material discharged.

The funnel flow is recovered with a slight increment on the internal friction coefficient. Figure 5-9(b) displays the flow patterns obtained for a discharge using $b_1 = 0.85$. It is observed a wider region of the stagnant zone, releasing material of the upper levels. Comparing with previous internal friction coefficient, it is observed that the uppermost level has been released at $15m^3$ of material discharged.

The flow patterns corresponding to the reference internal friction coefficient, $b_1 = 1.00$, are plotted in Figure 5-9(c). The funnel is achieved with the discharge of $15m^3$ of material – material from the last level has been discharged; and the stagnant zones are wider as expected. A more detailed description of its discharge was explained in previous section.

A higher value than the reference example was used for the internal friction coefficient, in order to force a more pronounced flow funnel. Figure 5-9(d) shows the flow patterns for a value of $b_1 = 1.15$ (corresponding to a Mohr-Coulomb internal friction angle $\theta \approx 34.77°$). As the internal friction coefficient is increased, the stagnant zone is more pronounced toward the centre of the silo defining a vertical narrow region of flow closer to the axisymmetric axis. Since the funnel flow is strongly defined, the material corresponding to the upper levels of the markers is released since the first $10m^3$ of the material discharged.

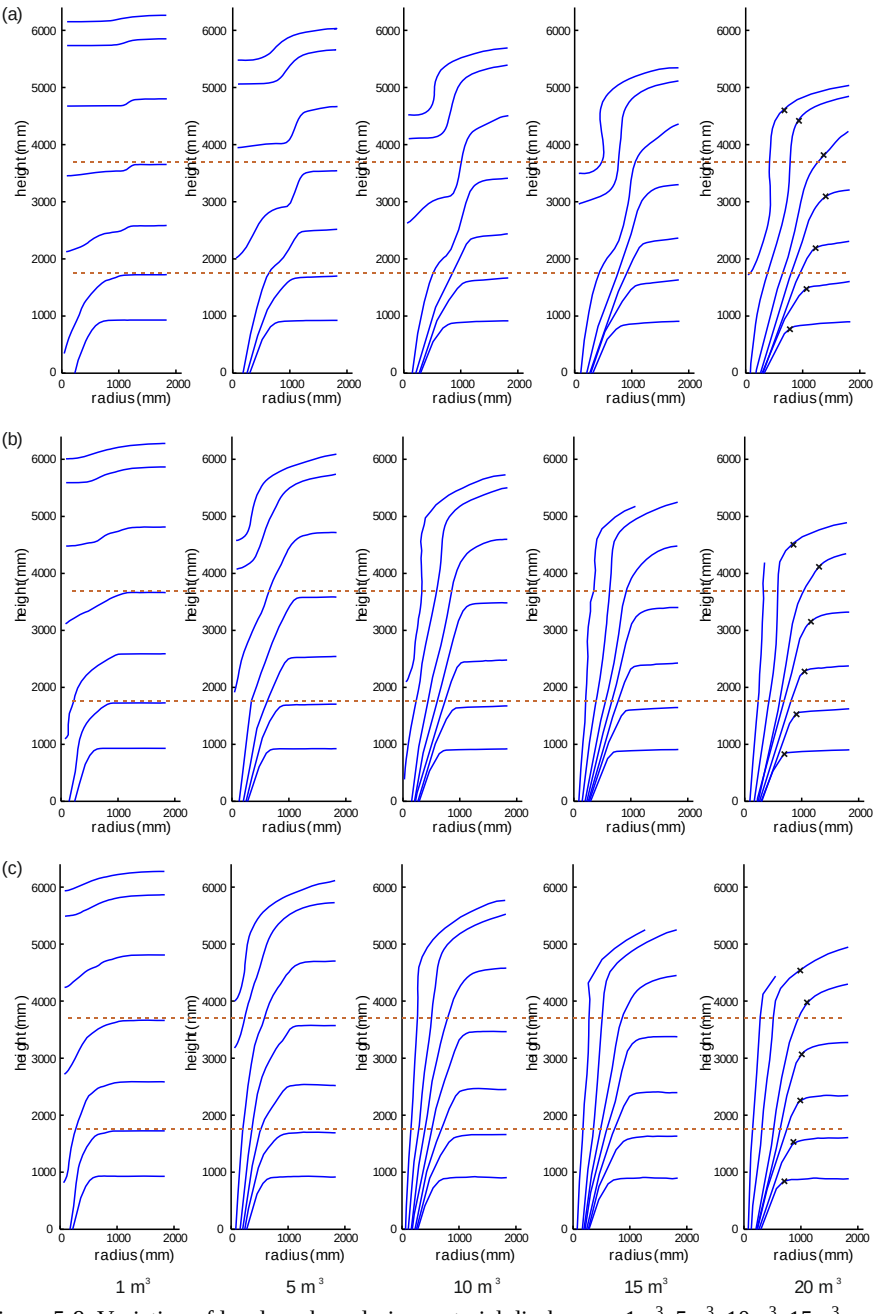

Figure 5-9. Variation of level markers during material discharge – $1m^3$, $5m^3$, $10m^3$, $15m^3$, and $20m^3$ – for different internal friction angles: (a) $b_1 = 0.70$, (b) $b_1 = 0.85$, (c) $b_1 = 1.00$, and (d) $b_1 = 1.15$.

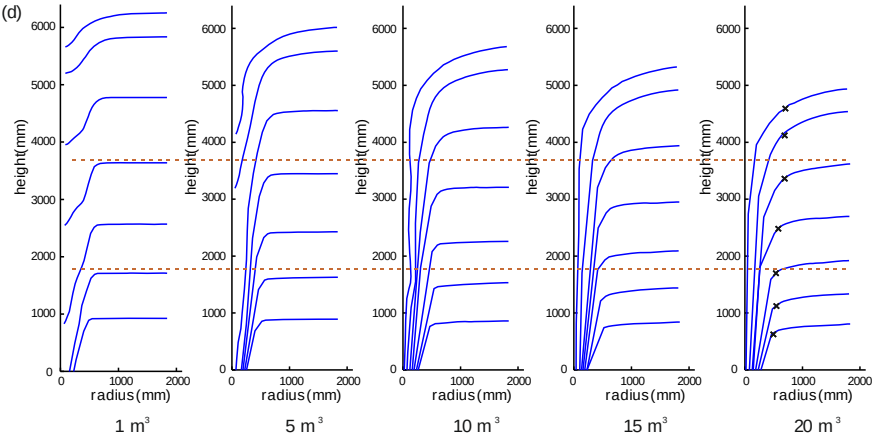

Figure 5-9 (Continued).

The influence of the internal friction coefficient on the discharge mechanisms could be summarized studying the flow patterns present at $20m^3$ for each friction coefficient value – fifth column of Figure 5-9. It was marked with a black cross mark at the inflection point of the curvature of each level of the markers. It is identified that the flow encompasses a wider region as the internal friction coefficient is smaller; for $b_1 = 0.70$ the loosen material present an elliptic region, while, for a granular media with $b_1 = 1.15$, the loosen material flow is defined in a narrow vertical region.

The second study consists of the analysis of the opening size variation for the outlet on the discharge of the silo. From the previous set of examples, it is identified a strong influence on the flow type due to the internal friction coefficient; even though, it is indispensable to study the dependency of the flow as the dimensions of the outlet are modified. The study analyses the flow patterns during discharge for three different outlet sizes and constraining the value of the internal friction coefficient with the reference example $b_1 = 1.00$. The radiuses to explore, for a full-circular section outlet, are: 170mm, 240mm, and 310mm –the outlet radius used in the reference example shown in the previous section is 240mm, and its corresponding flow patterns were plotted in Figure 5-9.

Figure 5-10 compares the variation of the level markers as a function of the flow type for the remaining two radiuses at $1m^3$, $5m^3$, $10m^3$, $15m^3$, and $20m^3$. The continuous blue line denotes the evolution of the seven levels of markers, and the dotted red lines are used, as in previous figure, as a reference for the height of the second and fourth levels. It is observed that, for both discharges, the predominant flow is of the funnel type. Even though, the patterns show a variation on the definition of the stagnant zones and the flow region on the silo.

Figure 5-10(a) shows the evolution of levels for the markers for the smallest radius used; the flow patterns show a broader stagnant zone than for larger radiuses, see Figure 5-9(c) and Figure 5-10(b) for $R = 240\ mm$ and $R = 310\ mm$ respectively. The flow region is defined by a vertical narrow zone located at the centre of the silo; although, it is observed a delay on the discharge of the upper levels – the material on these levels remains inside the silo after $20m^3$ of material discharged.

The largest radius of the outlet shows, likewise, a semi-mass flow discharge. In contrast with the smaller outlets, the core of the funnel flow spreads toward the walls on the upper levels of the silo. This reduction of the stagnant zone on the upper levels appears even at the first stages of the discharge ($1m^3$ and $5m^3$ of discharged material in Figure 5-10(b)).

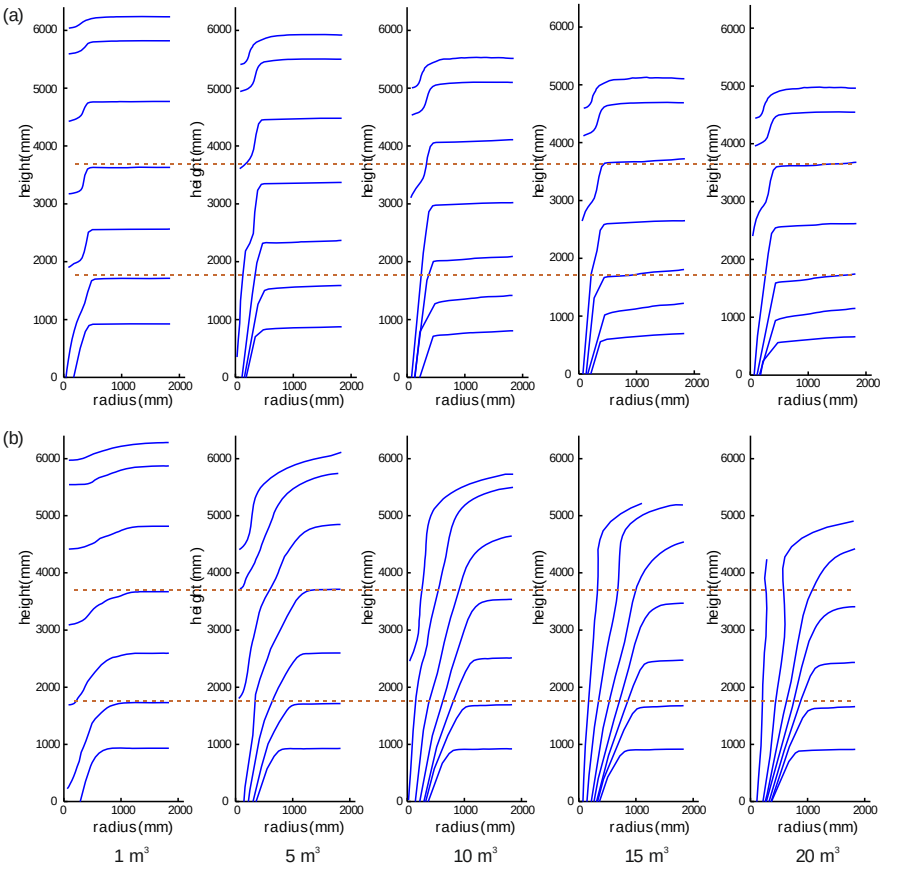

Figure 5-10. Variation of level markers during material discharge – $1m^3$, $5m^3$, $10m^3$, $15m^3$, and $20m^3$ – for different outlet radius: (a) $R = 170\ mm$, (b) $R = 310\ mm$.

5.1.3.3. Velocities field during silo discharge

Velocity fields on the silo are information required to determine design parameters as the residence time distribution, mixing properties of the material, and the rate of wall wear [75]. Numerical simulations allow processing the data accordingly to understand different features of the phenomenon. In this section, the velocity contours obtained for different amounts of material discharged and the maximum velocities obtained during the whole process are discussed.

Plotting the contours of the velocity field is an alternative procedure to understand the discharge mechanisms on a silo. In this context, the contours corresponding to different volumes of discharged material, internal friction coefficient $b_1 = 1.00$ and an outlet radius $R = 170\ mm$, are shown in Figure 5-11. It is observed that the funnel flow develops since the first cubic meters of material are discharged.

Accordingly to the flow zones proposed by Brown and Hawksley [75], Figure 5-1, the flow is characterized mainly by a stagnant zone (described by a relative null velocity of the material) and a vertical motion presented by the whole material located above the outlet. As it is expected, the maximum velocities are present on the outlet region; it is considered a zone of loose material where its motion is conditioned through a free fall, where friction between particles is almost neglected.

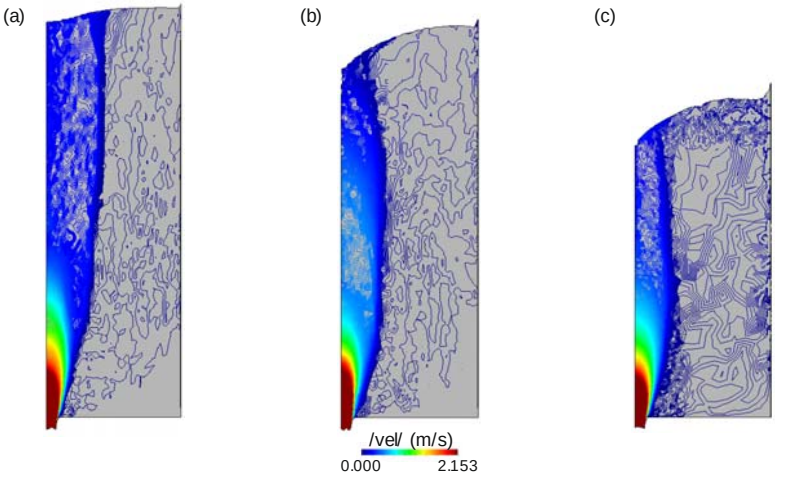

Figure 5-11. Velocity contours for material with internal friction coefficient $b_1 = 1.00$ through an outlet with radius $R = 170\ mm$ for different amounts of material discharged: (a) $1m^3$, (b) $5m^3$, and (c) $20m^3$.

The transition between a stagnant zone and a flow zone is defined by the presence of a discontinuity on the velocities. This discontinuity is not necessary be coincident with a stress discontinuity since it could be present in a continuous stress field [75]. The term discontinuity for velocities is not as strict as for stresses; in terms of a velocity field, it is defined by a large velocity gradient over a small distance.

The discontinuity on the velocities field is shown in Figure 5-12 by means of horizontal cuts at different height levels for the same amounts of material discharged presented in previous figure – $1m^3$, $5m^3$, and $20m^3$.

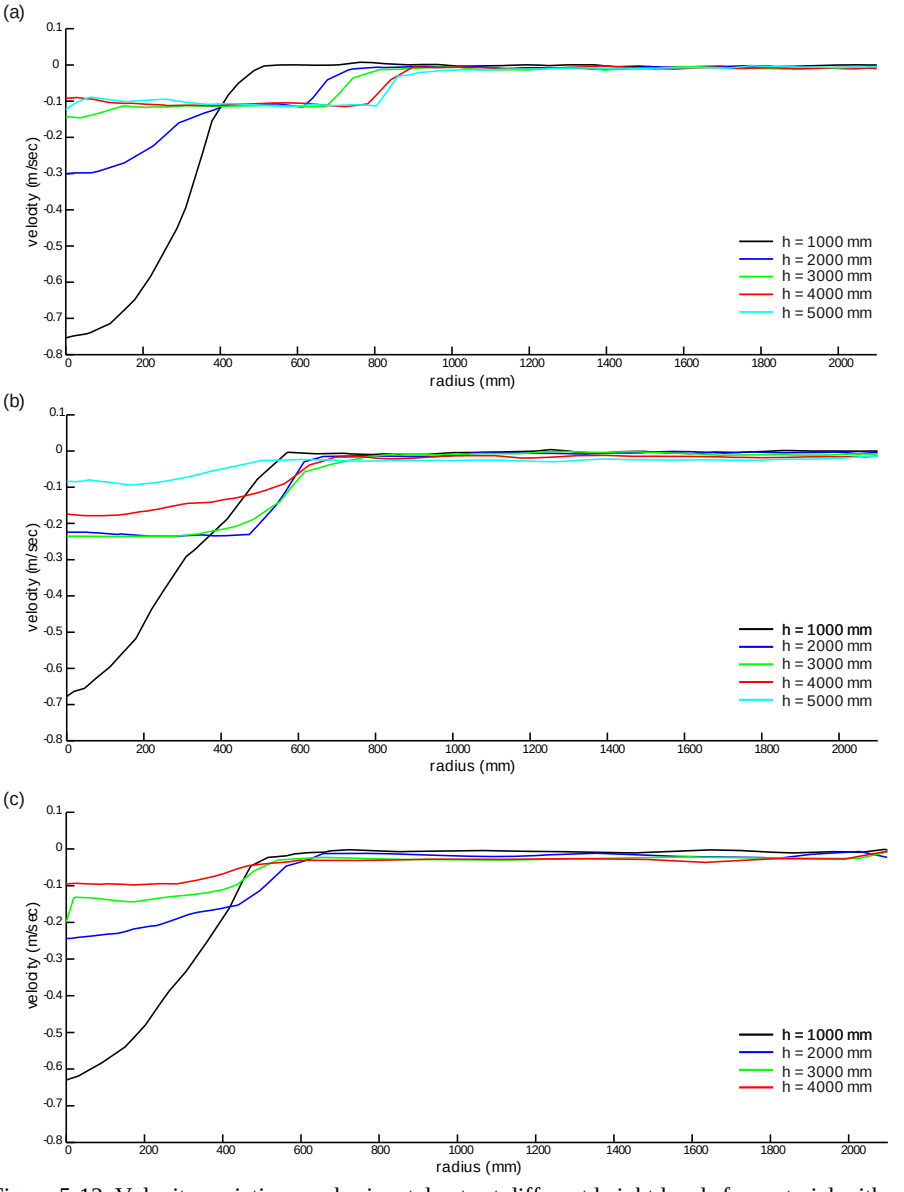

Figure 5-12. Velocity variations on horizontal cuts at different height levels for material with internal friction coefficient $b_1 = 1.00$ through an outlet with radius $R = 170\ mm$ for different amounts of material discharged: (a) $1m^3$, (b) $5m^3$, and (c) $20m^3$.

It is observed clearly, at the three stages of the discharge, how at the flow zone the velocities present a certain constant value, and then abruptly, changes toward the stagnant zone to a relative null value. In this transition, it is observed the narrow region that defines the discontinuity on the velocities field. For the first cubic meter of discharged material, Figure 5-12(a), the granular flow of the material close to the bottom of the silo presents a higher magnitude than for $5m^3$ and $20m^3$ of discharge; this is considered since it represent the transitory regime from the opening of the outlet. For $5m^3$ and $20m^3$ of material discharged, Figure 5-12(b) and Figure 5-12(c) respectively, this magnitude diminishes as well as the velocities on the upper levels increases. Likewise, the flow zone presents a narrowing of the section that defines the vertical motion of the granular material once the steady regime is reached – it narrows from a distance of 800 mm to 600 mm approximately.

Velocity fields supplement the understanding of the granular flow. It can be observed, from previous figures, that the discharge is characterized by a vertical sliding of a "rigid block" of material – nourished by the material from the upper levels – and that , after a certain distance from the outlet, the material is loosen and the particles gain velocity toward the outlet.

The maximum absolute velocities appearing during the whole discharge allow identifying the smoothness of the flow during the process. Figure 5-13 shows the comparison of the maximum velocities reached during the discharge of two models – for a material with internal friction angle $b_1 = 1.00$ and an outlet dimension $R = 170\ mm$ and $R = 240\ mm$ respectively. From those curves two main features are identified: the discharged of the material takes place in a steady state regime during the full process; and second, as it is expected, the maximum velocities on the material are increased as the silo's outlet radius is larger.

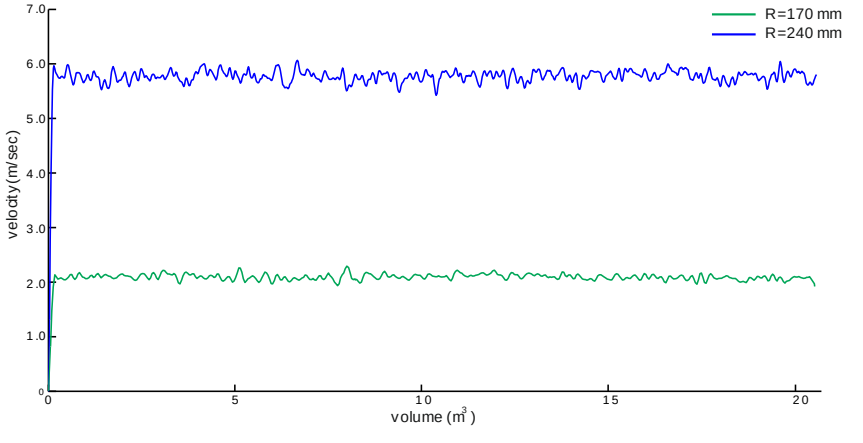

Figure 5-13. Maximum absolute velocities for a material with internal friction angle $b_1 = 1.00$ comparing two different outlets – $R = 170\ mm$ and $R = 240\ mm$.

5.1.3.4. Pressure distribution

Probably the most relevant result from the analysis is the pressure distribution acting on the silo wall. Unfortunately, wall pressures for this experimental test are not reported on the referenced technical report [89] since measurement difficulties appeared during the experiments. Nevertheless, numerical pressure distributions can be analysed from the previous validation campaign of the flow patterns.

It is expected that numerical pressures distribution differ from hydrostatic distributions in a static condition. These differences result due to the influence of the internal friction angle and wall friction, which the last, gradually transfers vertical loads into the walls.

Firstly, we reproduce numerically the hydrostatic analysis, in which the silo is hypothetical filled with water and the resulting numerical pressure is compared with the hydrostatic distribution. In order to reproduce the mechanical behaviour of the fluid by means of our constitutive model, the internal friction coefficient of the material was set to zero, $b_1 = 0.00$.

Figure 5-14(a) shows the wall pressure distribution for different bulk modulus compared with the hydrostatic pressure distribution. The difference between the curves is a consequence of the compressibility of the elastic part of the model; the theoretical hydrostatic pressure is recovered when the bulk modulus is increased, defined by the continuous black line in Figure 5-14 (a).

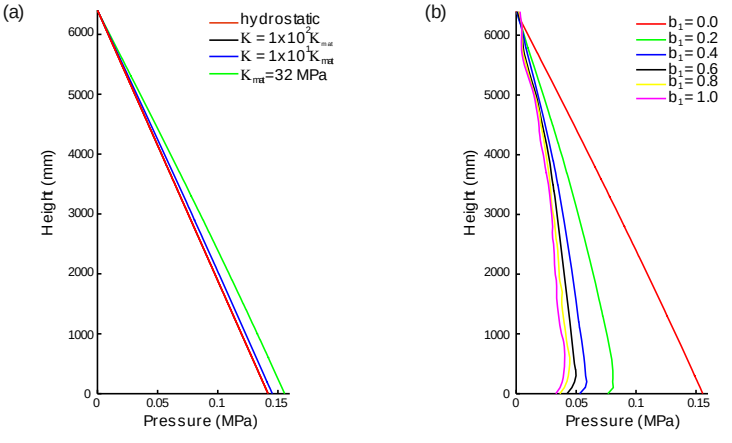

Figure 5-14. Wall pressures when material confined: (a) wall pressure distribution for different bulk modulus compared with the hydrostatic pressure; (b) variation of pressure distributions on the silo's wall for different internal friction coefficients.

Our concern now is to examine the response of the numerical results when the internal friction coefficient is increased. These results are shown in Figure 5-14(b). It is observed that the maximum pressures on the wall are reached for hydrostatic pressures – null internal friction angle; once the material recovers the friction be-

tween particles, a redistribution of the pressures takes place, reducing the pressure exerted on the walls as the internal friction angle increases.

Likewise, the pressures reached on the silo's wall and the granular material depend on the geometry of the problem itself; Figure 5-15 presents these pressures distributions for different volumes of material discharged using two different opening size on their outlets – $R = 170\ mm$ and $R = 170\ mm$. Figure 5-15(a.1) shows the pressure evolution on the material for the smallest radius, $R = 170\ mm$; it is observed that the stresses fields suffer a redistribution when the material is released. The pressures on the material located at the wall are increased up to 50% just as the outlet is opened – as it is displayed by the variations on the values for a material confined and at $1m^3$ of material discharged. In contrast with the material pressures, the wall pressures do not suffer a substantial increment when the material is released, see Figure 5-15(a.2). In this case, the radial stress is incremented at the bottom of the silo and reduced almost linearly toward its upper level.

For both properties, material pressure and wall pressure, the maximum values are present at the bottom of the silo. During the discharge, pressures along the wall are reduced, since there is a lower amount of material inside the silo, but the maximum values at the bottom remain constant. This monotonic behaviour is expected, since it corresponds to a concentric discharge – maximum values for the highest amount of material in the silo, which decrease as it is discharged.

The evolution of the stresses during the material discharge is similar for the outlet of radius $R = 240\ mm$. Figure 5-15(b.1) shows the material pressures for different amounts of discharge; the comparison with those obtained with the smaller outlet shows that the mechanical response of the material is similar, presenting an increment up to 50% of the magnitude on the pressures at the bottom once the outlet is opened. The difference on the pressure redistribution between both outlets size cases is that, for the wider opening, the level of pressures on the material near the wall maintains the same magnitude – almost for the two first meters from the bottom of the material.

The pressures exerted by the material on the wall, for different volumes of discharge, are shown in Figure 5-15(b.2). The evolution of the pressures shows the same behaviour than for the smaller outlet, being the only difference a slightly increment on the magnitude of the pressures. Since the wall pressures for both discharges show a similar response, it is expected that the increment on the material pressures be caused by a redistribution of the gravitational loads of the material.

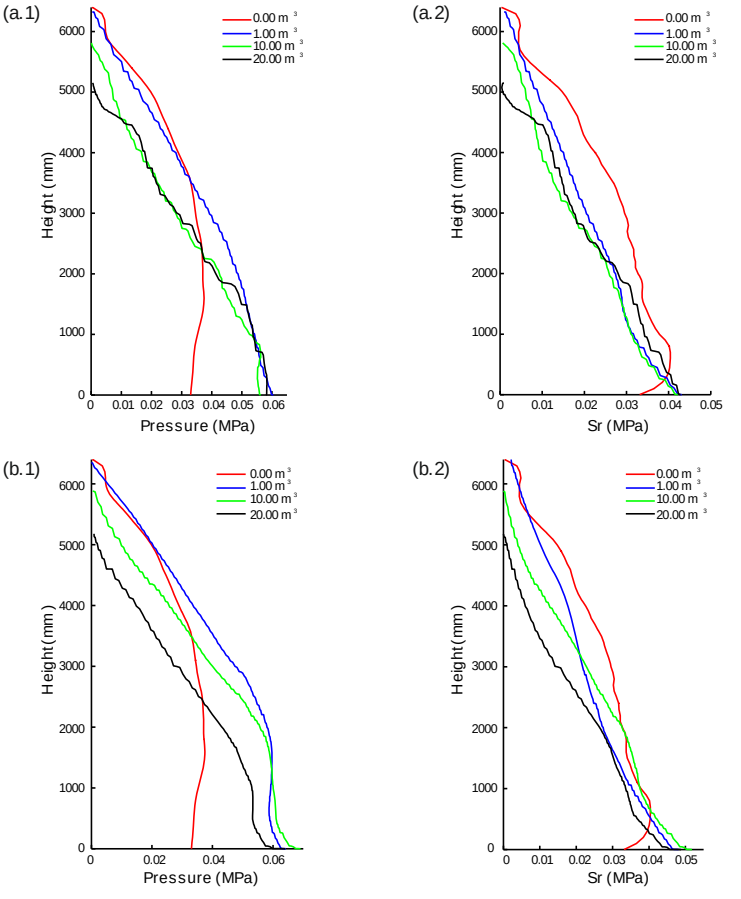

Figure 5-15. Evolution of pressures distributions during the discharge of a: (a) Silo with an outlet of $R = 170\ mm$: (b) Silo with an outlet of $R = 240\ mm$. It is displayed first the material pressures, then wall pressures exerted by the material.

5.2. Tumbling mills modelling

This section focuses on the numerical simulations of granular material in a tumbling mill. The model capability to simulate tumbling processes is verified via the numerical simulation of the experimental test of a rotational drum conducted by [94]. The experimental model was proposed to study the power required to set and keep in motion a charge composed of dry sand; for the numerical simulations, the power

draw is also computed and validated against the experimental data, in which the power is plotted in terms of the rotational speed of the drum.

The following sections are divided as follows: first, it is given some basic concepts about the behaviour of the charge in tumbling mills; thereafter, it is described the experimental setup reported by [94]. Finally, the comparison of the curves corresponding to the torque and power required for the system are given.

5.2.1. A brief description of the charge in a tumbling mill

Comminution of the material consumes 50% of the total mineral processing cost [17]. Studies have found that the grinding of granular material in tumbling mills are inefficient, since large amount of energy is wasted due to the impact of the material does not shred the granular particles [99]. The study of charge motion during the milling process allows us to understand how energy is consumed and which efforts could be done in order to optimize the operating conditions of the drum.

Due to the large amount of energy required for the comminution of the material, it is necessary to optimize the operating conditions of the process. As may be surmised, this optimization task is a rather difficult one, mainly because material behaviour within the drum is poorly understood, being hard to establish the milling internal dynamics. Different techniques have been proposed in order to monitor the performance of a tumbling mill. Among them are found: the use of mill noise and mill vibrations, to measure the degree of filling [92], the force exerted by the material on the lifters [99], and the power readings during the grinding process, in order to interpret the filling degree of the material [17].

Measuring the driving torque and relate it to the process by numerical models can be one possible way to validate, control, and optimise the grinding system. Since the numerical model herein presented is developed in the framework of continuum mechanics, it is straightforward the calculation of the system energy, via the balance equations, for its validation with experimental results.

It is important to have in mind the complex nature of the milling process when creating models, to decrease the gap between model and reality, more physically precise models are necessary. Measurements are important for improving the milling efficiency and gaining more understanding of the process itself. A step towards a more physically correct numerical description of mill systems was the combined DEM-FEM model presented by [53]. With the DEM-FEM, model forces and mechanical waves, as well as structural responses and their influence on the charge motion can be studied. The model gives the opportunity to optimize the material selection of the mill structure. In the work by [52], a combined SPH-FEM model was used in simulations of tumbling mill processes.

The *PFEM* is a numerical tool with the potential to track the positions of the particles inside the drum due to its robustness for large deformation problems. Despite the material during the tumbling process is not considered as a *dense granular medium* and neither its kinematics corresponds to *slow granular flows* – since the large velocities during the process and the spreading and collisions of the particles –

the numerical simulation, presented in the following sections, allows us to validate the model in terms of the power required to set and keep in motion the full system.

5.2.2. Experimental measurement of power consumption for a tumbling mill – experimental setup

The model capability to simulate tumbling processes is verified comparing with the experimental test reported by [94]. The experiment consists of the measurement of the power consumption during the comminution of a mill charge, varying the granular mass and the rotational velocity of the drum.

The measurements were conducted on a laboratory scaled ball mill. The scaled model has an inner diameter $\phi_i = 284\ mm$ and a depth $l = 441\ mm$; the displacement of the charge is controlled by eight semicircular bumps of diameter $\phi_b = 25\ mm$ spaced uniformly as *lifters*. The charge consists of dry sand of density about $2500 kg/m^3$ and porosity around 33%. Figure 5-16 shows the drum dimension as well as the placement of the lifters.

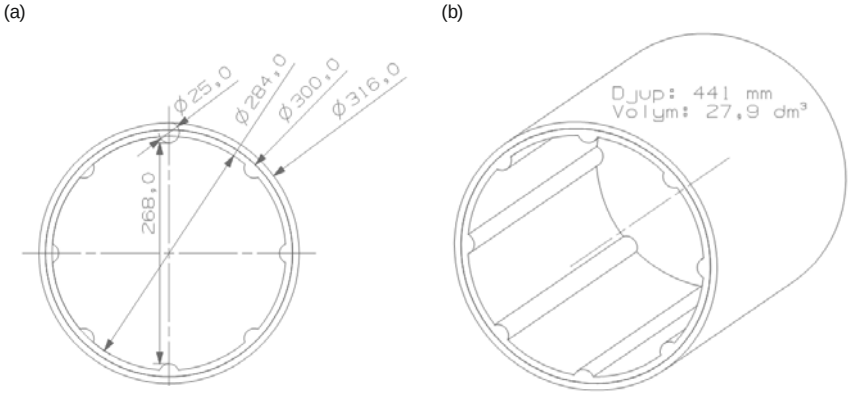

Figure 5-16. Scaled model of a tumbling ball mill, all measures in mm: (a) Front view, (b) Model depth [94].

The computation of the power is given in terms of the torque applied to the drum and its angular speed. The torque was measured as the reaction force applied on a load cell at a given distance from the rotation centre, and the average rotational speed of the system was obtained measuring the number of revolutions during a long period. Due to the impulsive nature of the charge, it is convenient to measure the average torque and angular speed, to define a relatively invariant measure of the required power [16].

The rotational speed at which the drum was subjected to, is defined in terms of a critical speed of the system, given by the following equation [94]:

$$\omega_{\text{crit}} = 60\frac{\sqrt{g/r_i}}{2\pi} \tag{5.1}$$

where g is the gravitational constant, r_i the inner radius, and ω_{crit} the speed, given in rpm. Figure 5-17 shows the averaged measured power for the system correlated to the degree of filling of the drum and its critical speed.

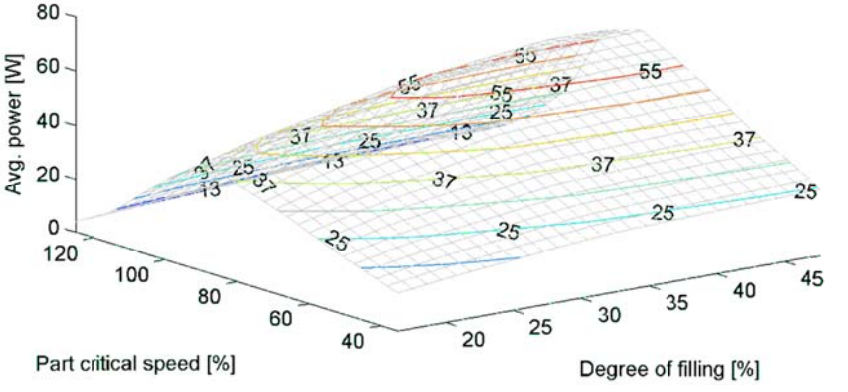

Figure 5-17. Averaged power measured on dry sand [94].

5.2.3. Numerical simulation of a tumbling mill

As mentioned before, the proposed constitutive model is in principle only suited for representing *dry dense granular materials*. In the present example of a tumbling mill, the drum reaches relatively high rotational speeds and the granular particles tend to separate from each other. The assumption of dense flow, thus, is not strictly valid in the context of this example, and therefore, an accurate representation of the motion of the material within the drum cannot be expected. However, our interest does not lay on an accurate simulation of such local details, but rather on examining the *overall* behaviour of the system in terms of the *mechanical power* required to maintain the tumbling process.

Accordingly, numerical and experimental torque values will be compared for three different rotational speeds – 35%, 65%, and 95% of the system critical speed. The smallest rotational speed will be used to calibrate the internal friction coefficient and the relaxation time, b_1 and τ_R respectively, while the other two cases will be used for the model validation.

The degree of filling selected of the drum is 35%. The geometry of the model corresponds directly to the experimental setup using an internal diameter of $\phi_i = 284\ mm$, and eight semi-circular bumps of diameter $\phi_b = 25\ mm$ as the lifters

of the mill. The experimental drum is modelled using a two-dimensional plain-strain state of depth $l = 441\ mm$.

The initial spatial discretization has approximately 2250 nodes and 4500 linear triangular elements. As regards time discretization, time steps of $\Delta t = 1/10000\,\text{sec.}$ are used. The granular material/mill structure plate interaction is modelled with the same algorithm used for the silo example; in this case the wall friction coefficient is set to the same value than in the bulk domain.

As for the material properties of the granular material, the internal friction coefficient and the wall friction coefficient is set to $b_1 = 0.30$, and the cohesion parameter to $b_2 = 0.01Pa$ – a relatively small value of cohesion just to ensure numerical stability via the von Mises regularization earlier described. Likewise, the employed bulk and shear modulus are $\kappa = 32\ \text{MPa}$ and $G = 7\ \text{MPa}$, respectively. The viscoplastic regularization is a function of the relaxation time τ_R; for these tests, the relaxation time is $\tau_R = 5\times10^{-6}\ \text{sec}$.

5.2.3.1. Torque comparison

In order to calculate the power required by the mill to keep its rotational speed, the balance of the mechanical energy of the system is used. This balance states that the sum of the rate of change of the kinetic energy κ_e and the rate of the internal mechanical work $\mathcal{P}_{\text{int}}$ of a continuum is equal to the rate of external mechanical work $\mathcal{P}_{\text{ext}}$ [42], as given by the following equation

$$\frac{D}{Dt}\kappa_e(t) + \mathcal{P}_{\text{int}}(t) = \mathcal{P}_{\text{ext}}(t) \qquad (5.2)$$

Since the kinetic energy is a function of the velocity field and the internal mechanical work is a function of the stress field, it is fundamental to obtain a smooth response of those fields. The velocity contours, shown in Figure 5-18, determine the kinematic response of the charge while the drum rotates. This velocities distribution presents the same pattern in the transient and stationary regime, varying the magnitudes reached in each stage.

The motion of the charge is defined by an overturn of the material from the wall toward the centre, where the larger velocities show up at the outer region of the material and relative null velocities are located on the core of the material. A relevant difference between the transient and stationary regimes is that, on its acceleration stage, the material presents a higher degree of consolidation, see Figure 5-18(a). Instead, when the material reaches the stationary regime, Figure 5-18(b), it is observed that the material experiences a relaxation.

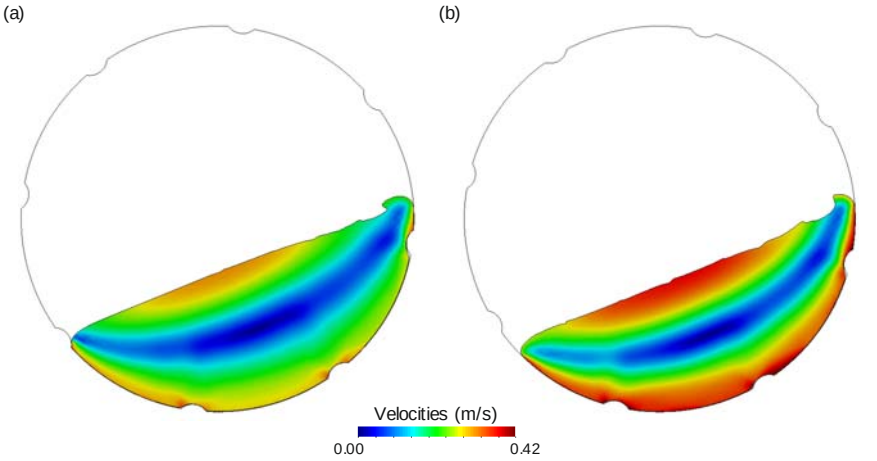

Figure 5-18. Velocity contours for the granular flow (m/s) at a rotational speed of 35% of critical speed: (a) transitory regime, acceleration process, (b) stationary regime, after two revolutions.

Pressure contours are displayed in Figure 5-19. It is worth noting that computed pressures are relatively smooth, a fact that indicates that the used mixed formulation is fulfilling the purpose of overcoming the deleterious effects of volumetric locking. Likewise, it can be observed that pressures in the tensile regime are, at least, one order of magnitude smaller than those in the compressive regime. The contours indicate that the maximum compressive pressures are given on the charge propelled by the bump or lifter, and that, after the material overpass the bump, a region of loose material is formed presenting small or null compressive pressures, see Figure 5-19(b).

The torque obtained from the numerical simulations is computed using the internal power defined in equation (5.2), and the rotational speed of the system. The experimental torque data reported corresponds to a full revolution in its steady state. Therefore, in order to compare with numerical simulations, it is required to measure the torque in a steady state. The loading conditions for the tumbling mill are defined by an acceleration period of two seconds until the rotational speed is reached; thereafter, it is set a complete revolution to reach the steady regime at the second revolution with constant velocity, which is the one to be compared.

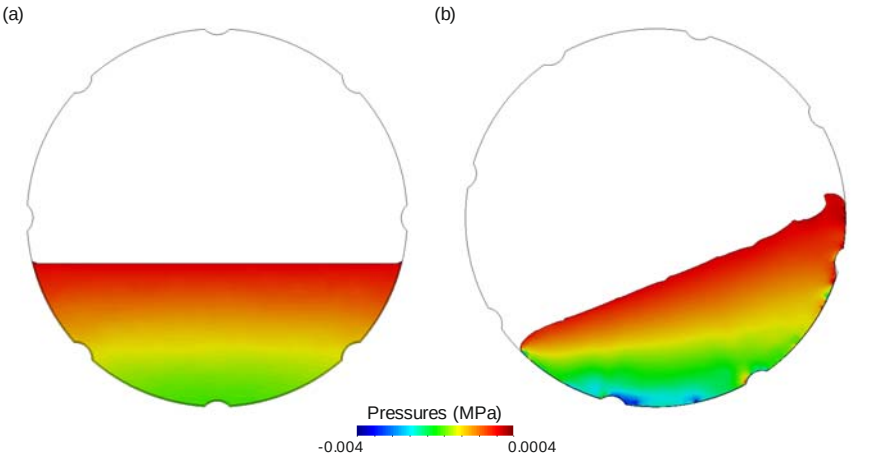

Figure 5-19. Pressure distribution on the material (MPa): (a) material at rest, (b) material on stationary regime after two revolutions at constant velocity.

Figure 5-20 shows the evolution of the torque curve of the numerical simulation, for a rotational speed at 35% of the critical speed, during the three loading stages – an acceleration period of two seconds, a revolution considered on transient regime, and the stationary regime reached at the second revolution.

The maximum value of the torque is reached at the transition between the acceleration stage and the condition of constant rotational speed. It is observed a slight diminution of the torque value on the first revolution; this is due to the relaxation that the material suffers until it reaches its steady state.

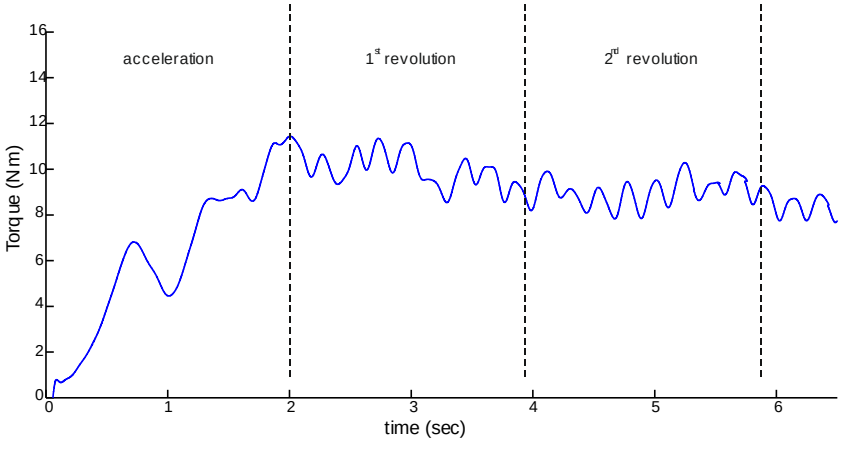

Figure 5-20. Torque evolution – transient and stationary response.

Comparison between experimental and numerical torque for different rotational speeds is shown in Figure 5-21. For the experimental data, a continuous red line is used and the experimental values are denoted by a red mark; on the other hand, numerical values are represented by a continuous black line. The comparison shows the values for a full revolution of the drum and the motion is considered in a steady state; for the numerical simulations it is used the information obtained after the second revolution at constant velocity.

Figure 5-21(a) shows the torque comparison for a rotational speed corresponding to 35% of the system's critical speed, which is the one used for calibration purposes. While a reasonable overall agreement is achieved in terms of a mean response, discrepancies are detected in the oscillating pattern around this mean value. Indeed, experimental torque oscillates more abruptly, and at a higher frequency, than its numerical counterpart does. It can be easily shown that the period of the oscillations in the numerical results is related with the circumferential spacing of the bumps in the drum.

The comparison with experimental data for higher velocities presents the same behavior than in the above commented reference example. Figure 5-21(b) shows the comparison for a rotational speed at 65% of the critical speed. The torque presents, as in the previous example, an oscillatory response that corresponds to the interaction of the material with the bumps of the drum. It is remarked that the amplitude of the oscillations in the computed results are notably higher than in the previous case, attributed for the increment of the rotational speed.

Lastly, the torque for a rotational speed of 95% is given in Figure 5-21(c). The same oscillation pattern is observed, with a further increase in the amplitude. This fact confirms the influence of the rotational speed in the amplitude of the oscillations predicted by the numerical model. This influence, however, is not perceived in the experimental graphs (the amplitude in this case is, on average, similar in the three studied cases). Nevertheless, the model is able to capture with reasonable accuracy the mean torque in the three cases.

This is confirmed by the comparison of averaged power of the experimental data and the one obtained by numerical simulation for the three different rotational speeds, see Figure 5-22. As expected, the highest accuracy is observed for the lowest rotational speed, for this is the one used to calibrate the model. As the speed is increased, the deviation between experimental and numerical results increases, albeit it remains at moderate levels. In conclusion, despite the limitation of the model, the overall results in terms of power consumption can be deemed reasonably accurate.

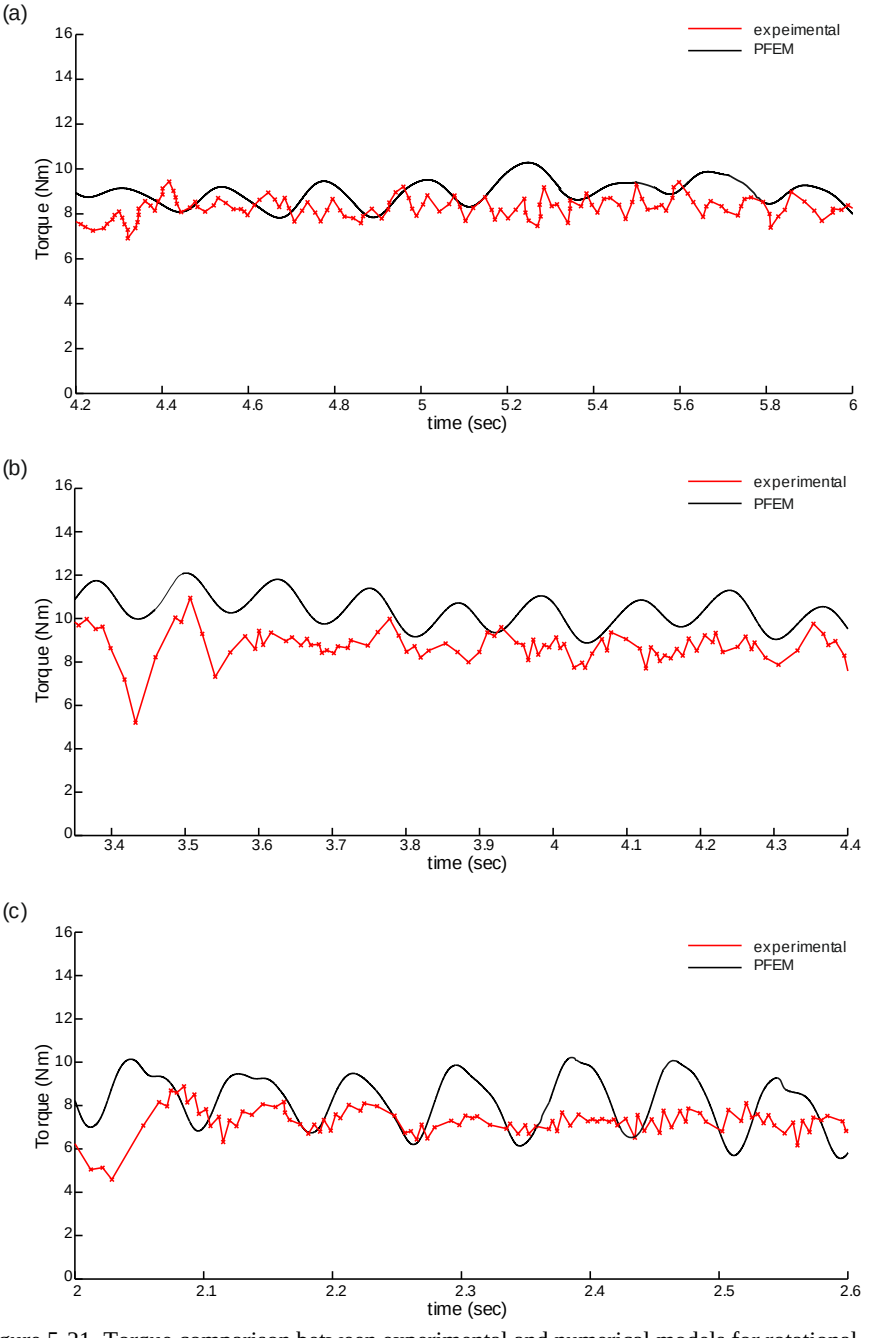

Figure 5-21. Torque comparison between experimental and numerical models for rotational speeds at: (a) 35% of critical speed – reference example, (b) 65% of critical speed, (c) 95% of critical speed.

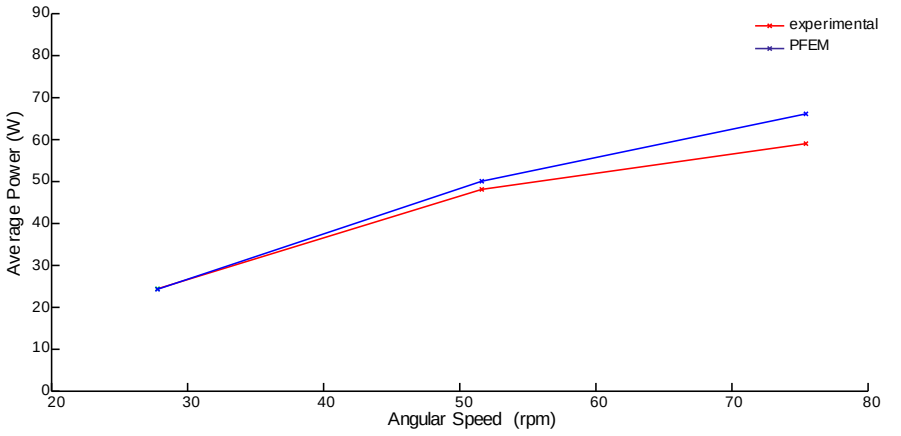

Figure 5-22. Average power comparison for the three different rotational speeds.

5.2.3.2. Inclusion of milling balls

Comminution of granular material within a rotating drum by crushing caused by the impact of steel balls is a problem of high interest for many industries – ceramics, composites, foods, minerals, paints, inks and pharmaceuticals, etc. As a first step towards the full simulation of this admittedly challenging problem, we explore in this example the possibilities of the proposed numerical model to capture, at least, the mechanical interaction between several (hard) bodies and dry sand; thus, crushing effects are not contemplated in the simulation.

The charge for the model is formed by the same charge volume than in previous examples, among sand and fifteen rods of two different diameters, namely 10 rods of $\phi_1 = 15mm$ and 5 rods of $\phi_2 = 10mm$, see Figure 5-23. The material and numerical parameters are the same of those given in the introduction of section 5.2.2.

Since there is no available experimental data for this simulation, the mechanical response of the charge for this example, including the steel rods, is compared with the numerical simulation defined previously as the reference example composed only by dry sand, Figure 5-21(a).

Figure 5-24(a) shows a snapshot of the pressure field in the stationary regime. The rods define local areas where the pressures present the maximum values – it is found on the material located between the rods and the drum wall and between the rods themselves.

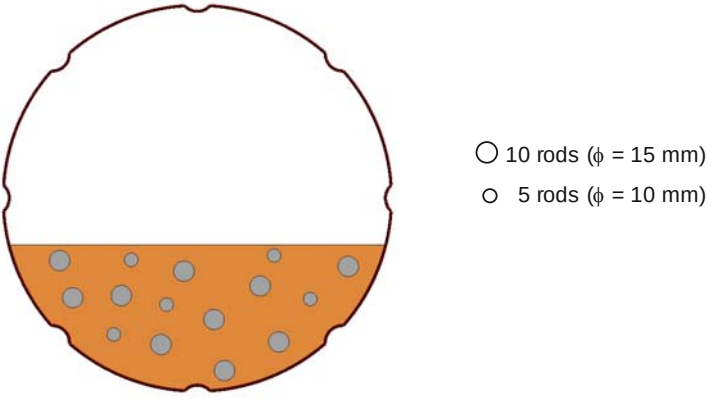

Figure 5-23. Numerical model of dry sand and steel rods for a tumbling ball mill.

The influence of the rods on the material is observed via the *plastic multiplier*. Since the model is formulated in the framework of plasticity, this parameter identifies the material in the plastic or elastic regime. For the charge conformed by dry sand, the plastic multiplier lies on the range of full plasticity while for the material interacting with the rods, zones where the material does not reach completely plasticity can be appreciated. Figure 5-24 (b), shows this concept by means of an elastic factor, defined herein as $\alpha = (1-\Delta\lambda)^{-1}$, where $\Delta\lambda$ denotes the plastic multiplier; $\alpha = 0$ stands for a full plasticity regime and $\alpha = 1$ for a full elastic regime.

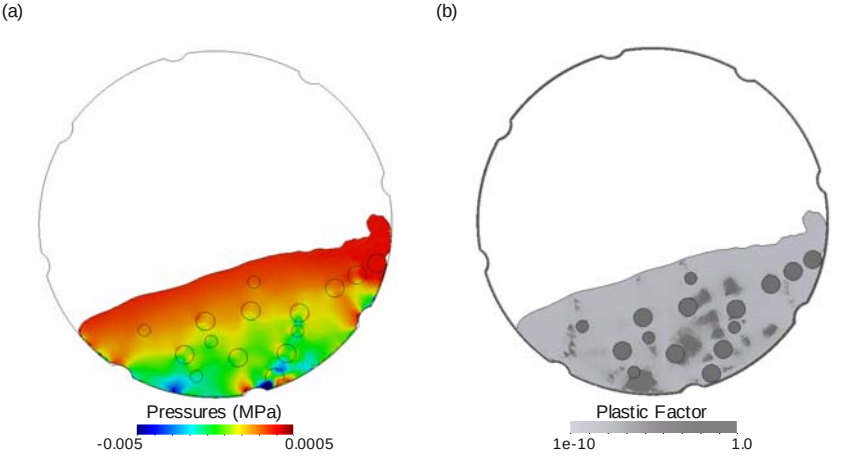

Figure 5-24. Mechanical variables in the charge during motion: (a) volumetric pressures in the material, (b) plastic multiplier.

Figure 5-25 shows the numerical comparison of both charges (with and without steel rods) for a degree of filling of the drum of 35% and using the referential rota-

tional speed of 35% of the critical speed. It may be observed that, as it could be expected, the torque of the charge with the steel rods increases significantly. Likewise, the torque in the case of dry sand with steel rods shows a higher degree of oscillations during the motion of the charge, a fact that may be attributable to the displacement and impact of the rods during the process.

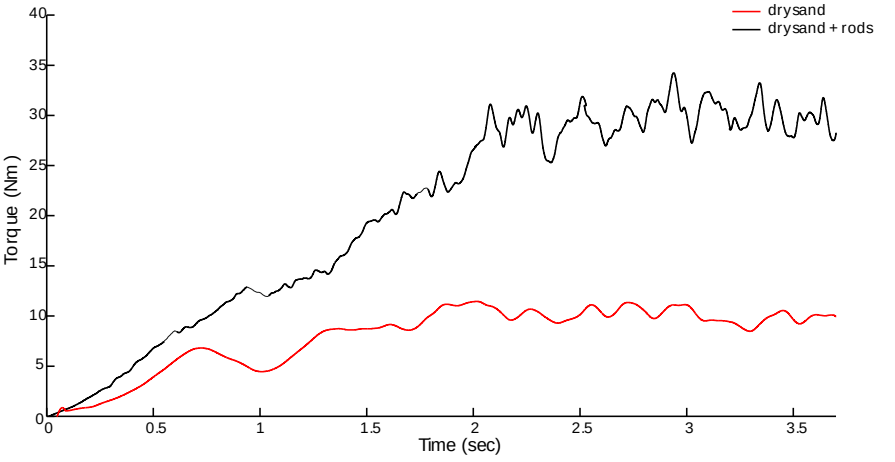

Figure 5-25. Torque comparison for a charge at 35% of degree of filling at 35% of the critical speed, with and without steel rods.

The magnitude of the torque could be only considered as correct when comparing with experimental data; even though, it is considered that its magnitude was increased significantly. This large increment is considered due to the modelling of the steel balls by the two-dimensional plane strain model. Some alternatives could be considered to characterize more precisely this response as reducing the density of the steel.

Chapter 6
Conclusions

In this chapter, the conclusions of this work as well as some final remarks are presented.

6.1. Concluding remarks

The overall goal of this work was to develop a numerical tool for the simulation of granular flows on industrial applications. A phenomenological approach was adopted to mathematically represent the kinematic behaviour of granular flows and to properly characterize stagnant and flow zones, as well as the jamming transition in the material. The scope of the proposed approach is limited to cohesionless materials and slow flows.

Simulations of two types of industrial processes, namely, silo discharge and motion of a charge in a tumbling mill, have illustrated the potential of the proposed constitutive model, in combination with the Particle Finite Element Method (*PFEM*), as a robust modelling tool, suitable to characterize *dry dense granular flows* in industrial processes.

On the modelling of granular materials

- Due to the phenomenological richness exhibited by granular materials, nowadays it is not possible to characterize their full response in a unified constitutive model, being of fundamental importance reducing the conditions to simulate, according to the phenomena under study, in order to define a reliable model.

- A continuum formulation within the framework of large deformation plasticity was proposed. The continuum approach allows us to capture variables such as pressures and velocity fields that other methods, such as the Discrete Element Method (*DEM*), are not always able to represent adequately.
- Due to the large deformations presented during granular flows, the *PFEM* algorithm is proposed as a robust methodology to simulate these conditions. Based on a Lagrangian formulation, this approach is able to characterize both transient and stationary conditions.
- The proposed constitutive model, based on a visco-elasto-plastic model, shows a good ability to predict the kinematic behaviour of dense granular flows. The elasto-plastic constitutive model characterizes the solid-like state, while the jamming transition and the non-dependence on the shear rate when flowing is given by the visco-plastic regularization.

Continuum description of dense granular flows

- The assumption of modelling *dry* or *cohesionless dense granular flows* through a continuum approach has been proved appropriate as long as the domain under study is larger enough than the particle size.
- The mechanical properties of cohesionless dense granular materials are governed by the frictional interaction between particles; in that sense, it is considered as a non-cohesive granular media when the interstitial fluid between particles is neglected. The definition of dense granular flows embraces those flowing conditions characterized by small velocities and deformations with no significant volumetric variations.
- The constitutive model was developed within the framework of large plastic/small elastic deformations through a hypoelastic model. To extend the model to scenarios in which large volumetric variations take place, it would be necessary to seek for alternative ways of formulating the elastic part of the model.
- In this work, for the tensile regime, the yield surface is regularized using a von Mises type model. This regularization has proven more robust and easier to implement than classic "cap" models. The impact of adopting this admittedly objectionable regularization – it presumes that the material can sustain a certain degree of tensile stresses – is minimal since the percentage of material of the domain in tensile stress state ranges from 0.4 to 5.17%, see Table 6-1.

  In the case of the examples corresponding to the spreading of a granular media on a horizontal plane, as it was expected, the percentage of material on stress states with positive pressures remained at low levels (around 0.4%) and only for the case with the larger initial aspect ratio, $a = 6.2$, this percentage increased up to 1.735%. The silo discharge example showed the smallest percentage of material (0.395%) since the only region on this stress state was toward the outlet. Finally, as discussed before, due to the large velocities present on the material, the tumbling mill example showed the larger percentage; still, it is observed that for the reference example (a rotational speed

of 35% of the critical speed), this percentage is less than 2% of the total material. From these examples, it is concluded that the regularization of the apex of the Drucker-Prager yield surface with an extension of a von Mises model (which, recall, was introduced to increase the robustness of the integration scheme) does not have a significant impact on the physical consistency of numerical predictions due to the small amount of material undergoing tensile stresses.

Example	$V(p>0)/V_{\text{tot}} \times 100$
Spreading $a = 0.41$	0.418
Spreading $a = 1.91$	0.402
Spreading $a = 6.2$	1.735
Silo, $R_{out} = 170mm$	0.395
Mill, $V_{mill} = 35\%V_{cr}$	1.818
Mill, $V_{mill} = 65\%V_{cr}$	3.837
Mill, $V_{mill} = 95\%V_{cr}$	5.171

Table 6-1. Percentage of total volume in a stress state with positive pressures of representative examples presented in this document.

- Due to the nearly incompressible behaviour exhibit by dense granular flows, the description of the deformation via a solely deviatoric non-associative plastic potential is proposed. In addition, it has been shown that the proposed model satisfies the dissipation inequality.

Numerical formulation

The modelling of granular flows deals with large displacements and deformations of the material; for this reason, it was necessary to define an algorithm, robust enough, to perform these simulations. For this work, it was necessary to establish and couple different numerical, in order to achieve efficient and robust performance in the simulations.

- The implementation of the *Impl-Ex* scheme for the numerical integration of the model increased the robustness compared with a typical implicit integration scheme. The explicit extrapolation of the plastic slip rate $\Delta\lambda$ has greater impact at those stress states located toward the apex of the Drucker-Prager yield surface, in where, a typical implicit scheme is in general undetermined.
- The continuous particle discretization of the domain allowed us to control the mesh homogeneity by inserting and removing particles as required as well as

repositioning them through geometric metrics. Likewise, this dynamic discretization allowed us to define non-uniform meshes – as those described for the silo discharge in the previous chapter– whereas for computational efficiency, it was necessary to define a finer mesh, where large strains are present, and at the same time a coarse mesh where the material is stagnant and no significant variations are presented.

- Due to the reconnecting process that involves classic *PFEM*, the definition of the boundary through the α-shape method has been seen as the natural algorithm for its construction; however, we consider that this method (without further refinement) leads to inconsistencies in the conservation of mass and to the presence of pressure instabilities. The definition of a constraint boundary, as a material surface, circumvents these drawbacks. The algorithm for this treatment of the free boundary does not represent an additional effort since the remeshing process, described in Chapter 4, embraces many of the tasks necessary to its definition.
- The other modification proposed to classic *PFEM* is associated to the transference of the internal variables information between the converged mesh and the one after the remeshing. Due to large variation in the position and the number of particles between meshes, it is found that the transference through mesh projection is more suitable in terms of computational cost – in the processes of insertion and removal of particles the standard nodal smoothing process could be executed but for the repositioning of particles a local search has to be done in order to interpolate the nodal information.
- The solid-granular material interaction is modelled by a proposal for a contact method based on the Contact Domain Method (*CDM*) [77]. The contact interface is defined in terms of a tolerance gap and its construction is given in a natural manner from the reconnecting process that naturally takes place in the *PFEM*. A significant contribution for this contact methodology has been to define the constitutive model for the interface domain similarly than the proposed for the granular flows presented in equation (3.23). This constitutive equation has proved sufficient to model properly the wall friction angle – a fundamental parameter to model granular flows. This approach entails an easier implementation and more robust algorithm than the classic *CDM*.
- In contrast to classic *PFEM*, which defines the contact conditions for the solid/granular material interaction in terms of the geometric α-shape method, in this approach, the contact conditions are ensured via a tolerance gap (for the impenetrability condition) and the detachment by the component normal to the surface in a tensile regime.

Numerical simulations – validations and industrial applications

Due to the vast typology of the kinematics of granular materials, it is a hard task to find experimental tests that present significant information about their behaviour. The tests reported in Ref. [62] are taken to calibrate and validate our numerical model. For the simulations of the two industrial applications, shown in previous

chapter, experimental tests conducted with the aim to study the flow patterns and the power consumption, for the silo discharge and the tumbling mill respectively, were compared.

Spreading of a granular media on a horizontal plane

- The experimental test reported by [62] shows a proper manner to calibrate and validate our numerical model, but also it is identified as a reliable guide to calibrate materials for others problems – as the iron ore pellets for the silo discharge and the sand in the tumbling mill – where the material parameters are not totally clarified.
- It has been shown that the numerical model proposed in this work is able to capture two fundamental observations reported in the experimental tests in Ref. [62], namely, that the deposit profile is independent of the mass M, being only a function of the initial aspect ratio a; and that the interaction with the substrate does not affect the behaviour of the collapsing pile (it only affects for very large initial aspect ratios).
- A discrepancy with the tests described in Ref. [62] is that of the velocity for the removal of the cylinder. Ref. [62] states that the removal of the cylinder is given in a period of time smaller than the critical time – measured in terms of the cylinder pile height. Yet, it was found, via numerical simulations, that the removal of the cylinder actually takes longer than this critical time. It was also found that, although the velocity of removal affects the transient response, its influence of the final shape of the deposit profile is negligible.
- Numerical simulations allowed us to understand more in depth the inner mechanisms that are present during the flow of granular materials. Using the elastic factor $\alpha(\Delta\lambda)$, it was possible to discern which regions are in the elastic regime and which undergo plastic deformations (flow zones).
- The oscillations given on the pressures and vertical stresses, measured at the bottom of confined material, presented a barely perceptible dissipation along time. The visco-elastic regularization, based on a Kelvin-Voigt model, succeed in dissipating the spurious oscillations due to dynamic effect.

Silo discharge modelling

- Flow patterns given for a concentric discharge of iron ore pellets were compared with experimental results. The resemblance between experimental and numerical results in most stages of the discharge can be deemed acceptable from an engineering point of view.
- Simulation varying material parameters and the opening of the outlet allowed us to acquire a firmer grasp on the flow mechanisms that take place during the silo discharge. The internal friction coefficient affects directly the definition of a mass or a funnel flow; for small values, the mass flow dominates while for larger values, funnel flow takes place.
- Even though the type of flow is essentially a function of the internal friction parameter, it has been observed that the opening of the outlet also plays a fundamental role in this respect. The spreading of the core of the funnel flow

is smaller as long as the opening of the outlet remains small; for larger openings, the funnel tends to open toward the walls at the upper levels of the material.

- Although wall pressures could not be compared with experimental results, since they were not reported for this problem, it was possible to state a good agreement of the bulk pressure provided by the model and the theoretical hydrostatic pressures on a fluid. Once the flow patterns were validated, it was possible to determine the bulk pressures and the stresses exerted by the material on the walls.
- It is taken for granted that the concentric discharge is not a limit case when studying the silos discharge. From the previous examples it was corroborated that the maximum pressures are given once the material is released and the pressures suffer redistribution, showing a monotonic behaviour at reducing the magnitude of the pressures. However, it was not the scope of this work to study of the silo's structure while discharging but to explore the performance of the numerical tool for modelling this problem.

Tumbling mills modelling

- Tumbling mill processes involve, in general, rapid granular flows, which are not in principle full candidates to be modelled by the considered model – in principle, it is only suited for representing *dry dense granular materials*. In spite of this fact, the numerical model was tested in order to explore the system response in terms of the energy balance and also in order to characterize the tumbling mill process. The predictions furnished by the proposed numerical model showed a well agreement with experimental [94] results when examining the overall behaviour of the system in terms of the mechanical power required to maintain the tumbling process.
- In Ref. [94] , the experimental model was proposed to study the power required to set and keep in motion a charge composed of dry sand; for the numerical simulations, the power draw was computed through the energy balance equation. The computation of the power was given in terms of the torque applied to the drum and its angular speed.
- For this example, the calibration of the model was obtained comparing the averaged torque of the experimental tests for the smaller rotational speed at a certain volume filling of the drum. As the speed was increased, the deviation between experimental and numerical results increased, albeit it remains at moderate levels. In conclusion, despite the limitation of the model, the overall results in terms of power consumption can be deemed reasonably accurate. The comparison of the consumption of the power of the system shows a higher degree of accuracy for lower rotational speeds, which indicates that the simulations for large rotational speeds could be improved by enriching the constitutive model with some means to represent rapid granular flows.
- Numerical results (which incidentally, showed a smoother response than the experimentally reported behaviour) allowed us to examine the influence of

the lifters on the oscillations of the torque. These oscillations presented an increase of their magnitude as the rotational speed increases.

- The *PFEM* showed to be a powerful numerical tool to perform multi-body simulations such as the inclusion of steel balls in the charge of the tumbling mill. The magnitude of the torque for the same amount of material and same rotational speed was compared for the case of the charge with and without the steel rods. The magnitude of the torque showed a substantial increment, which could not be validated since the lack of experimental data for this example. This large increment may be due to the fact that the modelling of the steel balls is carried out in a two-dimensional plane strain model. Some alternatives could be considered to characterize more precisely this response as reducing the density of the steel.

Appendix A
PFEM remeshing enhancement

The reconnecting process of the Particle Finite Element Method (*PFEM*) allows handling large deformation problems in a Lagrangian or material description due to its inherent reconnecting process. Despite this advantage, the constraining of a finite number of particles for characterizing the domain entails in some problems, a remaining distortion and non-uniformity for the mesh.

The remeshing process, herein described, has been proved to enhance the solution in terms of a more uniform distribution of the particles. As mentioned in Section 3.1.2, the procedure of the algorithm consists in three main steps: the insertion, removal, and collapsing of particles.

A.1. Insertion of particles

The insertion of particles is proposed for those elements in which the connecting nodes tend to disperse, increasing the corresponding area. The algorithm is controlled by an algebraic metric for the size of the elements. The relative size metric τ^{size} determines those elements unusually large with respect a reference element. The metric is given by the ratio of the area of the physical triangle α to the area of the reference triangle w.

$$\tau^{size} = \alpha / w \tag{A-1}$$

For those elements with $\tau^{size} > \tau^{ins}_{tol}$, it is inserted a new particle in the element's centre of mass, as shown in Figure A-1(a).

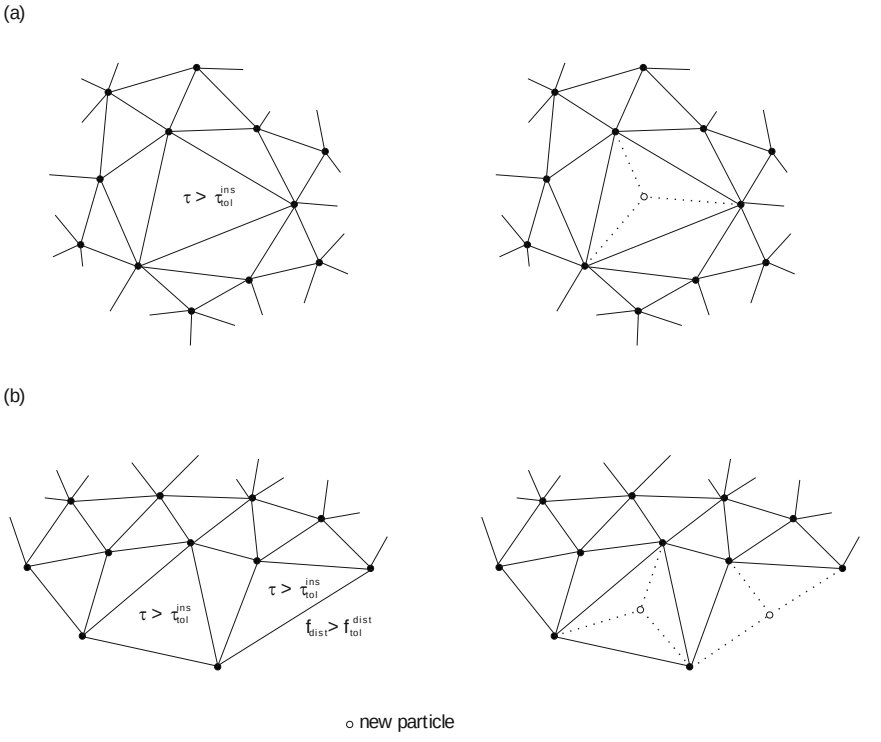

Figure A-1. Insertion of particles in elements: (a) criterion for interior elements, (b) criteria for boundary elements.

For those boundary elements, the insertion is restricted taking into account the shape of the element as a second parameter. As mentioned in [2], it is essential to control that no internal angle is close to 180º. This is verified by determining the ratio f_{dist} between the circumscribed and inscribed circles radiuses of the boundary triangular element, R_c and R_i respectively.

$$f_{dist} = R_c / R_i \qquad \text{(A-2)}$$

This *shape* or *distortion* metric is a scalar value in the range of $f_{dist} = [2, \infty]$. For those equilateral elements, the ratio of the circumscribed and inscribed circles of the equilateral triangles is $f_{dist} = 2$, as shown in Figure A-2(a). The metric increases its magnitude when any distortion is presented – in other words, any of the internal angles is wider with respect the others, see Figure A-2(b).

Depending on this distortion metric, the position of the new particle will vary. If the angle of the vertex of the internal node defines a distortion metric greater than a metric tolerance, $f_{dist} > f_{\text{tol}}^{dist}$, it is included the new particle at the middle of the

two boundary nodes of the element; if not, it is placed in its centre of mass as in the interior elements. Both cases are shown in Figure A-1(b).

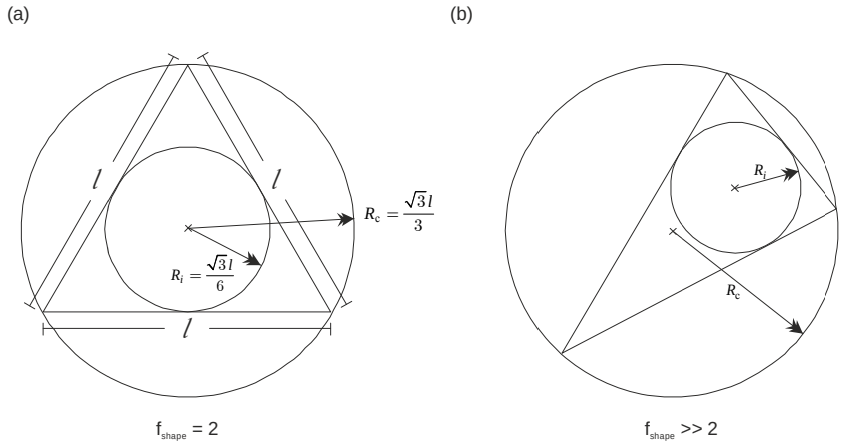

Figure A-2. Circumscribed and inscribed circle relations for triangles.

A.2. Removal or collapsing of particles

In contrast with the process for the particles insertion, the removal of particles is defined at a nodal level. The size metric, given in equation (A-1), is computed for each element connecting a node for certain patch and averaged for a nodal value, given by:

$$\tau_{nodal}^{size} = \sum_{i=1}^{n} \alpha_i / w_i \qquad \text{(A-3)}$$

where n is the number of elements of the patch. If the averaged value is smaller than the tolerance value, $\tau_{nodal}^{size} < \tau_{\text{tol}}^{\text{rem}}$, the particle it is removed, as shown in Figure A-3(a).

For boundary elements, the criterion is according to the length of the boundary segment, see Figure A-3(b). The distance between adjacent nodes is measured; if the distance is smaller than a tolerance length $l < l_{\text{tol}}^{\text{rem}}$, the nodes are collapsed – defining a new particle located at the centre of the collapsing particles coordinates.

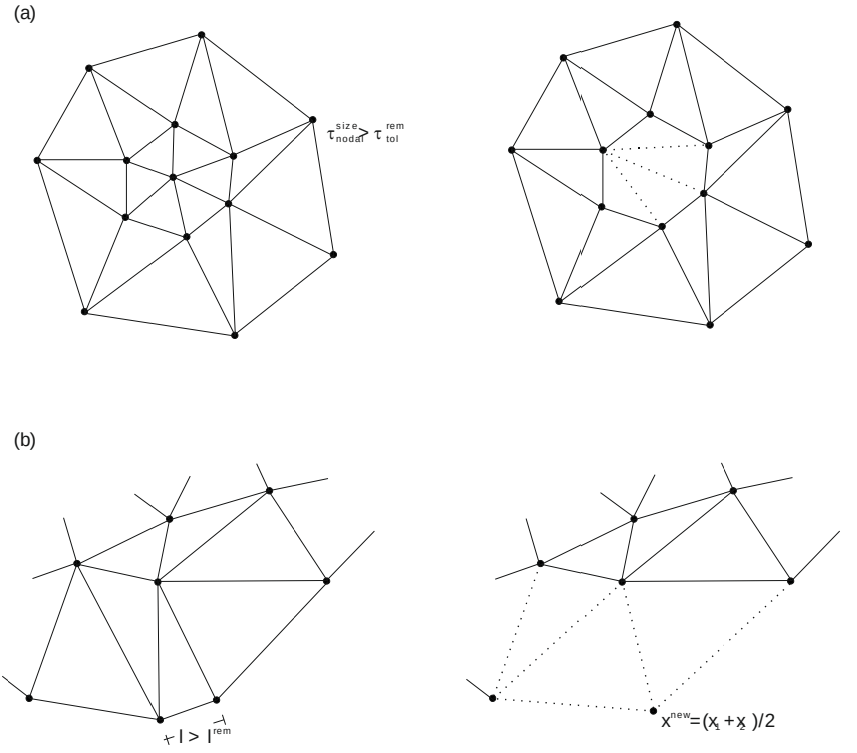

Figure A-3. Removal of particles in the domain: (a) criterion for interior particles, (b) criterion for boundary particles.

A.3. Repositioning of particles

The criteria for insertion and removal of particles, presented in previous sections, control the size homogeneity on the mesh but the elimination of remaining distortion in some elements is not guaranteed. After these procedures, the reconnection of particles through a Delaunay tessellation is computed; thereafter, the quality of the mesh is studied in order to ensure its smoothness. For this purpose, the algebraic quality metrics proposed in [59] are followed.

The algorithm for the repositioning of particles takes place at a nodal level, similarly than the removal of particles procedure. The analysis is effected at an elemental level (computation of the algebraic metrics) and weighing their contribution to the connecting particle of the patch. Depending on the averaged value on the node, the particle is reallocated.

Knupp, in Ref. [59], proposed the quality metric, defined by f_q, by the multiplicative combination of the *relative size* and *shape* metrics, given by f_{size} and f_{shape} respectively.

$$f_q = f_{size} \cdot f_{shape} \tag{A-4}$$

It is a dimensionless value, referenced to an ideal element, which has a specific size and shape. This quality metric is defined in the rank $f_q = [0,1]$ – with $f_q = 0$ for those elements completely degenerated and $f_q = 1$ for those elements with the same size and shape than the reference value, f_{tol}.

The relative size metric determines those elements unusually large or small, relative to the reference element. The metric is defined as

$$f_{size} = \min\left(\tau^{size}, 1/\tau^{size}\right) \tag{A-5}$$

where τ^{size} is the ratio of the areas given by equation (A-1). The metric follows the same rank $f_{size} = [0,1]$ than the quality metric – with $f_{size} = 1$, if and only if the physical element has the same area as the reference triangle, and $f_{size} = 0$ if the physical element differs [59].

The shape quality metric computes the distortion that an element presents. It is calculated in order to be compared with an equilateral triangle, and it is independent of the node of the triangle at which is computed. The shape metric is defined by

$$f_{shape} = \frac{\sqrt{3} r \sin\theta}{1 - r\cos\theta + r^2} \tag{A-6}$$

where $r = \sqrt{\lambda_{22}/\lambda_{11}}$, is the ratio of two adjacent lengths. Similarly, the shape metric follows the same rank than the mentioned above – $f_{shape} = 1$ for those elements which are equilateral triangles and $f_{shape} = 0$ for those completely distorted [59].

Once the metric for each triangular element is computed, this value is averaged at a nodal level by the contribution of each connected element at the nodes. In this sense, the metric is modified to a nodal value, f_q^{patch}. For that $f_q^{patch} < f_{tol}$, the nodal position is reallocated by the well-known Laplacian or barycentric smoothing process [33]. Defining P_j as any node connecting particle coordinates to the reference node coordinates P; the method consists in minimizing the lengths of the edges of the patch.

$$P^* = \frac{1}{n}\sum_{j=1}^{n} \left\| \overrightarrow{PP_j} \right\|^2 \tag{A-7}$$

A.4. Collapsing of two adjacent boundary lengths due to the presence of high concavity on the boundary

The collapsing of two adjacent boundary lengths is a singularity in the finite element method given in large deformation problems due to a boundary constraint. In the existence of a pronounced large interior angle of the adjacent boundary lengths, it is possible to be a source of mesh overlapping. The algorithm described in this section is proposed to solve this condition by a geometrical manipulation of the boundary and it is posed to reduce at the minimum its affectation on the mass conservation.

The control of the concavity is defined in terms of a tolerance angle, φ_{tol} . The algorithm takes place whenever the external angle of the adjacent segments is smaller than the tolerance one, see Figure A-4 (a).

$$\varphi < \varphi_{tol} \tag{A-8}$$

The reposition of the node k is located at the centre of mass of a fictional triangle defined by the boundary particles jlk , Figure A-4(b); defining a new position k' and a new angle φ', see Figure A-4(c). For geometrical properties, this new angle is greater than the defined as the tolerance angle.

$$\varphi < \varphi_{tol} < \varphi'$$

The new adjacent boundary segments, lk' and $k'j$ respectively, must satisfy in the following remeshing process the dimension criterion described in previous section A.2.

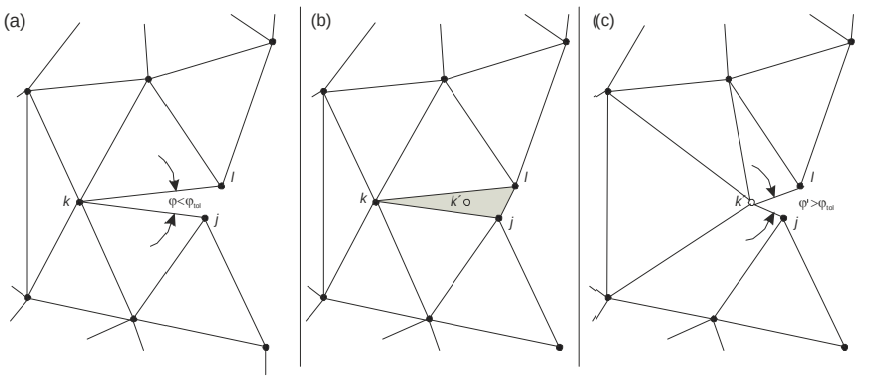

Figure A-4. Collapsing of two adjacent boundary segments for pronounced concavity: (a) Computation of angle of two adjacent boundary segments, (b) Definition of the centre of mass of fictitious element *jlk*, and (c) Repositioning of node *k* at the previous calculated centre of mass *k'*.

An alternative procedure is the real collapse of both adjacent lengths by collapsing nodes l and j of Figure A-4(a). The drawbacks found following this approach

are mainly two: the insertion of a greater volume or mass in the domain; and, in a second place, the unbalance continuity in stresses and pressures since k being a boundary particle would be defined as an interior one.

The full algorithm for the remeshing process is described in Box 3-1

Given a converged mesh Ω_n in t_{n+1}

1. Insertion of particles if needed
   1.1 Computing of size metric τ^{size}
   1.2 For interior elements
   - if $\tau^{size} > \tau_{\text{tol}}^{\text{ins}}$, to insert new particle at the centre of mass of the element.
   1.3 For boundary elements
   - if $\tau^{size} > \tau_{\text{tol}}^{\text{ins}}$ and $f_{dist} > f_{\text{tol}}^{dist}$, to insert new particle at the middle of two boundary nodes of the element
   - elseif $\tau^{size} > \tau_{\text{tol}}^{\text{ins}}$, to insert new particle at the centre of mass of the element.
2. Removal of particles if needed
   2.1 Computing of size metric τ^{size}
   2.2 Averaged nodal metric for connecting node of the patch

$$\tau_{nodal}^{size} = \sum_{i=1}^{n} \alpha_i / w_i$$

   2.3 if $\tau_{nodal}^{size} < \tau_{\text{tol}}^{\text{rem}}$, to remove connecting particle of the corresponding patch
   2.4 For boundary nodes, if $l < l_{\text{tol}}^{\text{rem}}$, to collapse adjacent particles defining a new particle at the middle of them
3. Collapsing of two adjacent boundary lengths
   3.1 Compute angle between each adjacent boundary lengths φ
   3.2 if $\varphi < \varphi_{tol}$
   - Calculate centre of mass *k'* of fictitious triangular element *jlk*
   - Reallocate particle *k* of the connecting boundary lengths to the new position *k'*.
4. Delaunay triangulation
5. Local smoothing to relocate particles if needed
   5.1 Compute relative size metric f_{size} for each element
   5.2 Compute shape metric f_{shape} for each element
   5.3 Compute quality metric $f_q = f_{\text{size}} \cdot f_{\text{shape}}$ for each element
   5.4 Averaged nodal metric for connecting node of the patch

$$f_q^{patch} = \sum_{i=1}^{n} f_q^i$$

   5.5 If $f_q^{patch} < f_{\text{tol}}$ perform Laplacian smoothing for corresponding node

Box A.1. Remeshing process for a dynamic particle discretization.

Appendix B
Algorithmic tangent constitutive tensor

This section covers the formulation of the algorithmic tensor arising from the linearization of the constitutive equation. It is presented following the order in which the constitutive model was defined: first, for the elasto-plastic model, and then, the contribution of the visco-plastic regularization.

B.1. Elasto-plastic description

The problem to solve is to find $\boldsymbol{c}^{\text{ep}}_{n+1}$ that satisfies the Lie derivative of the Kirchhoff stress tensor.

$$L_{\text{v}}\boldsymbol{\tau}_{n+1} = \boldsymbol{c}^{\text{ep}}_{n+1} : L_{\text{v}}\mathbf{e}_{n+1} \tag{B-1}$$

Recalling equation (3.23), the integration of the Kirchhoff stress tensor is given by the following expression

$$\boldsymbol{\tau}_{n+1} = \alpha\,\text{dev}\,\boldsymbol{\tau}^{\text{trial}}_{n+1} + p_{n+1}\boldsymbol{1} \tag{B-2}$$

where:

$$\alpha = \alpha(\Delta\lambda) := \frac{1}{1+2\mu\Delta\lambda} \tag{B-3}$$

Substituting the definition of the auxiliary state $\boldsymbol{\tau}^{\text{trial}}_{n+1}$, given by equation (3.11), and the pressure term of equation (2.34), the equation (B-2) reads:

$$\boldsymbol{\tau}_{n+1} = \alpha\text{dev}\hat{\boldsymbol{\tau}}_{n+1} + \alpha\text{dev}(\boldsymbol{c} : \mathbf{e}_{n+1}) + \kappa \ln J_{n+1}\boldsymbol{1} \tag{B-4}$$

where:

$$\hat{\boldsymbol{\tau}}_{n+1} = \boldsymbol{f}_{n+1} \cdot \boldsymbol{\tau}_n \cdot \boldsymbol{f}^{T}_{n+1} \tag{B-5}$$

Equation (B-5) is the description, in the current configuration, of the Kirchhoff stress tensor of the intermediate reference configuration, carried out by the *push-forward* operation.

In the following sections, the algorithm for an *Impl-Ex* and full implicit scheme are presented in order to gain a complete understanding of both models – the implementation for this work follows the implicit-explicit method.

B.1.1. *Impl-Ex* integration of the constitutive model

The *Impl-Ex* integration scheme is based on the full implicit integration of the stress tensor but combining an explicit extrapolation of the internal variables – the plastic multiplier $\Delta\lambda_{n+1}$, given in equation (3.34).

The Lie derivative for the Kirchhoff stress tensor defined in equation (B-1), following the *Impl-Ex* integration scheme, is computed "*freezing*" the plastic parameter $\alpha(\Delta\lambda_{n+1})$, in equation (B-3), on the current time step. The derivative of the stress field with respect the Almansi strain tensor is summarized as:

$$\begin{aligned} L_{\mathrm{v}}(\boldsymbol{\tau}_{n+1}) = {} & \alpha L_{\mathrm{v}}(\mathrm{dev}\hat{\boldsymbol{\tau}}_{n+1}) + \alpha L_{\mathrm{v}}(\mathrm{dev}(\boldsymbol{c} : \mathbf{e}_{n+1})) \\ & + \kappa L_{\mathrm{v}}(\ln J_{n+1})\boldsymbol{1} + (\kappa \ln J_{n+1}) L_{\mathrm{v}}(\boldsymbol{1}) \end{aligned} \tag{B-6}$$

Below is shown the process for computing the derivative for each term given in equation (B-6) separately.

- $L_{\mathrm{v}}(\alpha\mathrm{dev}\hat{\boldsymbol{\tau}}_{n+1})$

  The pull-back operation is performed over the definition of a deviatoric tensor

$$\phi_*^{-1}(\alpha\mathrm{dev}\hat{\boldsymbol{\tau}}_{n+1}) = \phi_*^{-1}\left[\alpha\left(\hat{\boldsymbol{\tau}}_{n+1} - \frac{1}{3}(\boldsymbol{1} : \hat{\boldsymbol{\tau}}_{n+1})\boldsymbol{1}\right)\right] \tag{B-7}$$

  Calculating the corresponding operations for the covariant and contravariant tensors, the equation above reads

$$\phi_*^{-1}(\alpha\mathrm{dev}\hat{\boldsymbol{\tau}}_{n+1}) = \alpha\left[\boldsymbol{\tau}_n - \frac{1}{3}(\mathbf{C} : \boldsymbol{\tau}_n)\mathbf{C}^{-1}\right] \tag{B-8}$$

  It is observed that the pull-back operation computed in equation (B-8) describes the deviatoric part of the Kirchhoff stress tensor $\boldsymbol{\tau}_n$ in the intermediate reference configuration t_n.

$$\phi_*^{-1}(\alpha\mathrm{dev}\hat{\boldsymbol{\tau}}_{n+1}) = \alpha\mathrm{DEV}\boldsymbol{\tau}_n \tag{B-9}$$

  Computing the directional derivative with respect $\Delta\mathbf{u}$ for the equation above

$$\frac{\partial}{\partial\varphi}(\alpha\mathrm{DEV}\boldsymbol{\tau}_n)\bigg|_{\varphi=0} = -\frac{1}{3}\alpha\left[(\mathrm{d}\mathbf{C} : \boldsymbol{\tau}_n)\mathbf{C}^{-1} + (\mathbf{C} : \boldsymbol{\tau}_n)\mathrm{d}\mathbf{C}^{-1}\right] \tag{B-10}$$

  The derivative for the right Cauchy-Green tensor $\mathbf{C}$ is deduced through the definition of the spatial velocity gradient $\mathbf{l}$, and the definition of the material Green-

Lagrange strain rate tensor, $\dot{\mathbf{E}}$ [42]. After some manipulation, it is easily deduced that:

$$\mathrm{d}\mathbf{C} = 2\mathrm{d}\mathbf{E} \tag{B-11}$$

The derivative of the inverse of the right Cauchy-Green tensor is computed using the identity definition of the tensor, $\mathbf{C}^{-1}\cdot\mathbf{C} = \mathbf{I}$; applying the chain rule and substituting definition given in equation (B-11), its derivative reads:

$$\mathrm{d}\mathbf{C}^{-1} = -\mathbf{C}^{-1}\cdot\mathrm{d}\mathbf{C}\cdot\mathbf{C}^{-1} = -2\mathbf{C}^{-1}\cdot\mathrm{d}\mathbf{E}\cdot\mathbf{C}^{-1} \tag{B-12}$$

Finally, equations (B-11) and (B-12) are substituted into equation (B-10) - expressing the derivative of the deviatoric part of the stress tensor in the material configuration.

$$\mathrm{d}(\alpha\mathrm{DEV}\boldsymbol{\tau}_n) = \frac{2}{3}\alpha\left[(\mathbf{C}:\boldsymbol{\tau}_n)\mathbf{C}^{-1}\cdot\mathrm{d}\mathbf{E}\cdot\mathbf{C}^{-1} - (\mathrm{d}\mathbf{E}:\boldsymbol{\tau}_n)\mathbf{C}^{-1}\right] \tag{B-13}$$

In order to express equation (B-13) in its spatial description, the pull-forward operation is applied, leading to

$$\phi_*[\mathrm{d}(\alpha\mathrm{DEV}\boldsymbol{\tau}_n)] = \frac{2}{3}\alpha[(\boldsymbol{1}:\hat{\boldsymbol{\tau}}_{n+1})\mathrm{d}\mathbf{e}_{n+1} - (\mathrm{d}\mathbf{e}_{n+1}:\hat{\boldsymbol{\tau}}_{n+1})\boldsymbol{1}] \tag{B-14}$$

After some manipulation, equation (B-14) reads

$$L_{\mathrm{v}}(\alpha\mathrm{dev}\hat{\boldsymbol{\tau}}_{n+1}) = \frac{2}{3}\alpha[\mathrm{tr}\hat{\boldsymbol{\tau}}_{n+1}\boldsymbol{\imath} - \boldsymbol{1}\otimes\hat{\boldsymbol{\tau}}_{n+1}]:\mathrm{d}\mathbf{e}_{n+1} \tag{B-15}$$

- $L_{\mathrm{v}}(\alpha\mathrm{dev}(\boldsymbol{c}:\mathbf{e}_{n+1}))$

The second term of equation (B-6) is rewritten by applying the definition of the elastic constitutive tensor, $\boldsymbol{c}$ given in equation (2.13). After some manipulation, this fourth order tensor is expressed in terms of the shear and bulk modulus, G and κ respectively.

$$\boldsymbol{c} = G\boldsymbol{\imath}^{\mathrm{dev}} + \kappa\boldsymbol{1}\otimes\boldsymbol{1} = \boldsymbol{c}^{\mathrm{dev}} + \boldsymbol{c}^{\mathrm{vol}} \tag{B-16}$$

where $G = 2\mu$. Substituting the definition given in equation (B-16) into the second term of equation (B-6), the derivative is expressed by:

$$L_{\mathrm{v}}(\alpha\,\mathrm{dev}(\boldsymbol{c}:\mathbf{e}_{n+1})) = L_{\mathrm{v}}\left(\alpha\boldsymbol{c}^{\mathrm{dev}}:\mathbf{e}_{n+1}\right) \tag{B-17}$$

Applying the derivative for each term of equation (B-17)

$$L_{\mathrm{v}}\left(\alpha\boldsymbol{c}^{\mathrm{dev}}:\mathbf{e}_{n+1}\right) = \alpha L_{\mathrm{v}}\boldsymbol{c}^{\mathrm{dev}}:\mathbf{e}_{n+1} + \alpha\boldsymbol{c}^{\mathrm{dev}}:\mathrm{d}\mathbf{e}_{n+1} \tag{B-18}$$

The Lie derivative expressed on the second term of the RHS of equation (B-18) corresponds to the deviatoric part of the Lie derivative of the elastic constitutive tensor $\boldsymbol{c}$. Its derivative is expressed as

$$L_{\mathrm{v}}(\boldsymbol{c}) = \boldsymbol{a}:L_{\mathrm{v}}\mathbf{e} \tag{B-19}$$

where deduction of $\boldsymbol{a}$ is given in detail in Ref. [13]; the index notation of this fourth order tensor is given by

$$\boldsymbol{a}^{jkl} = -4\mu\left[\Delta\mathbf{e}^{il}_{n+1}\delta^{jk} + \delta^{ik}\Delta\mathbf{e}^{lj}_{n+1}\right] - 2\lambda\left[\delta^{ij}\Delta\mathbf{e}^{kl}_{n+1} + \delta^{ik}\delta^{jl}\,\mathrm{tr}\,\Delta\mathbf{e}_{n+1}\right] \tag{B-20}$$

Substituting definition (B-19) into equation (B-18), the Lie derivative reads

$$L_{\mathrm{v}}\left(\alpha\boldsymbol{c}^{\mathrm{dev}} : \mathbf{e}_{n+1}\right) = \alpha\left(\boldsymbol{a}^{\mathrm{dev}}\left(\mathbf{e}_{n+1}\right) + \boldsymbol{c}^{\mathrm{dev}}\right) : \mathrm{d}\mathbf{e}_{n+1} \tag{B-21}$$

- $\kappa L_{\mathrm{v}}\left(\ln J_{n+1}\right)\boldsymbol{1}$

  Applying the chain rule, the derivative $d\left(\ln J_{n+1}\right)$ is computed as

$$d\left(\ln J_{n+1}\right) = \frac{1}{J_{n+1}}d\left(J_{n+1}\right) \tag{B-22}$$

Taking into account the definition of the Lie derivative of the Jacobian determinant, defined as

$$L_{\mathrm{v}}\left(J_{n+1}\right) = J_{n+1}\boldsymbol{1}^{-1} : L_{\mathrm{v}}\left(\mathbf{e}_{n+1}\right) \tag{B-23}$$

the directional derivative reads

$$d\left(J_{n+1}\right) = J_{n+1}\boldsymbol{1} : d\mathbf{e}_{n+1} \tag{B-24}$$

Substituting equation (B-24) into equation (B-22), we get

$$d\left(\ln J_{n+1}\right) = \frac{1}{J_{n+1}}d\left(J_{n+1}\right) = \boldsymbol{1} : d\mathbf{e}_{n+1} \tag{B-25}$$

Defining the derivative for the pressure term as

$$d\left(p_{n+1}\right) = \kappa\left(\boldsymbol{1} : d\mathbf{e}_{n+1}\right) \tag{B-26}$$

Finally, the derivative of the third term in the RHS of equation (B-6) is given by

$$d\left(p_{n+1}\right)\boldsymbol{1} = \kappa\left(\boldsymbol{1}\otimes\boldsymbol{1}\right) : d\mathbf{e}_{n+1} \tag{B-27}$$

- $p_{n+1}L_{\mathrm{v}}\left(\boldsymbol{1}\right)$

  The last term is defined directly from the following expression

$$d\left(\boldsymbol{1}\right) = -2d\mathbf{e}_{n+1} \tag{B-28}$$

Defining the derivative of the last term as

$$p_{n+1}d\left(\boldsymbol{1}\right) = -2p_{n+1}d\mathbf{e}_{n+1} \tag{B-29}$$

Taking into account each derivative defined for equation (B-6), the elasto-plastic algorithmic tangent tensor $\boldsymbol{c}^{\mathrm{ep}}$ that satisfies equation (B-1) is defined as

$$\boldsymbol{c}^{\mathrm{ep}} = \frac{2}{3}\alpha[\,\mathrm{tr}\hat{\boldsymbol{\tau}}_{n+1}\boldsymbol{\iota} - \boldsymbol{1}\otimes\hat{\boldsymbol{\tau}}_{n+1}\,] + \alpha\left(\boldsymbol{a}^{\mathrm{dev}}(\mathbf{e}_{n+1}) + \boldsymbol{c}^{\mathrm{dev}}\right) + \kappa(\boldsymbol{1}\otimes\boldsymbol{1}) + -2p_{n+1}\boldsymbol{\iota} \tag{B-30}$$

B.1.2. Implicit integration of the constitutive model

The implementation of the algorithmic tangent constitutive tensor in this work is developed with an *Impl-Ex* integration scheme; however, in this section the full description for an implicit integration scheme of the constitutive model is presented.

The implicit scheme is formulated deriving each term of equation (B-4) – the plastic parameter $\alpha(\Delta\lambda_{n+1})_{n+1}$, given in equation (B-3) is computed at the same time step.

$$L_{\mathrm{v}}\boldsymbol{\tau}_{n+1} = d(\alpha)\mathrm{dev}\hat{\boldsymbol{\tau}}_{n+1} + \alpha L_{\mathrm{v}}(\mathrm{dev}\hat{\boldsymbol{\tau}}_{n+1}) + d(\alpha)\mathrm{dev}(\boldsymbol{c}:\mathbf{e}_{n+1}) + \alpha L_{\mathrm{v}}(\mathrm{dev}(\boldsymbol{c}:\mathbf{e}_{n+1})) + \kappa\ln J_{n+1}\boldsymbol{1} \tag{B-31}$$

It is observed from equation (B-31) that the only term that remains to be defined is the directional derivative of the plastic parameter $\alpha(\Delta\lambda_{n+1})_{n+1}$. The derivative of this parameter, $\mathrm{d}\alpha(\Delta\lambda)$, is deduced using its definition given in equation (B-3).

$$\mathrm{d}\alpha = -\frac{2\mu}{(1+2\mu\Delta\lambda_{n+1})^2}\mathrm{d}(\Delta\lambda_{n+1}) = \xi\mathrm{d}(\Delta\lambda_{n+1}) \tag{B-32}$$

where

$$\xi = -\frac{2\mu}{(1+2\mu\Delta\lambda_{n+1})^2} \tag{B-33}$$

Recalling the definition of the slip rate, given in equation (3.22)

$$\Delta\lambda_{n+1} = \frac{\phi(\boldsymbol{\tau})^{\mathrm{trial}}_{n+1}}{2\mu(b_2 - b_1 p_{n+1})} \tag{B-34}$$

we observe that it is defined as a function of the yield function, evaluated in the auxiliary state $\boldsymbol{\tau}^{\mathrm{trial}}_{n+1}$, and the pressure. The derivative of the discretized slip rate, expressed in the RHS of equation (B-32), is computed deriving by parts equation (B-34):

$$\mathrm{d}(\Delta\lambda) = \frac{1}{2\mu(b_2 - b_1 p_{n+1})}\mathrm{d}\phi(\boldsymbol{\tau})^{\mathrm{trial}} + \frac{b_1\,\phi(\boldsymbol{\tau})^{\mathrm{trial}}}{2\mu(b_2 - b_1 p_{n+1})^2}\mathrm{d}\,p_{n+1} \tag{B-35}$$

The remaining term to be defined is the derivative of the yield surface – since the computation of the derivative of the pressure is expressed in equation (B-26).

- $\mathrm{d}\phi(\boldsymbol{\tau})^{\text{trial}}$

The derivative of the yield surface, defined in equation (3.14), is expressed as

$$\mathrm{d}\phi(\boldsymbol{\tau})^{\text{trial}} = \mathrm{d}\left(\left\|\operatorname{dev}\boldsymbol{\tau}_{n+1}^{\text{trial}}\right\|\right) + b_1\,\mathrm{d}\,p_{n+1}^{\text{trial}} \tag{B-36}$$

The expression for the derivative of the norm of the deviatoric part of the trial stress tensor, first term of the RHS of equation (B-36), reads

$$\begin{aligned}\mathrm{d}\left(\left\|\operatorname{dev}\boldsymbol{\tau}_{n+1}^{\text{trial}}\right\|\right) = \frac{1}{2\left\|\operatorname{dev}\boldsymbol{\tau}_{n+1}^{\text{trial}}\right\|}\Big[&\mathrm{d}\left(\operatorname{dev}\boldsymbol{\tau}_{n+1}^{\text{trial}}\right) : \operatorname{dev}\boldsymbol{\tau}_{n+1}^{\text{trial}} + \\ &\operatorname{dev}\boldsymbol{\tau}_{n+1}^{\text{trial}} : \mathrm{d}\left(\operatorname{dev}\boldsymbol{\tau}_{n+1}^{\text{trial}}\right)\Big]\end{aligned} \tag{B-37}$$

Using the definition of the trial stress tensor, equation (3.11), and aided by the previous calculations defined in equations (B-15) and (B-21), the derivative of the deviatoric part of the trial reads

$$\begin{aligned}\mathrm{d}\left(\operatorname{dev}\boldsymbol{\tau}_{n+1}^{\text{trial}}\right) = \Big\{&\frac{2}{3}\left[\operatorname{tr}\hat{\boldsymbol{\tau}}_{n+1}\boldsymbol{\imath} - \boldsymbol{1}\otimes\hat{\boldsymbol{\tau}}_{n+1}\right] \\ &+\boldsymbol{a}^{\text{dev}}\left(\mathbf{e}_{n+1}\right) + \boldsymbol{c}^{\text{dev}}\Big\} : \mathrm{d}\mathbf{e}_{n+1}\end{aligned} \tag{B-38}$$

Due to the symmetry of the Kirchhoff stress tensor and the definition of the derivative of the deviatoric part of the stress tensor given in the equation above, the expression in equation (B-37) is rewritten as

$$\begin{aligned}\mathrm{d}\left(\left\|\operatorname{dev}\boldsymbol{\tau}_{n+1}^{\text{trial}}\right\|\right) = \frac{\operatorname{dev}\boldsymbol{\tau}_{n+1}^{\text{trial}}}{2\left\|\operatorname{dev}\boldsymbol{\tau}_{n+1}^{\text{trial}}\right\|} : \Big\{&\frac{2}{3}\left[\operatorname{tr}\hat{\boldsymbol{\tau}}_{n+1}\boldsymbol{\imath} - \boldsymbol{1}\otimes\hat{\boldsymbol{\tau}}_{n+1}\right] \\ &+\boldsymbol{a}^{\text{dev}}\left(\mathbf{e}_{n+1}\right) + \boldsymbol{c}^{\text{dev}}\Big\} : \mathrm{d}\mathbf{e}_{n+1}\end{aligned} \tag{B-39}$$

The notation of equation (B-39) is shortened as

$$\mathrm{d}\left(\left\|\operatorname{dev}\boldsymbol{\tau}_{n+1}^{\text{trial}}\right\|\right) = \beta : \mathrm{d}\mathbf{e}_{n+1} \tag{B-40}$$

where:

$$\beta = \frac{\operatorname{dev}\boldsymbol{\tau}_{n+1}^{\text{trial}}}{2\left\|\operatorname{dev}\boldsymbol{\tau}_{n+1}^{\text{trial}}\right\|} : \left\{\frac{2}{3}\left[\operatorname{tr}\hat{\boldsymbol{\tau}}_{n+1}\boldsymbol{\imath} - \boldsymbol{1}\otimes\hat{\boldsymbol{\tau}}_{n+1}\right] + \boldsymbol{a}^{\text{dev}}\left(\mathbf{e}_{n+1}\right) + \boldsymbol{c}^{\text{dev}}\right\} \tag{B-41}$$

The second term of the RHS of equation (B-35) corresponds to the derivative of the pressure. As mentioned before, the computation of this derivative was carried out in the previous section and defined by equation (B-26).

Substituting equation (B-40) and (B-26) into equation (B-36), the derivative of the yield surface reads

$$\mathrm{d}\phi(\boldsymbol{\tau})^{\text{trial}} = \beta : \mathrm{d}\mathbf{e}_{n+1} + b_1\,\mathcal{K}\left(\boldsymbol{1} : \mathrm{d}\mathbf{e}_{n+1}\right) \tag{B-42}$$

The derivative of the discretized slip rate, given in equation (B-35), is completely defined by equations (B-42) and (B-26). Substituting those terms and regrouping them, the derivative of the slip rate reads

$$\mathrm{d}(\Delta\lambda) = [\,\gamma_1\beta + \kappa \mathbf{1}(\gamma_1 b_1 + \gamma_2)\,] : \mathrm{d}\mathbf{e}_{n+1} \tag{B-43}$$

where:

$$\gamma_1 = \frac{1}{2\mu(b_2 - b_1 p_{n+1})} \quad \text{and} \quad \gamma_2 = \frac{b_1 \cdot \phi(\boldsymbol{\tau})^{\text{trial}}}{2\mu(b_2 - b_1 p_{n+1})^2} \tag{B-44}$$

Finally, the description of the derivative of the plastic parameter $\alpha(\Delta\lambda)$ for a full implicit integration scheme is obtained. Substituting equation (B-45) into equation (B-32)

$$\mathrm{d}\alpha = \xi[\,\gamma_1\beta + \kappa \mathbf{1}(\gamma_1 b_1 + \gamma_2)\,] : \mathrm{d}\mathbf{e}_{n+1} \tag{B-45}$$

B.2. Visco-plastic regularization

The integration of the visco-plastic regularization in the algorithmic tangent tensor is given obtaining the directional derivative of equation (3.32)

$$\mathrm{d}\boldsymbol{\tau}_{n+1}^{\text{vp}} = \eta\,\mathrm{d}\boldsymbol{\tau}_{n+1}^{\text{trial}} + (1-\eta)\,\mathrm{d}\boldsymbol{\tau}_{n+1}^{\text{ep}} \tag{B-46}$$

The derivative of the trial stress tensor fulfils the following expression

$$\mathrm{d}\boldsymbol{\tau}_{n+1}^{\text{trial}} = \boldsymbol{c}^{\text{trial}} : \mathrm{d}\mathbf{e}_{n+1} \tag{B-47}$$

where the elastic algorithmic tangent modulus $\boldsymbol{c}^{\text{trial}}$ is defined as

$$\boldsymbol{c}^{\text{trial}} = \boldsymbol{c} + \boldsymbol{a}(\mathbf{e}_{n+1}) \tag{B-48}$$

where the expressions for $\boldsymbol{c}$ and $\boldsymbol{a}$ were given previously. The deduction of equation (B-48) is given in more detail in Ref. [13].

The second term was defined in previous section, where the elasto-plastic constitutive tensor is given by equation (B-30) – for an implicit / explicit integration scheme (*Impl-Ex*). Finally, the visco-plastic description of the algorithmic constitutive tensor is stated as follows.

$$\boldsymbol{c}^{\text{vp}} = \eta\boldsymbol{c}^{\text{trial}} + (1-\eta)\boldsymbol{c}^{\text{ep}} \tag{B-49}$$

Appendix C
Linearization of the variational problem

The non-linear variational problem is solved using a traditional iterative Newton-Raphson. The linearization is computed in terms of the directional or Gâteaux derivatives of the residual vectors, defined by equations (3.42) and (3.43), with respect to the incremental displacement $\Delta\mathbf{u}$ and the pressure π.

C.1. Linearization of the continuum description

The derivatives of the residual vectors are shown separately in terms of each computed component. The process is similar for each term: it is carried out expressing each equation in the reference configuration t_n via the pull-back operator; thereafter, it is performed the directional derivative; and finally, the expression is returned to its description in the current configuration via the **p**ush-forward operator.

- $\delta_{\Delta\mathbf{u}} R^u$

The directional derivative of equation (3.42), with respect the incremental displacement $\Delta\mathbf{u}$, is computed on the vector of internal forces $\delta_{\Delta\mathbf{u}} G^{\text{int,mix}}$ – since it is the only term being a function of the incremental displacement. The derivative of the vector of internal forces, given in equation (3.42), is performed in the intermediate reference configuration. The following equation relates both the reference and current configurations in terms of the determinant of the deformation gradient tensor J.

$$\int_{\Omega_{n+1}} d\Omega_{n+1} = \int_{\Omega_o} J\, d\Omega_o \qquad \text{(C-1)}$$

Applying the property of the determinant of the product of two tensors, into equation (3.2), the Jacobian determinant reads

$$J = j_{n+1} \cdot j_n \tag{C-2}$$

The Cauchy stress tensor, using equations (C-1) and (C-2), is expressed in terms of the Kirchhoff stress tensor in the intermediate reference configuration as

$$\int_{\Omega_{n+1}} \boldsymbol{\sigma}_{n+1}\, d\Omega_{n+1} = \int_{\Omega_n} j_{n+1}\boldsymbol{\sigma}_{n+1}\, d\Omega_n = \int_{\Omega_n} \tilde{\boldsymbol{\tau}}_{n+1}\, d\Omega_n \tag{C-3}$$

note that $\tilde{\boldsymbol{\tau}}$ stands for the Kirchhoff stress tensor relative to the intermediate reference configuration $t = t_n$.

The description in the reference configuration of a given tensor, described in the current configuration, is established by the *pull-back* operator. The pull-back operation for a contravariant tensor is given by

$$\chi_*^{-1}(\bullet)^{\#} = \boldsymbol{f}^{-1} \cdot (\bullet)^{\#} \cdot \boldsymbol{f}^{-T} \tag{C-4}$$

and for a covariant tensor

$$\chi_*^{-1}(\bullet)^{b} = \boldsymbol{f}^{T} \cdot (\bullet)^{b} \cdot \boldsymbol{f} \tag{C-5}$$

Equation (3.42) is described in the reference configuration by the proper use of the pull-back operators as:

$$\begin{aligned} G_n^{\text{int,mix}} = \int_{\Omega_n} \frac{1}{j_n} \boldsymbol{f}_{n+1} \cdot \text{DEV}\tilde{\mathbf{S}}_{n+1} : \bar{\nabla}_n(\delta w) d\Omega_n + \\ \int_{\Omega_n} \frac{1}{j_n} \boldsymbol{f}_{n+1} \cdot \left(J\tilde{p}\mathbf{C}_{n+1}^{-1} \right) : \bar{\nabla}_n(\delta w) d\Omega_n \end{aligned} \tag{C-6}$$

where $\tilde{p}$ is the pressure corresponding to the relative Kirchhoff stress tensor $\tilde{\boldsymbol{\tau}}$, $\tilde{\mathbf{S}}$ and $\bar{\nabla}_n$ the Second Piola-Kirchhoff stress tensor and the gradient operator, respectively, referenced to the intermediate configuration.

The LHS of equation (C-6) is condensed to simplify the development of the Jacobian matrix.

$$G_n^{\text{int,mix}} = \int_{\Omega_n} \frac{1}{j_n} \boldsymbol{f}_{n+1} \cdot \tilde{\mathbf{S}}_{n+1} : \bar{\nabla}_n(\delta w) d\Omega_n \tag{C-7}$$

where:

$$\tilde{\mathbf{S}}_{n+1} = \text{DEV}\tilde{\mathbf{S}}_{n+1} + J\tilde{p}\mathbf{C}^{-1} \tag{C-8}$$

Defining the vector of internal forces in the intermediate reference configuration, its derivative is computed applying the chain rule

$$\mathrm{D}_{\Delta\mathbf{u}}\left(G_n^{\mathrm{int,mix}}\right)=\int_{\Omega_n}\frac{1}{j_n}\mathrm{D}_{\Delta\mathbf{u}}\left(\boldsymbol{f}_{n+1}\right)\cdot\tilde{\mathbf{S}}_{n+1}:\bar{\nabla}_n(\delta w)d\Omega_o+\int_{\Omega_n}\frac{1}{j_n}\boldsymbol{f}_{n+1}\cdot\mathrm{D}_{\Delta\mathbf{u}}\left(\tilde{\mathbf{S}}_{n+1}\right):\bar{\nabla}_n(\delta w)d\Omega_n \tag{C-9}$$

Observation C-1

The derivative of the gradient of the test function δw vanishes since it is not a function of the displacement field.

Below, the directional derivative for each term ($\boldsymbol{f}_{n+1}, \tilde{\mathbf{S}}_{n+1}$) is defined. Thereafter, each term is substituted into equation (C-9). The deformation gradient tensor $\boldsymbol{f}$ is defined in terms of the scalar parameter φ and the incremental displacement $\Delta\mathbf{u}$:

$$\boldsymbol{f}(\mathbf{u}+\varphi\Delta\mathbf{u})=\boldsymbol{1}+\overline{\nabla}\mathbf{u}+\varphi\overline{\nabla}(\Delta\mathbf{u}) \tag{C-10}$$

The Gâteaux derivative of equation (C-10) is given by

$$\frac{\mathrm{d}}{\mathrm{d}\varphi}\boldsymbol{f}(\mathbf{u}+\varphi\Delta\mathbf{u})\Big|_{\varphi=0}=\overline{\nabla}(\Delta\mathbf{u}) \tag{C-11}$$

The second derivative, corresponding to the relative second Piola-Kirchhoff stress tensor $\tilde{\mathbf{S}}$, is defined applying the chain rule with respect the Green-Lagrange strain tensor

$$\frac{\mathrm{d}}{\mathrm{d}\varphi}\tilde{\mathbf{S}}(\mathbf{u}+\varphi\Delta\mathbf{u})\Big|_{\varphi=0}=\frac{\mathrm{d}}{\mathrm{d}\mathbf{E}}\tilde{\mathbf{S}}:\frac{\mathrm{d}}{\mathrm{d}\varphi}\mathbf{E} \tag{C-12}$$

The derivative for the Second Piola Kirchhoff stress tensor by the Green-Lagrange strain tensor is expressed in the intermediate reference configuration as

$$\boldsymbol{C}^{\mathrm{ep}}=\left(\frac{\mathrm{d}\tilde{\mathbf{S}}}{\mathrm{d}\mathbf{E}}\right)_{n+1} \tag{C-13}$$

From equation (C-13), the algorithmic tangent constitutive tensor is deduced – see Appendix B.

The directional derivative of the Green-Lagrange strain tensor, defined in the second term of the product of the RHS of equation (C-12), after some manipulation of the terms reads

$$\frac{\mathrm{d}}{\mathrm{d}\varphi}\mathbf{E}(\mathbf{u}+\varphi\Delta\mathbf{u})\Big|_{\varphi=0}=\frac{1}{2}\left[\boldsymbol{f}^T\cdot\nabla(\Delta\mathbf{u})+\nabla(\Delta\mathbf{u})^T\cdot\boldsymbol{f}\right] \tag{C-14}$$

Substituting equation (C-13) and (C-14) into equation (C-12)

$$\frac{\mathrm{d}}{\mathrm{d}\varphi}\tilde{\mathbf{S}}(\mathbf{u}+\varphi\Delta\mathbf{u})\Big|_{\varphi=0}=\frac{1}{2}\boldsymbol{C}^{\mathrm{ep}}:\left[\boldsymbol{f}^T\cdot\nabla(\Delta\mathbf{u})+\nabla(\Delta\mathbf{u})^T\cdot\boldsymbol{f}\right] \tag{C-15}$$

Due to the major symmetry of the algorithmic tangent tensor, equation (C-15) is rewritten as

$$\frac{\mathrm{d}}{\mathrm{d}\varphi}\tilde{\mathbf{S}}(\mathbf{u}+\varphi\Delta\mathbf{u})\Big|_{\varphi=0} = \boldsymbol{C}^{\mathrm{ep}} : \left[\boldsymbol{f}^{T}\cdot\nabla(\Delta\mathbf{u})\right] \tag{C-16}$$

Substituting both equations (C-11) and (C-16) into equation (C-9), the derivative of the internal forces with respect the incremental displacement reads:

$$\mathrm{D}_{\Delta\mathbf{u}}\left(G_n^{\mathrm{int,mix}}\right) = \mathrm{D}_{\Delta\mathbf{u}}\left(G_n^{\mathrm{int,mix}}\right)^{\mathrm{geo}} + \mathrm{D}_{\Delta\mathbf{u}}\left(G_n^{\mathrm{int,mix}}\right)^{\mathrm{mat}} \tag{C-17}$$

where $\mathrm{D}_{\Delta\mathbf{u}}\left(G_n^{\mathrm{int,mix}}\right)^{\mathrm{geo}}$ and $\mathrm{D}_{\Delta\mathbf{u}}\left(G_n^{\mathrm{int,mix}}\right)^{\mathrm{mat}}$ will define the geometric and material parts of the Jacobian or stiffness matrix respectively; in the reference configuration t_n, defined as:

$$\mathrm{D}_{\Delta\mathbf{u}}\left(G_n^{\mathrm{int,mix}}\right)^{\mathrm{geo}} = \int_{\Omega_n}\frac{1}{j_n}\bar{\nabla}_n(\Delta\mathbf{u})\cdot\tilde{\mathbf{S}}_{n+1} : \bar{\nabla}_n(\delta w)d\Omega_n \tag{C-18}$$

and

$$\mathrm{D}_{\Delta\mathbf{u}}\left(G_n^{\mathrm{int,mix}}\right)^{\mathrm{mat}} = \int_{\Omega_n}\frac{1}{j_n}\boldsymbol{f}_{n+1}\cdot\boldsymbol{C}^{\mathrm{ep}} : \boldsymbol{f}_{n+1}^{T}\cdot\bar{\nabla}_n(\Delta\mathbf{u}) : \bar{\nabla}_n(\delta w)d\Omega_n \tag{C-19}$$

The description in the current or spatial configuration of a given tensor, described in the reference configuration t_n, is computed by the *push-forward*, defined for a contravariant tensor as

$$\chi_*(\bullet)^{\#} = \boldsymbol{f}\cdot(\bullet)^{\#}\cdot\boldsymbol{f}^{T} \tag{C-20}$$

and for a covariant tensor

$$\chi_*(\bullet)^{b} = \boldsymbol{f}^{-T}\cdot(\bullet)^{b}\cdot\boldsymbol{f}^{-1} \tag{C-21}$$

The description of equation (C-17) in the current or spatial configuration reads

$$\mathrm{D}_{\Delta\mathbf{u}}\left(G_{n+1}^{\mathrm{int,mix}}\right) = \mathrm{D}_{\Delta\mathbf{u}}\left(G_{n+1}^{\mathrm{int,mix}}\right)^{\mathrm{geo}} + \mathrm{D}_{\Delta\mathbf{u}}\left(G_{n+1}^{\mathrm{int,mix}}\right)^{\mathrm{mat}} \tag{C-22}$$

where:

$$\mathrm{D}_{\Delta\mathbf{u}}\left(G_{n+1}^{\mathrm{int,mix}}\right)^{\mathrm{geo}} = \int_{\Omega_{n+1}}\nabla_{n+1}(\Delta\mathbf{u})\cdot\boldsymbol{\sigma}_{n+1} : \nabla_{n+1}(\delta w)d\Omega_{n+1} \tag{C-23}$$

and

$$\mathrm{D}_{\Delta\mathbf{u}}\left(G_{n+1}^{\mathrm{int,mix}}\right)^{\mathrm{mat}} = \int_{\Omega_{n+1}}\nabla_{n+1}(\Delta\mathbf{u}) : \boldsymbol{c}^{\mathrm{ep}} : \nabla_{n+1}(\delta w)d\Omega_{n+1} \tag{C-24}$$

- $\delta_{\pi}R^{u}$

The directional derivative of equation (3.42) with respect the pressure is defined as $\mathrm{D}_{\pi}G^{\mathrm{int,mix}}$. With the vector of internal forces defined in the current reference configuration for a decoupled Second Piola-Kirchhoff stress tensor, equation (C-6), the derivative in terms of the pressure, reads

$$\mathrm{D}_{\pi}\left(G_n^{\mathrm{int,mix}}\right)=\int_{\Omega_n}\frac{1}{j_n}\boldsymbol{f}_{n+1}\cdot J\,\mathrm{D}_{\pi}(\tilde{p})\,\mathbf{C}_{n+1}^{-1}:\bar{\nabla}_n(\delta w)d\Omega_n \tag{C-25}$$

The unique term defined as function of the pressure is the pressure itself. Its derivative is defined as

$$\frac{\mathrm{d}}{\mathrm{d}\varphi}(\pi+\varphi\delta q)\bigg|_{\varphi=0}=\delta q \tag{C-26}$$

Equation (C-26) is substituted into (C-25) to define the derivative of the vector of the internal forces with respect to the pressure

$$\mathrm{D}_{\pi}\left(G_n^{\mathrm{int,mix}}\right)=\int_{\Omega_n}\delta q j_{n+1}\boldsymbol{f}_{n+1}\cdot\mathbf{C}_{n+1}^{-1}:\bar{\nabla}_n(\delta w)d\Omega_n \tag{C-27}$$

Similarly than for the first derivative term, equation (C-27) is described in the spatial configuration applying the push-forward operator

$$\mathrm{D}_{\pi}\left(G_{n+1}^{\mathrm{int,mix}}\right)=\int_{\Omega_{n+1}}\delta q\,\nabla_{n+1}(\delta w)d\Omega_{n+1} \tag{C-28}$$

- $\delta_{\Delta\mathbf{u}}R^{\mathrm{q}}$

The directional derivative of equation (3.43) with respect to the incremental displacements is defined as $\mathrm{D}_{\Delta\mathbf{u}}R_o^{\mathrm{q}}$.

$$\mathrm{D}_{\Delta\mathbf{u}}R_o^{\mathrm{q}}=\int_{\Omega_o}\delta q\mathrm{D}_{\Delta\mathbf{u}}\left(\frac{\ln J}{J}\right)d\Omega_o \tag{C-29}$$

Equation (C-29) is rewritten by computing the derivative of the quotient as

$$\mathrm{D}_{\Delta\mathbf{u}}R_o^{\mathrm{q}}=\int_{\Omega_o}\delta q\left(\frac{1-J}{J^2}\right)\mathrm{D}_{\Delta\mathbf{u}}(J)d\Omega_o \tag{C-30}$$

The derivative $\mathrm{D}_{\Delta\mathbf{u}}(J)$ is computed applying the chain rule and using the definition of the derivative of a determinant, obtaining:

$$\mathrm{D}_{\Delta\mathbf{u}}(J)=\frac{\partial J}{\partial\mathbf{F}}:\frac{\partial\mathbf{F}}{\partial\varphi}\bigg|_{\varphi=0}=J\mathbf{F}^{-T}:\bar{\nabla}_o(\Delta\mathbf{u}) \tag{C-31}$$

Substituting equation (C-31) into equation (C-30)

$$\mathrm{D}_{\Delta\mathbf{u}}R_o^{\mathrm{q}}=\int_{\Omega_o}\delta q\left(\frac{1-J}{J^2}\right)J\mathbf{F}^{-T}:\bar{\nabla}_o(\Delta\mathbf{u})d\Omega_o \tag{C-32}$$

The expression of equation (C-32) in the current configuration is obtained using equation (C-1) and rewriting the double contraction term as $\mathbf{F}^{-T}:\bar{\nabla}_o(\Delta\mathbf{u})=\mathrm{tr}\left[\mathbf{F}^{-1}:\bar{\nabla}_o(\Delta\mathbf{u})\right]$; finally, the equation reads

$$\mathrm{D}_{\Delta\mathbf{u}}R_{n+1}^{\mathrm{q}}=\int_{\Omega_{n+1}}\delta q\left(\frac{1-J}{J^2}\right)\mathrm{tr}\left[\nabla_{n+1}(\Delta\mathbf{u})\right]d\Omega_{n+1} \tag{C-33}$$

- $\delta_\pi R^{\mathrm{q}}$

The derivative of equation (3.43) in terms of the pressure defined as $\mathrm{D}_\pi R_o^{\mathrm{q}}$ reads:

$$\mathrm{D}_\pi R_o^{\mathrm{q}} = \int_{\Omega_o} \frac{1}{\kappa} \delta q \, \mathrm{D}_\pi(\pi) d\Omega_o \tag{C-34}$$

and the directional derivative term $\mathrm{D}_\pi(\pi)$ is obtained straight forward as

$$\mathrm{D}_\pi R_o^{\mathrm{q}} = \int_{\Omega_o} \frac{1}{\kappa} \delta q \delta\pi \, d\Omega_o \tag{C-35}$$

The equation (C-35) is expressed in the current configuration using equation (C-1)

$$\mathrm{D}_\pi R_{n+1}^{\mathrm{q}} = \int_{\Omega_{n+1}} \frac{1}{J\kappa} \delta q \delta\pi \, d\Omega_{n+1} \tag{C-36}$$

The summary of the linearization of the non-linear variational problem is given in Box C.1.

Derivative $\delta_{\Delta\mathbf{u}} R^u$

$$\mathrm{D}_{\Delta\mathbf{u}}\left(G_{n+1}^{\mathrm{int,mix}}\right) = \mathrm{D}_{\Delta\mathbf{u}}\left(G_{n+1}^{\mathrm{int,mix}}\right)^{\mathrm{geo}} + \mathrm{D}_{\Delta\mathbf{u}}\left(G_{n+1}^{\mathrm{int,mix}}\right)^{\mathrm{mat}}$$

where:

$$\mathrm{D}_{\Delta\mathbf{u}}\left(G_{n+1}^{\mathrm{int,mix}}\right)^{\mathrm{geo}} = \int_{\Omega_{n+1}} \nabla_{n+1}(\Delta\mathbf{u}) \cdot \boldsymbol{\sigma}_{n+1} : \nabla_{n+1}(\delta w) d\Omega_{n+1}$$

$$\mathrm{D}_{\Delta\mathbf{u}}\left(G_{n+1}^{\mathrm{int,mix}}\right)^{\mathrm{mat}} = \int_{\Omega_{n+1}} \nabla_{n+1}(\Delta\mathbf{u}) : \boldsymbol{c}^{\mathrm{ep}} : \nabla_{n+1}(\delta w) d\Omega_{n+1}$$

Derivative $\delta_\pi R^u$

$$\mathrm{D}_\pi\left(G_{n+1}^{\mathrm{int,mix}}\right) = \int_{\Omega_{n+1}} \delta q \nabla_{n+1}(\delta w) d\Omega_{n+1}$$

Derivative $\delta_{\Delta\mathbf{u}} R^{\mathrm{q}}$

$$\mathrm{D}_{\Delta\mathbf{u}}\left(R_{n+1}^{\mathrm{q}}\right) = \int_{\Omega_{n+1}} \delta q \left(\frac{1-J}{J^2}\right) \mathrm{tr}\left[\nabla_{n+1}(\Delta\mathbf{u})\right] d\Omega_{n+1}$$

Derivative $\delta_\pi R^{\mathrm{q}}$

$$\mathrm{D}_\pi\left(R_{n+1}^{\mathrm{q}}\right) = \int_{\Omega_{n+1}} \frac{1}{J\kappa} \delta q \delta\pi \, d\Omega_{n+1}$$

Derivative $\boldsymbol{c}^{\mathrm{ep}}$ – derived in Appendix B

$$\boldsymbol{c}^{\mathrm{ep}} = \frac{2}{3}\alpha\left[\mathrm{tr}\hat{\boldsymbol{\tau}}_{n+1}\boldsymbol{i} - \boldsymbol{1} \otimes \hat{\boldsymbol{\tau}}_{n+1}\right] + \alpha\left(\boldsymbol{a}^{\mathrm{dev}}(\mathbf{e}_{n+1}) + \boldsymbol{c}^{\mathrm{dev}}\right) + \kappa(\boldsymbol{1} \otimes \boldsymbol{1}) + -2p_{n+1}\boldsymbol{i}$$

Box C.1. Linearization of the non-linear variational problem (equations (3.42) and (3.43)) – a continuum description.

C.2. Stiffness matrix – spatial discretization

The discretization of the system of equations is computed in terms of equations (3.44)-(3.47). The numerical approximations of the gradient of the incremental displacement, $\nabla(\Delta\mathbf{u})$ and $\nabla(\delta w)$ read

$$\nabla\left(\Delta\mathbf{u}^h\right)=\sum_{i=1}^{n_p}\nabla(N_i)\Delta\mathbf{u}_i^h \tag{C-37}$$

$$\nabla\left(\delta w^h\right)=\sum_{i=1}^{n_p}\nabla(N_i)\delta w_i^h \tag{C-38}$$

Equation (3.42) is rewritten in terms of vectors of nodal forces as

$$\left[\mathbf{R}^u\right]^h=\left[\mathbf{F}^{\text{int,mix}}\right]-\left[\mathbf{F}^{\text{ext}}\right]+\left[\mathbf{F}^{\text{ine}}\right] \tag{C-39}$$

where:

$$\left[\mathbf{F}^{\text{int,mix}}\right]_I^h=\int_{\Omega^e}\boldsymbol{\sigma}^h\cdot\nabla(N_I)d\Omega^e \qquad (I=1:3) \tag{C-40}$$

$$\left[\mathbf{F}^{\text{ext}}\right]_I^h=\int_{\Omega^e}N_I\rho^h\mathbf{b}^h d\Omega^e+\int_{\Gamma^e}N_I\bar{\mathbf{t}}^h d\Gamma^e \qquad (I=1:3) \tag{C-41}$$

$$\left[\mathbf{F}^{\text{ine}}\right]_I^h=\int_{\Omega^e}N_I\rho^h\dot{\mathbf{v}}^h d\Omega^e \qquad (I=1:3) \tag{C-42}$$

Similarly, it is defined the residual vector $\left[R^q\right]_I^h$ from the discretization of equation (3.43) is discretized as

$$\left[\mathbf{R}^q\right]_I^h=\int_{\Omega^e}N_I\left(\frac{\ln J^h}{J^h}-\frac{1}{\kappa}N_A\pi_a\right)d\Omega^e=0; \quad (I=A=1,2,..,n_p) \tag{C-43}$$

The discretization of the linearization of the residual vector, shown in previous section, defines Jacobian or stiffness matrix. The discretization of the term corresponding to the linearization of the vector of internal forces in terms of the incremental displacement $\mathrm{D}_{\Delta\mathbf{u}}\left(G^{\text{int,mix}}\right)$, given by equation (C-22), reads as

$$\left[K^{uu}\right]_{IJ}^h=\left[K^{\text{geo}}\right]_{IJ}^h+\left[K^{\text{mat}}\right]_{IJ}^h \tag{C-44}$$

where:

$$\left[K^{\text{geo}}\right]_{IJ}^h=\int_{\Omega^e}\nabla(N_J)\cdot\boldsymbol{\sigma}^h\cdot\nabla(N_I)d\Omega^e \tag{C-45}$$

$$\left[K^{\text{mat}}\right]_{IJ}^h=\int_{\Omega^e}\nabla(N_J)\cdot\left[\mathbf{c}^{\text{ep}}\right]^h\cdot\nabla(N_I)d\Omega^e \tag{C-46}$$

The discretization of the linearization of the vector of internal forces with respect to the pressure $\mathrm{D}_{\pi}\left(G^{\text{int,mix}}\right)$, given in equation (C-28), is defined as

$$\left[K^{u\pi}\right]_{IA}^{h} = \int_{\Omega^e} \nabla(N_I) N_A \, d\Omega^e \tag{C-47}$$

Following the same process for the linearization terms of the second equation in terms of the incremental displacement $\mathrm{D}_{\Delta\mathbf{u}}\left(R^{\mathrm{q}}\right)$ and pressure $\mathrm{D}_{\pi}\left(R^{\mathrm{q}}\right)$, equations (C-33) and (C-35) respectively, the discretization for each term reads

$$\left[K^{\pi u}\right]_{IA}^{h} = \int_{\Omega^e} N_I \left(\frac{1-J^h}{\left(J^h\right)^2}\right) \nabla(N_A) \, d\Omega^e \tag{C-48}$$

and

$$\left[K^{\pi\pi}\right]_{IA}^{h} = \int_{\Omega^e} \frac{1}{\kappa} N_I N_A \, d\Omega^e \tag{C-49}$$

It is observed that the *mass* matrix defined by the term $\left[K^{\pi\pi}\right]_{IA}^{h}$ requires three integration points due to the product of the shape functions $N_I N_A$.

Finally, the elemental Jacobian or stiffness matrix is defined from equations (C-44), (C-47), (C-48), and (C-49).

$$\mathbf{K}_{IA}^{h} = \begin{bmatrix} \mathbf{K}^{uu} & \mathbf{K}^{u\pi} \\ \mathbf{K}^{\pi u} & \mathbf{K}^{\pi\pi} \end{bmatrix}_{IA}^{h} \tag{C-50}$$

A summary of the definition and implementation of the discretized stiffness matrix is given in Box C.2

Element stiffness matrix $\mathbf{K}^e$

$$\mathbf{K}^e = \begin{bmatrix} \mathbf{K}^{uu} & \mathbf{K}^{u\pi} \\ \mathbf{K}^{\pi u} & \mathbf{K}^{\pi\pi} \end{bmatrix} = \begin{bmatrix} \left(K^{uu}\right)_{Ii,Jj} & \left(K^{u\pi}\right)_{Ii,A} \\ \left(K^{\pi u}\right)_{I,Ak} & \left(K^{\pi\pi}\right)_{I,A} \end{bmatrix} \qquad \begin{matrix} (I,J,A=1:3) \\ (i,j,k=1:2) \end{matrix}$$

where:

$$\left[K^{uu}\right]_{Ii,Jj} = \left[K^{\text{geo}}\right]_{Ii,Jj} + \left[K^{\text{mat}}\right]_{Ii,Jj}$$

$$\left[K^{\text{geo}}\right]_{Ii,Jj} = \delta_{ij} \frac{\partial N_I}{\partial x_k} \frac{\partial N_J}{\partial x_l} \sigma_{lk} \left|\Omega^e\right|$$

$$\left[K^{\text{mat}}\right]_{Ii,Jj} = \frac{\partial N_I}{\partial x_k} c^{\text{ep}}_{iklj} \frac{\partial N_J}{\partial x_l} \left|\Omega^e\right|$$

$$\left[K^{u\pi}\right]_{Ii,A} = \frac{\partial N_I}{\partial x_i} N_A \left|\Omega^e\right|$$

$$\left[K^{\pi u}\right]_{I,Ak} = \left(\frac{1-J}{J^2}\right) N_I \frac{\partial N_A}{\partial x_k} \left|\Omega^e\right|$$

$$\left[K^{\pi\pi}\right]_{I,A} = \frac{1}{\kappa} N_I N_A \left|\Omega^e\right|$$

Vector of residual forces $\left[\mathbf{R}^u\right]$

$$\left[\mathbf{R}^u\right] = \left[\mathbf{F}^{\text{int,mix}}\right] - \left[\mathbf{F}^{\text{ext}}\right] + \left[\mathbf{F}^{\text{ine}}\right] = 0$$

where:

$$\left[\mathbf{F}^{\text{int,mix}}\right]_I^e = \int_{\Omega^e} \boldsymbol{\sigma}^e \cdot \nabla(N_I)\, d\Omega^e$$

$$\left[\mathbf{F}^{\text{ext}}\right]_I^e = \int_{\Omega^e} N_I \rho^e \mathbf{b}^e d\Omega^e + \int_{\Gamma^e} N_I \bar{\mathbf{t}}^e\, d\Gamma^e$$

$$\left[\mathbf{F}^{\text{ine}}\right]_I^e = \int_{\Omega^e} N_I \rho^e \dot{\mathbf{v}}^e d\Omega^e$$

Vector of residual forces $\left[\mathbf{R}^q\right]$

$$\left[\mathbf{R}^q\right]_I^e = \int_{\Omega^e} N_I \left(\frac{\ln J^e}{J^e} - \frac{1}{\kappa} N_A \pi^e\right) d\Omega^e$$

And

$$\left|\Omega^e\right| = \int_{\Omega^e} d\Omega^e$$

Box C.2. Element stiffness matrix $\mathbf{K}^e$ and vector of residual forces $\mathbf{R}$ (integration for a three nodes linear triangle in the current configuration t_{n+1}).

Appendix D
Mixed formulation in axisymmetric problems

In this section, we develop the vector of generalized forces and the stiffness matrix corresponding to the mixed formulation for the axisymmetric case.

D.1. Vector of nodal forces

From equation (3.42) we know that the expression for the internal work is given by[10,11].

$$G^{\text{int,mix}} = \int_{\Omega_{n+1}} \sigma_{ij} : \nabla_{n+1}(\delta w)_{ij}\, d\Omega_{n+1} \tag{D-1}$$

where $\sigma_{ij} = \text{dev}(\sigma)_{ij} + \pi 1_{ij}$ .The extension to the axisymmetric case is formalized as

$$G^{\text{int,mix,axi}} = \int_{\Omega^e_{n+1}} \sigma^{\text{mix,axi}}_{ij} : \nabla^{\text{axi}}_{n+1}(\delta w)_{ij}\, d\Omega^{\text{axi}}_{n+1} \tag{D-2}$$

[10] The formulation for this Appendix is directly described in a discretized notation.

[11] As mentioned in previous chapters, the superscript "mix" refers to the definition of $\boldsymbol{\sigma}$ in terms of $\mathbf{u}$ and π .

where:

$$\sigma_{n+1}^{\text{mix,axi}} = \begin{bmatrix} \sigma_{11} & \sigma_{12} & 0 \\ \sigma_{21} & \sigma_{22} & 0 \\ 0 & 0 & \sigma_{33} \end{bmatrix} \tag{D-3}$$

and

$$\nabla_{n+1}^{\text{axi}} (\delta w)_{ij} = \begin{bmatrix} \dfrac{\partial (\delta w)_1}{\partial x_1^{n+1}} & \dfrac{\partial (\delta w)_1}{\partial x_2^{n+1}} & 0 \\ \dfrac{\partial (\delta w)_2}{\partial x_1^{n+1}} & \dfrac{\partial (\delta w)_2}{\partial x_2^{n+1}} & 0 \\ 0 & 0 & \dfrac{\delta w_1}{x_1^{n+1}} \end{bmatrix} \tag{D-4}$$

Taking into account equations (D-3) and (D-4), the expression for the internal work, defined in equation (D-2), is split in terms of , on the one hand, a matrix $[2\times 2]$ (r and z components) and, on the other hand, the term (33) corresponding to θ :

$$G^{\text{int,mix,axi}} = \int_{\Omega_{n+1}^e} \sigma_{ij}^{\text{mix,axi}} \nabla_{n+1}^{\text{axi}} (\delta w)_{ij} \Big|_{i,j:1,2} d\Omega_{n+1}^{\text{axi}} + \int_{\Omega_{n+1}^e} \sigma_{33}^{\text{mix,axi}} \nabla_{n+1}^{\text{axi}} (\delta w)_{33} \, d\Omega_{n+1}^{\text{axi}} \tag{D-5}$$

From equation (D-5), and taking into account the approximations given in equations (3.46) and the expression of its gradient in (C-38), the vector of internal forces is defined as

$$\left[F^{\text{int,mix,axi}} \right]_{Ii} = \int_{\Omega_{n+1}^e} \sigma_{ij} \frac{\partial N_I}{\partial x_j} \Big|_{i,j:1,2} d\Omega_{n+1}^{\text{axi}} + \int_{\Omega_{n+1}^e} \sigma_{33} \frac{N_I}{x_1^{n+1}} \delta_{i1} d\Omega_{n+1}^{\text{axi}} \tag{D-6}$$

It is important to remark that the computation of $\sigma_{33} = \frac{1}{J_{n+1}} \tau_{33}$ requires three Gauss points for its integration; the problem arises from the computation of the deformation gradient tensor $\mathbf{f}_{n+1} = \mathbf{1} + \nabla_n (\Delta \mathbf{u}_{n+1})$, where the component $\mathbf{f}_{33}^{\text{axi}}$ has the following expression

$$\mathbf{f}_{33}^{\text{axi}} = 1 + \frac{u_1(\mathbf{x})}{x_1} = 1 + \frac{N_I(\mathbf{x}) u_{I1}}{x_1} \tag{D-7}$$

being a function that varies with respect to $\mathbf{x}$ (as opposed to the rest of components $\mathbf{f}_{ij} \big|_{i,j:1,2}$, that are constant at the element level). For this reason, the component σ_{33} of equation (D-6) and the computation of J_{n+1} require three Gauss points in their integration.

Finally, the expression of the incompressibility term, given in equation (3.43) is directly described for the axisymmetric case as

$$\left[R^{\mathrm{q,axi}}\right]_{Ii} = \int_{\Omega^e_{n+1}} N_I \frac{\ln J_{n+1}}{\left(J_{n+1}\right)^2} d\Omega^{\mathrm{axi}}_{n+1} - \int_{\Omega^e_{n+1}} \frac{1}{J_{n+1}\kappa} N_I N_A \pi_A d\Omega^{\mathrm{axi}}_{n+1} \qquad \text{(D-8)}$$

D.2. Stiffness matrix

The extension for the Jacobian matrix to the axisymmetric case is carried out in a similar way than in Appendix C, presenting each term of the derivatives of equations (3.48) and (3.52) separately.

- $\delta_{\Delta u} F^{\mathrm{int,mix,axi}}$

The vector of internal forces is decomposed as

$$F^{\mathrm{int,mix,axi}} = F^{\mathrm{int,mix,axi},(2\times 2)} + F^{\mathrm{axi},(33)} \qquad \text{(D-9)}$$

where:

$$F^{\mathrm{int,mix,axi},(2\times 2)} = \int_{\Omega^e_n} \frac{1}{J_n} \mathrm{f}^{axi}_{ik} \mathrm{S}^{axi}_{kj} \left.\frac{\partial N_I}{\partial x_j}\right|_{i,j:1,2} d\Omega^{axi}_n \qquad \text{(D-10)}$$

$$F^{\mathrm{int,mix,axi}} = \int_{\Omega^e_n} \frac{1}{J_n} \frac{N_I \delta_{i1}}{x^n_1} \mathrm{f}^{axi}_{33} \mathrm{S}^{axi}_{33} \, d\Omega^{axi}_n \qquad \text{(D-11)}$$

Similarly, the term of the derivative of the internal work with respect to the incremental displacement is split as

$$\delta_{\Delta u} F^{\mathrm{int,mix,axi}} = \delta_{\Delta u} F^{\mathrm{int,mix,axi},(2\times 2)} + \delta_{\Delta u} F^{\mathrm{axi},(33)} \qquad \text{(D-12)}$$

The first term of the RHS of equation (D-12) was calculated in Appendix C and it is equivalent, for an axisymmetric model, to:

$$\begin{aligned} \delta_{\Delta u} F^{\mathrm{int,mix,axi},(2\times 2)} = &\left(\int_{\Omega^e_{n+1}} \delta_{ij} \frac{\partial N_I}{\partial x_k} \frac{\partial N_J}{\partial x_l} \sigma^{axi}_{lk} \, d\Omega^e_{n+1} \right) \Delta\tilde{u}_{Ji} + \\ &\left(\int_{\Omega^e_{n+1}} \frac{1}{J_{n+1}} \frac{\partial N_I}{\partial x_k} \mathrm{c}^{\mathrm{ep}}_{iklj} \frac{\partial N_J}{\partial x_l} \, d\Omega^e_{n+1} \right) \Delta\tilde{u}_{Jj} \end{aligned} \qquad \text{(D-13)}$$

Notice that, from the first term of the RHS of equation (D-13), the geometric part of the stiffness matrix $\left[K^{\mathrm{geo}}\right]^h_{IJ}$ given in equation (C-45) in Appendix C, is defined. For the axisymmetric case, this term reads:

$$G^{\mathrm{axi}}_{IJ} = \int_{\Omega^e_{n+1}} \delta_{ij} \frac{\partial N_I}{\partial x_k} \frac{\partial N_J}{\partial x_l} \sigma^{axi}_{lk} \, d\Omega^e_{n+1} \qquad \text{(D-14)}$$

In the second term of the RHS of equation (D-13), the double dot contraction of the term $\mathrm{c}^{\mathrm{ep}}_{iklj} \delta e_{lj}$ is split as

$$c_{iklj}^{\text{ep}} \frac{\partial N_J}{\partial x_l} = c_{iklj}^{\text{ep}} \frac{\partial N_J}{\partial x_k} + c_{ik33}^{\text{ep}} \frac{\partial N_J}{\partial x_1^{n+1}} \tag{D-15}$$

and substituting equation (D-15) into equation (D-13), the expression of the integrand becomes expressible as

$$\int_{\Omega_{n+1}^e} \frac{1}{J_{n+1}} \frac{\partial N_I}{\partial x_k} c_{iklj}^{\text{ep}} \frac{\partial N_J}{\partial x_l} d\Omega_{n+1}^e = H_{IJ}^{\text{axi}} + \tilde{H}_{IJ}^{\text{axi}} \tag{D-16}$$

where:

$$H_{IJ}^{\text{axi}} = \int_{\Omega_{n+1}^e} \frac{1}{J_{n+1}} \frac{\partial N_I}{\partial x_k} c_{iklj}^{\text{ep}} \frac{\partial N_J}{\partial x_l} d\Omega_{n+1}^e \tag{D-17}$$

$$\tilde{H}_{IJ}^{\text{axi}} = \int_{\Omega_{n+1}^e} \frac{1}{J_{n+1}} \frac{\partial N_I}{\partial x_k} c_{ik33}^{\text{ep}} \frac{N_J}{x_1^{n+1}} d\Omega_{n+1}^e \tag{D-18}$$

On the other hand, the second term of the RHS of equation (D-12), after the *pull-back* operation, is given by

$$\partial_{\Delta u} F^{\text{axi},(33)} = \partial \hat{G}_{IJ}^{\text{axi},(33)} + \partial \hat{H}_{IJ}^{\text{axi},(33)} \tag{D-19}$$

where:

$$\partial \hat{G}_{IJ}^{\text{axi},(33)} = \int_{\Omega_n^e} \delta_{i1} \frac{N_I}{j_n x_1^n} \partial f_{33} S_{33} d\Omega_n^{\text{axi}} \tag{D-20}$$

$$\partial \hat{H}_{IJ}^{\text{axi},(33)} = \int_{\Omega_n^e} \delta_{i1} \frac{N_I}{j_n x_1^n} f_{33} \partial S_{33} d\Omega_n^{\text{axi}} \tag{D-21}$$

After computing the derivative of the corresponding component of the deformation gradient $\partial f_{33} = N_J u_{J1} / x_1^n$, equation (D-20) takes the form

$$\left[\partial \hat{G}_{IJ}^{\text{axi},(33)} \right]_n = \int_{\Omega_n^e} \delta_{i1} \frac{1}{j_n} \frac{N_I}{x_1^n} \frac{N_J}{x_1^n} \delta u_{J1} S_{33}^{axi} d\Omega_n^{\text{axi}} \tag{D-22}$$

whereas the corresponding component of the stiffness matrix of equation (D-22) is expressed in the current configuration t_{n+1} (after some manipulation) as

$$\hat{G}_{IJ}^{\text{axi},(33)} = \int_{\Omega_{n+1}^e} \delta_{i1} \delta_{j1} N_I N_J \frac{\sigma_{33}^{axi}}{\left(x_1^{n+1} \right)^2} d\Omega_{n+1}^{\text{axi}} \tag{D-23}$$

For the second term, expressed in equation (D-21), it could be proved that:

$$f_{33} \partial S_{33} = f_{33}^{-1} c_{33lj}^{ep,mix} \partial e_{lj} \tag{D-24}$$

and with the definition of the Euler-Almansi strain tensor, equation (D-24) can be rewritten as

$$f_{33}\partial S_{33} = f_{33}^{-1} c_{33lj}^{ep,mix} \frac{1}{2}\left(\frac{\partial u_l}{\partial u_j^{n+1}} + \frac{\partial u_j}{\partial u_l^{n+1}} \right)^{\text{axi}} \tag{D-25}$$

It is observed from equation (D-4) that equation (D-25) could be rewritten as

$$f_{33}\partial S_{33} = f_{33}^{-1} c_{33lj}^{ep,mix} \frac{\partial u_l}{\partial u_{n+1}}\bigg|_{l,j:1,2} + f_{33}^{-1} c_{3333}^{ep,mix} \frac{\partial u_1}{\partial u_1^{n+1}} \tag{D-26}$$

Finally, substituting equation (D-26) into equation (D-21) yields (in the reference configuration)

$$\left[\partial \hat{H}_{IJ}^{\text{axi},(33)}\right]_n = \int_{\Omega_n^e} \delta_{i1} \frac{N_I}{j_n x_1^n} f_{33}^{-1} c_{33lj}^{ep,mix} \frac{\partial N_J}{\partial u_l^{n+1}} \delta u_{Jj} d\Omega_n^{\text{axi}} + \int_{\Omega_n^e} \delta_{i1}\delta_{j1} \frac{N_I}{j_n x_1^n} f_{33}^{-1} c_{3333}^{ep,mix} \frac{N_J}{x_1^{n+1}} \delta u_{Jl} d\Omega_n^{\text{axi}} \tag{D-27}$$

Similarly than in the previous term of the stiffness matrix, from equation (D-27) the corresponding term of the stiffness matrix for equation (D-21) is obtained (expressed in the current configuration) as

$$\hat{H}_{IJ}^{\text{axi},(33)} = \int_{\Omega_{n+1}^e} \delta_{i1} \frac{1}{J_{n+1} x_1^{n+1}} N_I c_{33lj}^{ep,mix} \frac{\partial N_J}{\partial u_l^{n+1}} d\Omega_{n+1}^{\text{axi}} + \int_{\Omega_{n+1}^e} \delta_{i1}\delta_{j1} \frac{N_I}{J_{n+1}} c_{3333}^{ep,mix} \frac{N_J}{\left(x_1^{n+1}\right)^2} d\Omega_{n+1}^{\text{axi}} \tag{D-28}$$

Finally, using equation (D-14), (D-17), (D-18), (D-23), and (D-28), the term $\left[K^{uu}\right]_{IiJj}$ of the Jacobian matrix takes the form

$$\left[K^{uu}\right]_{IiJj} = G_{IJ}^{\text{axi}} + H_{IJ}^{\text{axi}} + \tilde{H}_{IJ}^{\text{axi}} + \hat{G}_{IJ}^{\text{axi},(33)} + \hat{H}_{IJ}^{\text{axi},(33)} \tag{D-29}$$

- $\delta_\pi F^{\text{int,mix,axi}}$

From the decoupling into deviatoric and volumetric part of the Second Piola-Kirchhoff stress tensor $\mathbf{S}^{\text{mix}} = \text{DEV}\mathbf{S} + Jp\mathbf{C}^{-1}$ the derivative of equation (D-9) with respect to the pressure is given by

$$\partial_\pi F^{\text{int,mix,axi}} = \int_{\Omega_n^e} \frac{1}{j_n} f_{ik}^{axi} J_{n+1} \partial p C_{kj}^{-1} \frac{\partial N_I}{\partial x_j^n}\bigg|_{i,j:1,2} d\Omega_n^{\text{axi}} + \int_{\Omega_n^e} \frac{1}{j_n} \frac{N_I \delta_{i1}}{x_1^n} f_{33}^{axi} J_{n+1} \partial p C_{33}^{-1} d\Omega_n^{\text{axi}} \tag{D-30}$$

The computation of the first term of the RHS of equation (D-30) was deduced in in Appendix C and given by equation (C-47):

$$\delta_{\pi} F^{\text{int,mix,axi}} = \int_{\Omega^e_{n+1}} \frac{\partial N_I}{\partial x_i^n} N_A \tilde{\pi}_A \, d\Omega^{\text{axi}}_{n+1} \tag{D-31}$$

For the second term of the RHS of equation (D-30), after some manipulation and taking into account the definition $C_{33}^{-1} = 1/(f_{33})^2$, we can write

$$\delta_{\pi} F^{\text{axi},(33)} = \int_{\Omega^e_{n+1}} \delta_{i1} \frac{1}{x_1^{n+1}} N_I N_A \tilde{\pi}_A \, d\Omega^{\text{axi}}_{n+1} \tag{D-32}$$

Finally, from equations (D-31) and (D-32), the corresponding term of the stiffness matrix $\left[K^{u\pi}\right]_{IiJj}$ is obtained:

$$\left[K^{u\pi}\right]_{IiJj} = L^{\text{axi}}_{IJ} + \hat{L}^{\text{axi},(33)}_{IJ} \tag{D-33}$$

where:

$$L^{\text{axi}}_{IJ} = \int_{\Omega^e_{n+1}} \frac{\partial N_I}{\partial x_i^n} N_A \, d\Omega^{\text{axi}}_{n+1} \tag{D-34}$$

$$\hat{L}^{\text{axi},(33)}_{IJ} = \int_{\Omega^e_{n+1}} \delta_{i1} \frac{1}{x_1^{n+1}} N_I N_A \, d\Omega^{\text{axi}}_{n+1} \tag{D-35}$$

- $\delta_{\Delta u} R^{\text{q,axi}}$

This derivative is deduced in equation (C-48) in Appendix C; it should be noted that for its extension to the axisymmetric case, we have to introduce the following decomposition

$$\delta_{\Delta u} R^{\text{q,axi}} = \int_{\Omega^e_{n+1}} N_I \left(\frac{1-J}{J^2}\right) \left[\frac{\partial N_A}{\partial x_k^{n+1}} \Delta u_{Ak} \big|_{k:1,2} + \frac{N_A}{x_1^{n+1}} \Delta u_{A1} \right] d\Omega^{\text{axi}}_{n+1} \tag{D-36}$$

On the other hand, the term $\left[K^{\pi u}\right]_{IiJj}$ of the stiffness matrix is given by

$$\left[K^{\pi u}\right]_{IiJj} = \int_{\Omega^e_{n+1}} N_I \left(\frac{1-J}{J^2}\right) \left[\frac{\partial N_A}{\partial x_k^{n+1}} \bigg|_{k:1,2} + \frac{N_A}{x_1^{n+1}} \right] d\Omega^{\text{axi}}_{n+1} \tag{D-37}$$

- $\delta_{\pi} R^{\text{q,axi}}$

This last term is deduced directly from equation (C-49) in Appendix C; its axisymmetric counterpart reads

$$\delta_{\pi} R^{\text{q,axi}} = \int_{\Omega^e_{n+1}} \frac{1}{J_{n+1} \mathcal{K}} N_I N_A \tilde{\pi}_A \, d\Omega^{\text{axi}}_{n+1} \tag{D-38}$$

and the corresponding term of the stiffness matrix $\left[K^{\pi\pi}\right]_{IJ}$ is

$$\left[K^{\pi\pi}\right]_{IA} = \int_{\Omega^e_{n+1}} \frac{1}{J_{n+1}\kappa} N_I N_A \, d\Omega^{\text{axi}}_{n+1} \tag{D-39}$$

Implementation for a three Gauss point integration

The integration of a given function g in an axisymmetric domain is rewritten by its integration as a solid of revolution

$$\int_{\Omega^e_{n+1}} g \, d\Omega^{\text{axi}}_{n+1} = \int_{\Omega^e_{n+1}} g\left(2\pi x_1^{n+1}\right) dA^e_{n+1} \tag{D-40}$$

As well as the component (33) of the deformation gradient $\mathbf{f}^{\text{axi}}$, equation (D-40) requires at least three Gauss points for its proper integration:

$$\int_{\Omega^e_{n+1}} g\left(2\pi x_1^{n+1}\right) dA^e_{n+1} = \sum_{i=1}^{n_{gp}} \tilde{\text{w}}_i \left|\mathbf{J}^e(\xi_i)\right| g(\xi_i)\left(2\pi x_{i,1}^{n+1}\right) \tag{D-41}$$

where $n_{gp} = 3$, $\tilde{\text{w}}_i$ are the corresponding quadrature weights, and $\mathbf{J}^e$ the Jacobian for the mapping to the parent domain, which for a three-node triangle is constant given by $\mathbf{J}^e = 2A^e$.

Taking into account equations (D-40) and (D-41), Box D.1 summarizes the implementation of the generalized force vectors and the stiffness matrix.

Stiffness matrix $\mathbf{K}^h$

$$\mathbf{K}^{h,\text{axi}} = \begin{bmatrix} \mathbf{K}^{uu} & \mathbf{K}^{u\pi} \\ \mathbf{K}^{\pi u} & \mathbf{K}^{\pi\pi} \end{bmatrix}^{\text{axi}} = \begin{bmatrix} \left(K^{uu}\right)^{\text{axi}}_{IiJj} & \left(K^{u\pi}\right)^{\text{axi}}_{IiA} \\ \left(K^{\pi u}\right)^{\text{axi}}_{IAk} & \left(K^{\pi\pi}\right)^{\text{axi}}_{IA} \end{bmatrix}$$

where:

$$\left[K^{uu}\right]_{IiJj} = \left[G^{\text{axi}}\right]_{IiJj} + \left[H^{\text{axi}}\right]_{IiJj} + \left[\tilde{H}^{\text{axi}}\right]_{IiJj} + \left[\hat{G}^{\text{axi},(33)}\right]_{IiJj} + \left[\hat{H}^{\text{axi},(33)}\right]_{IiJj}$$

$$\left[G^{\text{axi}}\right]_{IiJj} = \sum_{kg}^{3} \left\{ \delta_{ij} \frac{\partial N_I}{\partial x_k} \frac{\partial N_J}{\partial x_l} \sigma^{axi}_{lk} 2\pi x^{n+1}_{kg,1} \right\}\Big|_{x_g} \cdot \tilde{\text{w}}_{kg} \cdot 2A^e_{n+1}$$

$$\left[H^{\text{axi}}\right]_{IiJj} = \sum_{kg}^{3} \left\{ \frac{1}{J_{n+1}} \frac{\partial N_I}{\partial x_k} c^{\text{ep}}_{iklj} \frac{\partial N_J}{\partial x_l} 2\pi x^{n+1}_{kg,1} \right\}\Big|_{x_g} \cdot \tilde{\text{w}}_{kg} \cdot 2A^e_{n+1}$$

$$\left[\tilde{H}^{\text{axi}}\right]_{IiJj} = \sum_{kg}^{3} \left\{ \frac{1}{J_{n+1}} \frac{\partial N_I}{\partial x_k} c^{\text{ep}}_{ik33} N_J \delta_{j1} 2\pi \right\}\Big|_{x_g} \cdot \tilde{\text{w}}_{kg} \cdot 2A^e_{n+1}$$

Box D.1. Stiffness matrix $\mathbf{K}^{h,\text{axi}}$ and vector of residual forces $\mathbf{R}^{h,\text{axi}}$ for axisymmetric problems (integration for a three nodes linear triangle in the current configuration t_{n+1}).

$$\left[\hat{G}^{\mathrm{axi},(33)}\right]_{IiJj} = \sum_{kg}^{3} \delta_{i1}\delta_{j1} \left\{ N_I N_J \frac{\sigma_{33}^{axi}}{x_{kg,1}^{n+1}} 2\pi \right\}\Big|_{x_g} \cdot \tilde{\mathrm{w}}_{kg} \cdot 2A_{n+1}^{e}$$

$$\left[\hat{H}^{\mathrm{axi},(33)}\right]_{IiJj} = \sum_{kg}^{3} \left\{ \frac{1}{J_{n+1}} \delta_{i1} N_I c_{33lj}^{ep,mix} \frac{\partial N_J}{\partial x_l^{n+1}} 2\pi \right\}\Big|_{x_g} \cdot \tilde{\mathrm{w}}_{kg} \cdot 2A_{n+1}^{e} +$$

$$\sum_{kg}^{3} \left\{ \frac{1}{J_{n+1}} \delta_{i1}\delta_{j1} N_I c_{3333}^{ep,mix} \frac{N_J}{x_{kg,1}^{n+1}} 2\pi \right\}\Big|_{x_g} \cdot \tilde{\mathrm{w}}_{kg} \cdot 2A_{n+1}^{e}$$

$$\left[K^{u\pi}\right]_{IiA} = L_{IiA}^{\mathrm{axi}} + \hat{L}_{IiA}^{\mathrm{axi},(33)}$$

$$L_{IiA}^{\mathrm{axi}} = \sum_{kg}^{3} \left\{ \frac{\partial N_I}{\partial x_i^{n+1}} N_A 2\pi x_{kg,1}^{n+1} \right\}\Big|_{x_g} \cdot \tilde{\mathrm{w}}_{kg} \cdot 2A_{n+1}^{e}$$

$$\hat{L}_{IiA}^{\mathrm{axi},(33)} = \sum_{kg}^{3} \{ \delta_{i1} N_I N_A 2\pi \}\big|_{x_g} \cdot \tilde{\mathrm{w}}_{kg} \cdot 2A_{n+1}^{e}$$

$$\left[K^{\pi u}\right]_{IAk} = \sum_{kg}^{3} \left\{ N_I \left(\frac{1-J}{J^2} \right) \left(\frac{\partial N_A}{\partial x_j^{n+1}} x_1^{n+1} + N_A \delta_{j1} \right) 2\pi \right\}\Big|_{x_g} \cdot \tilde{\mathrm{w}}_{kg} \cdot 2A_{n+1}^{e}$$

$$\left[K^{\pi\pi}\right]_{IA} = \sum_{kg}^{3} \left\{ \frac{1}{J_{n+1}\kappa} N_I N_A 2\pi x_{kg,1}^{n+1} \right\}\Big|_{x_g} \cdot \tilde{\mathrm{w}}_{kg} \cdot 2A_{n+1}^{e}$$

Generalized forces $\left[\mathbf{F}^{\mathrm{int,mix,axi}}\right]_{Ii}$ and $\left[\mathbf{R}^{\mathrm{q,axi}}\right]_{I}^{h}$

$$\left[\mathbf{F}^{\mathrm{int,mix,axi}}\right]_{Ii} = \sum_{kg}^{3} \left\{ \left(\sigma_{ij} \frac{\partial N_I}{\partial x_j^{n+1}} + \sigma_{33} \frac{N_I}{x_{kg,1}^{n+1}} \delta_{i1} \right) 2\pi x_{kg,1}^{n+1} \right\}\Big|_{x_g} \cdot \tilde{\mathrm{w}}_{kg} \cdot 2A_{n+1}^{e} +$$

$$\left[\mathbf{R}^{\mathrm{q,axi}}\right]_{Ii} = \sum_{kg}^{3} \left\{ N_I \frac{\ln J_{n+1}}{\left(J_{n+1}\right)^2} 2\pi x_{kg,1}^{n+1} \right\}\Big|_{x_g} \cdot \tilde{\mathrm{w}}_{kg} \cdot 2A_{n+1}^{e} +$$

$$\sum_{kg}^{3} \left\{ \frac{1}{J_{n+1}\kappa} N_I N_A 2\pi x_{kg,1}^{n+1} \right\}\Big|_{x_g} \cdot \tilde{\mathrm{w}}_{kg} \cdot 2A_{n+1}^{e}$$

Box D.1. (Continued)

Appendix E
Visco-elastic regularization of the constitutive model

In order to dissipate the dynamic oscillations present in the stress fields, it is proposed a visco-elastic regularization of the constitutive model for granular flows. The regularization is based on a Kelvin-Voigt model in terms of the rate of deformation tensor. In this section are presented the definition of this additional term as well as the pertinent modifications for the implementation in the Jacobian matrix.

E.1. Kelvin-Voigt visco-elastic model

The rheological model of the Kelvin-Voigt model consists of the connection in parallel of a Newtonian damper and a Hookean elastic spring. The constitutive equation, for a small deformation formulation, is expressed for both terms giving

$$\boldsymbol{\sigma}(t) = E\boldsymbol{\varepsilon}(t) + \eta \frac{d\boldsymbol{\varepsilon}(t)}{dt} \tag{E-1}$$

where E is the Young modulus and η the dissipative coefficient. The first term of the RHS corresponds to the Hookean elastic spring while the second to the visco regularization itself.

The constitutive model proposed for dense granular flows is defined in the framework of large deformation plasticity; the first term corresponding to the elastic

term is defined by equation (2.35), and the term associated to the Newtonian damper is given by establishing the pressure as a function of its density[12].

$$\pi = \pi(\rho) \tag{E-2}$$

The time derivative of equation (E-2) is obtained applying the chain rule

$$\dot{\pi} = \frac{d\pi(\rho)}{d\rho}\dot{\rho} \tag{E-3}$$

The time derivative of the density, given in equation (E-3), is obtained aided by the definition of the rate form of the continuity mass equation.

$$\dot{\rho}(\mathbf{x},t) + \rho(\mathbf{x},t)\,\mathrm{div}\mathbf{v}(\mathbf{x},t) = 0 \tag{E-4}$$

Solving equation (E-4) for $\dot{\rho}$ and substituting the value into equation (E-3), the rate form of the pressure is described in terms of the velocity components.

$$\dot{\pi} = -\frac{d\pi(\rho)}{d\rho}\rho(\mathbf{x},t)\,\mathrm{div}\mathbf{v}(\mathbf{x},t) \tag{E-5}$$

Equation (E-5) is rewritten in terms of the rate of deformation tensor and a material bulk modulus parameter

$$\dot{\pi} = \kappa_2(\rho)\,\mathrm{tr}\,\mathbf{d} \tag{E-6}$$

where κ_2 is approximated by the two first terms of a Taylor expansion of a compressibility curve; and for the second term, the equality $\mathrm{tr}\,\mathbf{d} = \mathrm{div}\mathbf{v}$ is used, which is easily deduced using the definition of the rate of deformation tensor. Since the material is considerable incompressible, it is correct to assume a constant value for the bulk modulus.

The numerical approximation of the time derivative for the pressures allows us to relate the dissipative coefficient η with the bulk modulus κ_2, $\eta = \eta(\kappa_2)$, defining the corresponding term of the Newtonian damper. The pressure term, given in equation (2.34), with the Kelvin-Voigt regularization is expressed by

$$\pi = \kappa_1 \frac{\ln J}{J} + \eta\,\mathrm{tr}\,\mathbf{d} \tag{E-7}$$

The visco-elastic regularization has effect on the second equation of the mixed formulation given by equation (2.40). Rewriting this equation to include the additional term, it is expressed as

$$\int_{\Omega_t} \delta q \left(\frac{\ln J}{J} + \frac{\eta}{\kappa}\mathrm{tr}\,\mathbf{d} - \frac{1}{\kappa}\pi \right) \frac{1}{J} d\Omega_t = 0 \tag{E-8}$$

[12] Recalling that π stands for the pressure term associated to the Cauchy stress tensor and p for the pressure term corresponding to the Kirchhoff stress tensor.

Bibliography

[1] M. R. Aboutorabi, *An Endochronic Plasticity Model for the Coupled Non-linear Mechanical Response of Porous and Granular Materials*: University of Iowa, 1986.

[2] I. Babuska and A. K. Aziz, "On the Angle Condition in the Finite Element Method," *SIAM Journal on Numerical Analysis,* vol. 13, pp. 214-226, 1976.

[3] T. Belytschko, W. K. Liu, and B. Moran, *Nonlinear Finite Elements for Continua and Structures*: John Wiley & Sons, 2000.

[4] E. J. Benink, *Flow and Stress Analysis of Cohesionless Bulk Materials in Silos Related to Codes*, 1989.

[5] R. Boer and W. Brauns, "Kinematic hardening of granular materials," *Ingenieur-Archiv,* vol. 60, pp. 463-480, 1990/01/01 1990.

[6] J. W. Bonet, R. D., *Nonlinear Continuum Mechanics for Finite Element Analysis*: Cambridge University Press, 1997.

[7] T. Borzsonyi and R. Stannarius, "Granular materials composed of shape-anisotropic grains," *Soft Matter,* vol. 9, pp. 7401-7418, 2013.

[8] R. W. Boulanger and K. Ziotopoulou, "Formulation of a sand plasticity plane-strain model for earthquake engineering applications," *Soil Dynamics and Earthquake Engineering,* vol. 53, pp. 254-267, 2013.

[9] C. E. Brennen, *Fundamentals of Multiphase Flow*: Cambridge University Press, 2005.

[10] S. Brenner and R. Scott, *The Mathematical Theory of Finite Element Methods*: Springer, 2007.

[11] H. H. Bui, R. Fukagawa, K. Sako, and J. C. Wells, "Numerical Simulation of Granular Materials Based on Smoothed Particle Hydrodynamics (SPH)," *AIP Conference Proceedings,* vol. 1145, pp. 575-578, 2009.

[12] J. Cante, M. D. Riera, J. Oliver, J. Prado, A. Isturiz, and C. Gonzalez, "Flow regime analyses during the filling stage in powder metallurgy

processes: experimental study and numerical modelling," *Granular Matter,* vol. 13, pp. 79-92, 2011/02/01 2011.

[13] J. C. Cante, J. Oliver, and S. Oller, "Simulación numérica de procesos de compactación de pulvimateriales: aplicación de técnicas de cálculo paralelo," Escola Tècnica Superior d'Enginyers de Camins, Canals i Ports de Barcelona, Universitat Politècnica de Catalunya, 1995.

[14] J. Carbonell, E. Oñate, and B. Suárez, "Modeling of Ground Excavation with the Particle Finite-Element Method," *Journal of Engineering Mechanics,* vol. 136, pp. 455-463, 2010/04/01 2009.

[15] M. E. Cates, J. P. Wittmer, J. P. Bouchaud, and P. Claudin, "Jamming and static stress transmission in granular materials," *Chaos: An Interdisciplinary Journal of Nonlinear Science,* vol. 9, pp. 511-522, 1999.

[16] P. W. Cleary, "Charge behaviour and power consumption in ball mills: sensitivity to mill operating conditions, liner geometry and charge composition," *International Journal of Mineral Processing,* vol. 63, pp. 79-114, 2001.

[17] B. Clermont and B. de Haas, "Optimization of mill performance by using online ball and pulp measurements," *The Journal of the Southern African Institute of Mining and Metallurgy,* vol. 110, p. 8, March 2010 2010.

[18] P. Coussot, *Rheometry of Pastes, Suspensions, and Granular Materials: Applications in Industry and Environment*: Wiley, 2005.

[19] P. Coussot and M. Meunier, "Recognition, classification and mechanical description of debris flows," *Earth-Science Reviews,* vol. 40, pp. 209-227, 1996.

[20] S. C. Cowin and M. A. Goodman, "A Variational Principle for Granular Materials," *ZAMM - Journal of Applied Mathematics and Mechanics / Zeitschrift für Angewandte Mathematik und Mechanik,* vol. 56, pp. 281-286, 1976.

[21] P. A. Cundall and O. D. L. Strack, "A discrete numerical model for granular assemblies," *Géotechnique,* vol. 29, pp. 47-65, 1979.

[22] H. W. Chandler, "A variational principle for granular materials," *International Journal for Numerical and Analytical Methods in Geomechanics,* vol. 12, pp. 371-378, 1988.

[23] D. J. Chen, D. K. Shah, and W. S. Chan, "Interfacial stress estimation using least-square extrapolation and local stress smoothing in laminated composites," *Computers & Structures,* vol. 58, pp. 765-774, 1996.

[24] J. F. Chen, J. M. Rotter, J. Y. Ooi, and Z. Zhong, "Flow pattern measurement in a full scale silo containing iron ore," *Chemical Engineering Science,* vol. 60, pp. 3029-3041, 2005.

[25] J. F. Chen, J. M. Rotter, J. Y. Ooi, and Z. Zhong, "Correlation between the flow pattern and wall pressures in a full scale experimental silo," *Engineering Structures,* vol. 29, pp. 2308-2320, 2007.

[26] J. Chung and G. M. Hulbert, "A Time Integration Algorithm for Structural Dynamics With Improved Numerical Dissipation: The Generalized-alpha Method," *Journal of Applied Mechanics,* vol. 60, pp. 371-375, 1993.

[27] Y. F. Dafalias and L. R. Herrmann, "Bounding surface formulation of soil plasticity," in *Soil Mechanics - Transient and Cyclic Loads*, G. N. Pande and O. C. Zienkiewicz, Eds., ed Chichester, U.K.: John Wiley and Sons, 1982, pp. 253-282.

[28] C. R. Dohrmann and P. B. Bochev, "A stabilized finite element method for the Stokes problem based on polynomial pressure projections," *International Journal for Numerical Methods in Fluids,* vol. 46, pp. 183-201, 2004.

[29] J. Duran, *Sands, Powders, and Grains: An Introduction to the Physics of Granular Materials (Partially Ordered Systems)*: Springer, 1999.

[30] H. Edelsbrunner, D. Kirkpatrick, and R. Seidel, "On the shape of a set of points in the plane," *Information Theory, IEEE Transactions on,* vol. 29, pp. 551-559, 1983.

[31] S. A. Elaskar, L. A. Godoy, D. D. Gray, and J. M. Stiles, "A viscoplastic approach to model the flow of granular solids," *International Journal of Solids and Structures,* vol. 37, pp. 2185-2214, 2000.

[32] B. Erskine. (2013). *Sale key to N.S. mine's fate*. Available: http://thechronicleherald.ca/business/1119942-sale-key-to-ns-mine-s-fate

[33] P. J. Frey and P. L. George, *Mesh Generation: Application to Finite Elements*: Hermes Science, 2000.

[34] P. L. George and H. Borouchaki, *Delaunay Triangulation and Meshing: Application to Finite Elements*: Hermès, 1998.

[35] C. González-Montellano, F. Ayuga, and J. Y. Ooi, "Discrete element modelling of grain flow in a planar silo: influence of simulation parameters," *Granular Matter,* vol. 13, pp. 149-158, 2011/04/01 2011.

[36] C. González, "El Método PFEM: aplicación a problemas industriales de pulvimetalurgia," Doctoral, Escola Tècnica Superior d'Enginyers de Camins, Canals i Ports de Barcelona, Universitat Politècnica de Catalunya. Departament de Resistència de Materials i Estructures a l'Enginyeria, Barcelona, Spain, 2009.

[37] G. Gustafsson, "Mechanical characterization and modelling of iron ore pellets," Doctoral, Division of Mechanics of Solid Materials, Luleå University of Technology, Sweden, 2012.

[38] M. Harr, "Stress Distribution," in *The Civil Engineering Handbook, Second Edition*, ed: CRC Press, 2002.

[39] S. Hartmann, J. Oliver, R. Weyler, J. C. Cante, and J. A. Hernández, "A contact domain method for large deformation frictional contact problems. Part 2: Numerical aspects," *Computer Methods in Applied Mechanics and Engineering,* vol. 198, pp. 2607-2631, 2009.

[40] J. M. Hill and A. P. S. Selvadurai, "Mathematics and mechanics of granular materials," in *Mathematics and Mechanics of Granular Materials*, J. Hill and A. P. S. Selvadurai, Eds., ed: Springer Netherlands, 2005, pp. 1-9.

[41] D. Hirshfeld and D. C. Rapaport, "Granular flow from a silo: Discrete-particle simulations in three dimensions," *The European Physical Journal E: Soft Matter and Biological Physics,* vol. 4, pp. 193-199, 2001.

[42] G. A. Holzapfel, *Nonlinear Solid Mechanics: A Continuum Approach for Engineering*: John Wiley & Sons, 2000.

[43] D. Humphrey, "Strength and Deformation," in *The Civil Engineering Handbook, Second Edition*, ed: CRC Press, 2002.

[44] M. Hürlimann, D. Rickenmann, and C. Graf, "Field and monitoring data of debris-flow events in the Swiss Alps," *Canadian Geotechnical Journal,* vol. 40, pp. 161-175, 2003/02/01 2003.

[45] S. Idelsohn, E. Onate, F. Pin, and N. Calvo, "Fluid–structure interaction using the particle finite element method," *Computer Methods in Applied Mechanics and Engineering,* vol. 195, pp. 2100-2123, 2006.

[46] S. R. Idelsohn, E. Oñate, and F. Del Pin, "A Lagrangian meshless finite element method applied to fluid–structure interaction problems," *Computers & Structures,* vol. 81, pp. 655-671, 2003.

[47] S. R. Idelsohn, E. Oñate, and F. D. Pin, "The particle finite element method: a powerful tool to solve incompressible flows with free-surfaces and breaking waves," *International Journal for Numerical Methods in Engineering,* vol. 61, pp. 964-989, 2004.

[48] H. M. Jaeger, S. R. Nagel, and R. P. Behringer, "Granular solids, liquids, and gases," *Reviews of Modern Physics,* vol. 68, pp. 1259-1273, 1996.

[49] H. A. Janssen, "Versuche über Getreidedruck in Silozellen," *Vereines Deutscher Ingenieure,* vol. 39, pp. 1045-1049, 1895.

[50] A. W. Jenike, *Storage and Flow of Solids*: University of Utah, 1964.

[51] H. Jiang and Y. Xie, "A note on the Mohr–Coulomb and Drucker–Prager strength criteria," *Mechanics Research Communications,* vol. 38, pp. 309-314, 2011.

[52] P. Jonsén, B. I. Pålsson, and H.-Å. Häggblad, "A novel method for full-body modelling of grinding charges in tumbling mills," *Minerals Engineering,* vol. 33, pp. 2-12, 2012.

[53] P. Jonsén, B. I. Pålsson, K. Tano, and A. Berggren, "Prediction of mill structure behaviour in a tumbling mill," *Minerals Engineering,* vol. 24, pp. 236-244, 2011.

[54] M. Jung and U. Rüde, "Implicit Extrapolation Methods for Multilevel Finite Element Computations," *SIAM Journal on Scientific Computing,* vol. 17, pp. 156-179, 1996/01/01 1996.

[55] K. Kamran, R. Rossi, and E. Oñate, "A contact algorithm for shell problems via Delaunay-based meshing of the contact domain," *Computational Mechanics,* vol. 52, pp. 1-16, 2013/07/01 2013.

[56] T. Karlsson, M. Klisinski, and K. Runesson, "Finite element simulation of granular material flow in plane silos with complicated geometry," *Powder Technology,* vol. 99, pp. 29-39, 1998.

[57] A. S. Khan and S. Huang, *Continuum Theory of Plasticity*: Wiley, 1995.

[58] J. B. Knight, C. G. Fandrich, C. N. Lau, H. M. Jaeger, and S. R. Nagel, "Density relaxation in a vibrated granular material," *Physical Review E,* vol. 51, pp. 3957-3963, 1995.

[59] P. M. Knupp, "Algebraic mesh quality metrics for unstructured initial meshes," *Finite Elements in Analysis and Design,* vol. 39, pp. 217-241, 2003.

[60] R. Kobyłka and M. Molenda, "DEM modelling of silo load asymmetry due to eccentric filling and discharge," *Powder Technology,* vol. 233, pp. 65-71, 2013.

[61] K. Krabbenhøft, "A variational principle of elastoplasticity and its application to the modeling of frictional materials," *International Journal of Solids and Structures,* vol. 46, pp. 464-479, 2009.

[62] E. Lajeunesse, A. Mangeney-Castelnau, and J. P. Vilotte, "Spreading of a granular mass on a horizontal plane," *Physics of Fluids,* vol. 16, pp. 2371-2381, 2004.

[63] E. Lajeunesse, J. B. Monnier, and G. M. Homsy, "Granular slumping on a horizontal surface," *Physics of Fluids,* vol. 17, pp. -, 2005.

[64] A. O. Larese, E.; Ross, R., *A Coupled Eulerian-PFEM Model for the Simulation of overtopping in Rockfill Dams* vol. 133. Barcelona, Spain: International Center for Numerical Methods in Engineering, 2012.

[65] H. Ling, D. Yue, V. Kaliakin, and N. Themelis, "Anisotropic Elastoplastic Bounding Surface Model for Cohesive Soils," *Journal of Engineering Mechanics,* vol. 128, pp. 748-758, 2002/07/01 2002.

[66] G. R. Liu and B. Liu, *Smoothed Particle Hydrodynamics: A Meshfree Particle Method*: World Scientific, 2003.

[67] J. Lubliner, *Plasticity Theory*: Macmillan Publishing, 1990.

[68] A. Mangeney-Castelnau, F. Bouchut, J. P. Vilotte, E. Lajeunesse, A. Aubertin, and M. Pirulli, "On the use of Saint Venant equations to simulate the spreading of a granular mass," *Journal of Geophysical Research: Solid Earth,* vol. 110, p. B09103, 2005.

[69] M. Mier-Torrecilla, S. R. Idelsohn, and E. Oñate, "Advances in the simulation of multi-fluid flows with the particle finite element method. Application to bubble dynamics," *International Journal for Numerical Methods in Fluids,* vol. 67, pp. 1516-1539, 2011.

[70] B. K. Mishra and C. Thornton, "An improved contact model for ball mill simulation by the discrete element method," *Advanced Powder Technology,* vol. 13, pp. 25-41, 2002.

[71] N. Mitarai and F. Nori, "Wet granular materials," *Advances in Physics,* vol. 55, pp. 1-45, 2006.

[72] S. Moriguchi, R. Borja, A. Yashima, and K. Sawada, "Estimating the impact force generated by granular flow on a rigid obstruction," *Acta Geotechnica,* vol. 4, pp. 57-71, 2009/03/01 2009.

[73] A. Mota, W. Sun, J. Ostien, J. Foulk, III, and K. Long, "Lie-group interpolation and variational recovery for internal variables," *Computational Mechanics,* pp. 1-19, 2013/06/14 2013.

[74] Z. Mróz and S. Pietruszczak, "A constitutive model for sand with anisotropic hardening rule," *International Journal for Numerical and Analytical Methods in Geomechanics,* vol. 7, pp. 305-320, 1983.

[75] R. M. Nedderman, *Statics and Kinematics of Granular Materials*: Cambridge University Press, 2005.

[76] J. Oliver, J. C. Cante, R. Weyler, C. González, and J. Hernandez, "Particle Finite Element Methods in Solid Mechanics Problems," in *Computational Plasticity*. vol. 7, E. Oñate and R. Owen, Eds., ed: Springer Netherlands, 2007, pp. 87-103.

[77] J. Oliver, S. Hartmann, J. C. Cante, R. Weyler, and J. A. Hernández, "A contact domain method for large deformation frictional contact problems. Part 1: Theoretical basis," *Computer Methods in Applied Mechanics and Engineering,* vol. 198, pp. 2591-2606, 2009.

[78] J. Oliver, A. E. Huespe, and J. C. Cante, "An implicit/explicit integration scheme to increase computability of non-linear material and contact/friction problems," *Computer Methods in Applied Mechanics and Engineering,* vol. 197, pp. 1865-1889, 2008.

[79] E. Oñate, M. Celigueta, S. Idelsohn, F. Salazar, and B. Suárez, "Possibilities of the particle finite element method for fluid–soil–structure interaction problems," *Computational Mechanics,* vol. 48, pp. 307-318, 2011/09/01 2011.

[80] E. Oñate, S. R. Idelsohn, M. A. Celigueta, and R. Rossi, "Advances in the particle finite element method for the analysis of fluid–multibody interaction and bed erosion in free surface flows," *Computer Methods in Applied Mechanics and Engineering,* vol. 197, pp. 1777-1800, 2008.

[81] J. Y. Ooi and K. M. She, "Finite element analysis of wall pressure in imperfect silos," *International Journal of Solids and Structures,* vol. 34, pp. 2061-2072, 1997.

[82] A. Piccolroaz, D. Bigoni, and A. Gajo, "An elastoplastic framework for granular materials becoming cohesive through mechanical densification. Part I – small strain formulation," *European Journal of Mechanics - A/Solids,* vol. 25, pp. 334-357, 2006.

[83] J. Ravenet, "Silos problems," *Bulk Solids Handling,* vol. 1, p. 14, 1981.

[84] P. Richard, M. Nicodemi, R. Delannay, P. Ribiere, and D. Bideau, "Slow relaxation and compaction of granular systems," *Nat Mater,* vol. 4, pp. 121-128, 2005.

[85] M. W. Richman, "The Source of Second Moment in Dilute Granular Flows of Highly Inelastic Spheres," *Journal of Rheology,* vol. 33, pp. 1293-1306, 1989.

[86] I. Roberts, "Determination of the Vertical and Lateral Pressures of Granular Substances," *Proceedings of the Royal Society of London,* vol. 36, pp. 225-240, 1883.

[87] J. M. Rodríguez Prieto, "Numerical modeling of metal cutting processes using the particle finite element method (PFEM)," Doctoral Degree, Resistència de Materials i Estructures a l'Enginyeria, Universitat Politècnica de Catalunya, 2014.

[88] K. H. Roscoe, A. N. Schofield, and C. P. Wroth, "On The Yielding of Soils," 8, Géotechnique, 1958.

[89] J. M. Rotter, J. Y. Ooi, J. F. Chen, P. J. Tiley, and I. Mackintosh, "Flow Pattern Measurement in Full Scale Silos," The University of Edinburgh, Edinburgh, Scotland, UK R95-008, 1995.

[90] C. Rycroft, K. Kamrin, and M. Bazant, "Assessing continuum postulates in simulations of granular flow," *Journal of the Mechanics and Physics of Solids,* vol. 57, pp. 828-839, 2009.

[91] S. K. Saxena, R. K. Reddy, and A. Sengupta, "Verification of a constitutive model for granular materials," *Proceedings of International Workshop on Constitutive Equations for Granular Non-cohesive soils,* pp. 629-645, July 1987 1987.

[92] G. Si, H. Cao, Y. Zhang, and L. Jia, "Experimental investigation of load behaviour of an industrial scale tumbling mill using noise and vibration signature techniques," *Minerals Engineering,* vol. 22, pp. 1289-1298, 2009.

[93] J. C. Simo and T. J. R. Hughes, *Computational Inelasticity*: Springer, 1998.

[94] J. Stener, "Development of Measurement System for Laboratory Scale Ball Mill," Master Thesis, Luleå University of Technology, Luleå, Sweden, 2011.

[95] Q. Sun, F. Jin, J. Liu, and G. Zhang, "Understanding force chains in dense granular materials," *International Journal of Modern Physics B,* vol. 24, pp. 5743-5759, 2010/11/20 2010.

[96] Q. Sun, F. Jin, and G. Zhang, "Mesoscopic properties of dense granular materials: An overview," *Frontiers of Structural and Civil Engineering,* vol. 7, pp. 1-12, 2013/03/01 2013.

[97] T. Sundström, "An Autogenous Mill Application in the Mining Industry," SPM Instrument, Strängnäs, Sweden2013.

[98] B. Tang, J. F. Li, and T. S. Wang, "Some improvements on free surface simulation by the particle finite element method," *International Journal for Numerical Methods in Fluids,* vol. 60, pp. 1032-1054, 2009.

[99] K. Tano, *Continuous Monitoring of Mineral Processes with Special Focus on Tumbling Mills: A Multivariate Approach*: Luleå University of Technology, 2005.

[100] U. S. G. S. USGS. (2010). *Landslides in Central America*. Available: http://landslides.usgs.gov/research/other/centralamerica.php

[101] K. C. Valanis and J. F. Peters, "An endochronic plasticity theory with shear-volumetric coupling," *International Journal for Numerical and Analytical Methods in Geomechanics,* vol. 15, pp. 77-102, 1991.

[102] R. Weyler, J. Oliver, T. Sain, and J. C. Cante, "On the contact domain method: A comparison of penalty and Lagrange multiplier implementations," *Computer Methods in Applied Mechanics and Engineering,* vol. 205–208, pp. 68-82, 2012.

[103] M. Wójcik and J. Tejchman, "Modeling of shear localization during confined granular flow in silos within non-local hypoplasticity," *Powder Technology,* vol. 192, pp. 298-310, 2009.

[104] T. F. Wolff, "Soil Relationships and Classification," in *The Civil Engineering Handbook, Second Edition*, ed: CRC Press, 2002.

[105] W. Wu, E. Bauer, and D. Kolymbas, "Hypoplastic constitutive model with critical state for granular materials," *Mechanics of Materials,* vol. 23, pp. 45-69, 1996.

[106] Y.-H. Wu, J. M. Hill, and A. Yu, "A finite element method for granular flow through a frictional boundary," *Communications in Nonlinear Science and Numerical Simulation,* vol. 12, pp. 486-495, 2007.

[107] H. S. Yu, *Plasticity and Geotechnics*: Springer, 2007.

[108] O. C. Zienkiewicz, R. L. Taylor, and J. Z. Zhu, "Finite Element Method - Its Basis and Fundamentals (6th Edition)," ed: Elsevier.

[109] O. C. Zienkiewicz and J. Z. Zhu, "The superconvergent patch recovery and a posteriori error estimates. Part 1: The recovery technique," *International Journal for Numerical Methods in Engineering,* vol. 33, pp. 1331-1364, 1992.